Systèmes communicants haut-débit et bas coûts par guide d'ondes en plastique

Florian Voineau

université de BORDEAUX

THÈSE PRÉSENTÉE

POUR OBTENIR LE GRADE DE

DOCTEUR DE

L'UNIVERSITÉ DE BORDEAUX

ÉCOLE DOCTORALE DES SCIENCES PHYSIQUES ET DE L'INGÉNIEUR

SPÉCIALITÉ ÉLECTRONIQUE

Par Florian VOINEAU

Systèmes communicants haut-débit et bas coûts par guide d'ondes en plastique

Sous la direction de : Éric KERHERVÉ

Soutenue le 11 Octobre 2018

Membres du jury :

M. VERDEYME, Serge	Professeur	XLIM Limoges	Président du jury
M. BOURDEL, Sylvain	Professeur	Grenoble INP	Rapporteur
M. PERSON, Christian	Professeur	IMT Atlantique	Rapporteur
M. BUSSON, Pierre	Docteur	STMicroelectronics	Examinateur
M. KERHERVÉ, Éric	Professeur	Bordeaux INP	Directeur de thèse
M. GHIOTTO, Anthony	Maître de Conférences	Bordeaux INP	Co-encadrant
M. MARTINEAU, Baudouin	Docteur	CEA Leti	Co-encadrant
Mme SIÉ, Mathilde	Docteur	STMicroelectronics	Co-encadrant
M. LARIE, Aurélien	Docteur		Membre invité
M. BELOT, Didier	Ingénieur HDR	STMicroelectronics / CEA Leti	Membre invité

Titre : Systèmes communicants haut-débit et bas coûts par guide d'ondes en plastique

Résumé :

L'évolution actuelle de la société vers un monde de plus en plus numérique et connecté nécessite des liens de communication à la fois haut-débit et bas coûts. A cette fin, les guides d'ondes en plastique proposés ces dernières années visant les bandes de fréquences millimétriques (mm) offrent un compromis performance / coût très attractif. Profitant ainsi de larges bande-passantes de l'ordre de plusieurs gigahertz (GHz), des performances des technologies CMOS avancées aux fréquences mm mais également de tolérances d'assemblage relâchées, des systèmes de communication avec de tels guides d'ondes en plastique pourraient offrir des débits de plusieurs gigabits par seconde (Gb/s) sur des distances de plusieurs mètres de manière abordable.

Dans ce travail, la conception d'un guide d'ondes en plastique est tout d'abord présentée en se basant à la fois sur des résultats théoriques et de simulation électromagnétique. Bien que les promesses de faible atténuation aient effectivement été confirmées, certaines limitations du confinement et de la robustesse aux contacts extérieurs sont également apparues. L'ajout d'une mousse protectrice est brièvement investiguée, mais une géométrie innovante de guide présentant des caractéristiques améliorées est principalement détaillée.

Des thématiques « systèmes » sont ensuite explorées afin de construire un système de communication utilisant ce nouveau canal de propagation. Une architecture combinant la modulation de phase en quadrature (QPSK) et le multiplexage en fréquence est ainsi introduite. L'interface entre le circuit et le guide d'ondes a par ailleurs été identifiée comme une limitation potentielle à la bande-passante globale du système. Par conséquent, une transition très large-bande a été conçue et testée pour lever ce verrou. De même, en raison des inconvénients des techniques usuelles de démodulation de signaux mm QPSK, une topologie originale utilisant les non-linéarités des oscillateurs à injection a été développée.

Enfin, la conception d'un émetteur mm en technologie silicium avancée (CMOS 28 nm FD-SOI) est décrite. Les contributions majeures incluent l'introduction de coupleurs hybrides intégrés à haute-performance ainsi que la réalisation d'un circuit de synchronisation. Celui-ci présente une large plage de capture et permet un fonctionnement à faible bruit de phase lorsque le système est verrouillé sur la cinquième harmonique du signal de référence. Des mesures sur signaux modulés ont également permis de mettre en évidence la capacité de l'émetteur à transmettre des débits très élevés de plusieurs Gb/s.

Mots clés : Faibles coûts, Guides d'ondes, Guides d'ondes en plastique, Haut-débit, Millimétrique, Plastique, QPSK, RF, Transitions

Title: Plastic Waveguides for High Speed Communications

Abstract:

In a world willfully transitioning to the *Digital Age*, the thirst for connectivity demands high-speed communication links at low cost. In this context, affordable plastic waveguides have been proposed as a disruptive propagation channel in the millimeter-wave (mmW) range. Benefiting from multi gigahertz (GHz) bandwidths and mmW capabilities of advanced CMOS technologies as well as relaxed assembly tolerances requirements, cost-effective communication systems based on plastic waveguides could offer multi gigabits per second (Gb/s) data rates over several meters distances.

In this work, the design of plastic waveguide channels is first discussed using both a theoretical approach and Electromagnetic (EM) simulations. Although low attenuation promises have been confirmed, some limitations are also highlighted, especially as regards confinement ability and robustness to external contacts. Solutions involving foam coating are briefly investigated and an innovative plastic waveguide design demonstrating improved characteristics is introduced.

System-level topics are then explored in order to build a communication system using the previously presented channel. A new architecture, which combines Quadrature Phase Shift Keying (QPSK) and frequency multiplexing, is found to be much more suitable. The transition from the circuit to the plastic waveguide has also been identified as a potential bandwidth bottleneck. Consequently, a wideband microstrip to WR-12 transition has been designed. Another limitation concerning the demodulation of QPSK mmW signals is investigated and an original topology using the non-linearities of Injection Locked Oscillators (ILO) has been developed.

Finally, the design of a mmW transmitter in an advanced silicon technology node (CMOS 28 nm FD-SOI) is described. Major contributions include the introduction of high-performance integrated hybrid couplers and the realization of a wide locking range synchronization circuit enabling low phase-noise operation when locked on the fifth harmonic of a reference signal. Measurements on modulated signals have validated the transmitter high data-rate capability of several Gb/s.

Keywords: High data rate, Low-cost, Millimeter-wave, Plastic waveguides, QPSK, RF, Transitions, Waveguides

Unité de recherche

Université de Bordeaux, Laboratoire IMS, CNRS UMR 5218, Bordeaux INP, 351 cours de la Libération, Bâtiment A31, 33405 Talence

Remerciements

A l'heure d'écrire ces lignes, je mesure le nombre conséquent de personnes m'ayant apporté leur aide ou leur soutien que ce soit au sein du laboratoire IMS, du CEA Leti ou de STMicroelectronics, où les différents épisodes de cette thèse se sont tour à tour déroulés. Je profite de ces quelques lignes pour leur adresser ici toute ma reconnaissance.

Je remercie tout d'abord Monsieur Serge Verdeyme pour avoir accepté de présider le jury de cette thèse, ainsi que Messieurs Sylvain Bourdel et Christian Person pour en avoir été les rapporteurs. Je remercie aussi Messieurs Pierre Busson, Aurélien Larie et Didier Belot pour leur participation en tant qu'examinateur et membre invité. Merci à tous pour l'intérêt que vous avez témoigné à mon travail !

Je remercie également mes encadrants de thèse pour tout ce qu'ils m'ont transmis pendant plus de 3 ans, tant sur le plan technique qu'humain. Merci à Baudouin Martineau pour sa bonne humeur, ses conseils toujours avisés et son sens pratique dans les expérimentations. Je réalise qu'il a bien fait de me pousser à faire une thèse, moi qui ne partais pourtant pas convaincu ! Merci à Mathilde Sié pour son énergie, son implication inébranlable et sa ténacité (« on ne lâche rien ! »). Merci à Anthony Ghiotto pour ses connaissances et son aide précieuse dans la conception d'une transition large-bande. Merci enfin à Eric Kerhervé pour avoir accepté d'être le directeur de cette thèse et pour m'avoir accueilli au sein de l'équipe CSH du laboratoire IMS.

Je remercie l'ensemble des thésards de l'IMS qui ont fait de mon séjour à Bordeaux un vrai moment de « plaisiriance » : Aurélien Larie, David Polge, Yoan Veyrac, Manuel Potereau, Jérémie Prades, Boris Moret, Florent Torres, Fabien Mesquita, Romain Berges, Raphaël Guillaume. J'ai également une pensée toute particulière pour Magali De Matos dont la bonne humeur et les compétences ont rendu possible un grand nombre des résultats expérimentaux présentés dans ce travail. Je réalise a posteriori qu'il faut une grande ouverture d'esprit pour accepter de déployer plus d'une dizaine de mètres de câble plastique dans un laboratoire RF ! Je remercie aussi Mickaël Perchicot pour son aide dans la recherche d'un partenaire industriel capable de fabriquer la Magic Wheel. Mickaël a de plus contribué, avec l'aide de Nhu Huan Nguyen et d'Anthony Ghiotto, à la validation expérimentale du prototype. Merci à Nathalie Deltimple pour sa bienveillance à la tête de l'équipe CSH et à Yann Deval (alias Super Breton !) pour la bonne humeur qu'il distille dans son laboratoire.

Je remercie le laboratoire LAIR du CEA Leti qui m'a chaleureusement accueilli pendant plus de 2 ans et fourni de précieux moyens de caractérisation. Merci à son chef Eric Mercier ainsi qu'à Pierre Vincent, son supérieur, ce dernier ayant aussi joué le rôle d'encadrant officiel au début de cette thèse au sein du Leti. Je tiens par ailleurs à remercier spécifiquement Alexandre Siligaris, Clément Jany et José Luis González Jiménez dont les discussions passionnantes, et souvent passionnées, concernant la conception de circuits aux fréquences millimétriques et leurs différentes architectures ont nourri ce travail. Je souhaite aussi remercier Cédric Dehos pour sa maîtrise du démonstrateur à 60 GHz « Eagle » et de l'oscilloscope temps réel (*Sans maîtrise la puissance n'est rien*), ainsi que pour ses connaissances pointues en matière de Systèmes Electroniques. Merci d'avoir également porté la casquette d'encadrant officiel CEA à un moment… enfin je crois ! Je voudrais rendre hommage à l'esprit

visionnaire de Didier Belot qui a cru à ce projet dès ses débuts, sans qui le stage et la thèse associée ne se seraient probablement pas concrétisés pour moi, et qui a œuvré pour le montage de projets de recherche en lien avec la thématique. Pour compléter ce tour d'horizon au sein du LAIR, je remercie l'ensemble des personnes avec lesquelles j'ai eu la chance de tisser des relations à la fois professionnelles et amicales, notamment grâce à une équipe soudée de thésards (et assimilés) : Guillaume Waltener, Raphaël Vansebrouck, Baptiste Grave, Jennifer (Zaini) Desèvedavy, Anthony Goavec, Marguerite Marnat, David Buffeteau, Zoltan Nemes, Tu Vo Tien, Saad Boutayeb, Abdessamad Boulmirat, César Vásquez.

Je remercie aussi bien évidemment l'entreprise STMicroelectronics pour m'avoir permis, par sa confiance et sa recherche de pointe, de réaliser un stage de fin d'études puis une thèse qui ont changé ma vie. A cet effet, je remercie Daniel Gloria, Luc Garcia et Jacky Uginet pour m'avoir accueilli successivement dans leur équipe respective. J'adresse de même un remerciement particulier à Delphine Maury pour m'avoir accordé sa confiance alors que la fin de mon contrat approchait. A Baudouin Martineau et Mathilde Sié, présents depuis le tout début de cette aventure, s'ajoute Romain Pilard dont la pédagogie et l'encadrement exceptionnels en tant qu'encadrant de stage m'ont permis d'acquérir un grand nombre de ses compétences en simulation électromagnétique en l'espace de quelques mois. Il est très clair que cette maîtrise a été déterminante dans l'obtention des résultats présentés aujourd'hui dans le second chapitre de ce document. Par ailleurs, la bonne ambiance rayonnante au sein de la désormais célèbre *Mich' RF Team* a été un élément essentiel dans mon engagement à accepter de faire une thèse. Je remercie ici ses dignes représentants actuels ou passés : Simon Bouvot, Alice Bossuet, Sandrine Oeuvrard, Jean-Marc Boucaud, Audrey Michard, Cybelle Bellem Goncalves, Arun Bhaskar, Elsa Lacombe, Joao Azevedo Goncalves, Cédric Durand, Yohann Solaro, Frédéric Gianesello, Sébastien Jan, Thomas Quemerais, Romain Debroucke, Michel Buczko, Hervé Petiton, Metig Hello, Jeff Nowakowski, José Lugo, Françoise Baille, Gérard Haury, Dimitri Goguet. Bienvenue aussi aux petits nouveaux : Ophélie Foissey, Vincent Gidel, Francesco Filice, Victor Fiorese, Thomas Capelli et Alexandre Flete !

Je remercie par la même occasion Florence Sonnerat d'œuvrer en la qualité de *Party Rock Manager* de l'équipe. Merci pour ta gentillesse, ta bonne humeur, ton altruisme, et bien plus encore !

Merci aussi à la bande des thésards de la *Team Galy* (Thomas Bédécarrats, Louise De Conti, Renan Lethiecq, Mohammed Tmimi) pour m'avoir accueilli à leur table tout en transformant mes repas à la cantine en moments de pure convivialité ☺. Un grand merci à mes autres compagnons de bonne fortune : Mathieu Vallet, Hani Sherry, Réda Kasri, Hanae Zegmout, Sotiris Athanasiou, Matteo Causo, Hani Malloug, Mirjana Videnovic-Misic, David Gaidioz, Robin Benarrouch, Jérémie Forest, Clément Beauquier.

Je remercie enfin toutes les personnes très compétentes qui m'ont apporté leur aide au sein de STMicroelectronics. Même si une liste exhaustive est malheureusement impossible, je remercie spécialement Vincent Knopik, Benoit Butaye, Lionel Vogt, Nicolas Pelloux, Clément Charbuillet, Philippe Cathelin et Thierry Schwartzmann pour leur contribution. De plus, je remercie tous mes collègues de l'équipe Design pour leur accueil bienveillant : Emmanuel Rouat, Patrice Garcia, Raphaël Paulin, Denis Pache, Christophe Arricastres, Valérie Danelon, Raffaele Bianchini, Jérôme Lajoinie, Jasmina Antonijevic, Laurent Chabert.

Pour finir, je remercie du fond du cœur ma famille et mes parents pour leur soutien indéfectible (à travers tous les sens que peut revêtir ce mot), leur amour intarissable et leurs valeurs exemplaires.

"Compassion has no limit. Kindness has no enemy."

Yogi Tea

Table of Contents

List of Tables ..... **v**

List of Figures ..... **vi**

List of Abbreviations ..... **xvi**

Chapter 1: Introduction **1**

1.1. Motivation 1
1.2. State of the Art 2
1.2.1. Twisted Copper Pairs 2
1.2.2. Optical Fibers 3
1.2.3. Millimeter-wave Free Space Propagation 4
1.2.4. Plastic Waveguide Systems 5
1.3. Thesis Outline 6
References 7

Chapter 2: Building a Plastic Waveguide Channel **9**

2.1. Review of the State of the Art 9
2.1.1. Historical Perspective and Current Applications of Metallic Waveguides 9
2.1.2. From D. Hondros and P. Debye to P. Reynaert: A Century of Progress 11
2.1.2.1. Historical Perspective 11
2.1.2.2. Latter developments and current state of the art review 12
2.2. Waveguide Basics 17
2.2.1. The Existence of Modes in Waveguides 17
2.2.2. The Rectangular (Metallic) Waveguide 18
2.2.3. Optical Fibers and Useful Approximations in Geometrical Optics 22
2.3. Understanding Dielectric Waveguides: The Dielectric Slab Example 28
2.3.1. Problem Description 28
2.3.2. Propagating Modes 28
2.3.3. Fields Confinement and Dispersion Relation Diagram 30
2.3.4. Attenuation 35
2.4. Choosing Design Parameters 35
2.4.1. Operating Frequency 35
2.4.2. Materials Choice 36
2.4.3. Footprint Consideration 38
2.4.4. Confinement and Environmental Considerations 39
2.4.5. Costs Considerations 42
2.4.6. Plastic Waveguides Design Guidelines 44
2.5. The Surrounding Environment and Contact Sensitivity Issue: An Innovative Design Proposal 45

2.5.1. Contact Sensitivity Issue 45
2.5.2. Magic Wheel: An Innovative Design Proposal 47
2.6. Excitation Conditions: On the Importance of Couplers 48
2.7. Measurement Results 53
2.7.1. Measurement Setup 53
2.7.2. Tubular Geometries 54
2.7.2.1. Low-Loss / Cow-Confinement Design 54
2.7.2.2. Maximum Confinement at the Edge of Single-Mode Operation 57
2.7.3. Magic Wheel Design 59
2.8. Conclusions and Comparison with the State of the Art 63
2.9. Perspectives 67
2.9.1. Orthogonal Polarization Modes Characterization 67
2.9.2. Micro-structured Millimeter Wave Plastic Waveguides 68
References 71

Chapter 3: Building a Millimeter-wave System around the Channel 75

3.1. System Level Specifications 75
3.2. Millimeter-wave System Basics 78
3.3. Application to Plastic Waveguide Systems 84
3.3.1. System Overview 84
3.3.2. Interconnects Challenges 86
3.3.3. Broadband Microstrip Line to Waveguide Transition 89
3.3.4. Comparison with the State of the Art 94
3.4. Link Budget Analysis 94
3.5. Analysis of Millimeter-wave QPSK Modulators and Demodulators 97
3.5.1. Canonical Demodulation of *M*-ary PSK Constellations 97
3.5.2. D-QPSK Demodulation Using Time-Delay Comparison 98
3.5.3. Carrier and Data Recovery with a Costas Loop 99
3.5.4. Limitations Summary of Millimeter-wave QPSK Demodulators 100
3.6. ILO Based Demodulation for High-Speed QPSK Systems 101
3.6.1. ILO Theoretical Basics 101
3.6.2. ILO Demodulation Concept: Frequency-domain Presentation 106
3.6.3. Demodulation Illustration in the Time-domain 108
3.6.4. Design Considerations 109
3.7. Demonstration at 60 GHz 111
3.8. Conclusions 113
3.9. Perspectives 114
3.9.1. Low Loss Interconnects 114
3.9.2. ILO Based Demodulation Further Investigations and Improvements 115
3.9.2.1. Pulse Shaping Impact 116
3.9.2.2. Feedback loop 117
References 118

Chapter 4: Designing a Millimeter-wave RFIC Targeting Multi-Gigabit Operation 121

4.1. Transmitter Architecture 121
4.2. Overview of STMicroelectronics 28 nm CMOS FD-SOI Technology and Comparison with the State of the Art 122
4.2.1. Front End of Line Performance 123

4.2.2. Back End of Line Performance 125
4.3. Low Power Oscillator 126
4.4. Injection Circuit for Locked Operation 128
4.5. Quadrature Signal Generation 131
4.6. QPSK Modulator 132
4.7. Low Power and High Efficiency Power Amplifier 135
4.8. Dual Band Combiner using Differential Vertical Hybrid Coupler 138
4.9. Optimized Low Capacitance RF Pads for Wideband Applications 140
4.10. Measurement Results 142
4.10.1. Preliminary Validation of the DVHC Component 143
4.10.2. Measurement Setup 144
4.10.3. Injection Locking Measurements 145
4.10.4. Modulated Signals Measurements 146
4.11. Conclusions and Comparison with State-of-the-Art Realizations 149
4.12. Perspectives 150
4.12.1. Dual-Band Implementation and Integration of the External Signal Reference 150
4.12.2. Serial Interface Integration and EVM Calibration 151
4.12.3. Versatile Multi-Modulation Compliancy 152
4.12.4. Dual Polarization Investigation 153
References 155

Chapter 5: Conclusions 157

3.10. Summary and Contributions 157
3.11. Future Work 158
3.12. List of Publications 159

Appendix A: Foam-coated Waveguide Study 161

Appendix B: Reflections in Low Loss Waveguides 167

Appendix C: Influence of Bends in Plastic Waveguides 173

C.1. Impact on Transmission Parameters 174
C.2. Impact on Reflection Parameters 175
C.3. Impact on Polarization Isolation 176
C.4. Impact of the Dielectric Constant of the Cladding 177
C.5. Conclusion 178

Appendix D: The Energy - Bandwidth Trade-off in Digital RF Modulations 181

D.1. Introduction 181
D.2. On-Off Keying (OOK) 182
D.3. Amplitude Shift Keying (ASK) 183
D.4. Pulse Amplitude Modulation (PAM) 183
D.5. Binary Phase Shift Keying (BPSK) 184
D.6. *M*-ary Phase Shift Keying (MPSK) 185
D.7. Quadrature Phase Shift Keying (QPSK) 186
D.8. Quadrature Amplitude Modulation (QAM) 187

D.9. BER Summary 187
References 190

Appendix E: Closed-Form Derivation of Adler's Equation 191

Appendix F: Demonstrator Comparison with the State of the Art..... 195

References 195

Appendix G: Frequency Plan 197

List of Tables

Table 2-1: Summary of TE_{mn} and TM_{mn} modes main characteristics in rectangular metallic waveguides. 20
Table 2-2: Comparison of circular dielectric waveguides with respect to rectangular, square and circular metallic waveguides in terms of fundamental and lowest higher order mode cut-off frequencies. 25
Table 2-3: Dielectric properties of ordinary polymers and crystalline materials provided for comparison....37
Table 2-4: External diameter comparison of some widespread transmission standards. ..39
Table 2-5: Summary of excitation schemes reported in the literature along with their respective advantages and drawbacks. 49
Table 2-6: Measured dimensions of tubular HDPE waveguide samples....54
Table 2-7: State of the Art comparison of plastic waveguides. 66
Table 3-1: Comparison of the most promising standards for consumer, professional and automotive markets. 77
Table 3-2: Summary of the ideal performances of the mmW plastic waveguide system...77
Table 3-3: Summary of dimensions [in millimeters] for the proposed microstrip line to waveguide transition. 91
Table 3-4: State of the art comparison of PCB transmission lines to waveguide transitions. 94
Table 3-5: Millimeter-wave QPSK demodulation techniques summary....100
Table 3-6: QPSK convergence criterion assuming a 3 dB SNR penalty....110
Table 3-7: Link performance summary for different modulations (Magic Wheel – 4 m). Note that QPSK is achieved using both Tx and Rx circuits while 16QAM and 64QAM are obtained with the Tx and a real-time oscilloscope as a demodulator. 112
Table 4-1: ILO transistors sizing and associated biasing and supply voltages. 127
Table 4-2: DVHC Performance comparison with state-of-the-art mmW hybrid couplers. 139
Table 4-3: Circuit comparison with state-of-the-art realizations featuring wideband mmW frequencies combining (only on-chip CMOS considered). 150
Table C-1: Considered radii of the PE plastic waveguide rods under scrutiny. 174
Table D-1: Summary of SER and BER closed-form formulas for different modulations. 188
Table D-2: Required SNR or $\frac{E_b}{N_0}$ to satisfy a BER of 10^{-12}. 189
Table F-1: Demonstrator comparison with the state of the art. 196

List of Figures

Figure 1-1: Theoretical data rate specifications of the different generations of USB and Thunderbolt standards as a function of their release year. 2
Figure 1 2: Transmission rate records per year, illustrating Keck's law in optical transmission, reproduced from [**Hecht, 2016**]. 3
Figure 1-3: Free space path loss assuming a 1 m-long line-of-sight propagation. 4
Figure 2-1: Figures taken from [**Fukuda, 2011**] presenting the proposed plastic waveguide system at 0.12 m (a) and 1 m (c). A close-up view of the antennas-based excitation is reported in (b) and an EM simulation is shown in (d). 12
Figure 2-2: Figures taken from [**Dolatsha, 2013**] presenting the proposed polarization-multiplexed scheme (a) and associated plastic waveguide interconnect (b) 13
Figure 2-3: Figures reproduced from [**Tytgat, 2013**] illustrating the proposed on-chip bondwire antenna as a cost-efficient interface between a plastic waveguide (a) and a mmW receiver based on a long plastic waveguide (b). 13
Figure 2-4: Figures reproduced from [**Kim, 2013**]. A new coupler to in-package antennas and a tubular low-loss waveguide are presented on the left and on the right sides respectively. 14
Figure 2-5: Figures from [**Volkaerts, 2015**] showing a tubular PTFE waveguide excited by different couplers on Rx/Tx sides in (a) and (b), and the operating system in (c) respectively. 14
Figure 2-6: Figures from [**Van Thienen, 2016**] introducing a novel coupler at both Tx/Rx levels combining flip-chip and SIW technologies in (a). The SIW to plastic waveguide connector exhibit only 3.4 dB loss at 120 GHz (b) so that the total loss between the chip and the waveguide is 3.4 dB (c). 15
Figure 2-7: Figures from [**Reynaert, 2017**] showing a solid PTFE core waveguide coated with a 6 mm diameter PTFE foam to improve immunity to external contact in (a). The impact of the foam regarding attenuation and group delay is presented in (b) and (c). 15
Figure 2-8: Figures from [**Nickel, 2014**] presenting a novel dielectric waveguide assembly made of a rectangular dielectric waveguide supported by embedded thin strings placed periodically. A protective tube prevents detrimental contacts and limits bending. 16
Figure 2-9: ISI in an overmoded waveguide due to mode-dependent group velocities. 18
Figure 2-10: Canonical design description of rectangular metallic waveguides. 19
Figure 2-11: Propagation constants diagram in a WR-12 standard air-filled metallic waveguide. 19
Figure 2-12: Fundamental TE_{10} mode in a WR-12 metallic waveguide. This mode is vertically polarized in the cross-section (a). E-field is distributed homogeneously in the vertical direction and has a sinusoidal distribution horizontally (b – log scale). 20
Figure 2-13: Theoretical conductor loss as a function of frequency for different metallic waveguide standards. Reproduced from [**Microwaves101, 2015**]. 21
Figure 2-14: Propagation constant and GDPUL in a standard WR-12 waveguide for the fundamental TE_{10} mode. 22
Figure 2-15: An optical fiber made of a circular core surrounded by a cladding medium. 22

Figure 2-16: Cylindrical dielectric waveguide with non-magnetic materials. 23
Figure 2-17: Section comparison of the circular dielectric waveguide with respect to various metal counterparts. All waveguides are designed to have a 90 GHz maximum single-mode frequency. The dielectric material has $\varepsilon_r = 2.3$.....25
Figure 2-18: Fundamental HE_{11} mode EM fields simulation in cylindrical dielectric waveguides ($\varepsilon_{r1} = 2.3, \varepsilon_{r2} = 1$): (a) E-field in a 60 GHz maximum single-mode frequency (represented at 120 GHz), (b) E-field in a 120 GHz maximum single-mode frequency (represented at 180 GHz), (c) E_y field component normalized at waveguide center (linear scale) and (d) E_y field component normalized at waveguide center (logarithmic scale). Blue curves and red curves represent E_y at 60 GHz in design (a) and E_y at 120 GHz in design (b) respectively. Solid lines and dot lines refer to E_y in y-direction and x-direction respectively. 26
Figure 2-19: Symmetrical slab dielectric waveguide with non-magnetic materials. 28
Figure 2-20: Graphical resolution of (p, q) couples for TM modes in slab dielectric waveguides (a) and impact of different ${\varepsilon_{r1}}/{\varepsilon_{r2}}$ ratios on fields confinement (b). 30
Figure 2-21: Slab waveguide half-thickness in the maximum single TE_1 / TM_1 mode regime versus frequency for different dielectric materials ($\varepsilon_{r2} = 1$). 31
Figure 2-22: Dispersion diagram of the dielectric slab waveguide ($\varepsilon_{r1} = 2.3, \varepsilon_{r2} = 1$) for the first 4 TM (solid) and TE (dotted) propagation modes (a). The Poynting confinement factor is also computed for the TM_1 mode (b). Thickness is chosen to have a 90 GHz maximum single TE_1 / TM_1 mode frequency (f_{c_1}). 32
Figure 2-23: Poynting confinement factor Γ_{TM_1} as a function of normalized cross-section A_{norm} 33
Figure 2-24: Dispersion diagram of the dielectric slab waveguide ($\varepsilon_{r1} = 2.3, \varepsilon_{r2} = {2.3}/{1.05}$) for the first 4 TE and TM propagation modes (a). The Poynting confinement factor (b) is also computed for the TM_1 mode (green) and compared to the configuration in Figure 2-22 (blue). Thickness is chosen to have a 90 GHz maximum single TE_1 / TM_1 mode frequency (f_{c_1}). 34
Figure 2-25: (a) Normalized E-field in the x-direction for the TM_1 mode ($\varepsilon_{r1} = 2.3, \varepsilon_{r2} = 1$). (b) Cross-sectional representation of the propagation in the geometrical optics framework. 34
Figure 2-26: Plane wave attenuation (dB/m) for different unbounded dielectric mediums computed @100 GHz. 38
Figure 2-27: Radius of a cylindrical dielectric waveguide as a function of its maximum single-mode frequency assuming $\varepsilon_{r1} = \varepsilon_r$ and $\varepsilon_{r2} = 1$. Red ($\varepsilon_r = 2$) and blue ($\varepsilon_r = 3$) curves are representative of typical bounds for usual polymers. 39
Figure 2-28: Simulated E-field in dielectric waveguides ($\varepsilon_{r1} = 2.3\ tan(\delta) = 3.8 \cdot 10^{-4}, \varepsilon_{r2} = 1$) with different maximum single-mode frequencies: 60 GHz (a) and 120 GHz (b). Only the fundamental HE_{11} mode is excited. Note that fields intensity are plotted using a log scale 40
Figure 2-29: Poynting confinement computed from the models presented in Figure 2-28 (a) (triangles) and Figure 2-28 (b) (circles). (a) Poynting confinement as a function of frequency and (b) Poynting confinement as a function of the normalized cross-sectional area. 40
Figure 2-30: Attenuation as a function of frequency (a) and illustration of the attenuation / confinement trade-off (b) from the models presented in Figure 2-28 (a) (triangles) and Figure 2-28 (b) (circles). 41
Figure 2-31: Normalized attenuation as a function of confinement from the models presented in Figure 2-28 (a) (triangles) and Figure 2-28 (b) (circles). 41

Figure 2-32: Figures taken from [**Fukuda, 2011**] illustrating the sensitivity to bends (bending radius is estimated to 255 mm). 41
Figure 2-33: Figure taken from [**Reynaert, 2017**] illustrating the sensitivity to bends.....42
Figure 2-34: Resin cost reported in France in March 2017 [**FrCustoms, 2017**] (left scale) and plastics converters demand in Europe in 2016 [**PlasticsEurope, 2018**] (right scale). ..43
Figure 2-35: Proposed plastic waveguide design methodology for fast prototyping. 44
Figure 2-36: Semi-infinite water slab surrounding a 2 mm diameter Teflon waveguide. (a) side view with symmetry conditions enforced and E-field computed at 120 GHz (logarithmic scale). (b) impact on transmission parameters in blue. Undisturbed propagation is provided for comparison in dash black. 45
Figure 2-37: Semi-infinite water slab surrounding a foam-coated 2 mm-diameter Teflon waveguide. (a) isometric view of the simulation model with E-field computed at 120 GHz for a 2 mm-thick foam (not represented since it is made of pure air) and (b) impact of the foam thickness on transmission parameters at different frequencies. 46
Figure 2-38: Description of the Magic Wheel waveguide as presented in [**Voineau, 2018**]. 47
Figure 2-39: Description of the coupler to excite a dielectric rod waveguide (grey) from a WR-12 metallic waveguide using a conically tapered section placed at the center of a large pyramidal horn antenna (not represented for visibility). An isometric view is presented in (a), a top view in (b) and a lateral view in (c). Orange lines indicate metallic conditions imposed by the horn while green lines indicate "radiation boundaries" around the "open" dielectric waveguide. 50
Figure 2-40: Simulated propagation constants at WR-12 port (left) and dielectric rod port (right) of the coupler. 50
Figure 2-41: Field description of possible modes at input and output ports of the coupler. At input, (a) shows that only the fundamental TE_{10}^{V} mode can propagate. At output, (b) and (c) correspond to the degenerated HE_{11}^{H} and HE_{11}^{V} modes respectively. The following higher order mode (d) is the centrally symmetric TM_{01} mode. 51
Figure 2-42: E-field complex magnitude (phase-independent) investigation in the coupler presented in Figure 2-39. Fields are plotted at 90 GHz assuming an input excitation from the WR-12 TE_{10} mode: (a) isometric view, (b) top view, (c) lateral view. Note that all E-field scales are logarithmic. 52
Figure 2-43: S-parameters simulation of the coupler. (a) Reflection parameters and (b) transmission parameters. Mode indices convention is the same as in Figure 2-41. 52
Figure 2-44: Plastic waveguides measurement setup. 53
Figure 2-45: Propagation constants of the first three modes in MOREL 1 waveguide. 55
Figure 2-46: Attenuation (a) and Poynting confinement factor (b) of the dominant HE_{11} mode in MOREL 1 waveguide. 55
Figure 2-47: Measurement results of a 77 cm-long MOREL 1 waveguide. Transmission parameters as measured (black) and gated on the first transmission peak (red) are plotted on the left graph. On the right side, S-parameters are represented in the time domain. ...56
Figure 2-48: Gated transmission parameters of a MOREL 1 waveguide for different lengths (except 2 m – as measured). 56
Figure 2-49: Group delay per unit length in a MOREL 1 waveguide. Simulation (dashed line) and measurement (solid lines) results show good agreement. 57
Figure 2-50: Propagation constants of the first three modes in the MOREL 2 waveguide.58
Figure 2-51: Attenuation (left) and Poynting confinement factor (right) of the dominant HE_{11} mode in MOREL 2 waveguide....58
Figure 2-52: Gated transmission parameters of MOREL 2 waveguide for different lengths. 59

Figure 2-53: Description of the fabricated PTFE Magic Wheel waveguide prototype. Indicated dimensions are derived from accurate measurements provided by the supplier. 59
Figure 2-54: Simulated propagation constants (left) of the lowest order modes in the Magic Wheel design (Figure 2-53) and associated fields maps (right). 60
Figure 2-55: Attenuation (left) and Poynting confinement factor (right) of the dominant HE_{11} mode in Magic Wheel waveguide. 60
Figure 2-56: Gated transmission parameters of Magic Wheel waveguides for different lengths. 61
Figure 2-57: Extracted length dependency using Magic Wheel prototypes reported in Figure 2-56. 61
Figure 2-58: GDPUL for the Magic Wheel waveguide samples shown in Figure 2-56. Measurements (solid lines) are perfectly in-line with the simulation (dash line). 62
Figure 2-59: Compared transmissions of disturbed / undisturbed Magic Wheel waveguides (red / blue) with respect to disturbed / undisturbed MOREL 2 waveguides (black / green) respectively. Solid lines correspond to waveguides as fabricated while dotted lines represent waveguides surrounded by a 1 mm-thick PTFE foam. 63
Figure 2-60: Simulated normalized attenuation (with respect to attenuation at maximum single-mode frequency) versus Poynting confinement. Black, blue and red lines correspond to solid HDPE core, MOREL 1 and MOREL 2 tubes (HDPE) respectively while the green line is related to the Magic Wheel waveguide design (PTFE). 64
Figure 2-61: Description of a dual-polarization coupler between a square metallic waveguide and a conically tapered plastic waveguide (conductors not shown for visibility). An isometric view is presented in (a), a top view in (b) and a lateral view in (c). Orange lines indicate metallic conditions imposed by the horn while green lines indicate "radiation boundaries" around the "open" dielectric waveguide. 67
Figure 2-62: Figures from [**Limpert, 2004**] showing the difference between conventional optical fibers and PCF (a), the wavelength dependent effective cladding index (b), the resulting "band-diagram" (c) and some examples of PCF with 1, 3 and 7 missing holes (d-e). 69
Figure 2-63: "Holey" fibers leveraging total internal reflection (a) and "Hollow core" fibers featuring an equivalent Bragg mirror (b). Figures reproduced from [**Cherif, 2009**]. 69
Figure 3-1: Plastic waveguides applications have been classified in three main categories. 76
Figure 3-2: Time domain and frequency domain description of a 2T-periodic digital clock by means of Fourier series. 78
Figure 3-3: Time domain and frequency domain description of a random data sequence by means of Power Spectral Density. 79
Figure 3-4: Integrated power (absolute value on the left and relative value on the right) as a function of the considered bandwidth. Note that the DC component of the spectrum represents 50% of the total signal power. Besides, the bandwidth defined in Equation (3-6) contains 86% of the total power. 80
Figure 3-5: Representation of a basic amplitude modulation Tx. 80
Figure 3-6: Representation of a basic amplitude demodulation Rx. 81
Figure 3-7: Wireless system interfacing Tx and Rx circuits thanks to antennas. 81
Figure 3-8: Through-air attenuation measured at sea level from 10 to 400 GHz. Attenuation peaks are attributed to molecular resonances. Figure taken from [**TU-Berlin, 2015**]. 83

Figure 3-9: Comparison of propagation loss mechanisms. The FSPL is computed at 60 GHz (red) and shows a logarithmic increase while attenuation in dielectric medium is linear (blue, green, orange, rose and purple lines correspond to 1, 2, 3, 4 and 5 dB/m respectively). 83
Figure 3-10: Wireline system interfacing Tx and Rx circuits through a plastic waveguide. 84
Figure 3-11: 3D overview of the proposed system based on plastic waveguides, illustrating the use of two QPSK-modulated frequency-multiplexed carriers per direction 85
Figure 3-12: Proposed PCB to plastic waveguide connector composed of a large-band PCB to WR-12 transition (a) and a WR-12 to plastic waveguide transition (b). This latter is taken from Chapter 2. 86
Figure 3-13: Typical examples of patch-coupled PCB to waveguide transitions. (a) Slot aperture coupling as proposed in [**Artemenko, 2011**] and (b) double patch resonance reproduced from [**Zhang, 2016**]. 87
Figure 3-14: Probe-coupled PCB to waveguide transition. The probe is placed at an appropriate distance from a "back-short" metallic wall to radiate inside the waveguide in the other direction. Illustration taken from [**Lou, 2008**]. 87
Figure 3-15: GaAs chip to WR-1.5 waveguide transitions (back-to-back). The transition operates from 500 to 725 GHz [**Hurm, 2012**] 88
Figure 3-16: Smooth PCB to waveguide transitions. (a) An antipodal fin-line design taken from [**Mozharovskiy, 2013**] and (b) a tapered-ridge waveguide design from [**Han, 2012**]. 88
Figure 3-17: Isometric split-view of the proposed microstrip to WR-12 transition composed of a (green) PCB housed in a (transparent) metal case with (colored) double ridges. Inset view: zoom on the PCB region showing the dielectric tip 89
Figure 3-18: Different views of the proposed metal case made of top and bottom parts: (a) isometric view of bottom part, (b) isometric view of top part, (c) top view of bottom part, (d) top view of top part. 90
Figure 3-19: Different views of the proposed PCB showing bare dielectric areas (green), copper coated areas (orange) and metallized through vias (blue): (a) top isometric view, (b) bottom view, (c) zoom on bottom view. 90
Figure 3-20: On the left, profiles in the metal housing for top (positive values) and bottom (negative values) parts are presented. On the right, the impedance is simulated at 75 GHz along the section and it is compared with theoretical results. 91
Figure 3-21: Simulated impact on S-parameters of an over-etching on L_2 design variable. (a) Transmission and (b) reflection parameters. Port 1 and port 2 correspond to the microstrip line and WR-12 waveguide respectively. 92
Figure 3-22: E-field magnitude simulated at 75 GHz around the dielectric tip confirming TE_{10} operation only. 92
Figure 3-23: Back-to-back transitions: (a) fabricated prototype with PCB ground plane visible, and (b) measured and simulated S-parameters. 93
Figure 3-24: Measured and simulated group delays of back-to-back transitions. 93
Figure 3-25: Link budget of the proposed system exhibiting a SNR of 22 dB. 95
Figure 3-26: Illustration of data rate and length limitations potentially encountered in plastic waveguide systems. 96
Figure 3-27: Constellations of QPSK and M-ary PSK and associated invariants. 98
Figure 3-28: Conceptual schematic of D-QPSK non-coherent demodulation based on time delay 98

Figure 3-29: Illustration taken from [**Huang, 2011**] of a mmW Costas Loop QPSK demodulator, containing a frequency locking loop (FD) and a phase locking loop (PD)..99
Figure 3-30: Demodulation sensitivity to PRBS length in BPSK (a) and QPSK (b) Costas loops from [**Huang, 2011**]. 100
Figure 3-31: ILO schematic made of a LC-tank (a) and time-domain illustration of the phase locking process (b). 101
Figure 3-32: Representations of Adler's equation. (a) Phase space and (b) time-domain evolutions (assuming $\phi_{ss} = 0$). In this latter, solutions obtained with different methods are compared showing perfect agreement with each other. 103
Figure 3-33: Time-domain evolution of the solution of Adler's equation (a) and associated convergence times plotted as a function of initial phase offset (b). Injection at the free-running frequency is considered in both plots. 104
Figure 3-34: Numerical simulations of convergence times for different values of ϕ_{ss} as a function of the initial phase offset φ_0 106
Figure 3-35: Schematic of the proposed ILO based QPSK demodulation architecture, featuring a variable-gain LNA, an ILO, a phase-shifter, an I/Q mixer and feedback loop for static and dynamic absolute phase compensation. 107
Figure 3-36: The occupied bandwidth of the incoming modulated signal (blue) largely exceeds the locking range of the ILO (green).....107
Figure 3-37: Illustration of the demodulation operation in the time domain for a random symbol sequence and arbitrary design parameters. (a) Schematic and relevant node designations, (b) injected and output phases, (c) demodulated data on I/Q paths. 108
Figure 3-38: SNR penalty as a function of the constellation rotation angle. 109
Figure 3-39: Convergence time constants associated to QPSK phase changes as a function of steady-state phase offset. 110
Figure 3-40: Versatile millimeter-wave propagation using the same transceivers: wireless for short ranges (top) and guided through plastic waveguides for longer ranges (bottom). 111
Figure 3-41: Demonstration of a 4 m link with modulated signals. Face view of the setup (a), waveguide fixation on the ceiling (b) and side view of the setup (c). 112
Figure 3-42: Measured OFDM after propagation in a 4 m-long Magic Wheel plastic waveguide showing 16QAM capability (SNR > 20 dB). 113
Figure 3-43: Single ridge waveguide to PCB transition in D band. (a) 3D view (transparent metal case for clarity), (b) simulated reflection parameters and (c) transmission parameters. Port 1 and Port 2 are assigned to the microstrip and the WR-6 sides respectively. 115
Figure 3-44: Comparison of two different pulse shapes. Solid lanes are related to perfect "square" modulation while dashed lines correspond to a trapezoidal approximation. (a) input and (b) output phases are given. 116
Figure 3-45: Data-assisted demodulation scheme (dashed line) is compared to normal demodulation (solid line) assuming that compensation occurs with a two symbol-time delay. (a) schematic, (b) injected and output phases over time, (c) output phase close-up view.....117
Figure 4-1: Overall schematic of the proposed dual-band QPSK transmitter. 121
Figure 4-2: Overall schematic of the realized 83.3 GHz QPSK transmitter. 122
Figure 4-3: Superior FD-SOI transistor performance. Cross-section comparative view of a Bulk transistor (a) and a FD-SOI transistor (b) respectively. Transition frequency f_T (c) and Maximum Available Gain at 60 GHz (d) as measured in 28 nm FD-SOI (including full back-end of line parasitics). Data reproduced from [**Shopov, 2014**]. 123

Figure 4-4: Summary of peak f_T (a) and f_{max} (b) for different technological processes as a function of the critical lithography dimension (i.e., emitter width or channel length). Note that red squares represent the results of the DOTSEVEN project (SiGe HBT), while the brown crosses are the best InP HBT data available. Figures reproduced from [**Rinaldi, 2018**]. 124
Figure 4-5: FinFET high-frequency behavior investigation. (a) f_T and f_{max} comparisons between the 28 nm (planar) and 14 nm (FinFET) technologies. (b) f_{max} and gate resistance evolution as a function of the channel length in the 14 nm FinFET process. Figures reproduced from [**Singh, 2018**]. 124
Figure 4-6: BEOL stacks comparison for advanced technology nodes available from STMicroelectronics (standard processes). 125
Figure 4-7: Transmission lines simulations for different technology nodes. (a) simulation model and (b) simulated attenuations. Orange, red, green and blue refer to BiCMOS 55 nm, CMOS 28 nm FD-SOI, CMOS 40 nm and CMOS 65 nm respectively. 126
Figure 4-8: Schematic of the realized Injection-Locked Oscillator featuring four tuning bits (biasing components not shown). 126
Figure 4-9: Different layout views of the realized ILO. 127
Figure 4-10: Simulated ILO main electrical metrics. (a) Oscillation frequency and output power for all 4-bit tuning states in free-running (dot) and injected (solid) modes. (b) Detailed ILO power consumption as a function of the oscillation frequency. 128
Figure 4-11: Schematic of the realized injection circuit. 129
Figure 4-12: Layout view of the realized 17 GHz input matching circuit. 129
Figure 4-13: Simulated input matching circuit. (a) Equivalent matching network and (b) simulated S-parameters. 129
Figure 4-14: Layout view of the realized 17 GHz DVHC. 130
Figure 4-15: Simulation results of the 17 GHz DVHC. 130
Figure 4-16: Resistance-feedback inverter design. (a) Realized differential inverters and (b) simulated impact of the resistance feedback on the generation of the fifth harmonic at 83.33 GHz and the power consumption (considering a single-ended feedback inverter). 131
Figure 4-17: Layout view of the realized 83 GHz DVHC used as a quadrature signal generator. 131
Figure 4-18: Simulation results of the realized quadrature signal generation implemented thanks to an appropriately scaled DVHC: (a) reflection parameters, (b) outputs isolation, (c) transmission parameters, (d) amplitude imbalance (grey) and phase quadrature (brown). For simplicity, all ports are loaded by 70 Ω differential loads and dummies are not simulated. Port numbers are taken from Figure 4-17. 132
Figure 4-19: Realized QPSK modulator. The proposed schematic allows phase reversal operation (a) as well as strong amplitude cancellation (c) depending on applied voltages. Simulated maximum gain versus frequency for these two operating modes are shown in (b). In (d), gain compression at 83.3 GHz is visible above 0 dBm, assuming a 70 Ω differential input impedance and an optimum output load impedance. All simulations include full-layout parasitics. 133
Figure 4-20: Layout of the realized modulator, including top metal accesses. Note that transistors are split for symmetry reasons. 134
Figure 4-21: Overall layout view of the realized quadrature signal generation and QPSK modulator. 134
Figure 4-22: Modulator Load-Pull analysis at 83.33 GHz showing large output matching tolerance. 135

Figure 4-23: Realized PA schematic made of two neutralized common-source stages and integrated transformers. Biasing and supply voltages are fed by center-taps. Decoupling capacitances and biasing resistances not shown for clarity. 136
Figure 4-24: Harmonic Balance simulations of the realized PA plotted with respect to the output power for different biasing conditions at 83.3 GHz. (a) Gain, (b) PAE and (c) Total power consumption. 136
Figure 4-25: S-parameters analysis of the realized PA. (a) Reflection parameters, (b) gain and reverse isolation, (c) Edwards-Sinsky parameters and (d) Rollet factor and magnitude of the S-matrix determinant. 137
Figure 4-26: Layout of the realized PA with inset views of the driver and power stages. 137
Figure 4-27: Layout view of the realized 75 GHz center frequency DVHC. 138
Figure 4-28: Simulation results of the realized DVHC centered at 75 GHz assuming 70 Ω differential impedance on all 4 ports. (a) Reflection and isolation parameters, and (b) transmission parameters and phase quadrature. 139
Figure 4-29: Layout of (a) shielded and (b) unshielded RF pads compatible with standard FC44S 100 µm-pitch assembly rules in 28 nm CMOS FD-SOI. Z-scale x10 for visibility. ..140
Figure 4-30: Impedance matching bandwidth analysis. (a) Typical use-case of a non-ideal balun with a pad parasitic capacitance, (b) odd mode analysis, (c) simplified analysis assuming an ideal transformer (k = 1) and (d) return loss as seen from the transformer to the LC resonator for different (C_{PAD}, L_S) couples. 141
Figure 4-31: Output balun overview. (a) Layout top view, (b) primary and secondary inductances as well as the coupling factor, (c) primary and secondary quality factors. ..142
Figure 4-32: Output matching network bandwidth simulation. (a) Layout overview, (b) reflection parameters, (c) equivalent circuit and (d) transmission parameter. Port 1 and Port 2 correspond to the 70 Ω differential DVHC port and the 50 Ω single-ended output port respectively. 142
Figure 4-33: DVHC validation measurements. (a) Through configuration circuit view, and associated (b) reflection and (c) transmission parameters. (d) Coupled configuration circuit view, and associated (b) reflection and (c) transmission parameters. Measurements (solid lines - 5 measured dies) are compared to Momentum simulations (dotted lines). 143
Figure 4-34: Illustration of the measurement setup. (a) Probe station seen from the left side, (b) right side view and (c) schematic view of the setup. V.A. and Mix. stand for variable attenuator and harmonic (down-converter) mixer respectively. 144
Figure 4-35: Locking range measurements for the $2^4 = 16$ configurations of the Kiri 75G circuit. 145
Figure 4-36: Measured phase noise at 77 GHz (blue) in the injection-locked regime compared to the 15.4 GHz reference phase noise (red – scaled to 77 GHz) from the E8257D signal generator. 146
Figure 4-37: QPSK demodulation at 100 MS/s. 147
Figure 4-38: QPSK demodulation at 4.5 GS/s. 147
Figure 4-39: BPSK demodulation at 4 GS/s. 148
Figure 4-40: BPSK demodulation of a 5.5 GS/s clock signal. 148
Figure 4-41: Simulation of a variable load on the ISO port of the 83 GHz DVHC as presented in Figure 4-17. (a) Phase quadrature contour plots with a 0.2° step, (b) amplitude imbalance contour plots with a 0.02 dB step, (c) phase quadrature contour plots (colored) with a 0.2° step and delimited 0 – 0.1 dB amplitude imbalance area (black), (d) schematic illustration of the modulated load on the ISO port. All simulations are carried out at 83 GHz assuming a 70 Ω differential impedance on other ports. 151

Figure 4-42: Segmented gates modulator. (a) OOK capable modulator and (b) PAM capable alternative design. 152
Figure 4-43: Schematic of a possible wideband FSK configuration relying on the proposed synchronized dual band architecture....153
Figure 4-44: Illustration of a circular polarization excitation scheme using a hybrid coupler. The 75 GHz DVHC is proposed in this case (simulation results)....153
Figure 5-1: Typical S-curves describing usual innovation cycles....158
Figure A-1: Computation of the Poynting confinement factor for the fundamental HE_{11} mode. (a) Representation of the z-component of the real part of the Poynting vector and (b) 3D-surface plot of the computed Poynting confinement factor as a function of the frequency and the foam thickness. 162
Figure A-2: Impact of a 2 mm-thick semi-infinite water slab on transmission. E-field envelope is computed at 120 GHz (log scale) when the slab is directly in contact with the waveguide (a) and when the slab is in contact of a 2 mm-thick air foam (c). Reflection and transmission parameters are provided in (b) and (d) respectively for different foam thicknesses. Undisturbed propagation represented in black dashed lines for reference. Besides, simulation resolution is estimated at – 40 dB. 163
Figure A-3: Foam-thickness impact on transmission parameters for 3 different frequencies (left scale) and cross-section area (right scale)....164
Figure A-4: Simulation of a simplified water drop positioned on the waveguide. (a) simulation model and (b) complex magnitude of the E-field computed at 120 GHz. 164
Figure A-5: Simulated S-parameters of the model presented in Figure A-4 (a). Reflection (a) and transmission (b) parameters are presented for a 0, 1 and 2 mm foam thickness in red, green and blue respectively. 165
Figure B-1: Network resulting from the imperfect excitation of a waveguide. 167
Figure B-2: Illustration of Equation (B-14) for different values of $\frac{Z_L}{Z_0}$ with a transition insertion loss of 1 dB per end. Propagation losses are neglected. 170
Figure B-3: Transmission ripples amplitude RipA as a function of the impedance mismatch for different attenuation conditions. 172
Figure B-4: Relation between Waveguide Loss Budget and impedance ratio (left) and corresponding Return Loss (right). All data are computed assuming RipA = 1 dB. 172
Figure C-1: Illustration of the simulation setup at 120 GHz for a 20 mm radius of curvature. Simulated bends are embedded with 10 mm straight waveguides at both ends. Waveports are used as excitation sources and radiation conditions are applied on all faces....173
Figure C-2: Simulated transmission parameters of the HE_{11} modes as a function of the normalized radius of curvature. (a) Transmission at 60 GHz and 120 GHz maximum single-mode frequencies represented in blue and red respectively. (b) Transmission at half maximum single-mode frequencies (30 GHz and 60 GHz in blue and red respectively). 174
Figure C-3: Simulated reflection parameters for the 60 GHz (blue) and 120 GHz (red) configurations already introduced in Figure C-2. Results are below simulation resolution limit. 176
Figure C-4: Curvature-induced mode couplings. (a) HE_{11} polarization rotation and (b) HE_{11} horizontal (solid lines) and vertical (dotted lines) modes couplings to TM_{01} mode. Red and blue lines refer to 60 and 120 GHz plastic waveguides already introduced in Figure C-2. 177

Figure C-5: Transmission through a bended plastic waveguide featuring a low dielectric permittivity step between the core and the cladding. Simulations at 60 GHz are presented in (a) and (c) with a 15 mm radius of curvature using linear and logarithmic scales respectively. (b) and (d) show similar simulations at 120 GHz with a 7.5 mm radius of curvature. All designs are scaled appropriately to operate at the maximum single-mode frequency.....178
Figure D-1: Illustration of OOK operation. (a) Time-domain representation of transmitted bits (red) and symbols (grey), and (b) constellation diagram (blue and red points). In the latter, Gaussian distributions are superimposed showing possible demodulation errors.....182
Figure D-2: Illustration of ASK operation. (a) Time-domain representation of transmitted bits (red) and symbols (grey), and (b) constellation diagram (blue and red points). In the latter, Gaussian distributions are superimposed showing possible demodulation errors.....183
Figure D-3: Illustration of PAM4 operation. (a) Time-domain representation of transmitted bits (red) and symbols (grey), and (b) constellation diagram (colored points). In the latter, Gaussian distributions are superimposed showing possible demodulation errors.....184
Figure D-4: Illustration of BPSK operation. (a) Time-domain representation of transmitted bits (red) and symbols (grey), and (b) constellation diagram (blue and red points). In the latter, Gaussian distributions are superimposed showing possible demodulation errors.....184
Figure D-5: Illustration of 16-PSK operation. (a) Time-domain representation of transmitted bits (red) and symbols (grey), and (b) constellation diagram (colored points). In the latter, points are broaden to illustrate the impact of noise. 185
Figure D-6: Illustration of QPSK operation. (a) Time-domain representation of transmitted bits (red) and symbols (grey), and (b) constellation diagram (colored points). In the latter, points are broaden to illustrate the impact of noise. 186
Figure D-7: Illustration of 16-QAM operation. (a) Time-domain representation of transmitted bits (red) and symbols (grey), and (b) constellation diagram (colored points). In the latter, points are broaden to illustrate the impact of noise. 187
Figure D-8: BER performance for different modulation schemes as a function of SNR (a) or $\frac{E_b}{N_0}$ (b).....189

List of Abbreviations

ABS	Acrylonitrile Butadiene Styrene
AOC	Active Optical Cable
AWG	Arbitrary Waveform Generator
ACLR	Adjacent Channel Leakage Ratio
BER	Bit Error Rate
BGA	Ball Grid Array
CMOS	Complementary Metal Oxide Semiconductor
DC	Direct Current (also meaning “0 Hz frequency”)
D-QPSK	Differential Quadrature Phase Shift Keying
DVHC	Differential Vertical Hybrid Coupler
EM	Electromagnetic
EVM	Error Vector Magnitude
FD-SOI	Fully Depleted Silicon on Insulator
FEM	Finite Elements Method
FSPL	Free Space Path Loss
GbE	Giga Bit Ethernet
GDPUL	Group Delay Per Unit Length
HBT	Heterojunction Bipolar Transistors
I/O	Inputs / Outputs
ICSP	Identical Consecutive Symbols Patterns
InP	Indium-Phosphide
IP	Internet Protocol
IPs	Intellectual Properties
ISI	Inter-Symbol Interference
ILO	Injection Locked Oscillator
LO	Local oscillator
MAN	Metropolitan Area Network

MIM	Metal-Insulator-Metal
mmW	Millimeter-wave
MOM	Metal-Oxide-Metal
MOST	Media Oriented Systems Transport
NRW	Non-Radiative Waveguide
OFDM	Orthogonal Frequency-Division Multiplexing
OMT	Ortho-Mode Transducer
OOK	On-Off Keying
PA (material context)	Polyamide – also known as Nylon
PA (circuit context)	Power Amplifier
PAE	Power Added Efficiency
PAM	Pulse Amplitude Modulation
PC	Polycarbonate
PCB	Printed Circuit Board
PCF	Photonic Crystal Fiber
PE	Polyethylene
PE-HD	Polyethylene High Density grade
PE-LD	Polyethylene Low Density grade
PET	Polyethylene terephthalate – also known as Mylar
PLL	Phase-Locked Loop
PMF	Polymer Microwave Fiber
PMMA	Poly(methyl methacrylate) – also known as acrylic or Plexiglas
PP	Polypropylene
PRBS	Pseudo Random Bit Sequence
PS	Polystyrene
PSD	Power Spectral Density
PSK	Phase Shift Keying
PTFE	Polytetrafluoroethylene – also known as Teflon
PU	Polyurethane
PVC	Polyvinyl chloride
PVT	Process - Voltage – Temperature
QAM	Quadrature Amplitude Modulation
QPSK	Quadrature Phase Shift Keying

RF	Radio Frequency
RFIC	Radio Frequency Integrated Circuit
Rx	Receiver
SiGe	Silicon-Germanium
SIW	Substrate Integrated Waveguide
SNR	Signal to Noise Ratio
Tx	Transmitter
UTP	Unshielded Twisted Pair
WAN	Wide Area Network

Chapter 1

Introduction

1.1 Motivation

Like a groundswell, the emergence of digital communications is deeply, and indisputably, modifying all aspects of our societies. People's thirst for mobile (wireless) connectivity keeps growing and growing, fed by the advent of new use cases such as music and video streaming, cloud-based storage or computing, 3D video contents, mixed-reality games, etc. In parallel, it is interesting to note that countless consumer products are turning into *connected* objects to deliver new services or more added value. In the industry, *digitalization* and *uberisation* are becoming ubiquitous trends and result in a necessary proliferation of communication technologies. The objective is to leverage on unused capacities to maximize customer satisfaction or experience. Assisted by artificial intelligence and remote diagnostics, healthcare will significantly change as well. Similarly, transports are currently at the edge of a profound revolution driven by the simultaneous integration of environment-friendly motorizations, advanced driving automation and advertisement functions. All of these imply a remarkable proliferation of embedded electronic circuits (sensors, actuators, microcontrollers, etc.) along with appropriate wired connections for both power supply and communication. Ultimately, even religion is already affected in spite of its traditional opposition to changes brought by scientific or technological progress. In fact, high-tech devices can now commonly help people in the practice of their faith and contactless e-payments are being deployed in worship places to simplify donations. Finally, as it is definitely not possible to find any single part of the society that will remain unchanged, the global mutation obviously seems inevitable.

From the specific hardware point of view, such a (r)evolution occurred thanks to tremendous progress in various applied physics topics, mainly solid-state physics, optics and microfabrication, that successfully fueled the industry. Node after Node, semiconductor technologies have kept on reinventing themselves every two years approximately, as stated by famous Moore's laws. Because of such a rapid innovation pace, transistors performances have progressed significantly in a few decades, thus offering higher and higher operating frequencies. Although progresses seem slower today due to Moore's law deceleration, mass-market Complementary Metal Oxide Semiconductor (CMOS) nodes can still enable radiofrequency (RF) and millimeter-wave (mmW) circuits in addition to multi GHz digital circuits. Moreover, higher integration possibilities through System-On-Chip architectures also offer an attractive path. To sum up, the availability of low-cost technologies with mmW capabilities pave the way to innovative high-speed systems offering disruptive cost / performance trade-offs.

1.2 State of the Art

Although performant circuitry is mandatory for high-speed communication, suitable transmission channels are also required. In general, ideal candidates would mainly offer low loss and wide bandwidth along with manufacturing and deployment costs as low as possible. It is the purpose of this section to summarize the performance of existing communication channels and highlight how they compete with each other. Innovative plastic waveguide systems are then proposed as an alternative.

1.2.1. Twisted Copper Pairs

Twisted Copper Pairs (TCP) exploit the concept of differential signaling to transmit baseband data over one pair of copper conductors (or several pairs in parallel). It is therefore a very straightforward transmission medium. One of the most widespread links, which is the very popular Universal Serial Bus (USB), uses TCP in different combinations depending on the considered release. Theoretical data rates are reported in Figure 1-1 from corresponding standards.

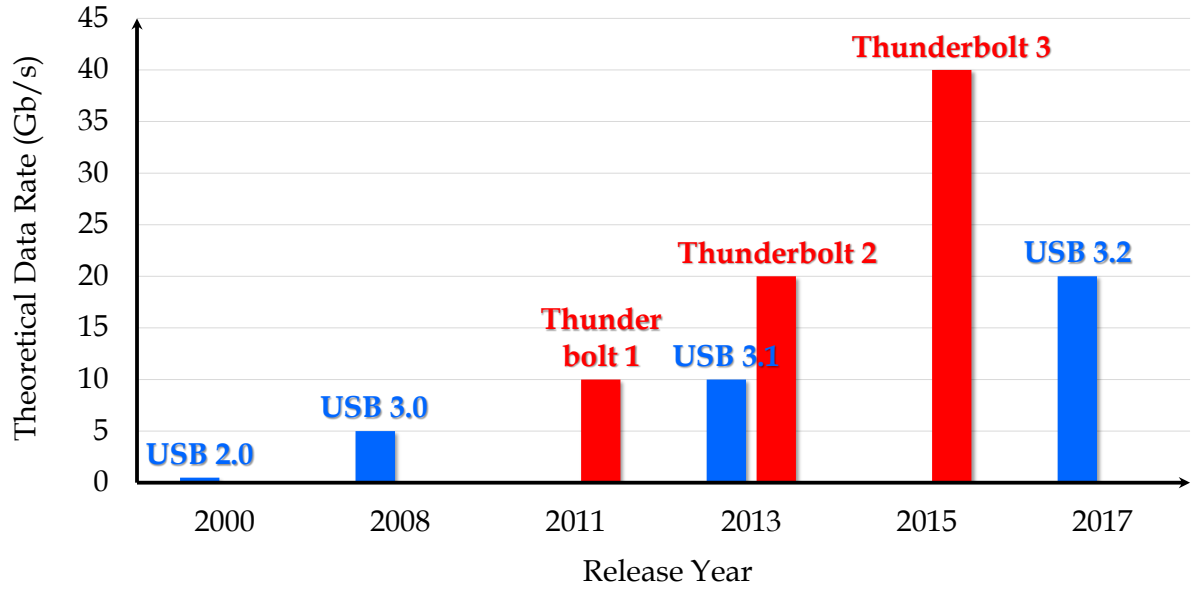

Figure 1-1: Theoretical data rate specifications of the different generations of USB and Thunderbolt standards as a function of their release year.

However, the intrinsic low-pass behavior in TCP drastically limits available bandwidths, and therefore achievable data rates. Resulting from the cable construction, distortions are yet predictable and possibly mitigated using active baseband transmitter (Tx) and receiver (Rx) circuits. This workaround solution is usually referred to as *Active* Cables and is implemented in Thunderbolt standards for example (Figure 1-1). It results in a definitely more expensive and power-hungry solution, and should be favored only when data rate or distance are the most relevant figures of merit.

Finally, another major limitation in TCP is high-frequency radiations. For frequencies above 100 MHz, conductors radiated power actually grows as the square of the frequency [**Datwyler, 2013**]. Because of electromagnetic compatibility reasons encountered in harsh

environments, like automotive or industrial applications, permitted emission levels are actually extremely low. External noise sensitivity from external sources is also increased at higher frequencies. Combining these constraints together, TCP may have to operate at reduced symbol rates, thus increasing circuit complexity. Shielded TCP may also be considered if extra cost and weight are acceptable. For example, USB 3 typically rely on such cables.

Although TCP cost and complexity may be increased, and additional active circuitry may be used to mitigate high-frequency limitations, such solutions are not desirable. Moreover, their scalability is arguable when considering future data rate requirements evocated before.

1.2.2. Optical Fibers

In parallel to Moore's law, optical fiber communications have been experiencing exponential progress for several decades as well. This trend is actually known as Keck's law and is represented in Figure 1-2. It represents transmission speed records over optical fibers, which typically lead to commercial products a few years later. Note that the introduction of Wavelength Division Multiplexing (WDM) in 1992 enabled major improvements. More recently, phase-shift encoding and coherent demodulation increased data rates even further [**Hecht, 2016**]. Therefore, aggregated data rates in the order of 1 Pb/s (= 10^6 Gb/s) are now obtained. On top of that, benefiting from very small cross-sections, optical fibers can be bundled in parallel up to several hundred per cables.

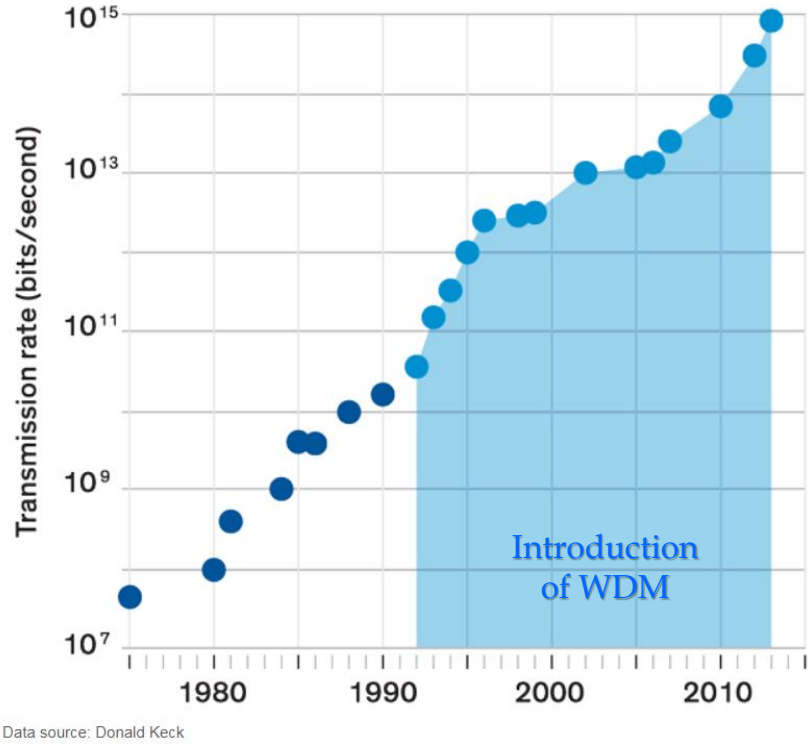

*Figure 1-2: Transmission rate records per year, illustrating Keck's law in optical transmission, reproduced from [**Hecht, 2016**].*

Propagation distances are also very long thanks to extremely low attenuation constants (as low as only 0.15 dB/km [**Ten, 2016**]) that makes it possible to reach several hundreds of kilometers. Combined together, above advantages have allowed optical solutions to become undisputable technologies for long-haul communications, like transoceanic cables, Wide Area Networks (WAN), Metropolitan Area Networks (MAN) or data centers core networks.

However, a major weakness of optical solutions is related to precise alignment requirements. In fact, a micron scale assembly should be guaranteed between end-to-end fibers and fiber end faces are to be precisely polished. These constraints are relaxed in Active Optical Cables (AOC) thanks to electrical interconnects and optical assembly at the factory level. Additional manufacturing costs to ensure mechanical reliability and compensate for thermal dilatation may still be detrimental for newly envisioned applications. In particular, shock and vibration tolerances as well as compliancy with low-cost installation processes introduce even more severe mechanical challenges. Even if technical solutions exist to meet these requirements, they are likely to reduce the cost-effectiveness of short optical fibers.

Besides, necessary electro-optical conversion circuits usually require expensive technologies involving III-V semiconductors. Therefore, optical systems are interesting for long distances, where the cost of interconnects becomes negligible in the total cost of the solution, but they may not be relevant for link distances inferior to 20 m. In this context, more robust and cost-effective solutions would be highly desirable.

1.2.3. Millimeter-wave Free Space Propagation

Theoretically, free space may be considered as a free and lightweight transmission medium. In practice, it is partially true since spectrum bandwidth is a clearly limited resource. Only a few frequency bands are allowed depending on national regulations, and among these, some of them are effectively license-free or *light-licensed*. As an example, the 57 – 66 GHz band has drawn a lot of attention in recent years because it offers enough bandwidth to enable multi Gb/s communications. Increasing further the operating frequency favorably allows for higher and higher absolute bandwidth. Benefiting from previously evocated mmW capability in CMOS technologies, data rates of 120 Gb/s have been published using high-order modulation schemes **[Tokgoz, 2018]**. Moreover, system-on-chips integrating both digital baseband circuitry and emitters / receivers circuits have a huge potential in terms of low power operation and cost reduction.

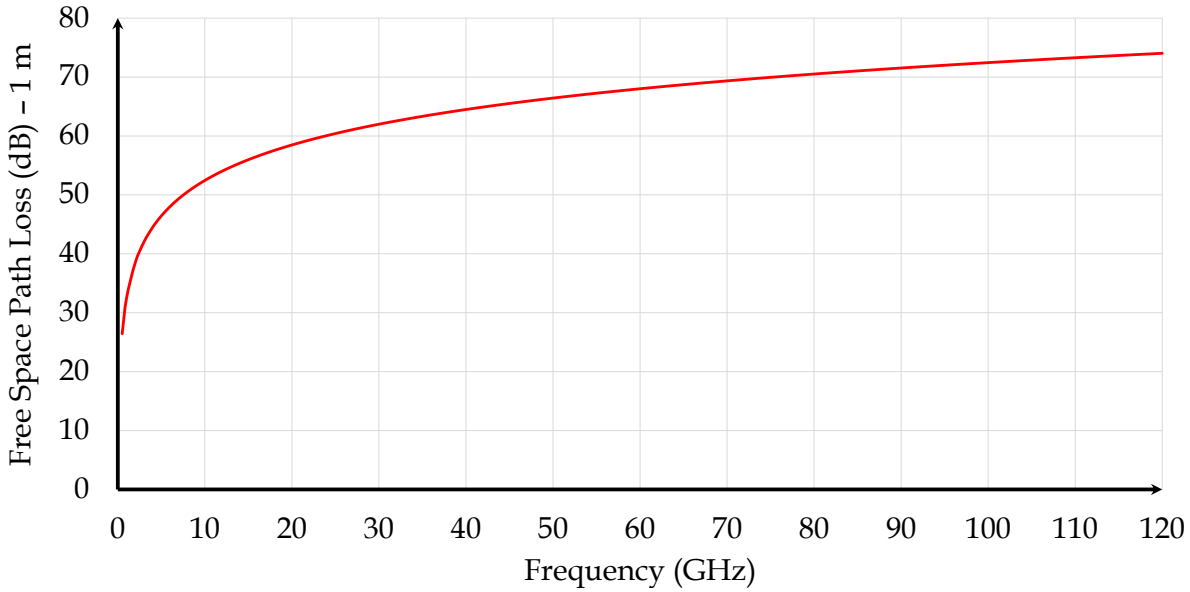

Figure 1-3: Free space path loss assuming a 1 m-long line-of-sight propagation.

Although promising, free space propagation still suffers from unguided transmission, causing spherical dilution, which may be seen as propagation losses from a system level point of view. Free space path loss increases logarithmically with frequency and distance as stated by Friis' law (Equation (1-1) - represented in Figure 1-3). Entering mmW frequencies thus induces a severe channel modification. As higher path losses are obtained, multipath actually becomes negligible, favoring quasi line-of-sight transmissions. This change comes with a few benefits like reduced fading probability or spatial duplexing but also makes the transmission greatly sensitive to possible obstacles between Tx and Rx antennas. In many applications, this loss of robustness is simply unacceptable without mentioning that, in practice, Tx and Rx are not necessarily aligned.

Friis' law

$$PL_{dB} = 20\log\left(\frac{4\pi L}{\lambda}\right) = 20\log\left(\frac{4\pi Lf}{c_0}\right) \quad (1\text{-}1)$$

1.2.4. Plastic Waveguide Systems

With the above conclusion in mind, plastic waveguide systems cleverly propose to guide mmW energy from the Tx to the Rx. Compared to traditional mmW systems, energy is no longer radiated in free-space but actually propagates inside a low loss waveguide with presumed robustness and bending capabilities. In other words, introducing a plastic waveguide could result in a more reliable communication channel that does not require Tx / Rx alignment any more. Additionally, a lower path loss is expected, enabling longer distances and / or higher signal-to-noise ratio (SNR).

In principle, a plastic waveguide system operates similarly to an optical one. The major difference is related to the operating wavelength, which is several orders of magnitude larger in plastic waveguides. Interestingly, this results in substantial changes from the technological point of view so that plastic waveguide systems share no common technologies with optical ones in practice. Larger wavelengths actually induce larger waveguide dimensions and compatibility with low cost plastic manufacturing. Machining tolerances as well as assembly constraints are also relaxed accordingly. From the circuit point of view, high volume CMOS technologies may be used for the whole system-on-chip transceivers, unlike optical circuits. Consequently, plastic waveguide systems have a very desirable cost-effective potential.

In recent years, a few demonstrations have been published exhibiting up to 25 Gb/s at a few centimeters [**Fukuda, 2011**]. Moderate distances up to 15 m have been demonstrated as well although data rates reduce drastically with distance [**Van Thienen, 2016**]. These metrics provide insightful bounds regarding the relevant perimeter of this technology. In fact, the competition with optical fibers for long-haul communications at extreme data rates is clearly out of reach. On the contrary, it could be a much more cost-effective solution for moderate length links (typically < 20 m) while still offering much higher data rates compared to TCP. Moreover, plastic waveguides benefit from favorable electromagnetic compatibility likewise optical fibers.

1.3 Thesis Outline

This manuscript is organized as follows. Chapter 2 will firstly describe the plastic waveguide channel. Early historical developments are briefly reviewed to position this concept with respect to conventional metallic waveguides and optical fibers and current plastic waveguides state of the art is presented. Some useful theoretical results are recalled in order to propose a design methodology and to ease the understanding. In that process, attenuation and confinement are discussed both qualitatively and quantitatively, highlighting the advantages and the limitations of the solution. Besides, an innovative plastic waveguide design is introduced and compared to usual tubular designs.

In Chapter 3, the discussion focuses on system level aspects and detailed specifications are derived by taking into account the most relevant applications on different markets. Leveraging on the plastic waveguide knowledge, an innovative system architecture is proposed. However, two bottlenecks have been identified in such an architecture. The first one regards achievable bandwidth between the circuit and the waveguide while the second is related to phase quadrature demodulation with low power constraints. Both are investigated and in each case, new concepts are suggested with promising results.

Circuit implementation in 28 nm CMOS FD-SOI is finally reported in Chapter 4. The design of a mmW transmitter is reviewed. Frequency combining with on-chip and broadband requirements is obtained successfully thanks to the introduction of a new differential hybrid coupler layout and dedicated RF / mmW pads. In fact, it appears that the new coupler exhibits very desirable performances and can be easily scaled with frequency. Characterization results of the realized circuit are shown, confirming wide sub-harmonic locking range as well as multi Gb/s data transmission capabilities.

Ultimately, conclusions are drawn in Chapter 5, summarizing realized works and important contributions. Note that relevant bibliography and perspectives are willfully provided at the end of each chapter for better consistency.

References

[**Datwyler, 2013**] Datwyler Cabling Solutions. "Braided shielding and the EMC behaviour of copper data cables," White Paper, 2013. Available Online at www.idacs.uk.com.

[**Fukuda, 2011**] S. Fukuda, Y. Hino, S. Ohashi, T. Takeda, H. Yamagishi, S. Shinke, K. Komori, M. Uno , Y. Akiyama, K. Kawasaki, and A. Hajimiri. "A 12.5+12.5 Gb/s full-duplex plastic waveguide interconnect," *IEEE Journal of Solid-State Circuits*, Vol. 46, No. 12, pp. 3113-3125, 2011.

[**Hecht, 2016**] J. Hecht. "Is Keck's law coming to an end?," *IEEE Spectrum*, Jan. 2016. Available Online at http://spectrum.ieee.org/semiconductors/optoelectronics/is-kecks-law-coming-to-an-end.

[**Ten, 2016**] S. Ten. "Ultra low-loss optical fiber technology," *Proceedings of the Optical Fiber Communications Conference and Exhibition*, pp. 1-3, 2016.

[**Tokgoz, 2018**] K. K. Tokgoz, S. Maki, J. Pang, N. Nagashima, I. Abdo, S. Kawai, T. Fujimura, Y. Kawano, T. Suzuki, T. Iwai, K. Okada, A. Matsuzawa. "A 120Gb/s 16QAM CMOS millimeter-wave wireless transceiver," *IEEE Solid-State Circuits Conference*, pp. 168-169, Feb. 2018.

[**Van Thienen, 2016**] N. Van Thienen, Y. Zhang, M. De Wit and P. Reynaert. "An 18Gbps polymer microwave fiber (PMF) communication link in 40nm CMOS," *Proceedings of the IEEE European Solid-State Circuits Conference*, pp. 483-486, 2016.

Chapter 2

Building a Plastic Waveguide Channel

2.1. Review of the State of the Art

2.1.1. Historical Perspective and Current Applications of Metallic Waveguides

The theoretical foundations of modern electromagnetic (EM) theory were first set by James Clerk Maxwell in 1873 driven by pure mathematical considerations [**Maxwell, 1873**]. Unifying electricity, magnetism and light, which were very different scientific topics at that time, and introducing the idea of electromagnetic wave propagation, the outcomes of this theoretical work are still impressive. Enriched by the contribution of Oliver Heaviside [**Nahin, 1988**] who introduced vector notation and derived it in its modern form, the Maxwell's theory was then experimentally validated by Heinrich Hertz by the end of the XIXth century [**Rautio, 2010**]. Interestingly in the history of science, Hertz experimental verification occurred after the theoretical prediction in a similar way as many other important discoveries like the existence of Neptune by Urbain Le Verrier (1846) or more recently the Higgs boson (2012).

Following the early developments of electromagnetics, the first (metallic) waveguide was proposed in 1893 by Sir Joseph John Thomson and was later demonstrated by Oliver Lodge in 1894. Lord Rayleigh performed in 1897 the first mathematical analysis of a hollow conducting cylinder of arbitrary cross-sectional shape and he was able to show that EM waves could actually propagate [**Rayleigh, 1897**]. Note that four years before, Heaviside – in spite of his indisputable geniality – had come to the opposite conclusion that guided waves would at least require a two-conductor geometry [**Heaviside, 1893**]. In his analysis, Rayleigh also predicted the existence of canonical modes with TE or TM fields as well as associated cut-off frequencies. This latter conclusion was found to be a major limitation for practical applications because high-frequency sources were missing. As a consequence, since synthesizable wavelengths were very long, wireless radio communication was very attractive while waveguides having dimensions comparable to the wavelength resulted in very impracticable implementations. The interest for waveguides disappeared except for very brief peaks during the development of vacuum tube applications in the early XXth century. The early metallic waveguide demonstrations and theoretical foundations thus fell into oblivion.

Surprisingly, hollow tube waveguides reappeared, revitalized by the work of two independent American researchers during the 1920 - 1930s: George C. Southworth and Wilmer L. Barrow [**Packard, 1984**]. Unaware of the previously reported work on the subject, they focused their attention on both experimental demonstrations and (re)derivation of a complete theoretical framework. Also unaware of each other because none of them published their early results, they made their first external announcement of their discovery in 1936 at the very same conference. It is interesting to note that Southworth and Barrow were actually pursuing somewhat different objectives and consequently started their research from different points. Nevertheless, a common characteristic of their work is the strong interaction between theory and practice, illustrating the manner science and technique may sometimes cross-fertilize each other.

Barrow's primary interest was in high-frequency horn antenna, a development that later provided solid foundations for radar applications in aeronautics. Even if higher frequencies and higher powers are used today, metallic waveguide is still the technology of choice for such radars because of very high power handling capability, relatively low loss and large bandwidth. Nowadays, metallic waveguides are also extensively used in instrumentation, especially above 110 GHz.

On the contrary, Southworth of Bell Labs Telephone Laboratories was much more interested in waveguide communications. In August 1933, after many years of informal work, he was finally authorized to build a long transmission line (265 m) to investigate the simultaneous transmission of a large number of telegraph and telephone signals. Because the TE_{01} mode in circular waveguides exhibits an attenuation constant which decreases with frequency, this particular mode drew a lot of attention. In spite of implementation difficulties, Southworth eventually reported an attenuation constant of ≈ 1.5 dB/km in his last paper [**Southworth, 1962**], thus envisioning an optimistic future for guided transmissions in addition to wireless ones.

Half a century later, it is clear that Southworth's foresight of the complementarity of wired and wireless transmissions actually materialized… except that the advent of microwave or millimeter-wave waveguides never really happened, overwhelmed by optical fiber solutions. Since the introduction of high-purity silica glass fibers by Nobel Prize winner Charles K. Kao in 1965 and leveraging the continuous technological improvements of optical components (mainly laser and photodiodes), optical fibers are dominating in high bandwidth and long distance applications like WAN or MAN communications or spine/leaf links in data centers. Benefiting from a considerable absolute bandwidth, very low propagation losses (0.1 - 1 dB/km), a small cross-section footprint (allowing easy parallelization of multiple fibers in the same cable), a light-weight design, a single-mode operation capability and an affordable fiber manufacturing process, optical fibers gather a lot of very desirable properties for communication. The recent development of air-core fibers and Photonic Crystal Fibers (PCF) also improved power handling and dispersion characteristics [**Harrington, 2000**] [**Cherif, 2009**].

The impressive performances of optical fibers, especially compared to traditional metallic waveguides, mainly result from 2 factors: huge wavelength reduction and modified waveguide design. Wavelengths in the range of ≈ 1 – 1.5 µm are typically involved in optical applications. On the other hand, microwave applications corresponds to centimeter range wavelengths. Moving from microwave to optics is then likely to offer a bandwidth increase of approximately the same 10 000 factor. Nevertheless, considering fundamental mode attenuation in metallic waveguides, it is clear that the higher the frequency, the higher the attenuation. Consequently, such a dramatic frequency jump would result in metallic

waveguides with useless attenuation constants and impractically small cross sections. To sustain optical frequencies, while still offering very low loss at the same time, the waveguide mechanism and materials had to be changed. It is the purpose of the following sections to highlight these fundamental changes. It is also worth remembering that optical fibers are still *waveguides* (strictly speaking, a structure guiding waves) just like transmission lines, coaxial lines or Non Radiating Waveguides (NRW).

Due to their pure dielectric nature, optical fibers are in fact named dielectric waveguides. The use of this term may not be restricted to a given frequency range as it will be discussed later. On the contrary, plastic waveguides, or alternatively Polymer Microwave Fibers (PMF), refer to a particular subset of dielectric waveguides targeting mmW frequencies and low cost polymer materials (Chapter 1). Therefore, the propagation in plastic waveguides is likely to be similar to the one found in optical fibers, except for the attenuation process dictated by the use of different materials. Cross-sectional dimensions in the order of a few millimeters (≈ 1 000x larger) will be obtained, relaxing manufacturing and alignment tolerances to enable a low-cost and robust waveguide. Leveraging mmW frequencies, this solution offers a multi-gigahertz bandwidth suitable for multi-gigabits communications. This Chapter will further investigate both theoretical and practical aspects of plastic waveguides. The comparison with traditional metallic waveguides and optical fibers will draw insightful conclusions.

2.1.2. From D. Hondros and P. Debye to P. Reynaert: A Century of Progress

This section will now present a brief historical overview in the field of plastic waveguides. The state of the art is then reviewed with a focus on both waveguides and excitation structures dedicated to high-speed communication.

2.1.2.1. Historical Perspective

Hondros & Debye reported the first analysis showing the possible propagation of TM waves in a dielectric cylinder in 1910 [**Hondros, 1910**]. It is interesting to note that, similarly to hollow metallic tube waveguides (see section 2.1.1), experimental validation of this theory was carried out a few years later by other physicists [**Zahn, 1916**]. Even though the outcomes of this work showed that proper RF propagation is possible in pure dielectric structures, the underlying understanding was incomplete and the full mathematical analysis of dielectric rod waveguides was finally published in 1936 by Carson, Mead and Schelkunoff [**Carson, 1936**]. One more time, the parallel with metallic waveguides is striking! Nevertheless, the apparent coincidence in 1936 of these major breakthroughs can be explained by the global motivation at that time to develop disruptive technologies serving the emerging communication industry as well as aeronautic applications, like radars.

In their paper, Carson et al. demonstrated the hybrid nature of the modes in circular dielectric rods, proving that such a difference compared to metallic tube waveguides actually result from different boundary conditions while propagation equations remain the same. Moreover, the fundamental HE_{11} mode cutoff frequency was found to be zero, meaning that any frequency could *theoretically* propagate on such a mode. The guiding effect and

attenuation properties have then been experimentally verified by many complementary works. However, low-confinement / low-loss configurations drew a lot of attention but faced important implementation difficulties. At the same time, in the 1950s, similar issues were also observed with other *open* surface-wave structures like Goubau wires [**Goubau, 1951**] due to weak confinement and strong sensitivity to external perturbations.

Soon after, the rapid development of optical fibers started in 1960s (see section 2.1.1) finally unveiled an extremely low-loss medium for long-distance and large bandwidth applications without the previously encountered external environment sensitivity. Unsurprisingly, this success also led to a temporary pause in the development of counterparts operating at lower frequencies.

2.1.2.2. Latter developments and current state of the art review

The pause lasted almost 60 years for two basic reasons. First, in a civilization transitioning to the Digital Age, optical fibers were offering a suitable solution to support the construction of long haul interconnects. In addition, the simultaneous availability of light emitters and receivers, essentially based on lasers and photodiodes, acted as technological enablers. In contrast, powerful and cost effective mmW and THz circuits have long been missing.

The concept of dielectric waveguides reappeared in early 2010s, enabled by the notable progress in mmW integrated circuits, especially cost effective CMOS technologies, and supported by the need to improve data rates above 10 Gb/s in standard wireline links at short or medium ranges (≤ 20 m). We report in this section the dielectric waveguides topologies published so far in this context as well as their excitation conditions (couplers).

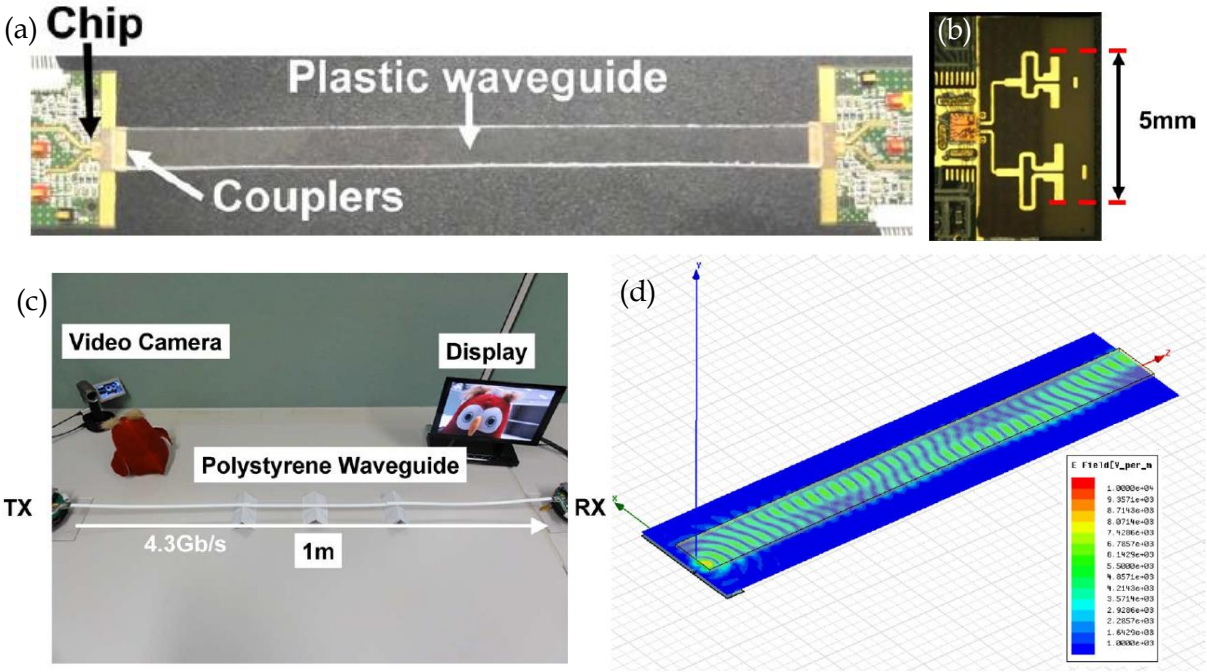

*Figure 2-1: Figures taken from [**Fukuda, 2011**] presenting the proposed plastic waveguide system at 0.12 m (a) and 1 m (c). A close-up view of the antennas-based excitation is reported in (b) and an EM simulation is shown in (d).*

In [**Fukuda, 2011**] a PS waveguide was demonstrated with a rectangular section of 8x1.1 mm² at 0.12 m and 1 m, as visible on Figure 2.1 (a) and Figure 2.1 (c) respectively. This system simultaneously exploits two carrier frequencies at 57 and 80 GHz in a full-duplex fashion. Two quasi-Yagi antennas on Printed Circuit Board (PCB) at 57 and 80 GHz are introduced as couplers in an offset configuration (Figure 2.1 (b)). Using Marcatili's approximate solutions [**Marcatili, 1969**], the authors showed that at least two modes may propagate inside their waveguide in the considered frequency range. Complementary EM simulations shows a strong coupling of these modes because of the offset excitation configuration (Figure 2.1 (d)). However, a multimode propagation is usually a detrimental situation. Moreover, Figure 2.1 (c) illustrates the strong sensitivity to external contact of the solution. Small trestles (probably made of paper or plastic) actually support the waveguide in the air and prevent direct ground contact.

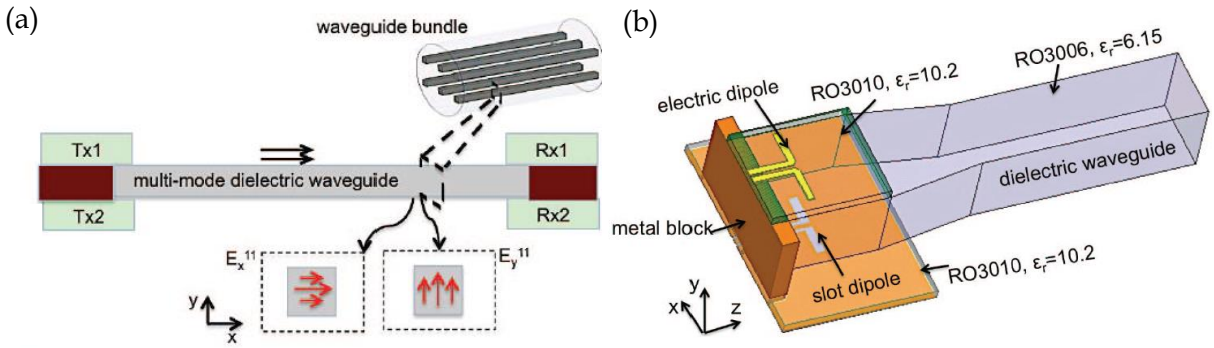

*Figure 2-2: Figures taken from [**Dolatsha, 2013**] presenting the proposed polarization-multiplexed scheme (a) and associated plastic waveguide interconnect (b).*

In 2013, a square dielectric waveguide was proposed in [**Dolatsha, 2013**] in the 90 – 120 GHz frequency range (Figure 2-2 (a)). Compared to [**Fukuda, 2011**], a high permittivity Rogers RO3006 dielectric material (ε_r = 6.15) is proposed to enhance field confinement and reduce pitch in the case of multiple links in parallel. This material choice, in addition to a higher operating frequency, and a single mode operation, leads to a considerably lower cross-section waveguide of only 0.85 x 0.85 mm². Disadvantaged by considerable attenuation (44 dB/m simulated at 100 GHz), this approach is suitable only for short distance applications such as chip-to-chip interconnects. Beyond this limitation, an interesting dual-mode excitation is also presented (Figure 2-2 (b)). In contrast to [**Fukuda, 2011**], two orthogonal modes are excited independently to provide an additional communication channel in parallel.

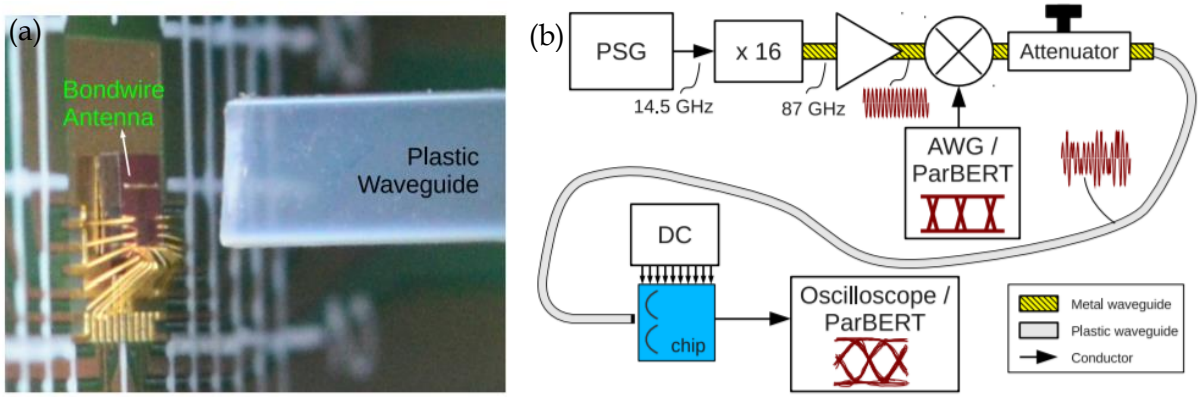

*Figure 2-3: Figures reproduced from [**Tytgat, 2013**] illustrating the proposed on-chip bondwire antenna as a cost-efficient interface between a plastic waveguide (a) and a mmW receiver based on a long plastic waveguide (b).*

In parallel, a team from the Katholieke Universiteit Leuven led by P. Reynaert published in 2013 a receiver chip dedicated to communication over a rectangular 2.2 x 0.9 mm² Polypropylene (PP) plastic waveguide (Figure 2-3 (b)). The specificity of this circuit is the presence of an on-chip bondwire dipole antenna (Figure 2-3 (a)). Even though this solution might be economically appealing, the large coupling losses and the mechanical stability of such a transition is doubtful. Moreover, the large tolerances of the low-cost bondwire technique raise concerns about the resonance frequency dispersion from die to die.

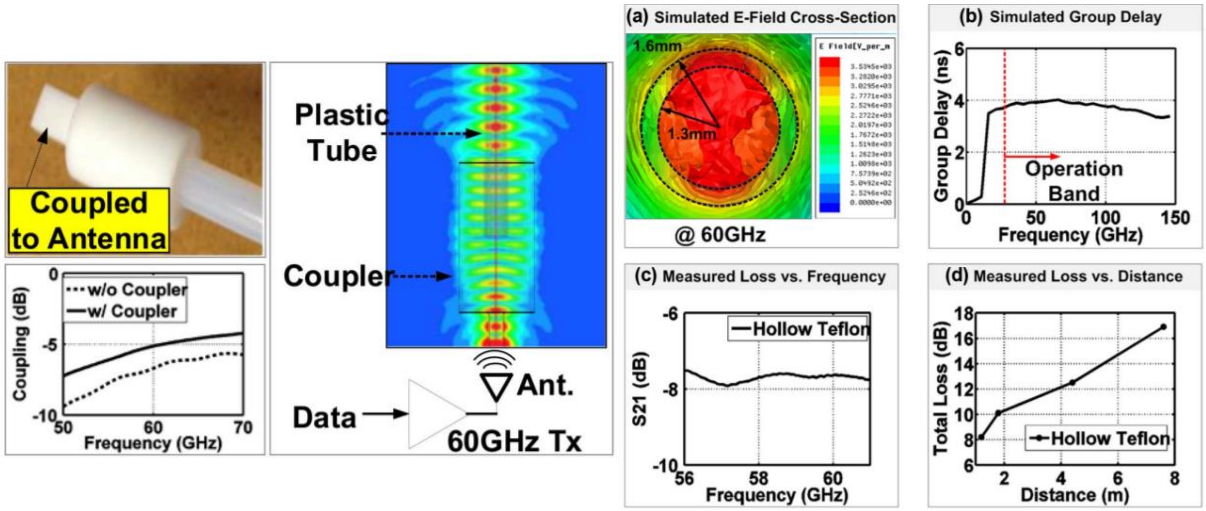

*Figure 2-4: Figures reproduced from [**Kim, 2013**]. A new coupler to in-package antennas and a tubular low-loss waveguide are presented on the left and on the right sides respectively.*

Since there was room for improvement especially at couplers level, another publication in late 2013 proposed to introduce a specific dielectric apparatus at the end of the waveguide to enhance the coupling to omnidirectional in-package antennas (Figure 2-4 left). Compared to [**Tytgat, 2013**], it was a significant improvement because a loss in the order of only 5 – 6 dB was reported and fragile antennas were embedded in a package. The presented waveguide also showed interesting features. First, the tubular Teflon cross-section is likely to be a much easier shape to extrude compared to rectangular ones. Benefiting from this hollow design as well as an operating frequency around 60 GHz, the waveguide has low loss (≈ 1.5 dB) but it is clear from Figure 2-4 right that measured frequency and length dependencies are not simple.

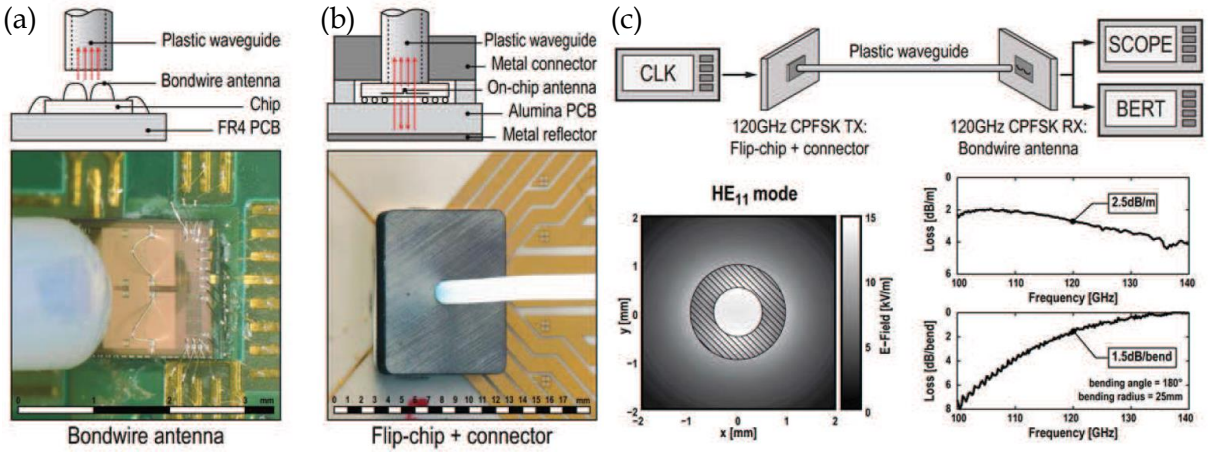

*Figure 2-5: Figures from [**Volkaerts, 2015**] showing a tubular PTFE waveguide excited by different couplers on Rx/Tx sides in (a) and (b), and the operating system in (c) respectively.*

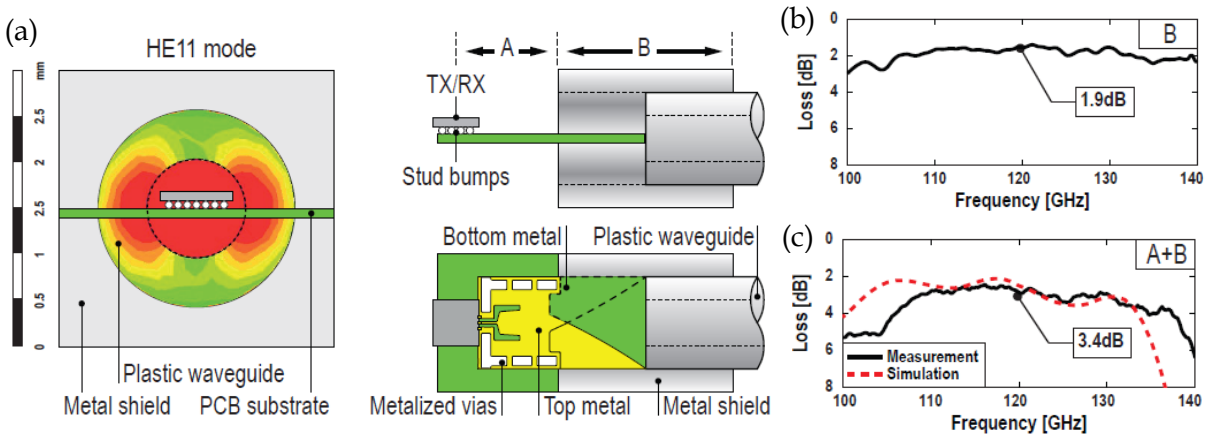

Figure 2-6: Figures from ***[Van Thienen, 2016]*** *introducing a novel coupler at both Tx/Rx levels combining flip-chip and SIW technologies in (a). The SIW to plastic waveguide connector exhibit only 3.4 dB loss at 120 GHz (b) so that the total loss between the chip and the waveguide is 3.4 dB (c).*

Following the previous introduction of hollow tubular waveguides, Reynaert's team presented in 2015 Tx/Rx circuits communicating at 120 GHz over a Ø 2 mm x Ø 1 mm Teflon (PTFE) plastic waveguide **[Volkaerts, 2015]** (Figure 2-5). While the system achieved a significant improvement to the state of the art regarding maximum data rate, the waveguide design was very similar to **[Kim, 2013]** and the Rx coupler was reused from **[Tytgat, 2013]** as visible in Figure 2-5 (a). However, an alternative coupler was implemented on Tx side for enhanced mechanical reliability and better coupling efficiency (Figure 2-5 (b)). A redesigned version of this coupler, successfully combining flip-chip and Substrate Integrated Waveguides (SIW) technologies, was finally implemented on both Tx/Rx sides in 2016 **[Van Thienen, 2016]** with 3.4 dB loss per coupler at 120 GHz (Figure 2-6). It was also noted that this result was an 8 dB improvement in comparison with **[Tytgat, 2013]**. This new coupler consequently permitted to extend the reach of the previous plastic waveguide system and improved maximum data rate at 1 m.

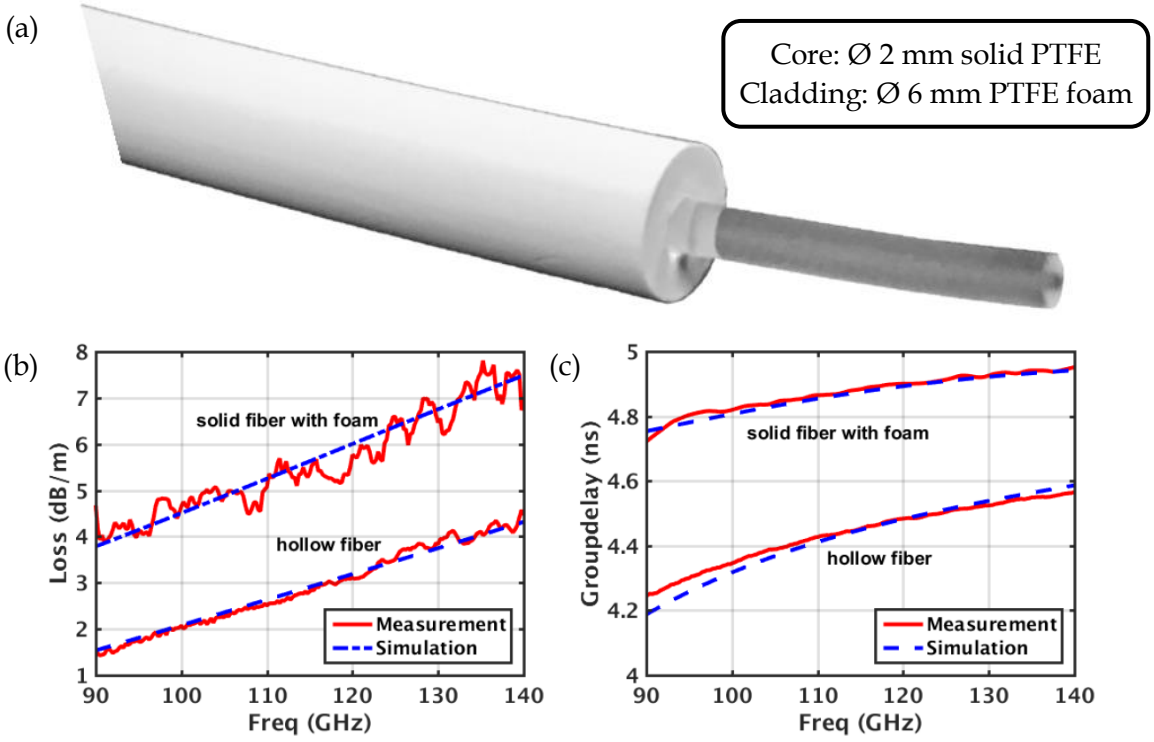

Figure 2-7: Figures from ***[Reynaert, 2017]*** *showing a solid PTFE core waveguide coated with a 6 mm diameter PTFE foam to improve immunity to external contact in (a). The impact of the foam regarding attenuation and group delay is presented in (b) and (c).*

The sensitivity to external contact was addressed by Reynaert's team in 2017 [**Reynaert, 2017**]. Contrary to previously reported works, the cladding material is no longer the surrounding air but a Ø 6 mm PTFE foam (Figure 2-7 (a)). On the one hand, the new design suffers from a 2.5 – 3 dB/m penalty (Figure 2-7 (b)). On the other hand, the large cladding thickness prevents direct contact on the core waveguide so that dielectric permittivity remains unchanged in the cladding region. Moreover, group delay dispersion over the 90 – 140 GHz is roughly divided by two (Figure 2-7 (c)) which further highlights the qualitative contribution of the cladding in the propagation mechanism. Unfortunately, no comparison is made to quantify the robustness of this assembly to external contact but based on simulation results presented in Appendix A, it may be considered as almost insensitive.

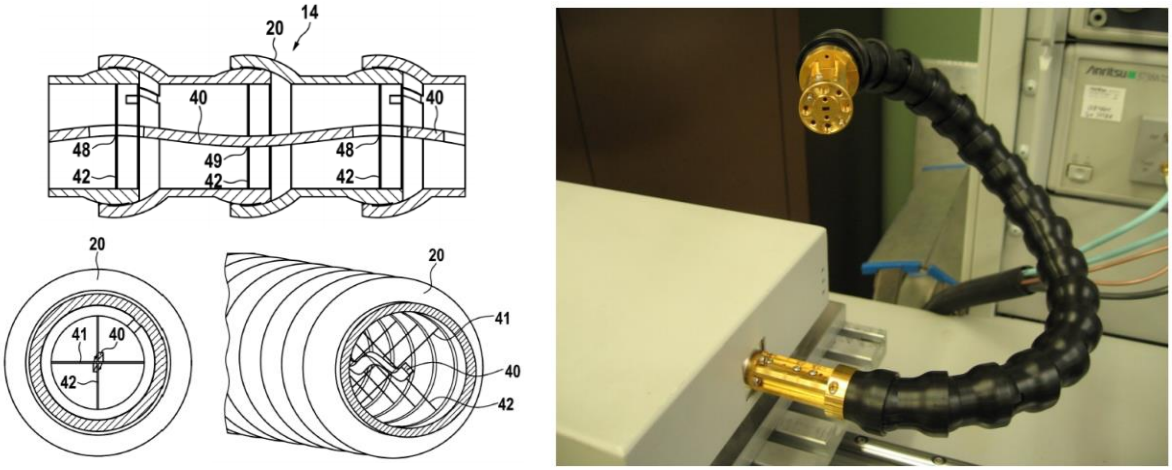

*Figure 2-8: Figures from [**Nickel, 2014**] presenting a novel dielectric waveguide assembly made of a rectangular dielectric waveguide supported by embedded thin strings placed periodically. A protective tube prevents detrimental contacts and limits bending.*

Due to their low loss and flexibility, plastic waveguides have also been investigated in the context of mmW measurements. A noticeable proposal to fix the external sensitivity issue can be found in [**Nickel, 2014**]. In this design, a protective tube encloses the plastic waveguide and prevents detrimental contacts and excessive bending (Figure 2-8). Although this solution could be an interesting alternative to rectangular metallic waveguides above 75 GHz, it is much more complex and less flexible compared to foam coating [**Reynaert, 2017**]. For cost-sensitive applications targeted in this project, it is clear that simple designs should be favored…while still offering sufficient reliability.

At this point of our review of the state of the art, it clearly appears that only circuit design-oriented analyses have been carried out in the previously reported publications regarding the waveguide and its excitation structure. First, only rectangular and tubular shapes have been investigated for plastic waveguides. Sometimes irrespectively of the single mode operation, the choice of some plastic waveguide geometries may even seems opportunistic (Appendix A). Couplers were not treated better with usually scarce details about the nature of the loss: impedance mismatch, misalignment, materials attenuation, excitation of undesired modes, etc. It should be pointed out that mechanical reliability may have been the primary concern here. For example, the underlying principle behind the proposed coupler in [**Kim, 2013**] is still not clear although the positioning benefit is obvious. Additionally in [**Van Thienen, 2016**], a modal analysis suggests that many modes might be excited in the proposed coupler.

With many successful demonstrations already published in less than a decade, pushing performance further now requires a comprehensive study at EM level of both the waveguide characteristics as well as its excitation conditions.

2.2. Waveguide Basics

2.2.1. The Existence of Modes in Waveguides

Very important properties of waveguides are related to *modes* propagation. Modes are actually defined as stationary solutions of the set of differential vector equations resulting from Maxwell's electromagnetic equations applied to the considered waveguide design. Note that the term *stationary* doesn't mean constant over time in this context, but refers to the possibility to factorize analytical expressions with a time varying term (uniformly applied in the geometry) and a space varying term (independent from the time variable). Similar to an orthogonal vector basis in vector geometry, guided modes represent a set of independent solutions that can be used to decompose a given propagation situation. This is called modal analysis.

The number of modes strongly depends on the waveguide and operating frequency. One or several modes should exist in the structure to sustain propagation, resulting in either a single-mode or an *overmoded* waveguide. Sometimes no mode is available so that propagation in the structure is in fact not permitted. This situation may be encountered in rectangular metallic waveguides (see section 2.2.2). Generally speaking, propagation is possible if at least one mode exists. However it is worth noting that this assumption may not be enough to guarantee proper propagation.

To investigate further this issue, it is necessary to examine modes characteristics in detail. These properties should then be compared with the excitation conditions in terms of:

- Fields matching: only modes with fields compatible with the source may be excited,
- Impedance matching: modes having impedances close to the source are favored,
- Phase velocity matching: modes having phase velocities close to the source are favored.

Modes offering the best matching characteristics are favored in the coupling with the source and then carry most of the power during the propagation. But multi-mode propagation is usually not a case of practical interest. Available modes typically have different propagation constants and attenuation constants. Such discrepancies can induce significant undesirable signal distortions that are exacerbated with long propagation distances. Among others, mode-dependent group velocities (intermodal dispersion) is very detrimental. After coupling, each excited mode carries a portion of the source power at its own group velocity so that modulated signal actually arrives in multiple times at the receiver as illustrated in Figure 2-9 where intramodal dispersion and attenuation are neglected for simplicity. This phenomenon is then likely to result in Inter Symbol Interference (ISI) and significant Signal to Noise Ratio (SNR) penalty for high-speed communications over long ranges.

Consequently, waveguide applications usually rely on single-mode operation. This later regime is then of particular interest in the context described earlier. However, one should note that this design choice substantially reduces coupling flexibility.

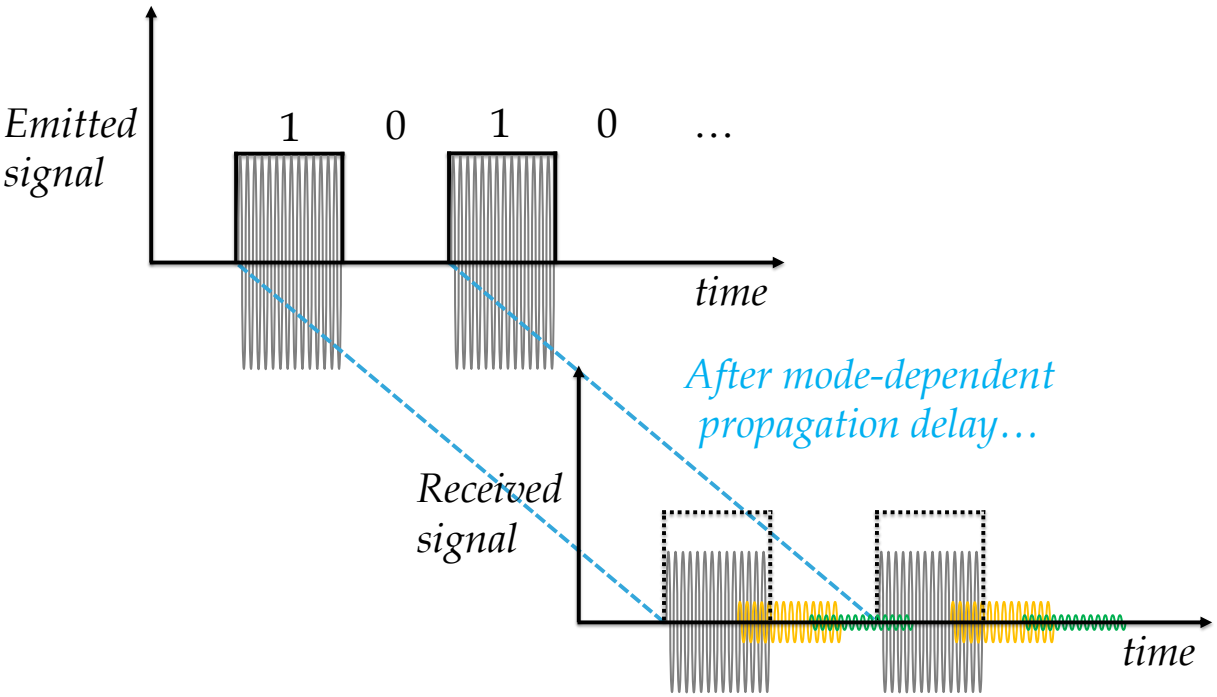

Figure 2-9: ISI in an overmoded waveguide due to mode-dependent group velocities.

To complete the discussion about propagation modes, one should also consider that some particular waveguides may exhibit an infinite number of modes at a given frequency. This is especially true for rectangular dielectric waveguides as presented in **[Yeh, 2008]**. Therefore, analytical derivation becomes extensively impracticable or impossible and analyses based on EM simulations are favored. Hopefully, a dominant mode with quasi single-mode characteristics may be found in most configurations. This fortunate simplification may originate from either a particular excitation favoring the dominant mode or / and a very low attenuation constant compared to other modes. This latter alternative was successfully introduced in optics through Hollow Core Photonic Crystal Fibers in which other modes have higher losses than the dominant one and then decay rapidly **[Cherif, 2009]**.

2.2.2. The Rectangular (Metallic) Waveguide

The well-known rectangular metallic waveguide geometry is illustrated in Figure 2-10. Generally speaking, a dielectric material with magnetic permeability μ and dielectric permittivity ε is enclosed between four perfect (lossless) conductor walls. Starting from Maxwell's equations straightforwardly leads to the existence of several TE and TM propagation modes **[Pozar, 2012]**. Note that no TEM mode can propagate in this single conductor configuration. The cut-off frequencies f_c are summarized in Table 2-1 along with major mode characteristics.

For a given waveguide with $a > b$, the lowest cut-off frequency is always obtained for the TE_{10} mode and satisfies Equation (2-1).

$$f_{c_{10}} = \frac{1}{2a\sqrt{\mu\varepsilon}} \tag{2-1}$$

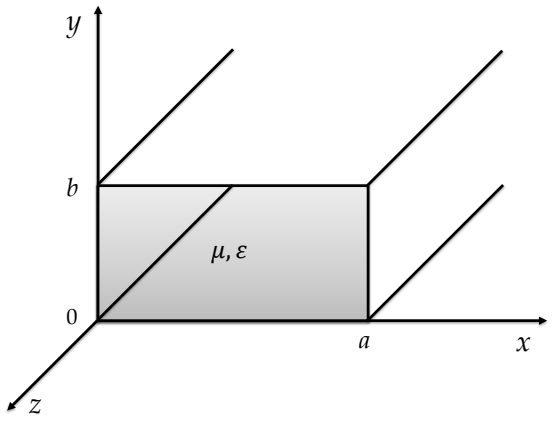

Figure 2-10: Canonical design description of rectangular metallic waveguides.

For frequencies $f < f_{c_{10}}$, any mode has an imaginary β resulting in evanescent waves instead of propagation. Consequently, only frequencies greater than $f_{c_{10}}$ are able to propagate in the structure. This high-pass behavior is also clearly visible in the analytical expression of the group velocity v_g that is undefined for evanescent waves and equals 0 at cut-off. This major discontinuity around cut-off is then responsible for a very dispersive – undesirable – behavior that slowly disappear at higher frequencies (Equation (2-2)).

$$\lim_{\omega \to \infty} v_g = \frac{1}{\sqrt{\mu\varepsilon}} = c \tag{2-2}$$

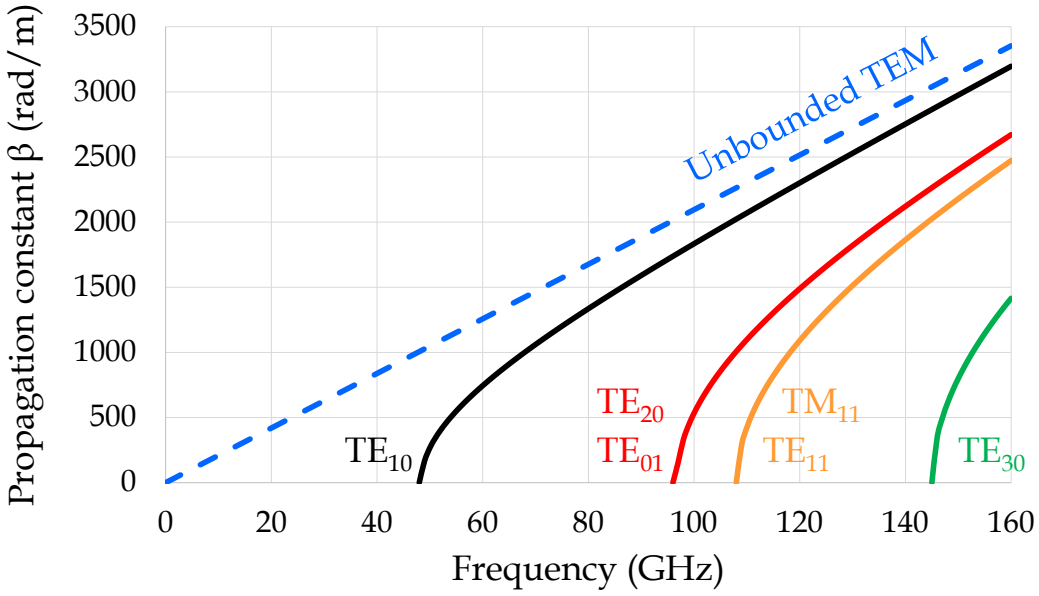

Figure 2-11: Propagation constants diagram in a WR-12 standard air-filled metallic waveguide.

Propagating modes in a WR12 standard section ($a = 3.1$ mm, $b = 1.55$ mm) are reported in Figure 2-11 for illustration purpose. At a given frequency, one can easily verify that any propagation constant is lower than the one of an unbounded TEM wave propagating in the material (pure air in this case). In other words, propagating modes are always contained in an area of the diagram defined by Equation and called *light cone*.

$$\beta \leq \beta_{Unbounded\ TEM} \tag{2-3}$$

	$\mathbf{TE_{mn}}$ **Mode**	$\mathbf{TM_{mn}}$ **Mode**
Cut-off frequency f_c	$\frac{1}{2\pi\sqrt{\mu\varepsilon}}\sqrt{(\frac{m\pi}{a})^2+(\frac{n\pi}{b})^2}$	$\frac{1}{2\pi\sqrt{\mu\varepsilon}}\sqrt{(\frac{m\pi}{a})^2+(\frac{n\pi}{b})^2}$
Cut-off wave number k_c	$\sqrt{(\frac{m\pi}{a})^2+(\frac{n\pi}{b})^2}$	$\sqrt{(\frac{m\pi}{a})^2+(\frac{n\pi}{b})^2}$
Propagation constant β	$\sqrt{\omega^2\mu\varepsilon-{k_c}^2}$	$\sqrt{\omega^2\mu\varepsilon-{k_c}^2}$
Guide wavelength λ_g	$\frac{2\pi}{\beta}>\frac{2\pi}{\omega\sqrt{\mu\varepsilon}}=\lambda_0$	$\frac{2\pi}{\beta}>\frac{2\pi}{\omega\sqrt{\mu\varepsilon}}=\lambda_0$
Phase velocity v_p	$\frac{\omega}{\beta}>\frac{1}{\sqrt{\mu\varepsilon}}$	$\frac{\omega}{\beta}>\frac{1}{\sqrt{\mu\varepsilon}}$
Group velocity v_g	$\frac{1}{\mu\varepsilon}\frac{\beta}{\omega}=\frac{1}{\sqrt{\mu\varepsilon}}\sqrt{1-\left(\frac{k_c}{\omega\sqrt{\mu\varepsilon}}\right)^2}$	$\frac{1}{\mu\varepsilon}\frac{\beta}{\omega}=\frac{1}{\sqrt{\mu\varepsilon}}\sqrt{1-\left(\frac{k_c}{\omega\sqrt{\mu\varepsilon}}\right)^2}$
Validity	$m\in\mathbb{N}$ $n\in\mathbb{N}$ $(m,n)\neq(0,0)$	$m\in\mathbb{N}^*$ $n\in\mathbb{N}^*$

Table 2-1: Summary of TE_{mn} and TM_{mn} modes main characteristics in rectangular metallic waveguides.

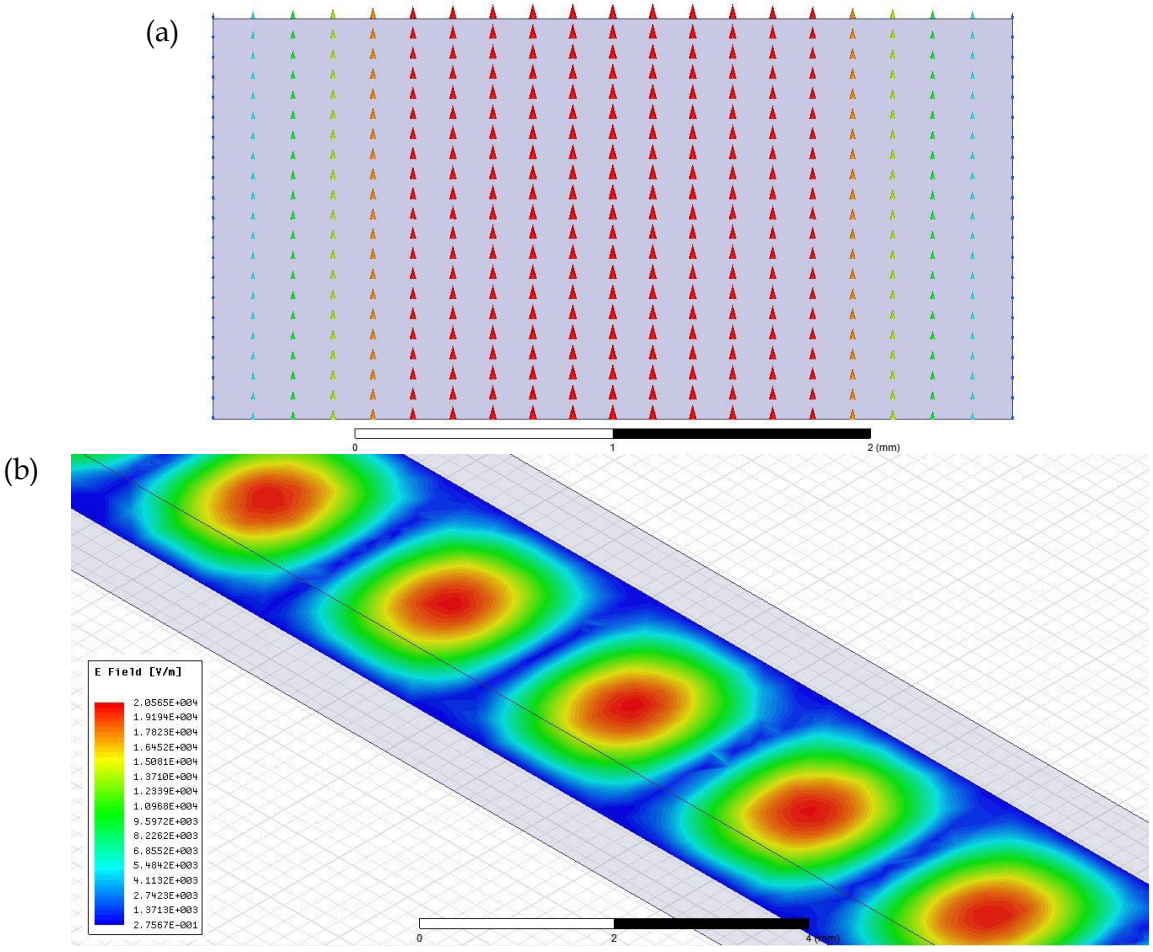

Figure 2-12: Fundamental TE_{10} mode in a WR-12 metallic waveguide. This mode is vertically polarized in the cross-section (a). E-field is distributed homogeneously in the vertical direction and has a sinusoidal distribution horizontally (b – log scale).

Finally, we conclude this section on rectangular waveguides with a special focus on single-mode operation. From Table 2-1 and Figure 2-11, it is very clear that propagating modes exhibit different group velocities as discussed in 2.2.1. Consequently, most applications use single-mode rectangular waveguides, especially in the context of high-speed and/or long-range guided communications. The fundamental TE_{10} mode is then particularly important and is described in Figure 2-12. It features a well-defined linear polarization orthogonal to the broad side with the peak energy located at the center (Figure 2-12 (a)). The propagation of alternative signals results in the presence of nodes and antinodes along the waveguide direction, as visible in Figure 2-12 (b) for the electric field.

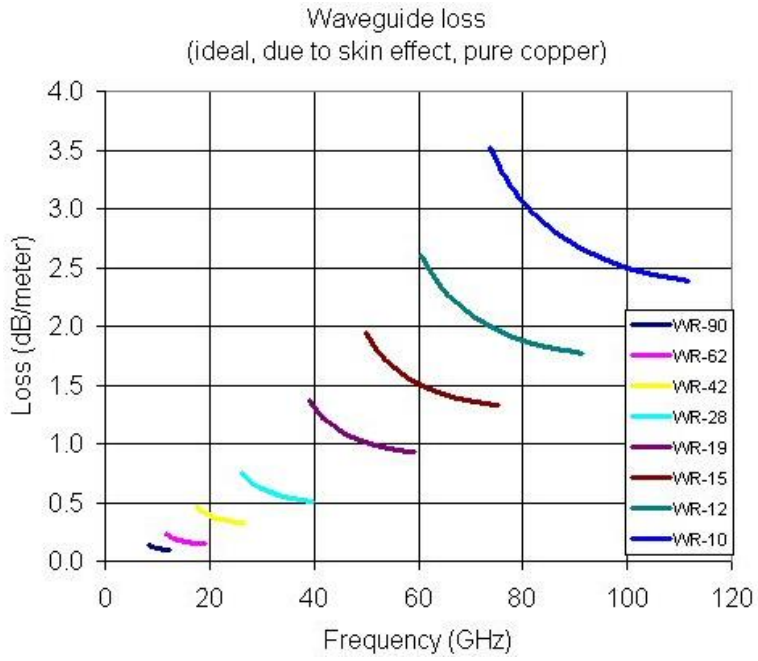

*Figure 2-13: Theoretical conductor loss as a function of frequency for different metallic waveguide standards. Reproduced from [**Microwaves101, 2015**].*

However, the friendly TE_{10} mode has two fundamental issues as regards long-distance communication. The first one is related to attenuation. Loss mechanisms in a waveguide are multiple and will not be covered in this thesis. Among others, conductor loss in hollow waveguides is a significant contributor. According to the theory found in [**Pozar, 2012**] and [**Microwaves101, 2015**], conductor loss strongly varies with frequency. Moving from a standard to a higher frequency one, the loss increases although for a given standard it reduces as a function of frequency. Moreover, as bandwidth increases at higher frequencies, the difference of attenuation between the edges of the band also increases. This behavior is very detrimental, especially for long waveguides transmitting high-data rates. Note that computations in Figure 2-13 only consider theoretical conductor loss so that higher losses are expected in practice due to surface roughness, fabrication tolerances, etc.

The second limitation of the TE_{10} mode is (intramodal) dispersion although it is actually common to any modes in metallic waveguides as reported earlier. To illustrate this point, GDPUL is computed in Figure 2-14 for a standard WR-12 waveguide. As expected, it clearly tends to infinity as frequency approaches cut-off and converges to $1/c_0 \approx 3.5$ ns/m for larger frequencies in agreement with Equation (2-2). In the 60 – 90 GHz range for which this waveguide is rated, GDPUL varies from 5.65 to 3.95 ns/m. From a signal-integrity point of view at system level, such a difference is high and significantly reduces achievable signal bandwidth and / or waveguide length.

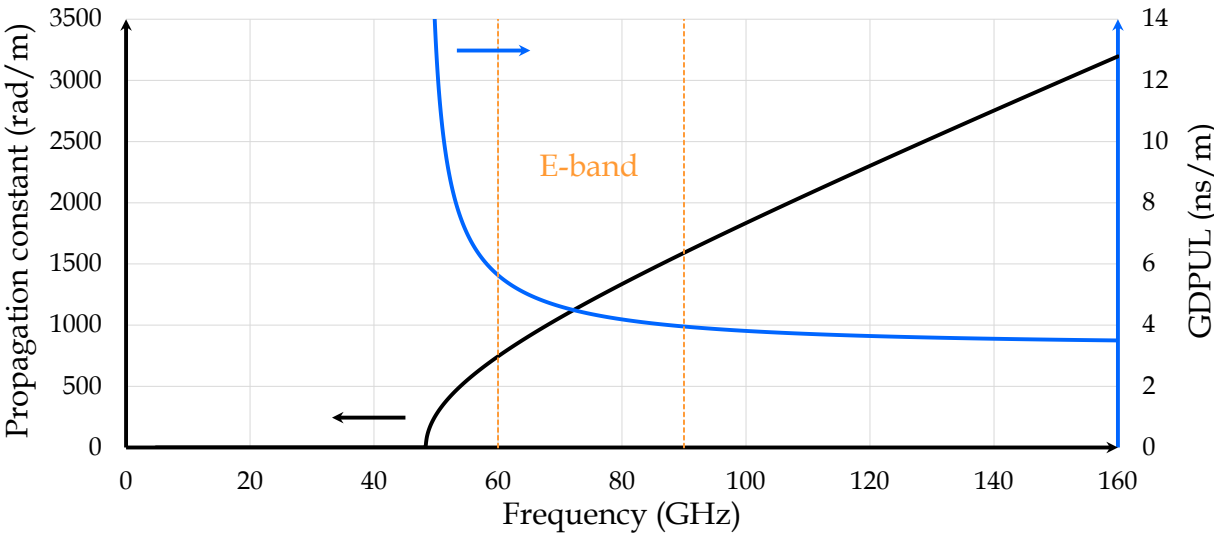

Figure 2-14: Propagation constant and GDPUL in a standard WR-12 waveguide for the fundamental TE_{10} mode.

2.2.3. Optical Fibers and Useful Approximations in Geometrical Optics

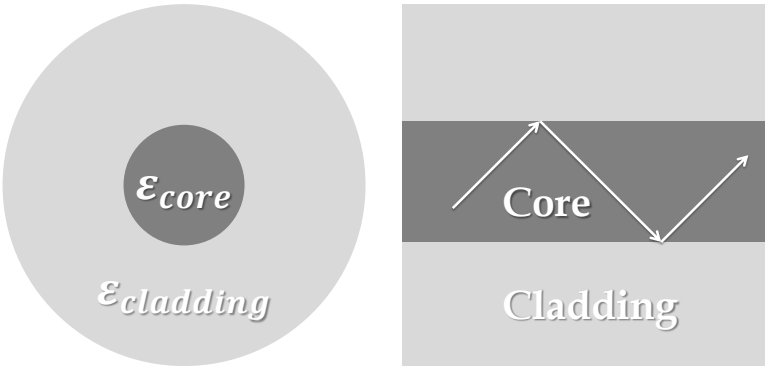

Figure 2-15: An optical fiber made of a circular core surrounded by a cladding medium.

Optical fibers are a special case of waveguides illustrated in Figure 2-15. A dielectric *core* material with dielectric constant ε_{core} is enclosed in a second dielectric *cladding* material with dielectric constant $\varepsilon_{cladding}$. Taking into account manufacturing constraints, the cylindrical geometry presented here is a case of special interest.

The solution of this typical propagation problem usually rely on Snell-Descartes equations in the context of geometrical optics. Combining Equations (2-4) and (2-5), one can easily derive the propagation condition of Equation (2-6). In other words, a dielectric constant discontinuity should exist between the core and the cladding to permit proper propagation. This type of optical fiber is defined as *step index* fiber.

$$n = \sqrt{\varepsilon_r} \tag{2-4}$$

$$n_{core} > n_{cladding} \tag{2-5}$$

$$\varepsilon_{core} > \varepsilon_{cladding} \tag{2-6}$$

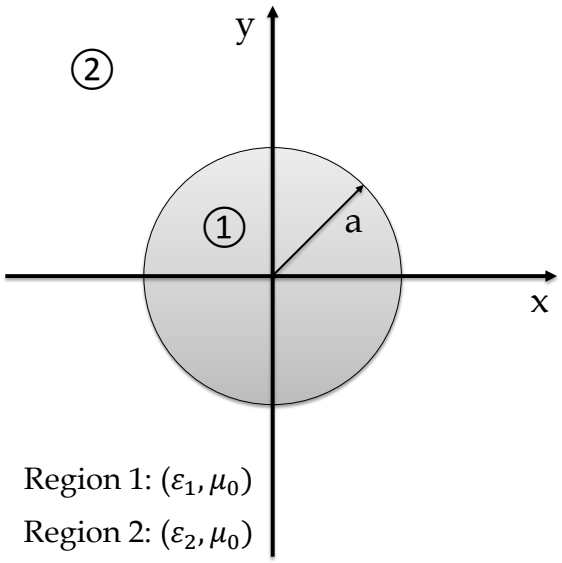

Figure 2-16: Cylindrical dielectric waveguide with non-magnetic materials.

Assuming that Equation (2-6) is satisfied in the cylindrical conditions of Figure 2-16, a modal analysis of this dielectric waveguide can be performed in the more general EM context. The theoretical and numerical progress in this era are compiled in [**Yeh, 2008**]. Because analytical derivation of the fields in this structure exceeds the scope of this discussion, we only comment on the main conclusions of this exercise:

- Satisfying both propagation equations and boundary conditions require finite fields in region 1 and rapidly decaying fields with respect to radius in region 2.
- Possible modes are formed by TE and TM modes as well as hybrid modes exhibiting an inextricable coupling of both.
- Pure TE and TM modes actually only exist in the perfect circular geometry and become hybrid when the section symmetry condition is lost (like in an elliptical section). Their main polarization is orthogonal to radius and as a consequence of the symmetry, they have no azimuthal dependence. They are then denoted as TE_{0m} or TM_{0m} modes.
- Hybrid modes are either named HE_{nm} (if $H_z / E_z < 0$) or EH_{nm} (if $H_z / E_z > 0$). In this context, *n* refers to the number of azimuthal cyclic variations while *m* is used to index these solutions based on increasing radial variations. Note that hybrid modes satisfy $n \neq 0$.
- The fundamental mode is a hybrid mode named HE_{11} having a theoretical zero cut-off frequency. This mode can then propagate at any frequency. It is also denoted as the *dominant mode*.
- Higher order modes have non-zero cut-off frequencies like in rectangular metallic waveguides (see section 2.2.2).
- Fields analysis and boundary conditions between core and cladding regions lead to:

$$q_2{}^2 = \beta^2 - k_2{}^2 = \beta^2 - k_0{}^2 \varepsilon_{r2} \geq 0 \quad (2\text{-}7)$$

$$p_1{}^2 = k_1{}^2 - \beta^2 = k_0{}^2 \varepsilon_{r1} - \beta^2 \geq 0 \quad (2\text{-}8)$$

Combining Equations (2-7) and (2-8), one can interestingly shows in Equation (2.9) that propagation constant β is bounded between k_2 (unbounded plane wave propagation in region 2) and k_1 (unbounded plane wave propagation in region 1).

$$k_2 \leq \beta \leq k_1 \tag{2.9}$$

In other words, propagation only occurs between the light cones of region 2 and 1. Contrary to metallic waveguides, it appears that cut-off condition is no longer satisfied for $\beta = 0$ but rather for $\beta = k_2$. This latter condition corresponds to an unbounded plane wave propagation in region 2 and then sets the limit between radiation and propagation. Consequently, for any mode with cut-off frequency f_c (defined by $q_2 = 0$), the quantity p_1 satisfies:

$$\omega_c = 2\pi f_c = \frac{p_1 c_0}{\sqrt{\varepsilon_{r2} - \varepsilon_{r1}}} \tag{2.10}$$

Where c_0 is the speed of light in vacuum. Fields analysis at cut-off frequency allows the computation of p_1 using following equations:

For TE_{0m} and TM_{0m} modes $$J_0(p_1 a) = 0 \tag{2.11}$$

For HE_{1m} and EH_{1m} modes $$J_1(p_1 a) = 0 \tag{2.12}$$

For HE_{nm} modes with $n \geq 2$ $$\left(\frac{\varepsilon_1}{\varepsilon_2} + 1\right) J_{n-1}(p_1 a) = \frac{p_1 a}{n-1} J_n(p_1 a) \tag{2.13}$$

For EH_{nm} modes with $n \geq 2$ $$J_n(p_1 a) = 0 \tag{2.14}$$

Where J_n is the n^{th}-order Bessel function of the first kind. Except for HE_{nm} modes, m is then related to the m^{th} root of J_n.

Since $J_1(0) = 0$, the HE_{11} mode has a zero cut-off frequency as presented earlier. One can also verify it is a unique property of this particular mode. The second lowest cut-off value is obtained for TE_{01} and TM_{01} modes for $p_1 a = 2.405$. Therefore, the single-mode frequency range can be computed using Equation (2.15).

Single-mode frequency range $$0 < f < \frac{2.405}{2\pi a} \frac{c_0}{\sqrt{\varepsilon_{r1} - \varepsilon_{r2}}} \tag{2.15}$$

Interestingly, this result is compared with metallic waveguide counterparts in Table 2-2 and insightful conclusions can be drawn. In fact, it is worth noting that, at a given maximum single-mode frequency, the dielectric waveguide is $\frac{\sqrt{\varepsilon_r}}{\sqrt{\varepsilon_{r1} - \varepsilon_{r2}}}$ bigger than the circular metallic waveguide. Assuming that $\varepsilon_r = \varepsilon_{r1}$ (loaded waveguide) and $\varepsilon_{r2} = 1$ (air-cladding) this factor is $\frac{\sqrt{\varepsilon_{r1}}}{\sqrt{\varepsilon_{r1} - 1}} \approx 133\%$ for typical plastic materials with $\varepsilon_{r1} \approx 2.3$. But the ratio is only 88% for air-filled circular metallic waveguides, meaning the dielectric waveguide has a smaller cross section. As regards rectangular metallic waveguides (assuming $a = 2b$), the diameter to the broad side ratio becomes $\frac{2.405\sqrt{\varepsilon_r}}{\pi\sqrt{\varepsilon_{r1} - \varepsilon_{r2}}} = \frac{2.405}{\pi} \frac{\sqrt{\varepsilon_{r1}}}{\sqrt{\varepsilon_{r1} - 1}} \approx 102\%$ and $\frac{2.405}{\pi} \frac{1}{\sqrt{\varepsilon_{r1} - 1}} \approx 67\%$ in similar conditions respectively. These results are illustrated in Figure 2-17.

		Fundamental cut-off frequency f_c	Lowest higher order mode cut-off frequency
Dielectric waveguide	Circular $r = a$	0	$\frac{2.405}{2\pi a}\frac{c_0}{\sqrt{\varepsilon_{r1} - \varepsilon_{r2}}}$
Metallic waveguide	Rectangular $a = 2b$	$f_{c_{10}} = \frac{c_0}{2a\sqrt{\varepsilon_r}}$	$f_{c_{20}} = f_{c_{01}} = \frac{c_0}{a\sqrt{\varepsilon_r}}$
	Square $a = b$	$f_{c_{10}} = f_{c_{01}} = \frac{c_0}{2a\sqrt{\varepsilon_r}}$	$f_{c_{11}} = \frac{c_0}{a\sqrt{2}\sqrt{\varepsilon_r}}$
	Circular $r = a$	$\frac{1.841}{\pi}\frac{c_0}{2a\sqrt{\varepsilon_r}}$	$\frac{2.405}{\pi}\frac{c_0}{2a\sqrt{\varepsilon_r}}$

Table 2-2: Comparison of circular dielectric waveguides with respect to rectangular, square and circular metallic waveguides in terms of fundamental and lowest higher order mode cut-off frequencies.

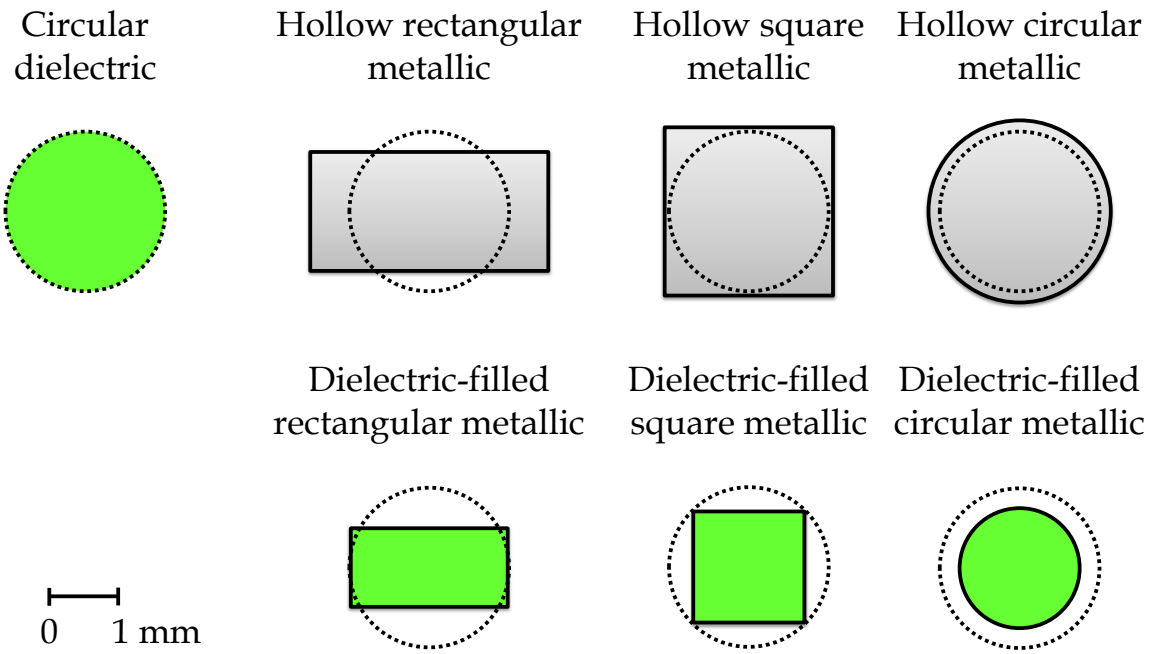

Figure 2-17: Section comparison of the circular dielectric waveguide with respect to various metal counterparts. All waveguides are designed to have a 90 GHz maximum single-mode frequency. The dielectric material has $\varepsilon_r = 2.3$.

Furthermore, it is also clear from Table 2-2 that circular dielectric waveguides have a significantly higher single-mode bandwidth due to zero cut-off frequency. However, this point should be mitigated as the confinement ability of the dielectric waveguide tends to zero for lower frequencies. In order to quantify this aspect, the Poynting confinement factor is defined below:

Poynting confinement factor

$$\Gamma = \frac{\iint_{core} \langle \boldsymbol{S} \rangle_t \cdot \boldsymbol{dA}}{\iint_{total} \langle \boldsymbol{S} \rangle_t \cdot \boldsymbol{dA}} \tag{2-16}$$

Contrary to metallic waveguides (for which Γ definition could be extended but would always rigorously result to 1), dielectric waveguides do not actually carry all the transmitted power through the core medium such that a remaining part of the power propagate through the cladding as well. Because propagation equations are strictly the same, this essential

difference is only the consequence of different boundary conditions. E-field tangential component is supposed to be zero at the edge of a hollow metallic section (perfect conductor assumption) while an equivalent condition is only satisfied when $r \to \infty$ in the dielectric waveguide problem. Consequently, outer fields in this latter case are defined by evanescent waves and Γ represents the ratio of power *effectively* carried inside the waveguide, or in other words, through the core.

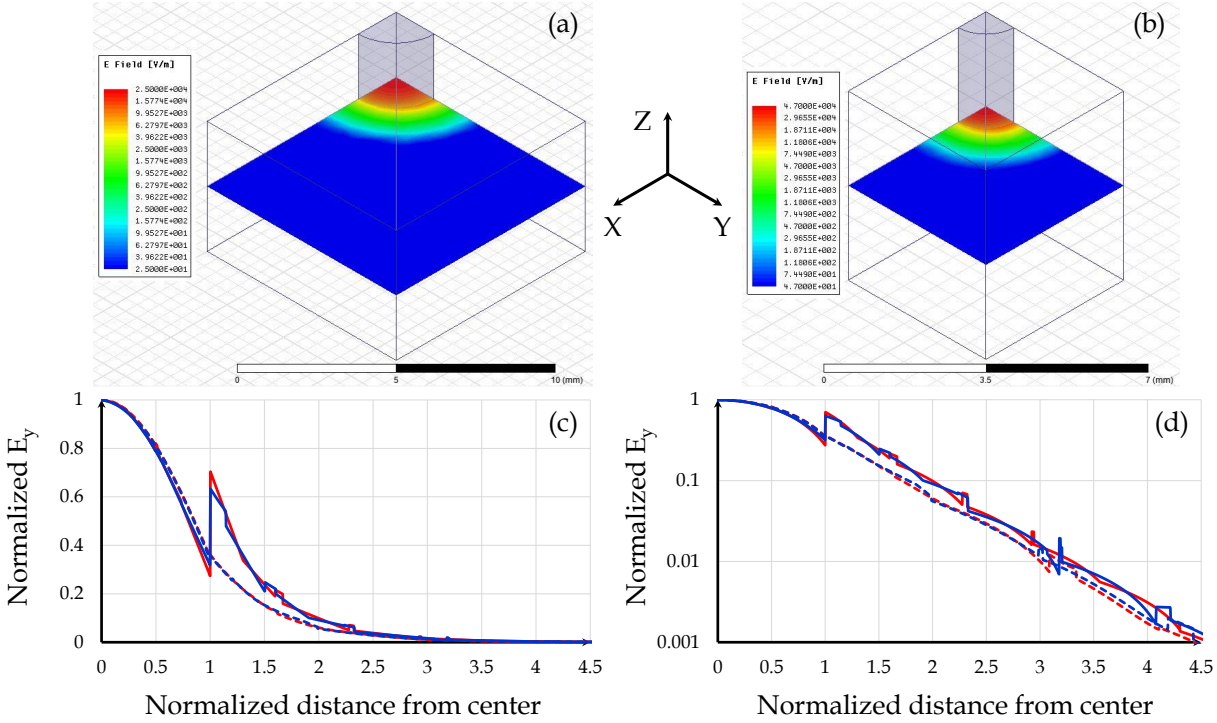

Figure 2-18: Fundamental HE_{11} mode EM fields simulation in cylindrical dielectric waveguides ($\varepsilon_{r1} = 2.3, \varepsilon_{r2} = 1$): (a) E-field in a 60 GHz maximum single-mode frequency (represented at 120 GHz), (b) E-field in a 120 GHz maximum single-mode frequency (represented at 180 GHz), (c) E_y field component normalized at waveguide center (linear scale) and (d) E_y field component normalized at waveguide center (logarithmic scale). Blue curves and red curves represent E_y at 60 GHz in design (a) and E_y at 120 GHz in design (b) respectively. Solid lines and dot lines refer to E_y in y-direction and x-direction respectively.

Since analytical expressions of the fields in both regions of the problem appear to be excessively complex, these expressions are not reported here. A numerical simulation is proposed instead in Figure 2-18 using a FEM solver. To ease comparisons across frequency variation, the design dimensions are shrank accordingly. All designs are simulated at the maximum single-mode frequency so that the normalized cross-sectional area defined by Equation (2-17) is kept constant in all designs. Combining Equations (2-17) and (2.15), this constant is obtained in Equation (2-18).

Normalized cross-sectional area

$$A_{norm} = \frac{4}{\pi}\frac{A}{{\lambda_0}^2} = \left(\frac{2a}{\lambda_0}\right)^2 \tag{2-17}$$

$$A_{norm\ @F_{max}} = \left(\frac{2.405}{\pi}\right)^2 \frac{1}{\varepsilon_{r1} - \varepsilon_{r2}} \tag{2-18}$$

From Figure 2-18, several conclusions can be drawn. First, the evanescent nature of the fields outside plastic waveguides (normalized distance > 1) is now obvious. Moreover, when

examining normalized E_y field components carefully, it clearly appears that, in spite of small approximations in the numerical solutions, these components superimpose if the distance to the waveguide center is normalized too. In other words, fields distribution scales with wavelength in this EM problem.

A strong field discontinuity is visible at the waveguide surface only in y-direction. This is caused by E-field normal component discontinuity while tangential component is continuous leading to E_y continuity in the x-direction. In the context of optical propagation, because the index step may be very small (typically $\Delta n \approx 1-5\% \leftrightarrow \Delta\varepsilon_r \approx 2-10\%$) the discontinuity becomes insignificant and can be neglected. Consequently considering symmetrical field distribution in x-/y-directions is a fair approximation. In addition, as fields extension outside the waveguide scales with wavelength, this effect is usually neglected as well at optical frequencies since only a few microns in the vicinity of the waveguide may significantly impact the propagation. These later approximations reduce the complexity of the EM problem thus relaxing the need for a complete complex fields description. This important result is actually the foundation of the well-known geometrical optics framework, for which simple light rays are considered with appropriate propagation rules. In short, we have proved here that this simplification, while being very suitable for optics, should definitely not be used in the context of plastic waveguides.

Finally, attenuation in circular dielectric waveguides is introduced. This phenomenon is of particular importance for system level considerations. However, exact derivations of the circular dielectric waveguide characteristics in the presence of an attenuation is not straightforward. Assuming weakly lossy materials and single-mode propagation, all field components can be modified to account for attenuation with a simple $e^{-\alpha z}$ factor (for $z > 0$) while propagation constants are supposed to remain identical. Accordingly, time-average transmitted power *P(z)* then varies with a factor $e^{-2\alpha z}$ (for $z > 0$). Consequently, *P(z)* verifies Equation (2-19).

$$\frac{dP}{dz} = -2\alpha P(z) = P_{loss}(z) \tag{2-19}$$

$$P_{loss}(z) = \sigma_1 \int_{Region\ 1} |\boldsymbol{E}_1|^2 dA + \sigma_2 \int_{Region\ 2} |\boldsymbol{E}_2|^2 dA \tag{2-20}$$

Lost power per *dz* length $P_{loss}(z)$ is given by Equation (2-20) with σ_1 and σ_2 the bulk conductivities of materials in region 1 and 2 respectively. Combining Equations (2-19) - (2-21), α is obtained in Equation (2-22).

$$P(z) = \frac{1}{2} Re\left\{ \int_{Region\ 1} (\boldsymbol{E}_1 \times \boldsymbol{H}_1^*) \cdot \boldsymbol{e}_z \, dA + \int_{Region\ 2} (\boldsymbol{E}_2 \times \boldsymbol{H}_2^*) \cdot \boldsymbol{e}_z \, dA \right\} \tag{2-21}$$

$$\alpha = \frac{8.686}{2} \frac{P_{loss}(z)}{P(z)} \quad \text{(dB/m)} \tag{2-22}$$

Note that z-independent expressions of field components are necessary in both Equations (2-20) and (2-21). To compute these quantities, the perturbation approach assumes that unperturbed fields (derived from a lossless design) can be used. Hopefully, this approximation is known to be excellent for usual dielectrics.

2.3. Understanding Dielectric Waveguides: The Dielectric Slab Example

In this part, a simplified 2D configuration is studied. While not being a case of practical interest, this simplification allows the derivation of insightful analytical expressions and interesting conclusions are drawn. Among them, and as expected from the usual geometrical optics framework, it is shown that propagation in 2D geometries is possible.

2.3.1. Problem Description

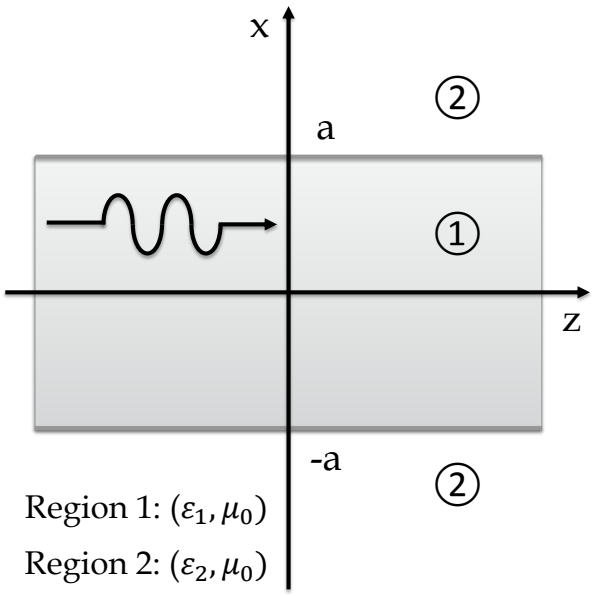

Figure 2-19: Symmetrical slab dielectric waveguide with non-magnetic materials.

A symmetrical 2D configuration is considered in Figure 2-19 with non-magnetic materials for simplicity reasons. The slab thickness is supposed to be 2*a* and we will only consider propagation in the +z-direction.

2.3.2. Propagating Modes

Fields analysis in this structure leads to the presence of pure TE and TM modes. Therefore, these modes can be excited independently contrary to the modes of cylindrical dielectric waveguides in Section 2.2.3 where an intrinsic coupling results in hybrid modes. For both TE and TM modes, field components have sinusoidal distributions in region 1 and decay exponentially in region 2. More specifically, field components in this latter region are proportional to e^{-qx} for a given mode, where $q = \frac{1}{L_{decay}}$ (m^{-1}) and L_{decay} is the typical decaying distance in the x-direction. As a consequence, when q approaches 0, fields get less and less bounded to the slab and radiation (in the x-direction) occurs for $q \leq 0$.

In region 1, according to the sinusoidal dependency, fields for a given mode are written in the general form of $\lambda \cos(px) + \mu \sin(px)$,$(\lambda, \mu) \in \mathbb{C}^2$. The physical interpretation of p (m^{-1}) is unfortunately not as direct as the one of q.

However, to satisfy propagation equations and boundary conditions, p and q are related through the propagation constant and the transcendental dispersion relation. We first investigate TM modes that satisfy the set of Equations (2-23) - (2-25).

$$q^2 = \beta^2 - \varepsilon_{r2}\left(\frac{\omega}{c_0}\right)^2 \tag{2-23}$$

$$p^2 = \varepsilon_{r1}\left(\frac{\omega}{c_0}\right)^2 - \beta^2 \tag{2-24}$$

$$\left[\sin(pa) - \frac{q}{p}\frac{\varepsilon_{r1}}{\varepsilon_{r2}}\cos(pa)\right]\left[\cos(pa) + \frac{q}{p}\frac{\varepsilon_{r1}}{\varepsilon_{r2}}\sin(pa)\right] = 0 \tag{2-25}$$

Finding (p, q) couples verifying this system is not straightforward and usually requires numerical solvers. However, it only takes a few simple manipulations from Equations (2-23) - (2-25) to Equations (2-26) and (2-27) to find appropriate couples graphically (Figure 2-20). In a Cartesian coordinate system, Equation (2-26) is actually a circle of radius $\frac{\omega a\sqrt{\varepsilon_{r1}-\varepsilon_{r2}}}{c_0}$ centered at the origin. Note that $q > 0$ in Equation (2-27) is imposed by the physical meaning of this quantity. However, no assumption was made on the sign of p. From Equation (2-27) it appears that any valid (p, q) couple results in another solution, which is $(-p, q)$. Replacing p by $-p$ leads to the exact same field distribution so that the two solutions are equivalent and only $p > 0$ are then considered (Figure 2-20 (b)).

$$(pa)^2 + (qa)^2 = (\varepsilon_{r1} - \varepsilon_{r2})\left(\frac{\omega a}{c_0}\right)^2 \tag{2-26}$$

$$qa = \frac{pa\tan(pa)}{\varepsilon_{r1}/\varepsilon_{r2}} > 0, \qquad qa = \frac{-pa\,\mathrm{cotan}(pa)}{\varepsilon_{r1}/\varepsilon_{r2}} > 0 \tag{2-27}$$

From Figure 2-20 (a), it is clear that the number of appropriate intersections (or possible TM modes) increases with frequency and is given by $\left\lceil\frac{\omega a\sqrt{\varepsilon_{r1}-\varepsilon_{r2}}}{c_0\,\pi/2}\right\rceil$. Therefore, the TM_1 mode exists whatever the frequency and several TM modes can propagate if $\frac{\omega a\sqrt{\varepsilon_{r1}-\varepsilon_{r2}}}{c_0} > \frac{\pi}{2}$.

Finally, TE modes are briefly discussed as well. Similarly, the set of Equations (2-28) - (2-30) are verified. Note that Equation (2-30) is independent from $\varepsilon_{r1}/\varepsilon_{r2}$. Solving for suitable (p, q) couples can be realized as previously described for TM modes.

$$q^2 = \beta^2 - \varepsilon_{r2}\left(\frac{\omega}{c_0}\right)^2 \tag{2-28}$$

$$p^2 = \varepsilon_{r1}\left(\frac{\omega}{c_0}\right)^2 - \beta^2 \tag{2-29}$$

$$\left[\sin(pa) - \frac{q}{p}\cos(pa)\right]\left[\cos(pa) + \frac{q}{p}\sin(pa)\right] = 0 \tag{2-30}$$

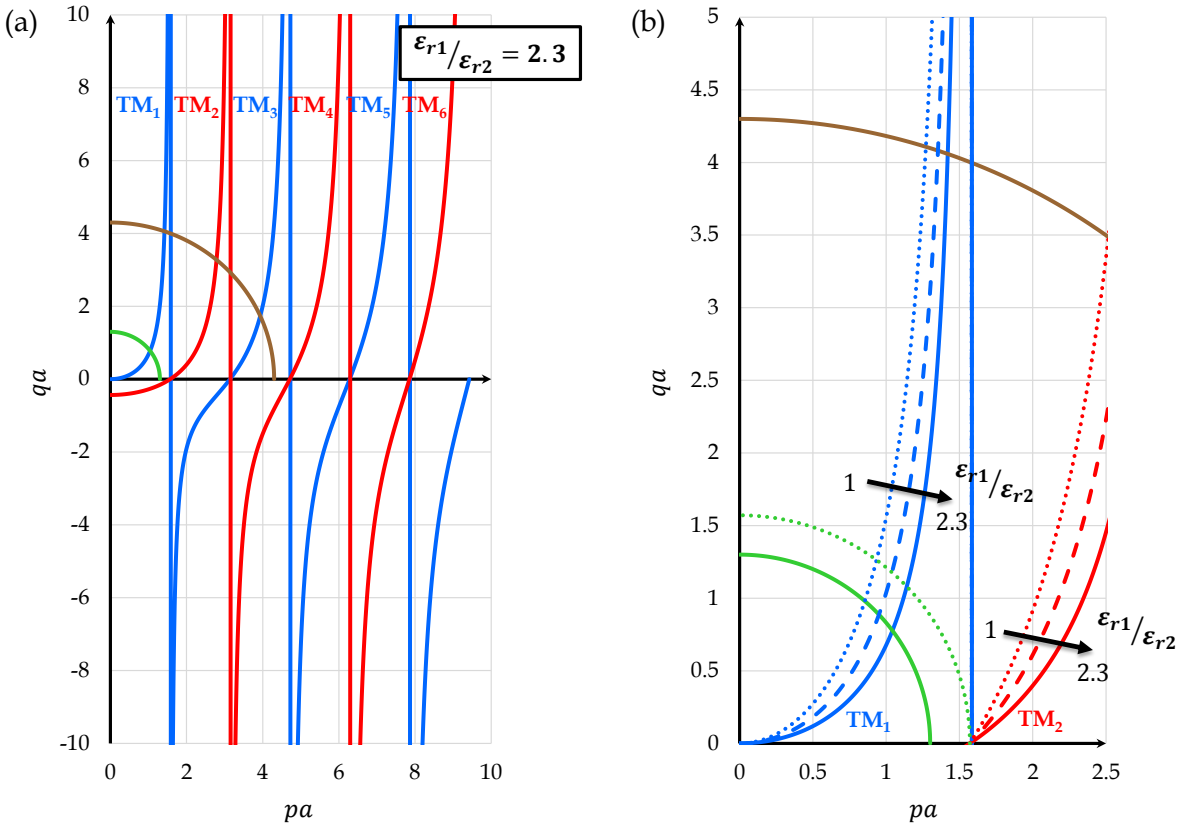

Figure 2-20: Graphical resolution of (p, q) couples for TM modes in slab dielectric waveguides (a) and impact of different $\varepsilon_{r1}/\varepsilon_{r2}$ ratios on fields confinement (b).

2.3.3. Fields Confinement and Dispersion Relation Diagram

For a slab of a given dimension, increasing the quantity qa permits to reduce fields extension out of the slab. In practice, this would make the waveguide more robust to its environment. A propagation "sweet spot" is found when only TM_1 and TE_1 modes can propagate with maximum confinement. This situation is obtained when Equation (2-31) is verified as illustrated in Figure 2-20 (b) with a dotted green line. In the following discussions, it is referred to as the maximum single TE_1 / TM_1 mode regime. Higher qa values are possible for TM_1 or TE_1 modes only if additional modes may also be able to propagate in the waveguide introducing a design trade-off.

Maximum single TE_1 / TM_1 mode regime

$$(\varepsilon_{r1} - \varepsilon_{r2})\left(\frac{\omega a}{c_0}\right)^2 = \left(\frac{\pi}{2}\right)^2 \qquad (2\text{-}31)$$

For given material properties, Equation (2-31) may be used to define a maximum single TE_1 / TM_1 mode frequency inversely proportional to the slab thickness as illustrated in Figure 2-21. Combining Equations (2-26), (2-27) and (2-31), the corresponding (p, q) couple is found to be constant in the maximum single TE_1 / TM_1 mode regime. In other words, L_{decay} linearly scales with wavelength as well as the slab thickness.

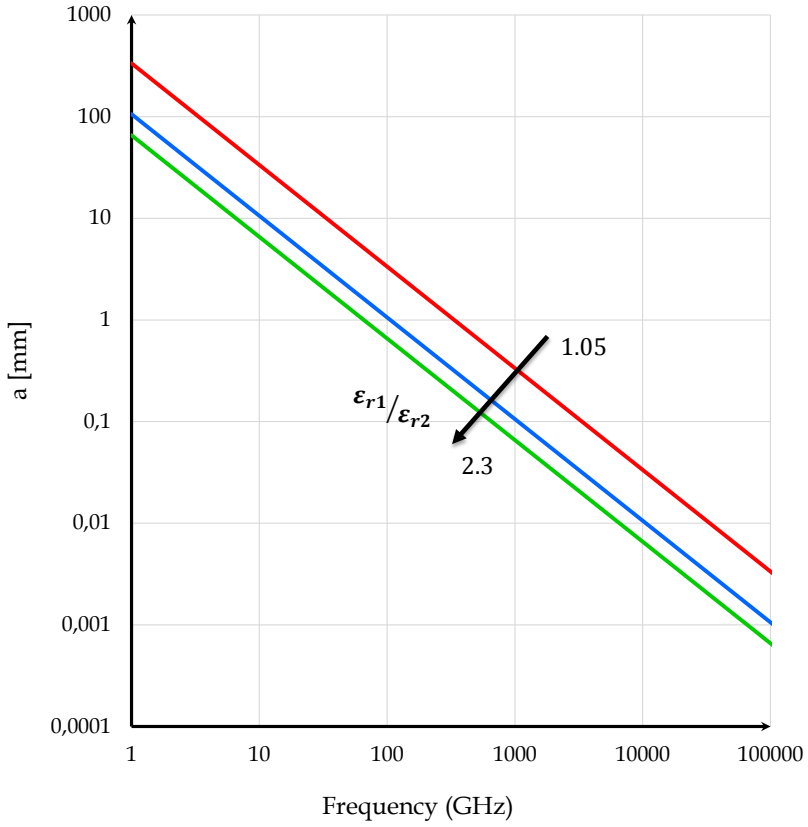

Figure 2-21: Slab waveguide half-thickness in the maximum single TE_1 / TM_1 mode regime versus frequency for different dielectric materials ($\varepsilon_{r2} = 1$).

Now if we consider a constant slab thickness, $\varepsilon_{r1} - \varepsilon_{r2}$ should be decreased accordingly to maintain (2-31) if maximum single TE / TM mode frequency is increased. For TM modes, the impact on (p, q) is shown in Figure 2-20 (b). A slight increase of the quantity qa is observed when $\varepsilon_{r1} - \varepsilon_{r2} \ll 1$, which is likely encountered in optical designs. To go further, it is worth noting from Figure 2-20 that qa is theoretically bounded in the maximum single TE_1 / TM_1 mode regime. The upper bound is found by letting $\varepsilon_{r1} = \varepsilon_{r2}$, leading to $qa \lesssim 1{,}263$. This is an asymptotic bound for TM_1 but the bound is reached for TE_1. Additionally, it is obviously possible to have $qa > 1{,}263$ beyond the maximum single TE_1 / TM_1 mode regime (overmoded waveguide) but one should keep in mind this quantity is always finite, meaning that the associated L_{decay} can only reach 0 asymptotically.

On the opposite, the case of qa approaching 0 for any given mode is investigated. In this situation, L_{decay} of the considered mode tends to infinity so that an increasing part of the mode carried energy travels outside the slab (in region 2). This is neither an expected behavior for a so-called slab waveguide nor a desirable operating regime as propagation becomes very sensitive to perturbations in region 2. As a consequence, the undesirable situation where $qa = 0$ defines a cut-off frequency for the associated modes. From Equations (2-25), (2-26) and (2-30), these frequencies are easily derived for any TE_n / TM_n mode as follows:

TE_n / TM_n cut-off frequency $$f_{cn} = \frac{nc_0}{4a\sqrt{\varepsilon_{r1} - \varepsilon_{r2}}}, n \in \mathbb{N}^* \quad (2\text{-}32)$$

From Equation (2-32) it is clearly visible that cut-off frequencies for TE and TM modes of the same order are identical. However, dispersion characteristics are different resulting in non-degenerated modes (Figure 2-22 (a)). Similarly to cylindrical dielectric waveguides in section 2.2.3, it is observed here that the propagation constant of any mode verifies

Equation (2.9) as well, so that propagation only occurs between two light cones related to the characteristics of region 1 and 2. Note that when this area is reduced, leading to $\varepsilon_{r1} \approx \varepsilon_{r2}$ (typically verified in optical waveguides), the discrepancies between TE and TM modes asymptotically disappear.

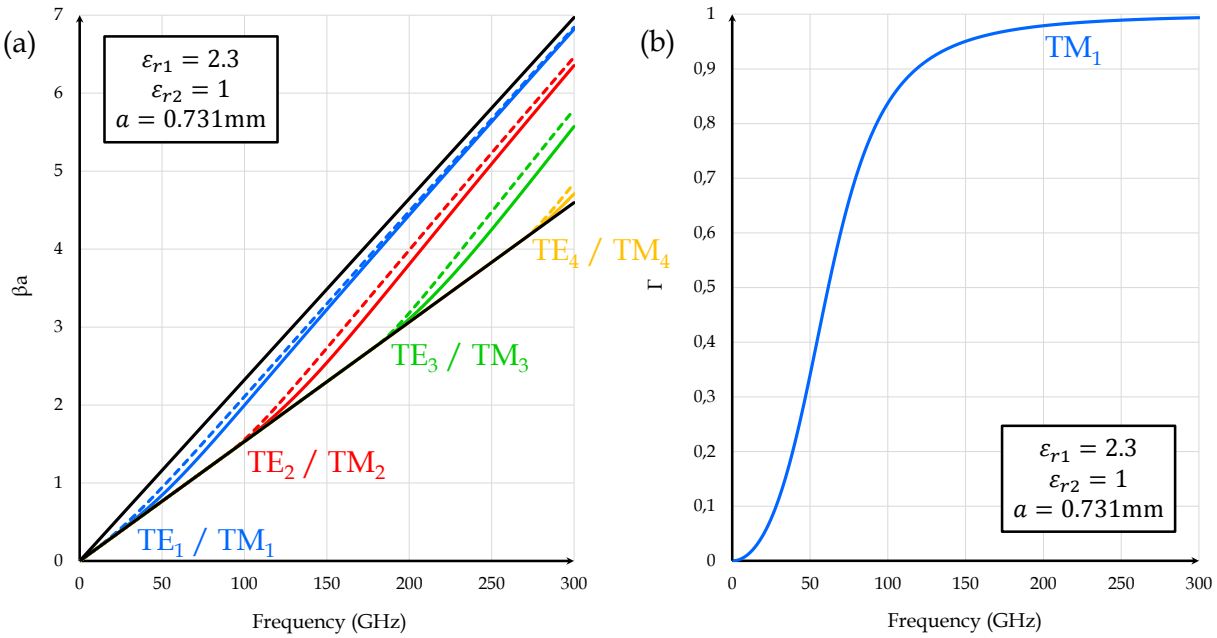

Figure 2-22: Dispersion diagram of the dielectric slab waveguide ($\varepsilon_{r1} = 2.3, \varepsilon_{r2} = 1$) for the first 4 TM (solid) and TE (dotted) propagation modes (a). The Poynting confinement factor is also computed for the TM₁ mode (b). Thickness is chosen to have a 90 GHz maximum single TE₁ / TM₁ mode frequency (f_{c_1}).

Finally, benefiting from the simplicity of the problem, the Poynting confinement factor Γ as defined in Equation (2-16) can be derived. After many analytical manipulations and integrations not reported here, this quantity can be written in the form of Equation (2-33) for the TM₁ mode. It is plotted in Figure 2-22 (b) as well and values noticeably lower than 1 (perfect confinement) are reported in agreement with previous discussion. Note that Γ_{TM_1} is a monotonically increasing function of pa.

$$\Gamma_{\mathrm{TM}_1} = \frac{1 + \frac{\sin(2\mathrm{pa})}{2\mathrm{pa}}}{1 + \frac{\sin(2\mathrm{pa})}{2\mathrm{pa}} + \left(\frac{\varepsilon_{r1}}{\varepsilon_{r2}}\right)^2 \frac{\cos(\mathrm{pa})^2}{\mathrm{pa}\tan(\mathrm{pa})}} \tag{2-33}$$

In order to study this relation, we also define the slab waveguide normalized cross-section using Equation (2-34) in a generalization of the definition given in Equation (2-17).

Slab waveguide normalized cross-section

$$\mathrm{A}_{norm} = \left(\frac{2a}{\lambda_0}\right)^2 \tag{2-34}$$

$$\mathrm{A}_n = \left(\frac{2a}{c_0} f_{c_n}\right)^2, n \in \mathbb{N} \tag{2-35}$$

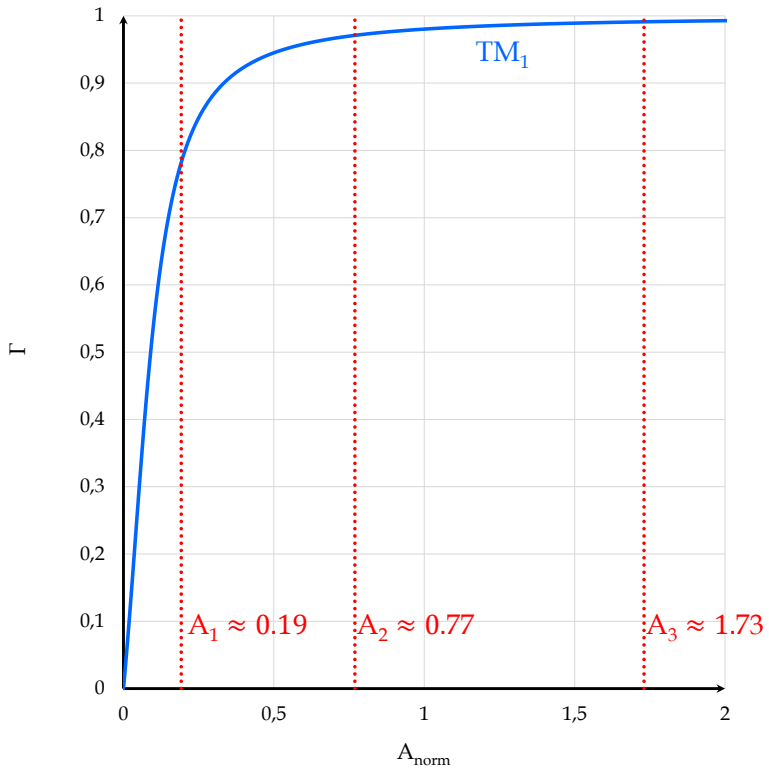

Figure 2-23: Poynting confinement factor Γ_{TM_1} as a function of normalized cross-section A_{norm}.

Figure 2-23 presents Poynting confinement factor Γ_{TM_1} as a function of A_{norm} in the very same slab waveguide as in Figure 2-22. Dimensionless normalized cross-sections are defined in Equation (2-35) to help identify regions based on the number of available TE / TM modes so that areas defined by $A_n \leq A_{norm} < A_{n+1}$ contain $2(n+1)$ propagating modes. For the dielectric slab waveguide with $\varepsilon_{r1} = 2.3$ and $\varepsilon_{r2} = 1$ in the maximum single TE_1 / TM_1 mode regime ($A_{norm} < A_1$), the maximum Γ_{TM_1} is 0.782. According to the maximum pa value discussed earlier in the maximum single TE_1 / TM_1 mode regime, Equation (2-33) leads to $\Gamma_{TM_1} \leq 0.84$ whatever the frequency and materials. These interesting results confirm the intrinsically low confinement ability of dielectric waveguides. Once again, a trade-off appears between confinement and quasi single-mode operation since better confinement is observed for overmoded slab waveguides.

To conclude this part, another comparison with geometrical optics is made by assuming $\varepsilon_{r1} = 2.3$ and $\varepsilon_{r1}/\varepsilon_{r2} = 1.05$. The slab thickness should be consequently increased to maintain $f_{c_1} = 90$ GHz and dispersion diagram and Poynting confinement factor are represented in Figure 2-24 (a) and Figure 2-24 (b) respectively. It is worth noting that Poynting confinement factor in the maximum single TE_1 / TM_1 mode regime ($f < 90$ GHz) is increased when the ratio $\varepsilon_{r1}/\varepsilon_{r2}$ gets closer to 1. This phenomenon is a direct consequence of electric-field discontinuities at the interfaces as illustrated in Figure 2-25 (a).

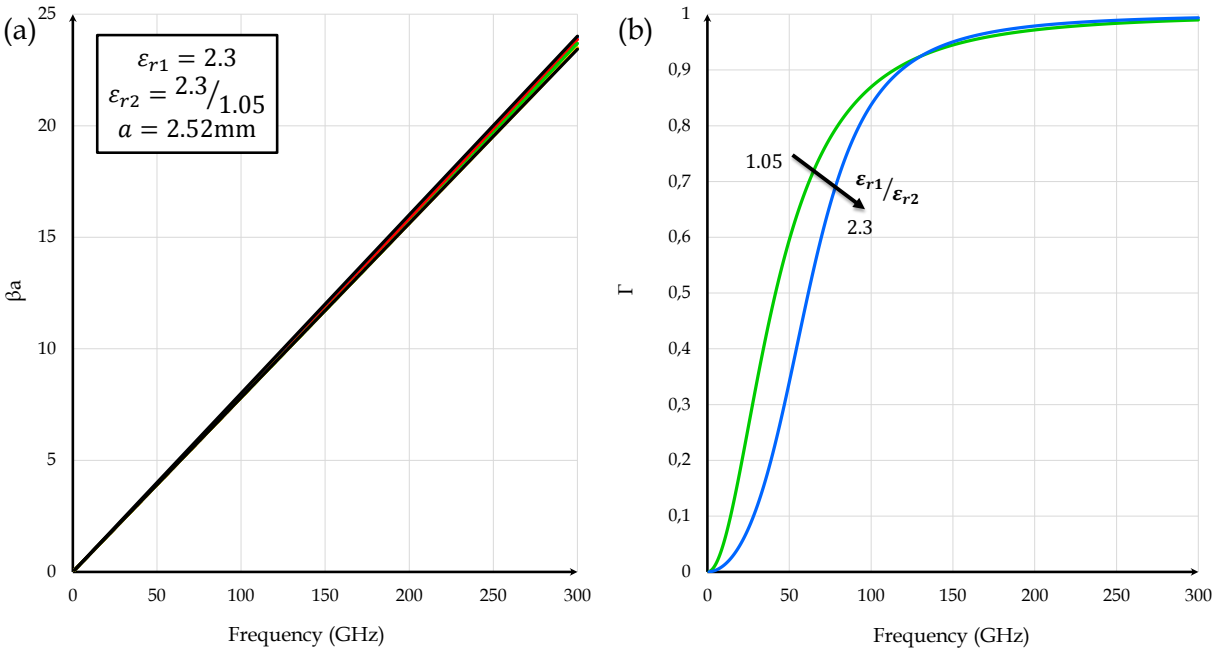

Figure 2-24: Dispersion diagram of the dielectric slab waveguide ($\varepsilon_{r1} = 2.3, \varepsilon_{r2} = {}^{2.3}/_{1.05}$) for the first 4 TE and TM propagation modes (a). The Poynting confinement factor (b) is also computed for the TM₁ mode (green) and compared to the configuration in Figure 2-22 (blue). Thickness is chosen to have a 90 GHz maximum single TE₁ / TM₁ mode frequency (f_{c_1}).

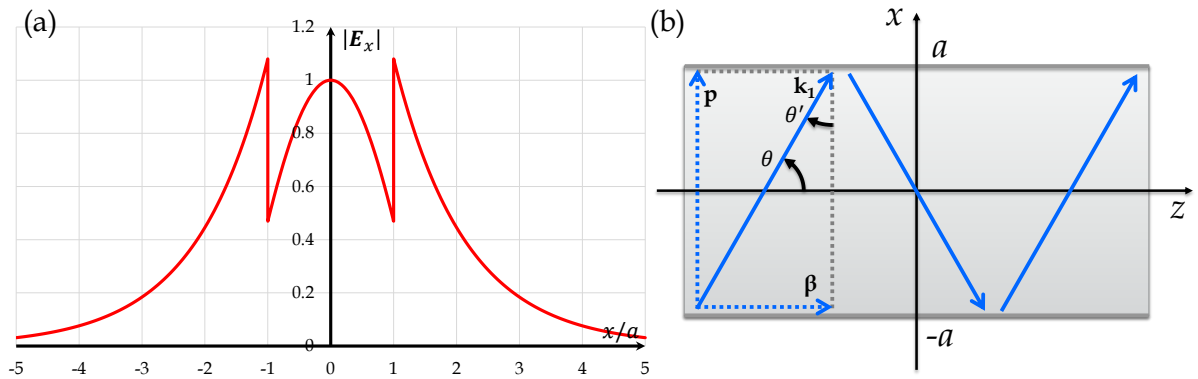

Figure 2-25: (a) Normalized E-field in the x-direction for the TM₁ mode ($\varepsilon_{r1} = 2.3, \varepsilon_{r2} = 1$). (b) Cross-sectional representation of the propagation in the geometrical optics framework.

Moreover, from Equation (2-24) it is possible to define θ to verify Equations (2-36) and (2-37). It now appears that for a given mode excited at a given frequency, propagation is not straight but inclined at an angle of $\theta \neq 0$. This phenomenon is clarified in Figure 2-25 (b). An expression of q can be obtained as a function of θ or $\theta' = \frac{\pi}{2} - \theta$ (2-38). Thanks to Equation (2-39), it is possible to rewrite propagation condition in the form of Equation (2-40) which is equivalent to (2-41) in the considered ranges. Fortunately, (2-41) is the exact expression of Snell-Descartes law but it is clear that the geometrical optics framework is not able to describe phenomena like improper energy confinement or multi-mode operation.

$$\beta = k_1 \cos(\theta) = \sqrt{\varepsilon_{r1}} \frac{\omega}{c_0} \cos(\theta) \tag{2-36}$$

$$p = k_1 \sin(\theta) = \sqrt{\varepsilon_{r1}} \frac{\omega}{c_0} \sin(\theta) \tag{2-37}$$

$$q^2 = \beta^2 - k_2^2 = k_1^2 \left(\cos(\theta)^2 - \frac{\varepsilon_{r2}}{\varepsilon_{r1}}\right) = k_1^2 \left(\sin(\theta')^2 - \frac{\varepsilon_{r2}}{\varepsilon_{r1}}\right) \tag{2-38}$$

$$\theta_l' = \operatorname{asin}\left(\sqrt{\frac{\varepsilon_{r2}}{\varepsilon_{r1}}}\right) = \operatorname{asin}\left(\frac{n_2}{n_1}\right) \tag{2-39}$$

$$q^2 = k_1^2(\sin(\theta')^2 - \sin(\theta_l')^2) > 0 \tag{2-40}$$

$$\theta' > \theta_l' \tag{2-41}$$

2.3.4. Attenuation

Assuming weakly lossy dielectric materials, the perturbative approach described in section 2.2.3 can be applied here as well. Even if analytical derivation in this geometry is possible, obtained expressions are very impracticable and are not reported here. However, it is clear that confinement plays a central role. Actually, as Poynting confinement factor increases, more and more power is carried inside the slab so that attenuation constant transitions from a regime dominated by dielectric losses in region 2 to another regime dominated by region 1. In practical cases, region 2 may be a very low loss dielectric material (usually air or foam). Consequently, attenuation increases monotonically with Poynting confinement factor thus exhibiting an attenuation / confinement trade-off.

Nevertheless, in most practical applications, this trade-off is of limited interest as strong confinement properties are usually desired.

2.4. Choosing Design Parameters

In this part, it is our objective to provide additional information and practical considerations for the plastic waveguide designer. Since all design parameters are interdependent, each subsection only investigates one parameter variation while others are kept constant unless otherwise stated. The cylindrical (fiber) geometry is selected to provide an example of practical interest in which analytical expressions are available. Finally, a design methodology is proposed.

2.4.1. Operating Frequency

Choosing the operating frequency is not usual in RF / mmW design because wireless systems are actually limited by stringent emission standards. In our case, guiding energy through plastic waveguides prevents from complying with these standards so that operating frequency can be willfully chosen. Additionally, no plastic waveguide standard currently exist at the time of these lines, leading to application-specific developments. Before compliancy and legacy become matters of concern, the frequency choice is therefore a new design parameter for system level optimization.

Note that additional useful benefits come with free frequency choice, like unbounded emitted power, blocker immunity, or ACLR tolerance. It is all about tolerating one's own

emitted pollution in the waveguide… so that welcomed design margins may be expected compared to usual wireless circuits.

From the waveguide design point of view, operating frequency primarily influences the waveguide footprint as illustrated in Equations (2.15) and (2-31). Attenuation characteristic is also strongly impacted by the frequency choice. In the case of TEM plane-wave propagation, attenuation characteristic induced by dielectric losses is expressed as follows. A linear dependency (in dB/m) is clearly visible.

$$\alpha_d^{TEM} = 8.686\sqrt{\varepsilon_r}\frac{2\pi f \tan(\delta)}{c_0}\frac{}{2} \qquad \text{(dB/m)} \qquad \text{(2-42)}$$

In the context of TE, TM or hybrid modes, this relation becomes more complex but it is still expected to converge asymptotically to Equation (2-42) as confinement increases. Consequently, we can consider that attenuation characteristics in high confinement plastic waveguides increase with frequency.

2.4.2. Materials Choice

In section 2.2.3, it was shown that propagation occurs only if two materials with different dielectric permittivity are present. Even though the low permittivity "cladding" material may be made of low permittivity plastic material, this medium is likely to be air (or possibly foam) for economical purpose. This hypothesis reduces materials selection to the choice of the "core" material only.

Then, the core material should be selected to comply with both dielectric and mechanical desired properties. Knowing environmental conditions is key at this step because plastics usually stands for *thermoplastic* materials recalling that their properties are strongly impacted by temperature but also by radiation, mechanical stress, etc. Moreover, depending on the targeted application, some restrictions may apply to some plastic materials containing potentially harmful substances (such as colorant, flame-retardant or UV-protection additives).

It is beyond the scope of this section to investigate further the mechanical properties of all possible dielectric materials suitable for plastic waveguides. We report below important mechanical properties to be verified to assess material suitability for a given application:

- Hardness,
- Density,
- Glass transition and melting temperatures,
- Chemical stability,
- Behavior in presence of ionizing radiation,
- Polymer grade influence.

The last point reminds us that most polymers are usually available in different grades, with variable properties from one grade to another. Comparing all polymers, including all their available grades, is then a time-consuming task. For this reason, materials with good dielectric properties may be preselected and we provide below a useful comparison of most common polymers for that purpose. Note that an extensive study including all polymer grades is not available in the mmW frequency range, unfortunately biasing the comparison. Besides,

frequency dependence is also neglected but it is a fair approximation for common materials at mmW frequencies [**Balanis, 1969**].

Materials	**Dielectric constants ε_r**	**Loss tangents $\tan(\delta)$ x 10^4**	**Conditions**	**References**
Polyethylene (PE)	2.31 – 2.30 2.31	3.8 3.8	26 – 38 GHz 60 – 140 GHz @26°C	[**Shimabukuro, 1988**] [**Afsar, 1987**]
Teflon (PTFE)	2.04 2.05 – 2.06 2.06 2.07 2.07	2.2 2 – 3 2.2 5.2 – 5.4 4.7	26 – 38 GHz 60 GHz @25°C 90 GHz @25°C 60 – 140 GHz @26°C 60 GHz	[**Shimabukuro, 1988**] [**Balanis, 1969**] [**Balanis, 1969**] [**Afsar, 1987**] [**Suzuki, 2008**]
Polypropylene (PP)	2.26 2.25	5.0 8.5 – 6.4	26 – 38 GHz 60 – 140 GHz @26°C	[**Shimabukuro, 1988**] [**Afsar, 1987**]
Mylar (PET)	3.5	300	54 GHz	[**Suzuki, 2008**]
PVC	2.74	93 – 96	76.5 – 94 GHz	[**Friedsam, 1997**]
Polystyrene (PS)	2.54 2.53 2.53 – 2.54 2.53	8 – 10 7 7 – 10 11.7	26 – 38 GHz 50 GHz 60 GHz @25°C 90 GHz @25°C	[**Shimabukuro, 1988**] [**Culshaw, 1962**] [**Balanis, 1969**] [**Balanis, 1969**]
Plexiglas (PMMA)	2.58 – 2.60 2.56 2.6	59 84 80 – 85	60 GHz @25°C 90 GHz @25°C 60 – 140 GHz @26°C	[**Balanis, 1969**] [**Balanis, 1969**] [**Afsar, 1987**]
Nylon (PA)	3.0	85 – 90	60 – 140 GHz @26°C	[**Afsar, 1987**]
ABS	2.8	120	100 GHz	[**Park, 2013**]
Polycarbonate (PC)	2.76	55	43 GHz @23°C	[**Shimizu, 2002**]
Alumina (Al_2O_3)	9.75	1.5 – 1.7	82.5 – 107.4 GHz	[**Kogami, 2000**]
Quartz	3.5 – 4.6	1 – 8	94 – 1000 GHz	[**Yeh, 2008**]

Table 2-3: Dielectric properties of ordinary polymers and crystalline materials provided for comparison.

From Table 2-3, dielectric constants of all these polymers are rather similar, basically ranging from 2 to 3. Loss tangents exhibit much broader variations from one material to the other. These variations are then responsible for very different attenuation constants as illustrated in Figure 2-26 in the case of unbounded plane wave propagation.

Besides, it is still insufficiently documented how dielectric properties are intricate to physical ones like temperature, humidity, etc. Important inconsistencies observed in Table 2-3 may actually result from environmental conditions discrepancies as well as from the use of different polymer grades and/or measurement methods. In [**Afsar, 1985**], the sensitivity to sample preparation has been pointed out as well. Generally speaking, this lack of consistent data is troublesome and not intellectually satisfying. In the context of mass-production for high-end harsh environments, like automotive or transports markets, efforts should be spent in order to characterize these properties accurately. Among others [**Balanis, 1969**] and

[**Afsar, 1987**] are the most documented sources. Dielectric properties used in this work are all summarized in Table 2-3 using the highlighted values in case of possible conflicts, unless otherwise specified.

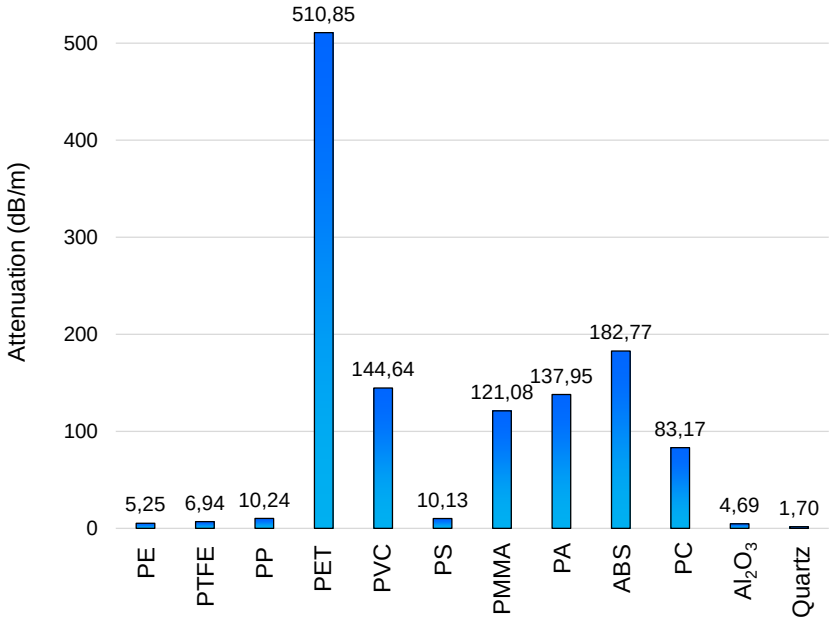

Figure 2-26: Plane wave attenuation (dB/m) for different unbounded dielectric mediums computed @100 GHz.

Finally, we conclude this section by opening the discussion to any dielectric material and wondering why plastics have drawn so much attention. Theoretically speaking, it is clear that any dielectric material could be envisioned to make a dielectric waveguide. For example, crystals like Quartz exhibit very interesting loss tangents. However, their poor flexibility is unacceptable in practical applications, without mentioning their prohibitive prices. While being mechanically attractive, elastomers like rubber suffer from poor dielectric properties at mmW. Chemical stability, and particularly water absorption rate, also discredit natural dielectric materials like wood or textiles. Glass is already used for optical fibers but hardness at roughly 1000x diameters is to be assessed and manufacturing processes require very high temperatures. On the contrary, it appears that many plastic materials advantageously combine all the mechanical properties mentioned above in this chapter, with acceptable or excellent dielectric properties, at inexpensive or affordable prices. Although not all of them are suitable for mmW propagation, some polymers like PE or PTFE appear as excellent candidates.

2.4.3. Footprint Consideration

As illustrated in a low-complexity waveguide geometry by Equation (2.15), it is clear that external diameter is derived from dielectric permittivity and maximum single-mode operation frequency. This relation is illustrated in Figure 2-27 for usual polymers satisfying $\varepsilon_r \approx 2-3$. Consequently, the footprint may not be considered as a design variable at a first glance. However, one can easily imagine that an excessive footprint is not acceptable for some applications. In that particular case, the operating frequency and/or bandwidth should be modified.

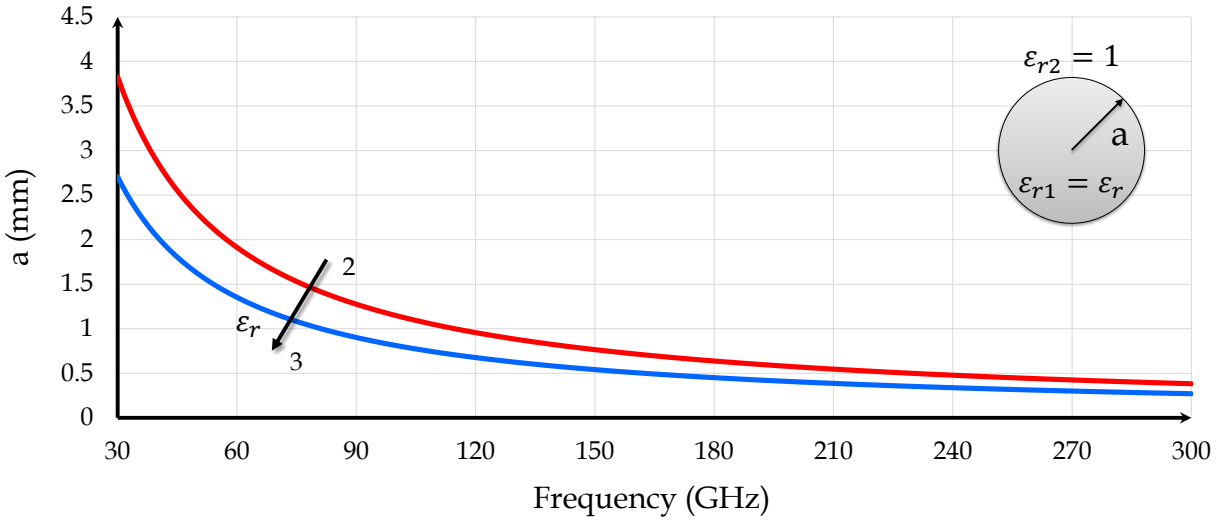

Figure 2-27: Radius of a cylindrical dielectric waveguide as a function of its maximum single-mode frequency assuming $\varepsilon_{r1} = \varepsilon_r$ and $\varepsilon_{r2} = 1$. Red ($\varepsilon_r = 2$) and blue ($\varepsilon_r = 3$) curves are representative of typical bounds for usual polymers.

To provide instructive comparison, Table 2-4 gives overall diameters of some widely spread cable or fiber standards. From a commercial point of view, one can imagine that successful plastic waveguide solutions to address these standards would require comparable or lower diameters than conventional solutions.

Transmission standards	**External diameters**	**References**
Ethernet UTP cat. 5e - 26 AWG	5.2 mm	[**Farnel, 2011**]
Ethernet UTP cat. 6 - 22 AWG	5.8 mm	[**WikiCat6, 2018**]
SMA cable (male connector)	7.9 mm (HEX)	[**WikiSMA, 2018**]
MOST cable - simplex	≈ 2 mm	(measured)
OS2 / OM2 / OM3 / OM4 fibers	2 - 3 mm	[**Fibercablesdirect, 2018**], [**3M, 2012**]

Table 2-4: External diameter comparison of some widespread transmission standards.

2.4.4. Confinement and Environmental Considerations

Similarly to the footprint, confinement is a design consequence. It was previously shown in 2.3.3 that confinement is an increasing function of frequency. This result is further illustrated in Figure 2-28 (a) and Figure 2-28 (b) for a dielectric rod waveguide.

In such a simple geometry, the radius is the only design parameter but it can actually be leveraged to increase confinement to 100% asymptotically. Whatever the frequency and the diameter, Figure 2-29 (b) shows that normalized cross-sectional area (A_{norm}) is a universal quantity governing Poynting confinement (Γ). This kind of relation has also been verified for other low complexity geometries, like rectangular cross-sectional shapes, and other low permittivity materials. However, it is clear that a confinement / footprint trade-off exists since A_{norm} is proportional to the footprint (assuming a given frequency). In the single-mode regime, note that $A_{norm} \leq 0.45$ leads to $\Gamma \leq 0.8$. The same value has also been derived for dielectric slab waveguides in section 2.3.3.

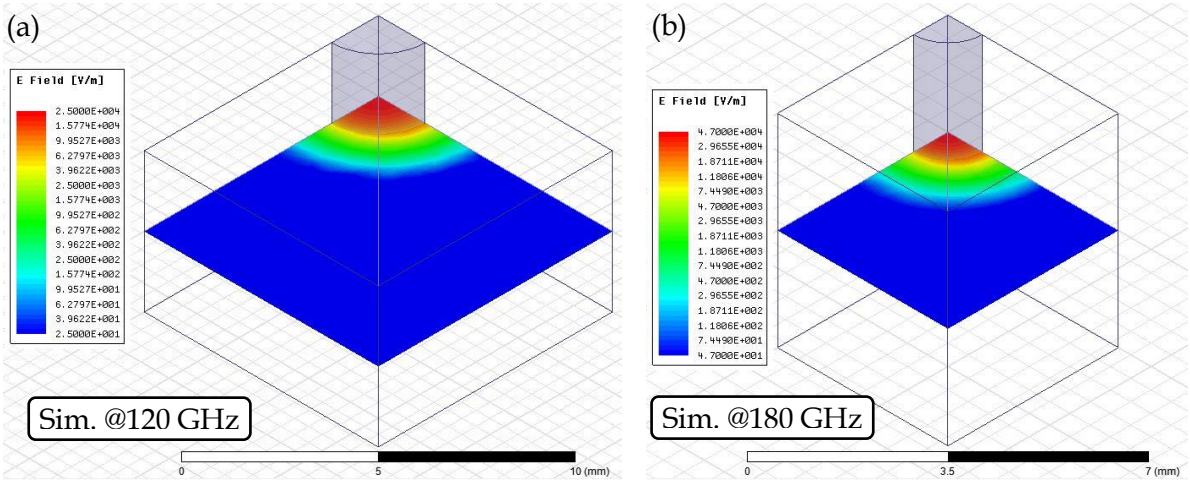

Figure 2-28: Simulated E-field in dielectric waveguides ($\varepsilon_{r1} = 2.3$ $tan(\delta) = 3.8 \cdot 10^{-4}, \varepsilon_{r2} = 1$) with different maximum single-mode frequencies: 60 GHz (a) and 120 GHz (b). Only the fundamental HE_{11} mode is excited. Note that fields intensity are plotted using a log scale.

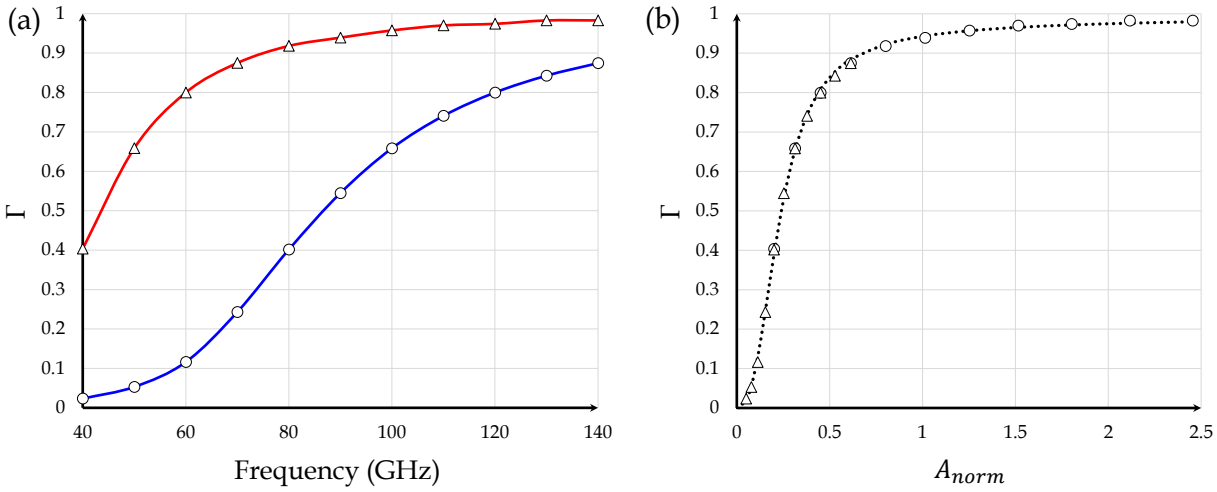

Figure 2-29: Poynting confinement computed from the models presented in Figure 2-28 (a) (triangles) and Figure 2-28 (b) (circles). (a) Poynting confinement as a function of frequency and (b) Poynting confinement as a function of the normalized cross-sectional area.

Finally, another trade-off is found when considering attenuation, as visible in Figure 2-30. Depending on maximum acceptable attenuation in a given system, maximum confinement limits can also be set. To investigate further the dependence of attenuation to confinement, normalized attenuation is defined in Equation (2-43) using the attenuation obtained at the maximum single-mode frequency. In the case of dielectric rod waveguides, Figure 2-31 shows a universal relation between these quantities as expressed empirically in Equation (2-44).

Normalized attenuation

$$\frac{\alpha}{\alpha_{@f=f_{MAX}}} \tag{2-43}$$

$$\frac{\alpha}{\alpha_{@f=f_{MAX}}} \approx \frac{\ln(1-\Gamma)}{\ln(0.2)} \approx 1.43 \log\left(\frac{1}{1-\Gamma}\right) \tag{2-44}$$

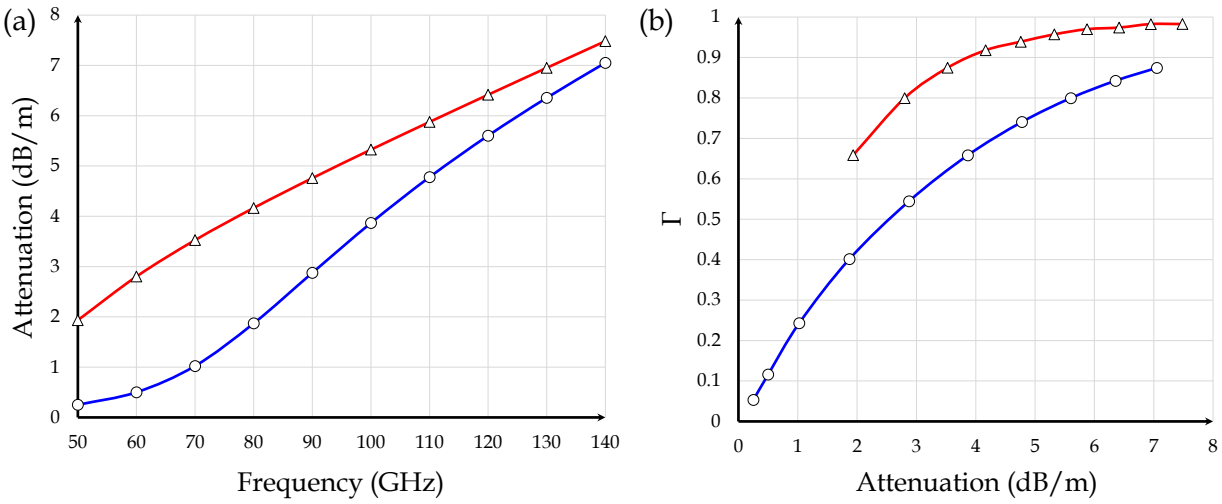

Figure 2-30: Attenuation as a function of frequency (a) and illustration of the attenuation / confinement trade-off (b) from the models presented in Figure 2-28 (a) (triangles) and Figure 2-28 (b) (circles).

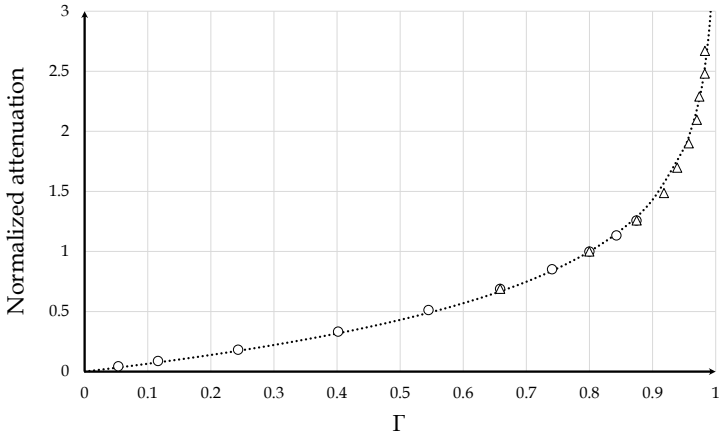

Figure 2-31: Normalized attenuation as a function of confinement from the models presented in Figure 2-28 (a) (triangles) and Figure 2-28 (b) (circles).

Assuming this relation holds for any Poynting confinement value, it now appears that the nature of the propagation in plastic waveguides (surface wave) obviously leads to $\Gamma < 100\%$ because attenuation can't reach infinity. In fact, any attempt to increase confinement eventually leads to higher and higher attenuation. One more time, this major difference with metallic counterparts highlights radically different propagation mechanisms. From an applicative point of view, and regardless the footprint, multi-mode propagation or attenuation consequences, one may wonder what is the minimum confinement needed and what are the *practical* consequences. However, the answers to these questions are not straightforward and may depend on the considered application as well.

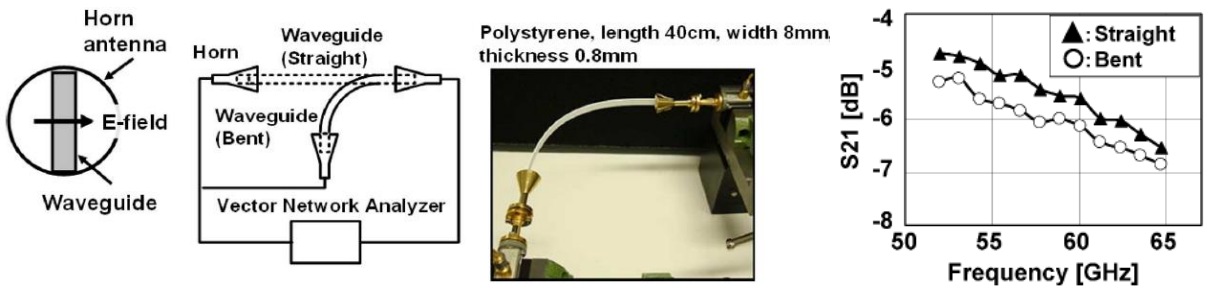

*Figure 2-32: Figures taken from **[Fukuda, 2011]** illustrating the sensitivity to bends (bending radius is estimated to 255 mm).*

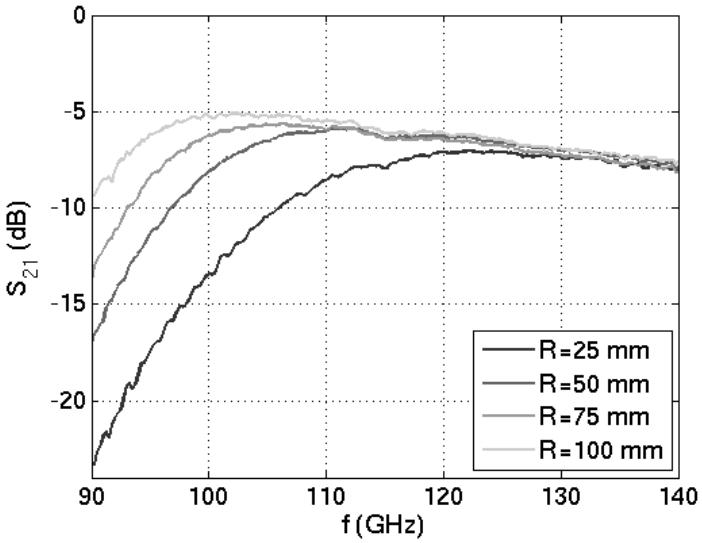

*Figure 2-33: Figure taken from [**Reynaert, 2017**] illustrating the sensitivity to bends.*

What seems although relatively clear is that any material placed in the vicinity of the waveguide (cladding region) induces a perturbation of the propagation. This aspect is exemplified in Appendix A.

Another practical disadvantage of $\Gamma < 100\%$ is the sensitivity to bend (Figure 2-32 and Figure 2-33). As long as the waveguide offers a perfectly straight propagation direction, the part of the energy traveling outside the waveguide is bound and no radiation occurs. However, this canonical situation is actually impossible in practice and, what is more, the ability to manage bends is in fact a mandatory property for envisioned applications of plastic waveguides. Unfortunately, bending plastic waveguides causes lateral radiation so that additional propagation losses are experienced.

From Figure 2-33, it is confirmed that bending losses increase with bending curvature. In other words, aggressive bends are responsible for higher losses. In that process, a noticeable frequency dependence is also noticed. While lower frequencies are impacted significantly, higher frequencies seem much more robust. This point is discussed further in section 2.7.

Finally, it is worth noting that similar loss also *qualitatively* occurs in bent optical propagation. Nevertheless, for a given bending radius, the bend appears smoother at optical frequencies compared to millimeter-wave because of reduced wavelength. On top of that, high curvatures are not permitted in optical fibers to prevent mechanical damage. It is then a fair approximation to neglect bending losses in optics… while they should definitely be considered carefully in millimeter-wave plastic waveguides.

2.4.5. Costs Considerations

The last …but not least… design parameter is the cost of the waveguide. It can be mainly detailed in two cost items: raw material cost and manufacturing cost. These items are extensively difficult to characterize because of crude oil prices dependency, supply and demand evolutions, geographic discrepancies, volume price scaling, etc. Moreover, manufacturing costs are not likely reported by manufacturers as they constitute economical strategic information.

In an attempt to provide comparison guidelines between materials, we report the costs and associated volumes of different polymer resins compiled from [**FrCustoms, 2017**] and [**PlasticsEurope, 2018**] in Figure 2-34. Considering the limitations reported before, it is worth noting that these data are only valid for a restricted period of time in a given region.

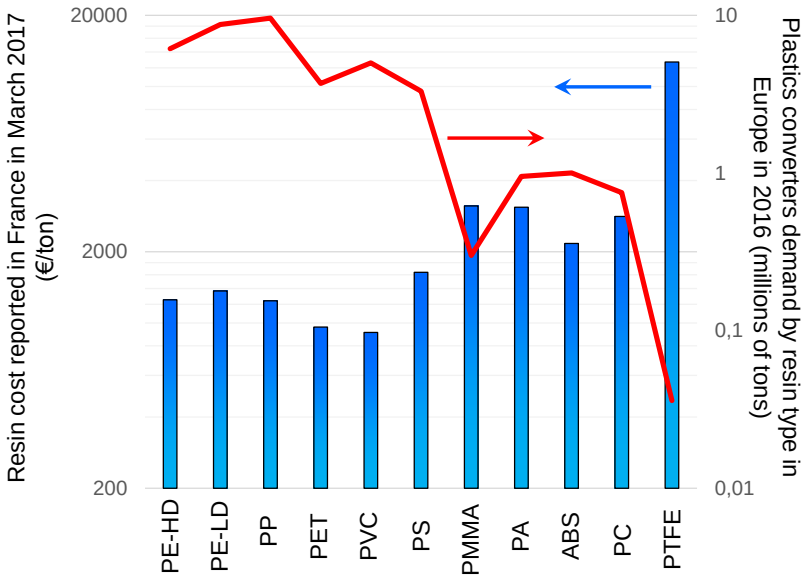

*Figure 2-34: Resin cost reported in France in March 2017 [**FrCustoms, 2017**] (left scale) and plastics converters demand in Europe in 2016 [**PlasticsEurope, 2018**] (right scale).*

From Figure 2-34, we can classify polymers in three categories. The first high volume and low-cost category is referred to as "Commodity Plastics" used in a wide range of applications (packaging, food containers, tubing, automotive parts, etc.). This category is principally composed of PE, PP, PET, PVC, PS.

On the other hand, we find "Engineering Plastics" dedicated to more specific industries, and resulting in much lower volumes and higher costs. The most famous examples in this category are PMMA, PA, ABS, PC. Compared to Commodity Plastics, these polymers usually offer better mechanical properties for more demanding applications. To name a few, ABS is used in Lego bricks due to very strong rigidity, underwear can be made of PA because of its high resistance to abrasion while PC strong resistance to impact makes it interesting for some automotive parts.

Finally, polymers like PTFE, delivering an exceptional combination of mechanical, electrical and chemical properties, are gathered in the "High Performance Polymers" category. These plastics focus on even more specific applications, pushing further the low volumes and high-cost market position. Moreover, in the case of PTFE, the wide temperature range from -150°C to 250°C makes it more difficult to manufacture. PTFE processing actually requires a much higher transformation temperature (close to 380°C) compared to Commodity Plastics (typically 200 – 250°C for extrusion processes). Because it is not compatible with extrusion processes, PTFE manufacturing of long continuous parts (like tubes or rods) rely on expensive sintering processes, which are well-known in powder metallurgy. To put in a nutshell, the global cost of a PTFE plastic waveguide can be roughly estimated to be 10x larger than a PE counterpart because of both resin higher cost and more expansive transformation process.

2.4.6. Plastic Waveguides Design Guidelines

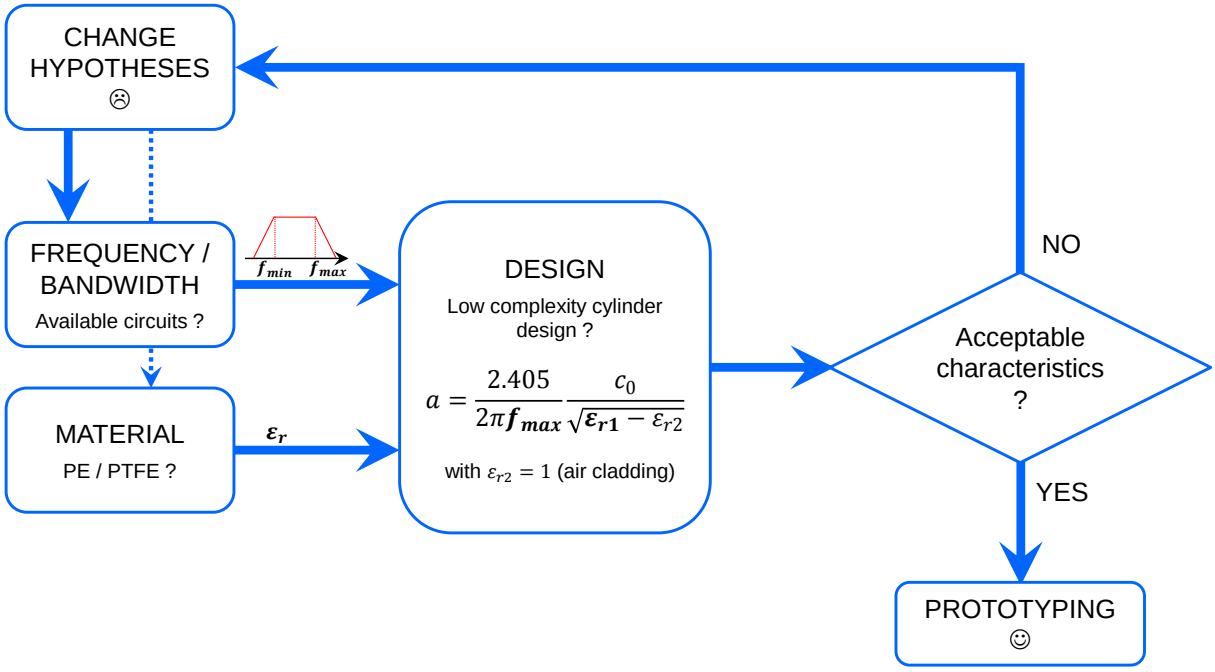

Figure 2-35: Proposed plastic waveguide design methodology for fast prototyping.

In this part, we propose to provide guidelines to accelerate plastic waveguide prototyping. The methodology is summarized in Figure 2-35. While choosing the operating frequency seems attractive for optimum performance, it may be a more pragmatic – and cost effective - choice to rely on already developed millimeter-wave transceivers first. Because wireless communications in unlicensed (57 - 64 GHz) or *license-light* (71 – 76, 81 – 86, 92 – 95 GHz) bands have been driving these developments for many years, these bands should be first considered when designing a plastic waveguide.

Once the frequency range has been chosen considering on-the-shelf circuit performance, the materials of the waveguide should be chosen. For general-purpose prototypes, the HD-PE appears to be a very good candidate thanks to a beneficial combination of good dielectric properties, good flexibility, low cost resin and low cost extrusion manufacturability. However, the maximum temperature for normal usage is limited to 70 - 90°C [**Teyssedre, 2010**]. For higher temperature operations, PTFE or expanded PTFE may be selected.

The dielectric properties of the selected material should then be used to derive the waveguide geometry. Since fast and cheap prototyping requires low complexity sections, the circular geometry is suggested. Note that this symmetric design does not ensure polarization maintaining. It is furthermore believed that maximum confinement is always desired, whatever the attenuation penalty, in order to provide maximum reliability. However, since multi-mode operation is not suitable for data communications, the maximum frequency considered in the system should be used in Equation (2.15) to derive the cylinder radius.

Ultimately, obtained waveguide characteristics should be verified. Because dielectric properties of PE and PTFE are quite similar, operating frequency and/or bandwidth should be modified if the combination of attenuation, confinement, footprint and mechanical property is not satisfactory.

2.5. The Surrounding Environment and Contact Sensitivity Issue: An Innovative Design Proposal

The environmental sensitivity of pure dielectric waveguides is further illustrated in this part. We first consider a case of practical interest: the impact of the user touching the waveguide, which is actually a very aggressive perturbation regarding the propagation conditions. To mitigate this effect, an innovative plastic waveguide design is proposed (Magic Wheel). Comparison measurements with respect to a simpler tubular design are provided in section 2.7.

2.5.1. Contact Sensitivity Issue

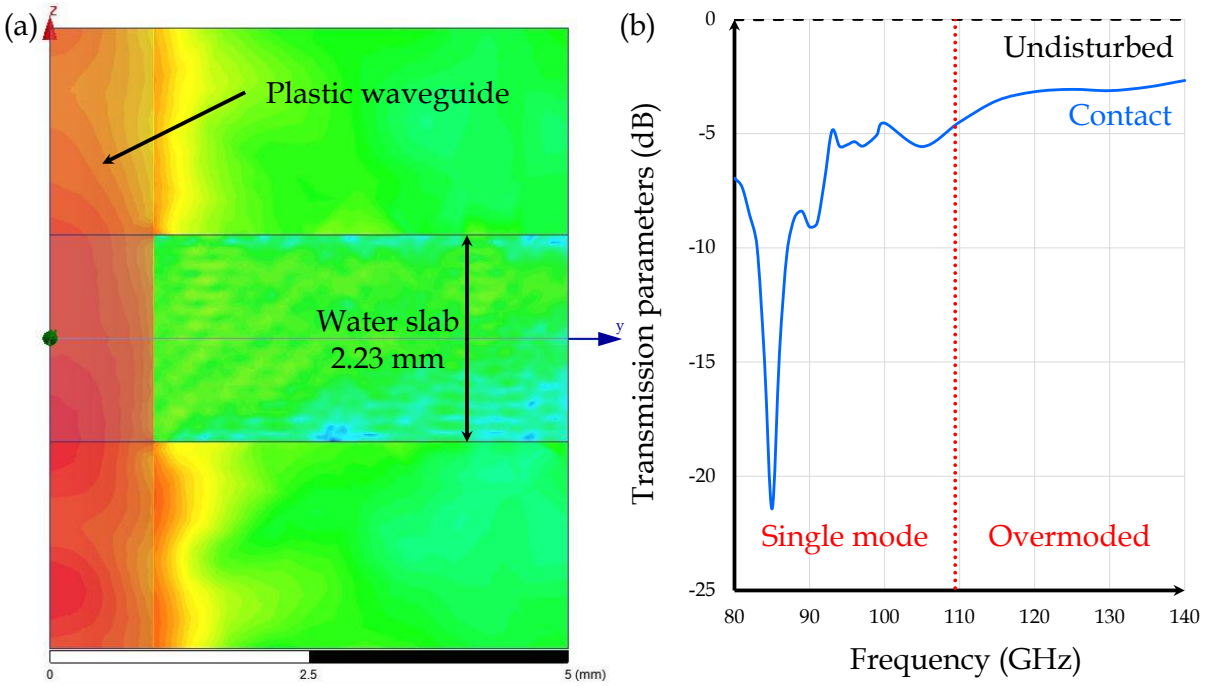

Figure 2-36: Semi-infinite water slab surrounding a 2 mm diameter Teflon waveguide. (a) side view with symmetry conditions enforced and E-field computed at 120 GHz (logarithmic scale). (b) impact on transmission parameters in blue. Undisturbed propagation is provided for comparison in dash black.

To illustrate the sensitivity to external perturbations, i.e. the presence of materials different from air around the waveguide, a numerical simulation is carried out in which a semi-infinite slab is introduced around a slightly overmoded dielectric rod (with confinement greater than 80%). This slab is uniformly filled of water ($\varepsilon_r = 80$) as a fair approximation of a human finger. Nevertheless, the slab thickness is only a 2.23 mm in this example because of computational limitations. A real finger (1.5 – 2 cm width) is thus likely to create an even more aggressive perturbation. Symmetry conditions are also enforced to simplify the model, as shown in Figure 2-36 (a).

Expected attenuation is almost negligible in the undisturbed configuration because of a very limited propagation distance (Figure 2-36 (b)). This result is to be compared to a noticeable insertion loss observed in the presence of the slab. From Figure 2-36 (a), it is clear

that the finger slab introduces significant return losses as well. By locally breaking the condition $\varepsilon_{r\_core} > \varepsilon_{r\_cladding}$, the wave guiding condition is actually no longer satisfied in the core rod, which causes energy radiation in the slab and reflected waves. Furthermore, the slab has a very long electrical-length due to water high dielectric permittivity, which potentially causes longitudinal resonances like in a 2D-cavity. This phenomenon is likely to be responsible for the considerable attenuation observed in Figure 2-36 (b) at 85 GHz. This hypothesis is further consolidated in Appendix A. Finally, with this possibility in mind, it is worth noting that finite 3D-pertubations (like a water drop instead of a slab) could induce much more frequency-dependent behaviors as the radial dimension may also resonate.

Another illustration is given in [**Fukuda, 2011**] where the long plastic waveguide is "floating" above the table thanks to little paper or plastic trestles (see section 2.1.2.2).

To put in a nutshell, these examples illustrate the lack of reliability of pure dielectric waveguides from an applicative point of view. Moreover, it is worth noting that an overmoded waveguide has been considered in Figure 2-36 to benefit from a higher Poynting confinement such that maximal robustness should be expected. Consequently, external contact is likely to be even more detrimental while operating in the single mode regime, a trend that seems confirmed by the basic results obtained at lower frequencies in Figure 2-36 (b).

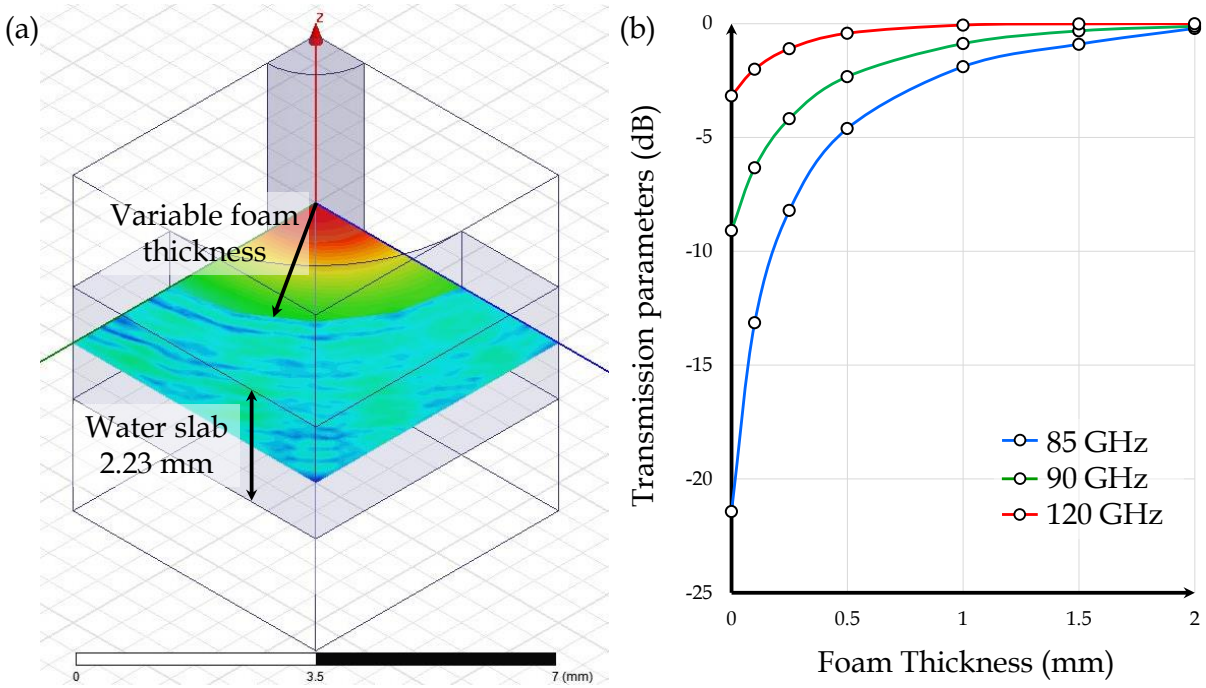

Figure 2-37: Semi-infinite water slab surrounding a foam-coated 2 mm-diameter Teflon waveguide. (a) isometric view of the simulation model with E-field computed at 120 GHz for a 2 mm-thick foam (not represented since it is made of pure air) and (b) impact of the foam thickness on transmission parameters at different frequencies.

In the context of an energy-efficient system, the external contact sensitivity cannot be mitigated relying on important link budget margins. On the contrary, link budget margins should be minimized advocating for a *reliable by design* plastic waveguide. A high-complexity plastic waveguide assembly embedding a protective tube has been proposed in [**Nickel, 2014**]. Nevertheless, this complex design is likely to suffer from high manufacturing costs. At the opposite, a very straightforward and efficient design modification is possible by introducing foam materials around the core waveguide (see section 2.1.2.2). The foam is essentially composed of air and ensures that propagation condition $\varepsilon_{r\_core} > \varepsilon_{r\_cladding}$ is always satisfied. The precedent simulation model can be simulated for various foam thicknesses. For

the sack of simplicity we assume that $\varepsilon_{r\_foam} = \varepsilon_{r\_air} = 1$. Therefore, the slab is progressively moved further when the (air) foam thickness is increased (Figure 2-37 (a)). Besides, detailed results are provided in Appendix A.

From the results of Figure 2-37 (b), the thicker the cladding is made, the better robustness is enforced, especially in the low-confinement region However, this solution suffers from multiple disadvantages:

- Enlarged footprint,
- Poor mechanical reliability – Hard foams like PU foams may not also offer the desired flexibility,
- Porous foams incompatibility – only foams containing dry air cavities should be preferred since porous foams are subject to humidity contamination. Otherwise, an external moisture barrier film should be added.
- Additional manufacturing process – the foam may be added after the extrusion process of the core rod or co-extruded with the core during the same process. In any case, at least a small cost penalty is expected.

While still having some practical limitations with foams, the idea of maintaining propagation condition thanks to a low complexity design modification is interesting and is further investigated in the following section.

2.5.2. Magic Wheel: An Innovative Design Proposal

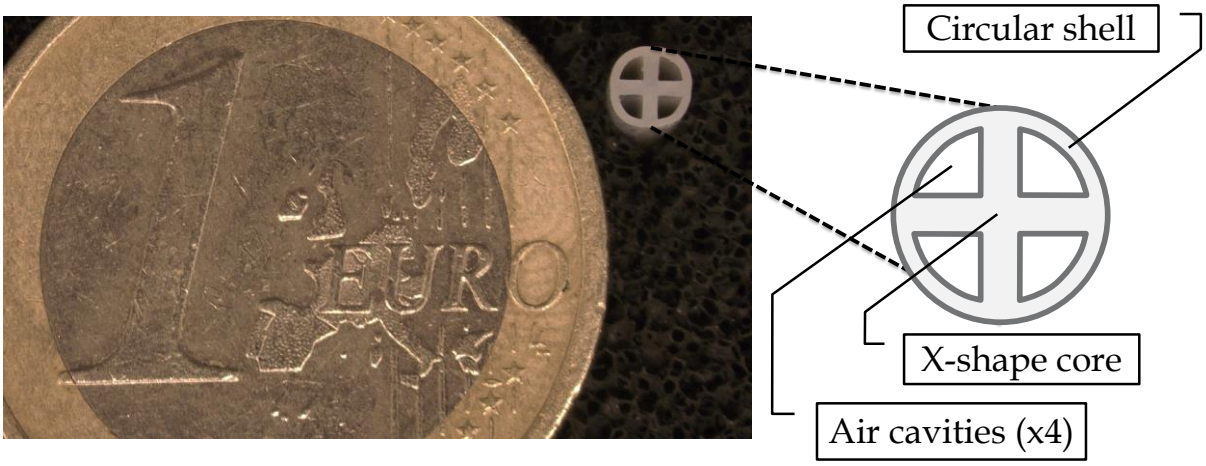

*Figure 2-38: Description of the Magic Wheel waveguide as presented in [**Voineau, 2018**].*

Initially proposed as an alternative to foam coated waveguides, the Magic Wheel waveguide was first introduced in [**Voineau, 2018**] as an attempt to provide both mechanical reliability and contact insensitivity. At the expense of a higher complexity cross-sectional shape, the design embeds a thin *shell* that defines four enclosed spaces, which collectively behave as a *cladding* (Figure 2-38). Consequently, the waveguide *core* is protected from detrimental external contacts similarly as a foam coating. However, the whole design can be made of the very same dielectric material and extruded all at the same time while still ensuring higher mechanical robustness.

Note that the core cross-section featuring two orthogonal branches is carefully designed so that:

- The shell is mechanically supported thus offering good rigidity and limiting shield deformation in the case of external contact.
- Two linearly polarized orthogonal modes are available in the structure – one in each branch of the cross – with very similar propagation properties and obvious polarization maintaining.
- The shell does not participate in the propagation. In other words, the shell should be designed thinner compared to the core branches to make sure that only a negligible part of the energy is effectively carried by the shell region, while most of it travels inside the core and cladding regions.

This design also features two favorable properties: single-mode operation capability and improved Poynting confinement in this regime with respect to lower complexity waveguides. Careful modal analysis is conducted using Ansys HFSS simulation tool. Simulation results are reported along with measurements in section 2.7.3.

2.6. Excitation Conditions: On the Importance of Couplers

In this section, we investigate suitable excitation structures for proper plastic waveguide propagation. Following the discussion in 2.2.1, relevant figures of merit can be listed below:

- Low insertion loss,
- Fields matching,
- Impedance matching,
- Phase velocity matching,
- Mode selectivity,
- Mechanical robustness,
- Coupling reproducibility,
- Low cost.

It has been shown in 2.1.2.2 that satisfying all these conditions is very difficult so that optimizing couplers for a given plastic waveguide may still be considered as an open research topic. Based on the literature, we can mainly identify four different approaches summarized in Table 2-5 with identified advantages and drawbacks.

Although on-chip or in-package coupling using near-field antenna radiation is appealing for the implementation of a compact and cost-effective solution, the poor control of the excited mode(s) and associated polarization, in addition to bandwidth limitation caused by the resonant behavior of the antenna, has led the community to consider the use of intermediate waveguide sections, particularly metallic waveguides. Introducing an intermediate section is not benign and this approach may be not be favored in a long-term perspective because the direct coupling at chip or package level has a higher potential…once reported issues will be solved.

	Advantages ☺	**Drawbacks ☹**
On-chip (or in-package) antenna coupling [**Tytgat, 2013**], [**Kim, 2013**], [**Volkaerts, 2015**]	• Ultra Compact • Low Cost	• Near-field antenna behavior ≠ far field • Poor control of excited mode(s) • High Loss • Limited Bandwidth • Mechanical stability?
PCB Antenna coupling [**Fukuda, 2011**], [**Dolatsha, 2013**]	• Compact • Low Cost	• Near-field antenna behavior ≠ far field • Moderate control of excited mode(s) • High Loss • Limited Bandwidth • Mechanical stability?
Transition with a WR standard metallic waveguide [**Hofmann, 2003**], [**Zhou, 2013**], [**Zhou, 2017**]	• Low Loss • Large Bandwidth • Easy characterization • Single mode regime • Well-known polarization	• Higher Cost • Bulky • Modest mechanical robustness
Transition with a dedicated metallic waveguide [**Volkaerts, 2015**], [**Van Thienen, 2016**]	• Low Loss • Large Bandwidth • Higher mechanical robustness	• Need a custom transition from chip to metallic waveguide • Higher Cost • Bulky

Table 2-5: Summary of excitation schemes reported in the literature along with their respective advantages and drawbacks.

For short-term concerns, and in order to ease characterization, the third approach is then utilized in this work and is presented in Figure 2-39. Once connected to a suitable WR to PCB transition, this solution could enable a conceptual connector. It is actually the purpose of Chapter 3 to present the necessary WR to PCB transition. For the moment, only the WR to plastic waveguide coupler is described here. To do so, a WR-12 standard is considered to provide a suitable reference plane in the 60 – 90 GHz range. In practice, it was even possible to extend the measurement range to 55 – 95 GHz in agreement with EM simulations of this standard. To match the largest dielectric waveguide to the metallic waveguide standard, this latter is enlarged with a standard taper mode converter or pyramidal horn antenna so that the tapered dielectric waveguide can be inserted inside. The waveguide can be mechanically maintained in the metallic aperture using low-density plastic foams introducing negligible perturbation compared to pure air. Such a simple transition has been reported in many references, further justifying the relevance of the proposed approach. In [**Hofmann, 2003**], characterization frequencies up to 600 GHz are demonstrated and positioning enhancement is proposed by adding a dielectric (foam) centering disc in the metallic aperture. [**Zhou, 2013**] and [**Zhou, 2017**] carried out a dielectric taper shape analysis and showed the superiority of a pyramidal taper placed at the center of the metallic waveguide.

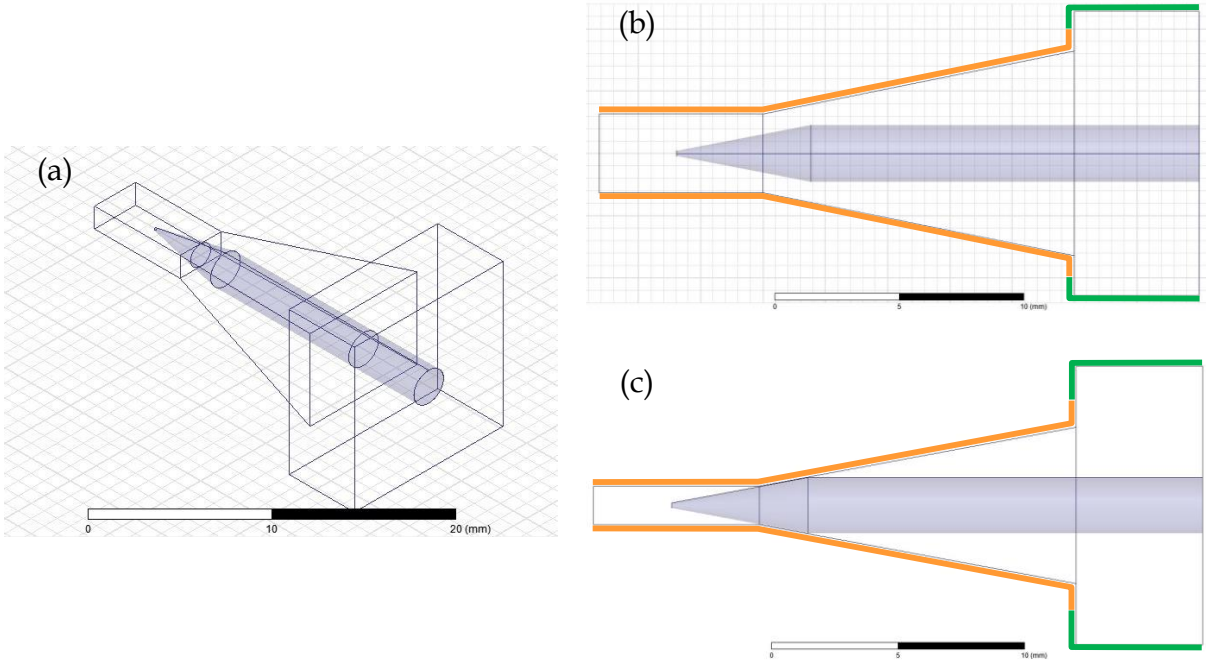

Figure 2-39: Description of the coupler to excite a dielectric rod waveguide (grey) from a WR-12 metallic waveguide using a conically tapered section placed at the center of a large pyramidal horn antenna (not represented for visibility). An isometric view is presented in (a), a top view in (b) and a lateral view in (c). Orange lines indicate metallic conditions imposed by the horn while green lines indicate "radiation boundaries" around the "open" dielectric waveguide.

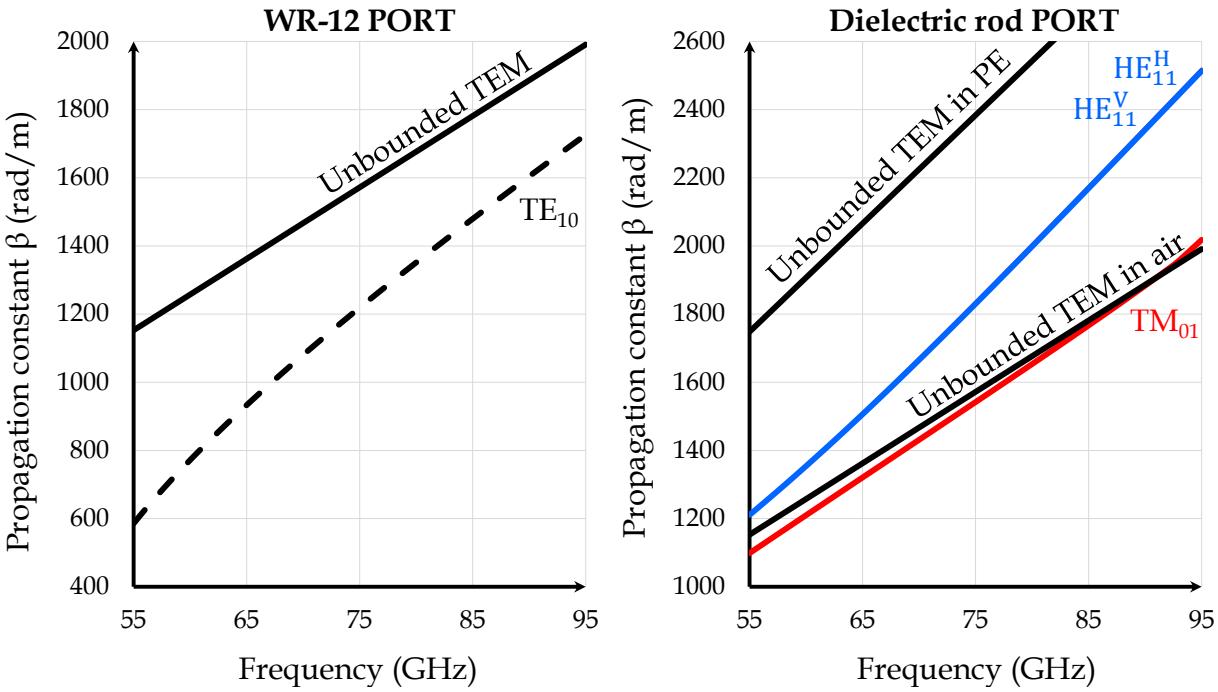

Figure 2-40: Simulated propagation constants at WR-12 port (left) and dielectric rod port (right) of the coupler.

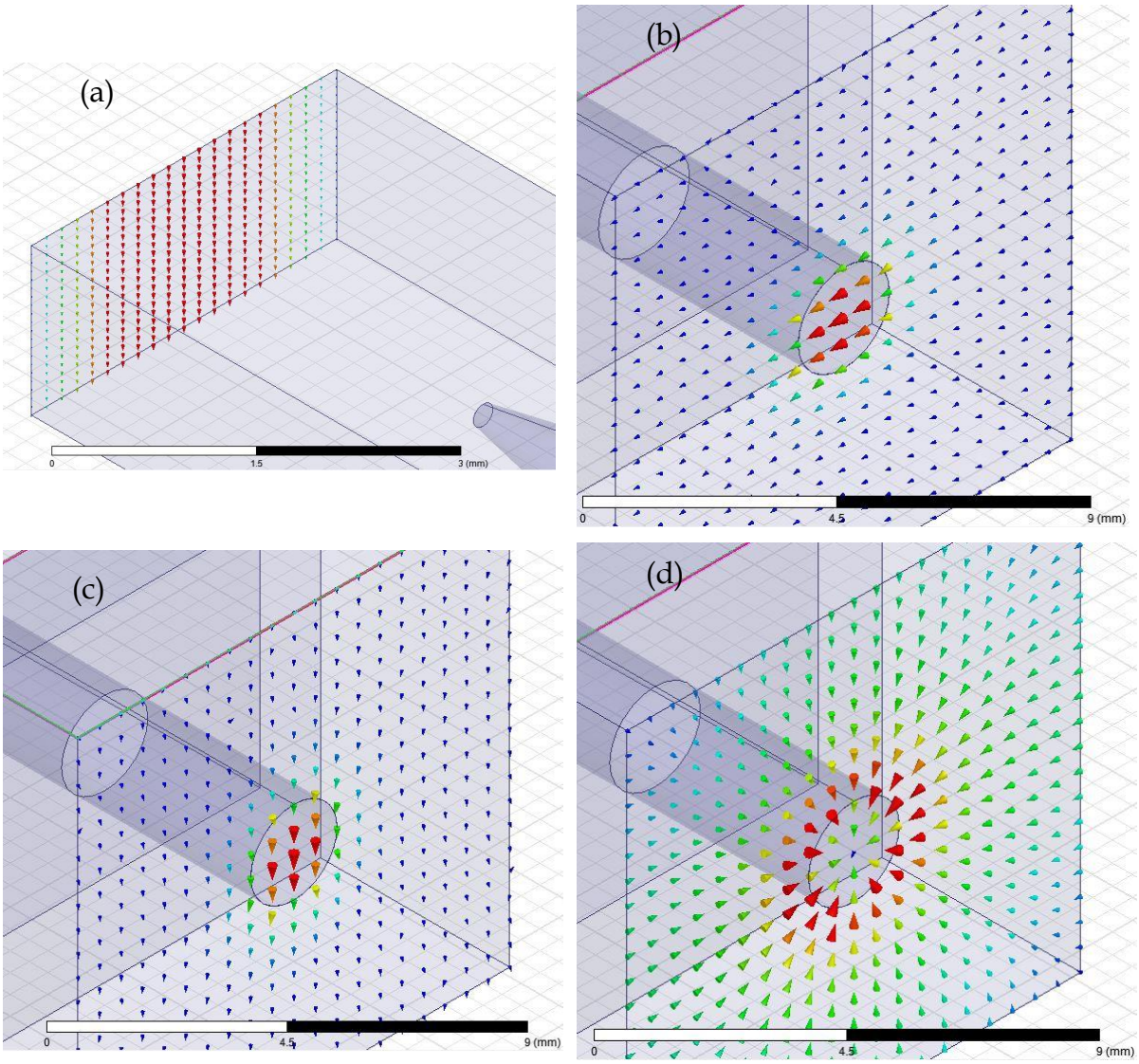

Figure 2-41: Field description of possible modes at input and output ports of the coupler. At input, (a) shows that only the fundamental TE_{10}^{V} mode can propagate. At output, (b) and (c) correspond to the degenerated HE_{11}^{H} and HE_{11}^{V} modes respectively. The following higher order mode (d) is the centrally symmetric TM_{01} mode.

In spite of an existing background related to the metallic / dielectric waveguides transition, it appears that no comprehensive analysis is available describing both mode excitation selectivity and cross-polarization isolation in the case of symmetrical waveguides. Consequently, a simplified simulation model of the proposed coupling scheme is proposed above to investigate these aspects. Due to computing limitations, it was not possible to simulate the whole structure. Instead, the horn aperture has been divided by four in order to reduce computational complexity. To maintain the flaring angle, the horn length (in the propagation direction) is also reduced accordingly. The simulation model is presented in Figure 2-39. Moreover, a canonical dielectric rod waveguide is considered with a 90 GHz maximum single-mode frequency. A modal analysis is presented in Figure 2-40 confirming single-mode operation at both WR-12 and dielectric rod ports. In this later, the fundamental mode is degenerated due to rotational isotropy with the presence of two orthogonally polarized modes having similar propagation constants. Note that no symmetry simplifications can be applied here because cross-polarization isolation is of primary interest. For that particular reason, no assumption is made on the nature of excited modes in the simulation. These possible modes are detailed in Figure 2-41.

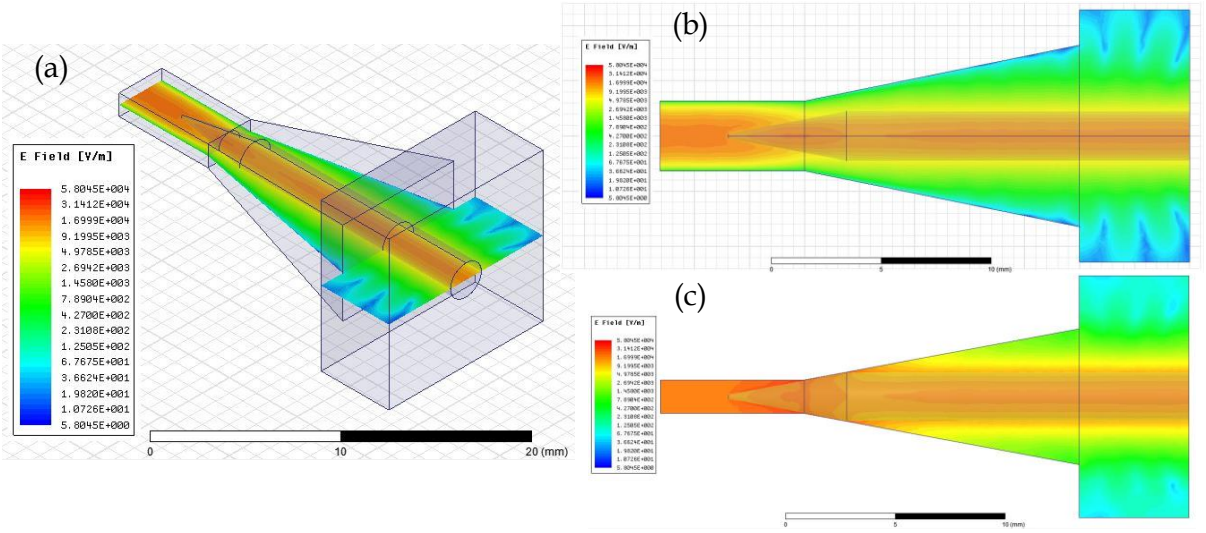

Figure 2-42: E-field complex magnitude (phase-independent) investigation in the coupler presented in Figure 2-39. Fields are plotted at 90 GHz assuming an input excitation from the WR-12 TE_{10} mode: (a) isometric view, (b) top view, (c) lateral view. Note that all E-field scales are logarithmic.

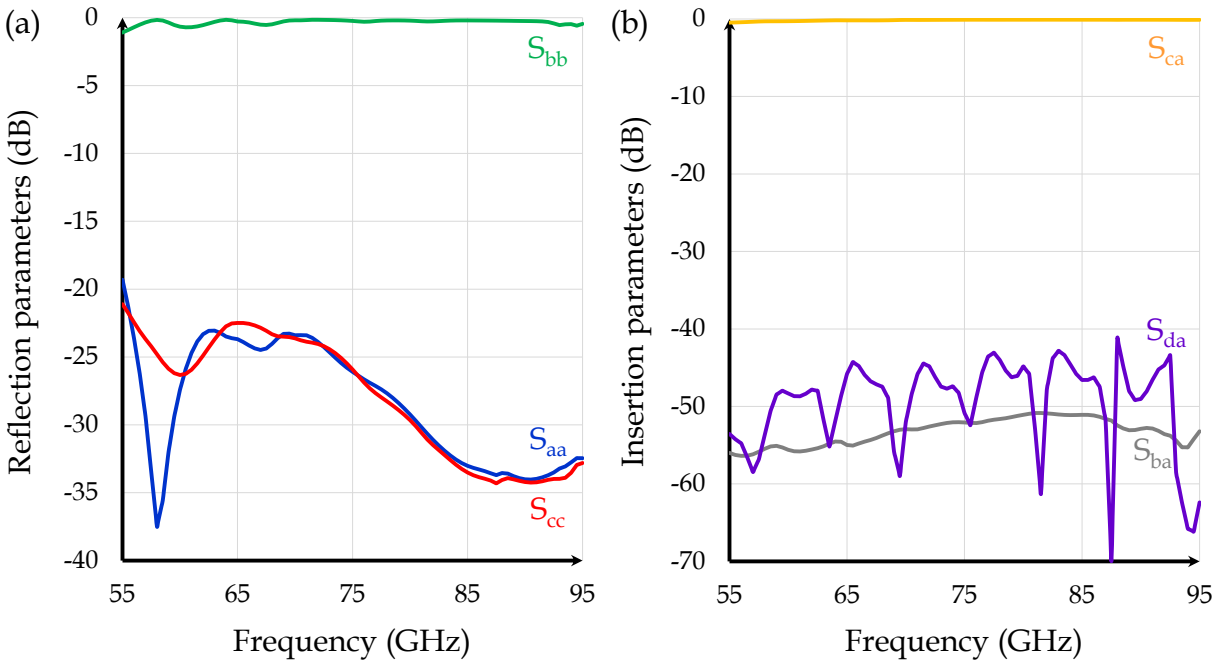

Figure 2-43: S-parameters simulation of the coupler. (a) Reflection parameters and (b) transmission parameters. Mode indices convention is the same as in Figure 2-41.

Simulated fields and S-parameters are presented in Figure 2-42 and Figure 2-43 respectively. Excellent return losses are obtained for the TE_{10} and HE_{11}^{V} modes over the entire considered bandwidth. On the contrary, the HE_{11}^{H} mode exhibits strong reflections ($S_{bb} \approx$ - 1 dB). Regarding insertion losses, an obvious transfer between TE_{10} and HE_{11}^{V} modes is observed with very low loss (< 1 dB) while transmission from TE_{10} to HE_{11}^{H} is negligible (cross-polarization > 50 dB). Finally, excitation of the higher order TM_{01} mode also appear insignificant. Even though propagation constants are closer (Figure 2-40), the noticeable fields discrepancies between TE_{10} and TM_{01} modes (Figure 2-41) induce very low coupling.

To sum up, the proposed coupler achieves an excellent transition between rectangular metallic waveguides and dielectric waveguides. Insertion loss lower than 1 dB is simulated with negligible return loss and very good mode selectivity (assuming a single-mode design).

However, as discussed earlier, this performance is obtained at the expense of a higher volume footprint, higher cost and moderate positioning reliability.

2.7. Measurement Results

In this section, a dielectric waveguide measurement bench is first discussed and 2 types of dielectric waveguides are then compared.

2.7.1. Measurement Setup

All measurement results given in this section are obtained using a similar setup described in Figure 2-44. MmW frequency extension modules extend the characterization capability to 110 GHz. These modules are connected to WR-12 standard metallic waveguides so that proper reference planes can be defined. The measurement frequency range is thus limited by the waveguide standard from 60 to 90 GHz (or 55 to 95 GHz in the best case).

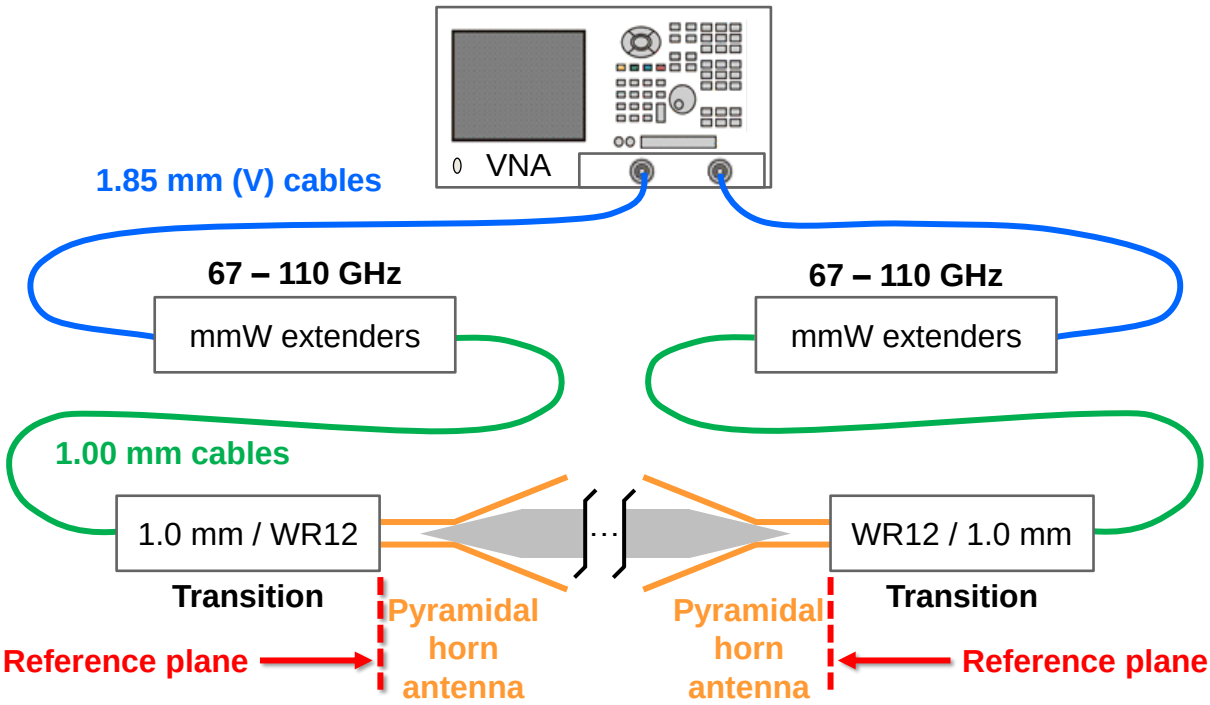

Figure 2-44: Plastic waveguides measurement setup.

Pyramidal horn antennas provide a mechanical support as well as a smooth transition between WR-12 waveguides and plastic waveguides (see section 2.6). Plastic waveguides ends are then manually tapered (length ≈ 10 – 15 mm) and low density porous plastic foams, as proposed in **[Hofmann, 2003]**, are used in both horns to increase measurements reproducibility. Finally, it is worth noting that the radiative properties of horn antennas are not of primary interest because near-field coupling is likely to be dominant. The horn antennas in this setup should then be considered as "couplers" rather than traditional antennas.

However, this basic setup faces many challenges:

- Poor reproducibility due to waveguide sensitivity to bends, external contacts and positioning inside the coupling horns,
- Polarization excitation uncertainty in the near-field coupling,
- Transition loss comparable to propagation loss for short samples.

Following the discussion given in Appendix B, the latter point can be mitigated thanks to long samples. However, such measurements were found to be extensively difficult in practice because of the first point (see section 2.4.4)

With these limitations in mind, measurement results are presented and discussed in the following sections.

2.7.2. Tubular Geometries

In this section, two tubular designs targeting single-mode operation are reported. The first design – later referred to as MOREL 1 – focusses on the low-confinement / low-attenuation regime. The second design – named MOREL 2 – implements another trade-off and explores maximum confinement at the edge of the single-mode operation frequency range. Dimensions are visible in Table 2-6. Note that tubular cross-sections were preferred to solid cores due to reduced attenuation characteristics. Both samples are made of HD-PE. According to section 2.4.2, simulations are carried out with $\varepsilon_r = 2.3$, $\tan(\delta) = 3.8 \cdot 10^{-4}$ and assuming lossless air cladding.

	MOREL 1	**MOREL 2**
Outer Diameter	1.9 mm	2.7 mm
Inner diameter	0.9 mm	1.35 mm
Filling ratio	~ 78 %	75 %

Table 2-6: Measured dimensions of tubular HDPE waveguide samples.

2.7.2.1. Low-Loss / Cow-Confinement Design

Simulated propagation characteristics in MOREL 1 are presented in Figure 2-45 and Figure 2-46. Because of the evident design symmetry, the fundamental HE_{11} mode can support two orthogonal polarizations with equal propagation constants. For this mode, attenuation ranging from 0.15 to 1.3 dB/m and Poynting confinement from ~ 6% to 53 % are obtained from 55 to 95 GHz, thus illustrating the low-confinement / low-attenuation trade-off. It is worth noting from Figure 2-45 that only the HE_{11} mode is available in this frequency range.

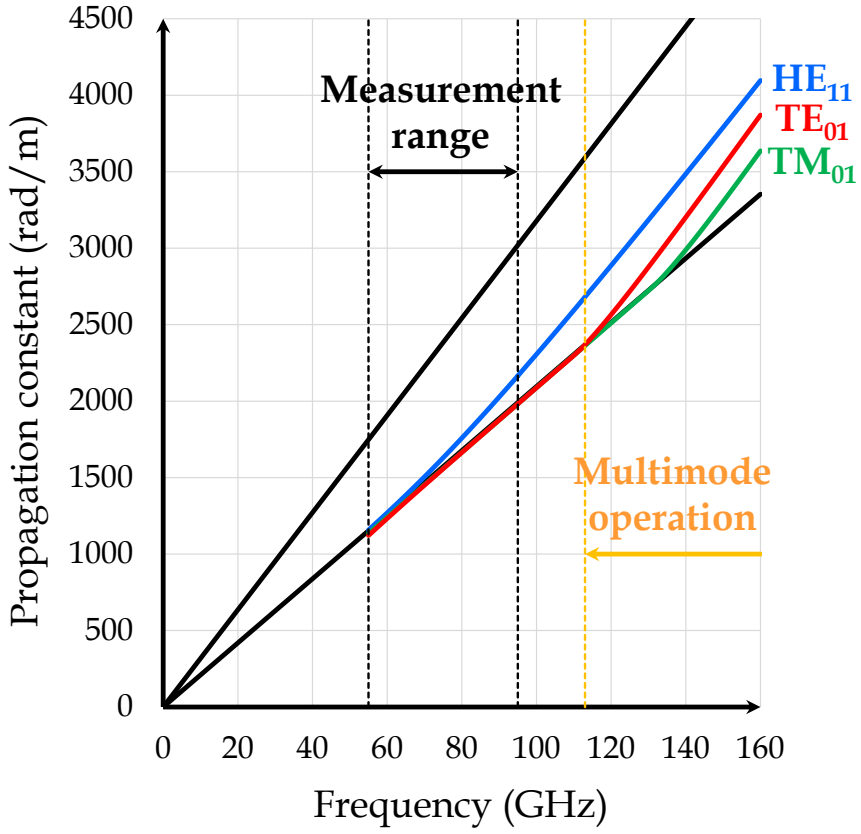

Figure 2-45: Propagation constants of the first three modes in MOREL 1 waveguide.

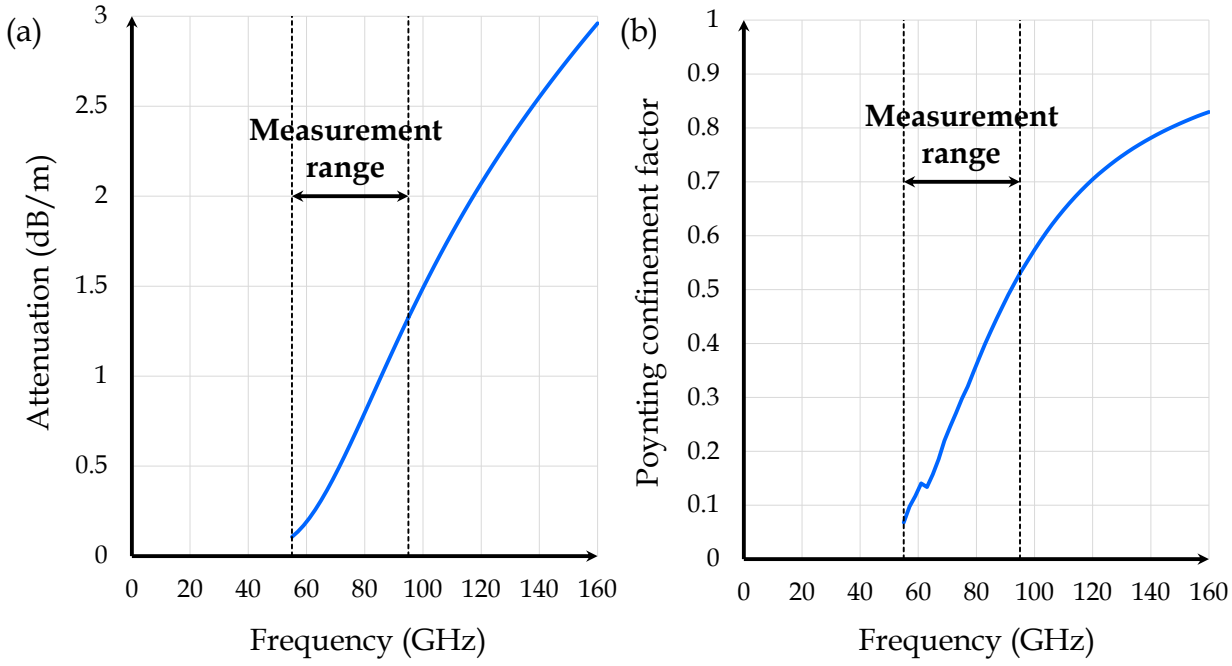

Figure 2-46: Attenuation (a) and Poynting confinement factor (b) of the dominant HE_{11} mode in MOREL 1 waveguide.

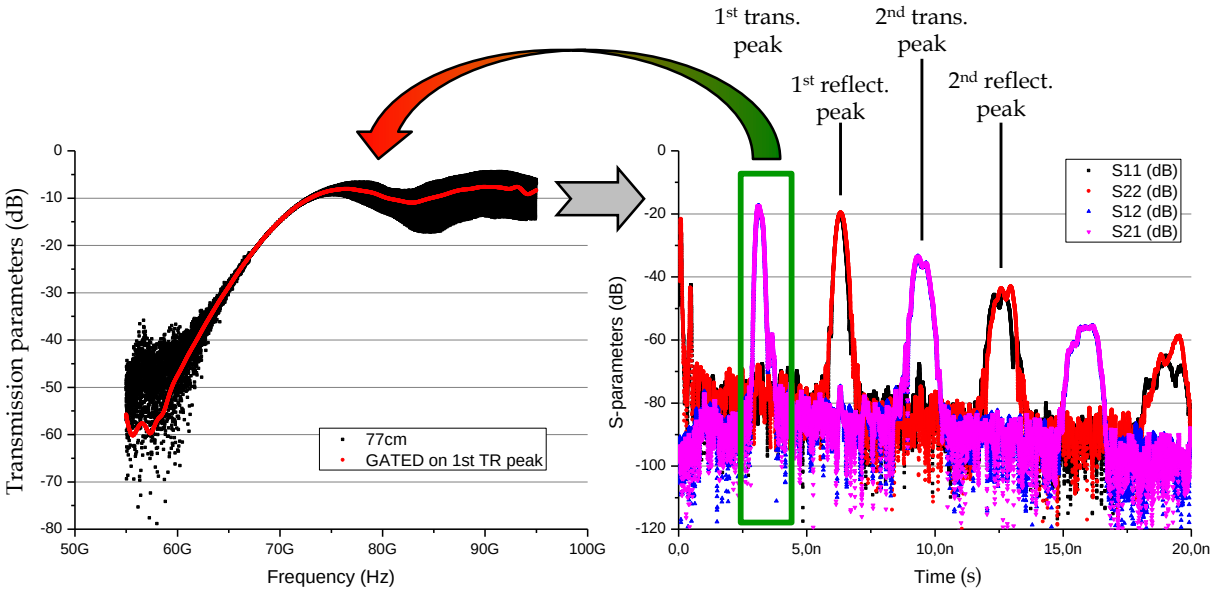

Figure 2-47: Measurement results of a 77 cm-long MOREL 1 waveguide. Transmission parameters as measured (black) and gated on the first transmission peak (red) are plotted on the left graph. On the right side, S-parameters are represented in the time domain.

A 77 cm-long sample of this waveguide has been measured and results are presented in Figure 2-47. At a first glance, it may seems that as measured transmission parameters are very noisy. In fact, measurement equipment should not be blamed because this effect actually results from unwanted reflections at couplers levels (see Appendix B). In other words, the apparent noise visible here is the signature of standing waves modulating the transmission. To remove this detrimental effect, it is possible to consider only the first transmission peak using "Time-Gating" options of the VNA. While this option considerably smooths data, all other transmission / reflection peaks are neglected. In this sense, we can consider gated-transmission results as pessimistic.

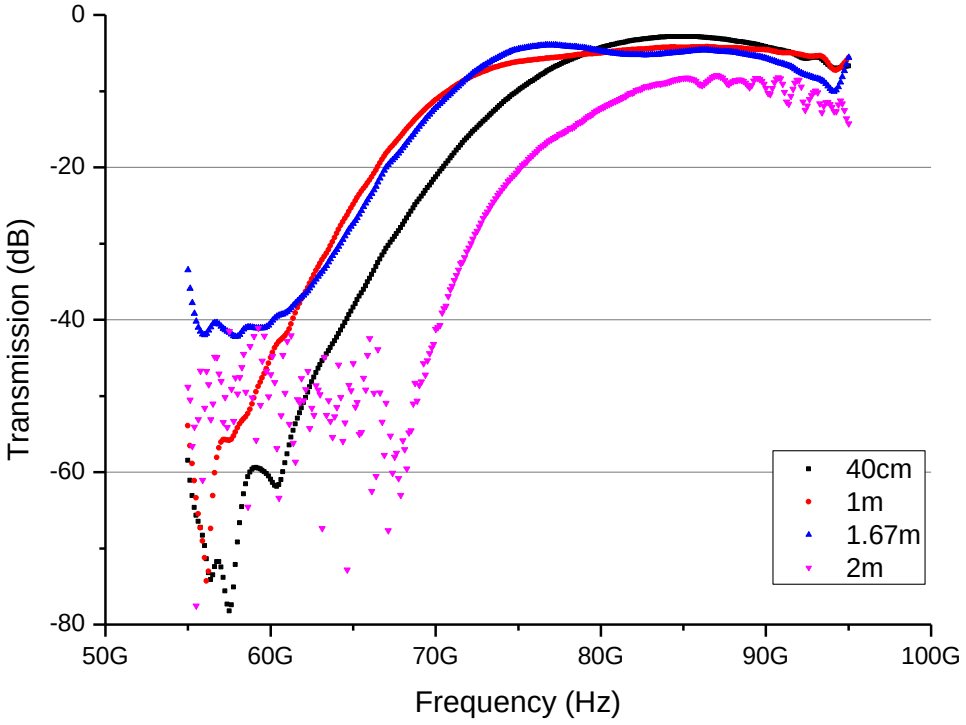

Figure 2-48: Gated transmission parameters of a MOREL 1 waveguide for different lengths (except 2 m – as measured).

This measurement process has been repeated for several waveguide lengths and results are summarized in Figure 2-48. A striking conclusion is that the longest samples do not always exhibit the largest losses. This is especially true for the 40 cm-long sample below 78 GHz. Besides, while simulated attenuation is an increasing function of frequency, measurements suggest a much more complex frequency dependence. Observations actually advocate for a high-pass behavior due to large attenuation at lower frequencies.

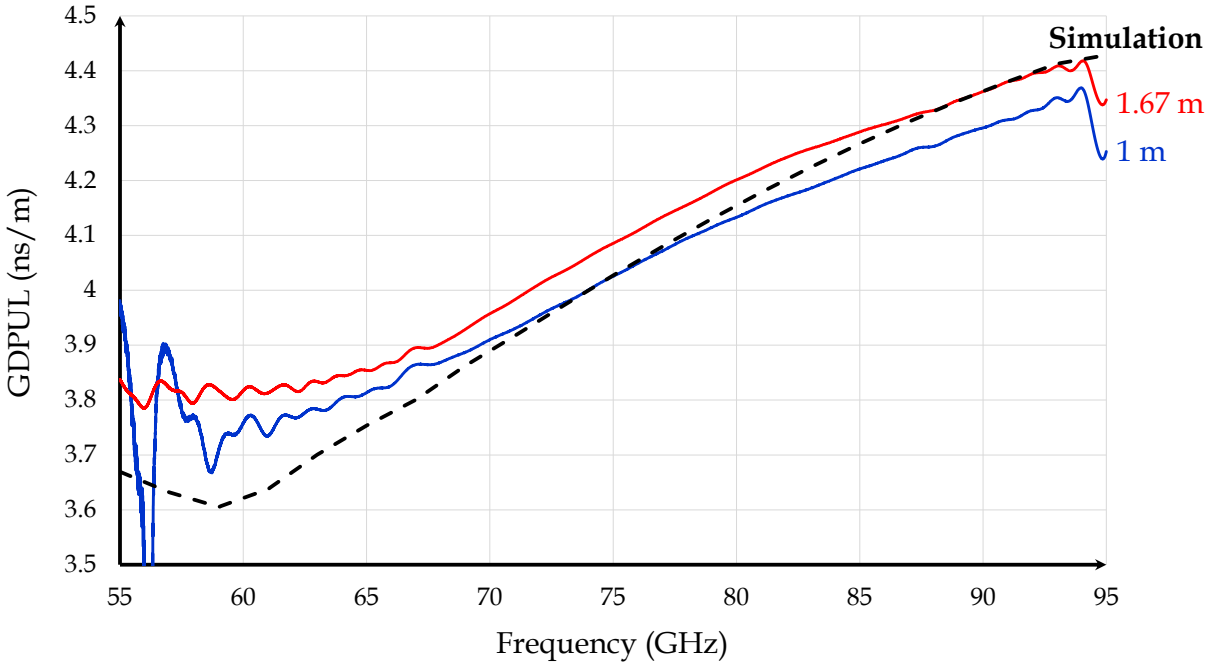

Figure 2-49: Group delay per unit length in a MOREL 1 waveguide. Simulation (dashed line) and measurement (solid lines) results show good agreement.

Finally, using the recorded phase of the transmission parameters, a group delay estimation can also be performed. Contrary to significant discrepancies noticed earlier regarding transmitted amplitudes, measurement results show great consistency and good agreement with simulation as visible in Figure 2-49. A moderate deviation is still observed at lower frequencies where the smallest confinement factor is expected (Figure 2-46 (b)). However, this effect should be interpreted carefully as the simulation setup tends to become increasingly inaccurate for very low confinement waveguide designs. In addition, measurement reproducibility is greatly reduced in such an operating mode because the waveguide is actually very sensitive to environment conditions. In Figure 2-49, it can still be noted that group-delay is larger than $1/c_0 \approx 3.3$ ns/m whatever the frequency, thus excluding free-space propagation mechanisms. We can conclude that all signals captured here are carried by the waveguide, as expected, even in smallest confinement conditions.

2.7.2.2. Maximum Confinement at the Edge of Single-Mode Operation

Similarly to section 2.7.2.1, the MOREL 2 waveguide propagation characteristics are simulated and presented in Figure 2-50 and Figure 2-51. As expected, a higher Poynting confinement (33 – 76 %), inducing higher attenuation (0.5 – 2 dB/m), is obtained compared to MOREL 1. Note that the TE_{01} higher-order mode gradually appears above 80 GHz, so that the edge of the single-mode regime can be characterized.

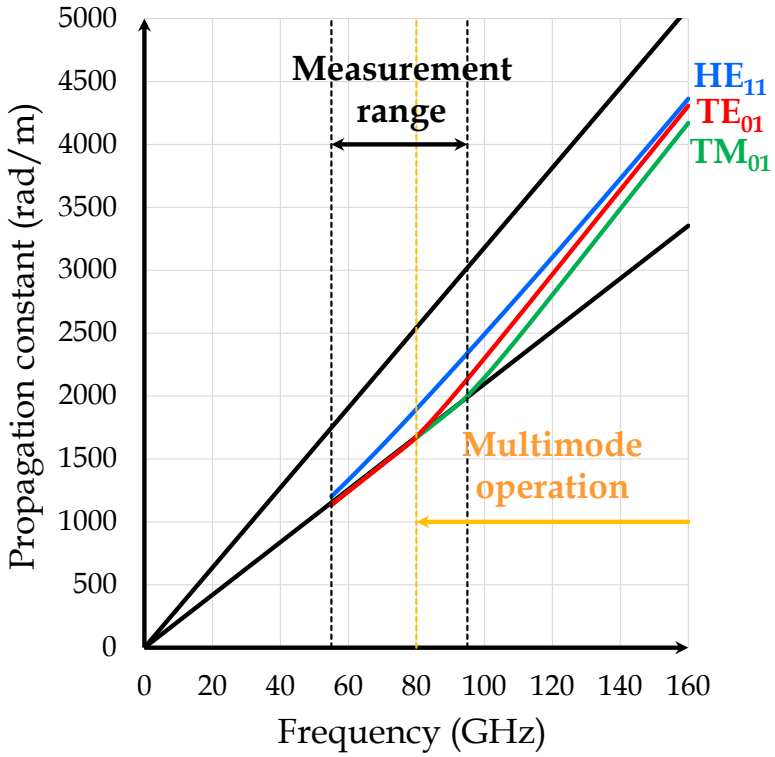

Figure 2-50: Propagation constants of the first three modes in the MOREL 2 waveguide.

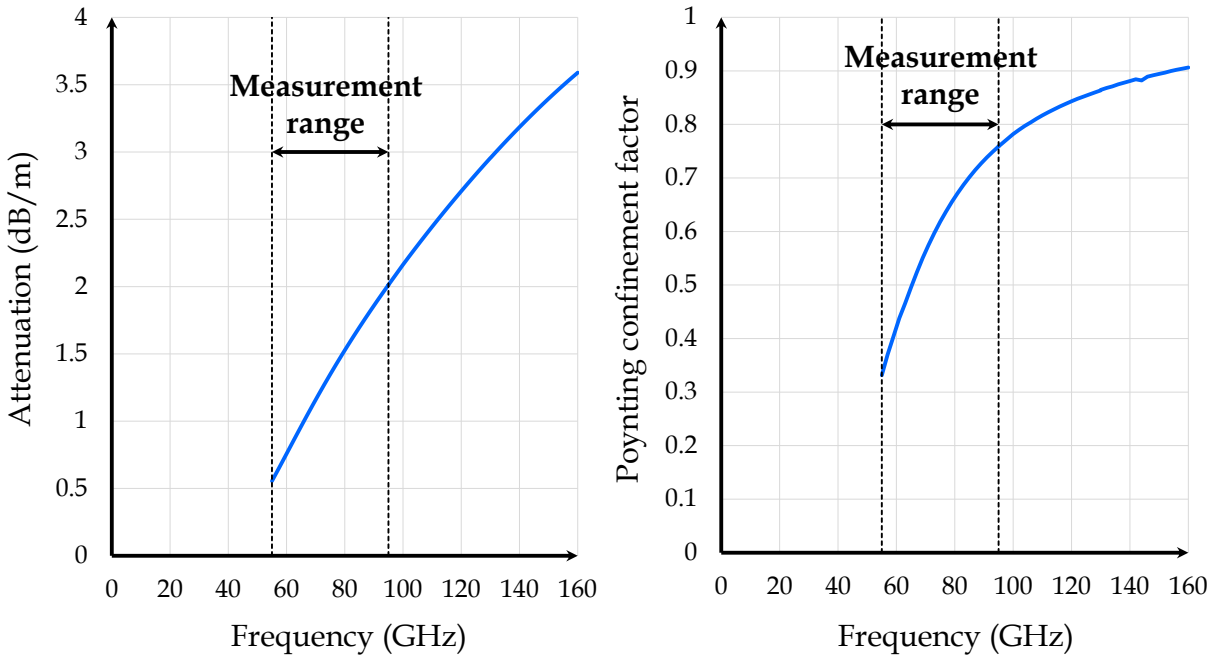

Figure 2-51: Attenuation (left) and Poynting confinement factor (right) of the dominant HE_{11} mode in MOREL 2 waveguide.

Measurement results are presented in Figure 2-52 for different sample lengths. Note that time-gating capability was enabled to remove detrimental ripples caused by transitions. Still, it seems that all samples suffer from a periodic modulation above roughly 85 GHz. When looking carefully, it appears clearly that the modulation frequency period is inversely proportional to the length. In addition, the significant ripples amplitude suggests that such a phenomenon is not a measurement artefact. Indeed, it could be caused by multimode propagation.

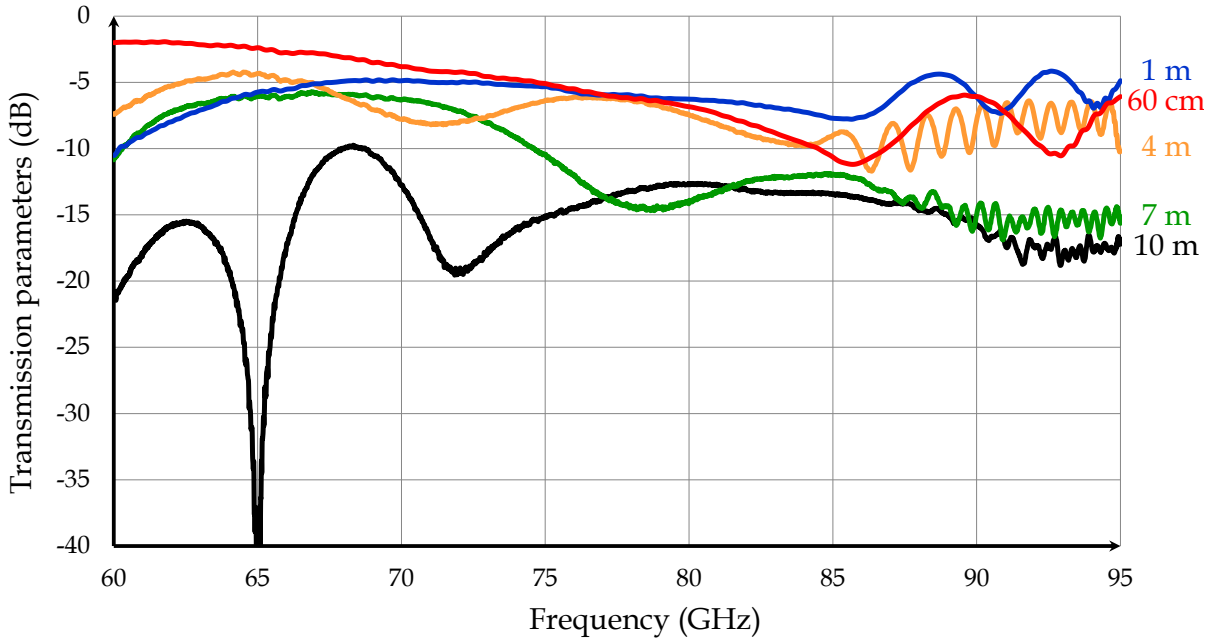

Figure 2-52: Gated transmission parameters of MOREL 2 waveguide for different lengths.

One more time, the behavior at lower frequencies mainly diverges from simulation, except for the shortest sample, which presents a linear attenuation from 60 to 80 GHz. However, the attenuation increase with frequency is much higher than simulated. Generally speaking, as regards length dependency, the same loss inconsistency as previously reported for MOREL 1 is also observed so that we are not able to conclude about propagation losses. Moreover, the sharp resonance at 65 GHz was found to be very dependent of the measurement setup since a 10 m-long waveguide should be inevitably bent. This sensitivity to bends increases with length and diminishes with frequency. Compared with MOREL 1 waveguides, the sharp attenuation below 80 GHz is not visible (but may still be present at frequencies < 60 GHz) suggesting that MOREL 2 is significantly better in this measured frequency range.

2.7.3. Magic Wheel Design

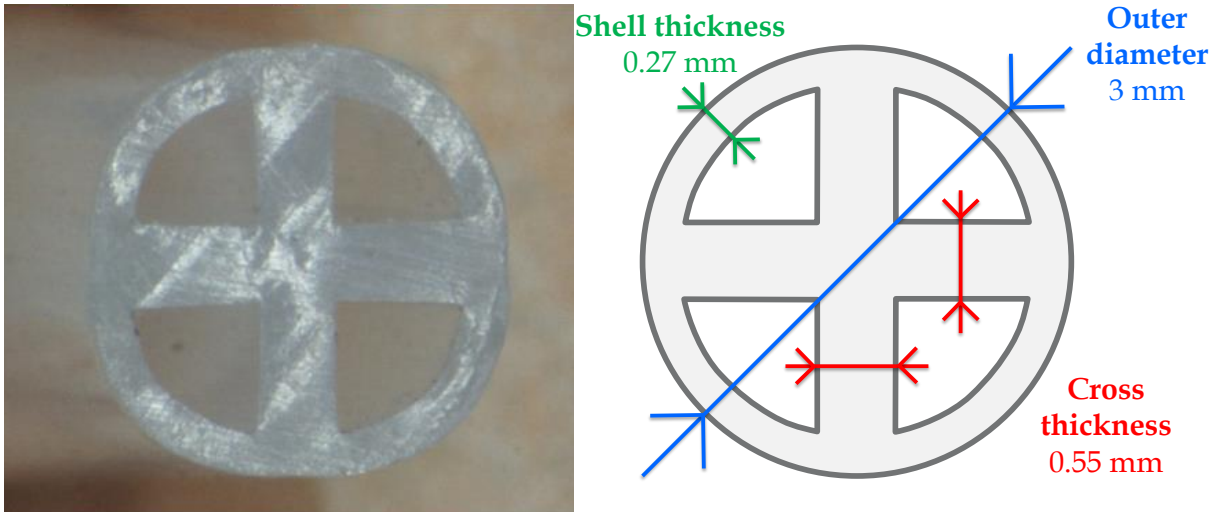

Figure 2-53: Description of the fabricated PTFE Magic Wheel waveguide prototype. Indicated dimensions are derived from accurate measurements provided by the supplier.

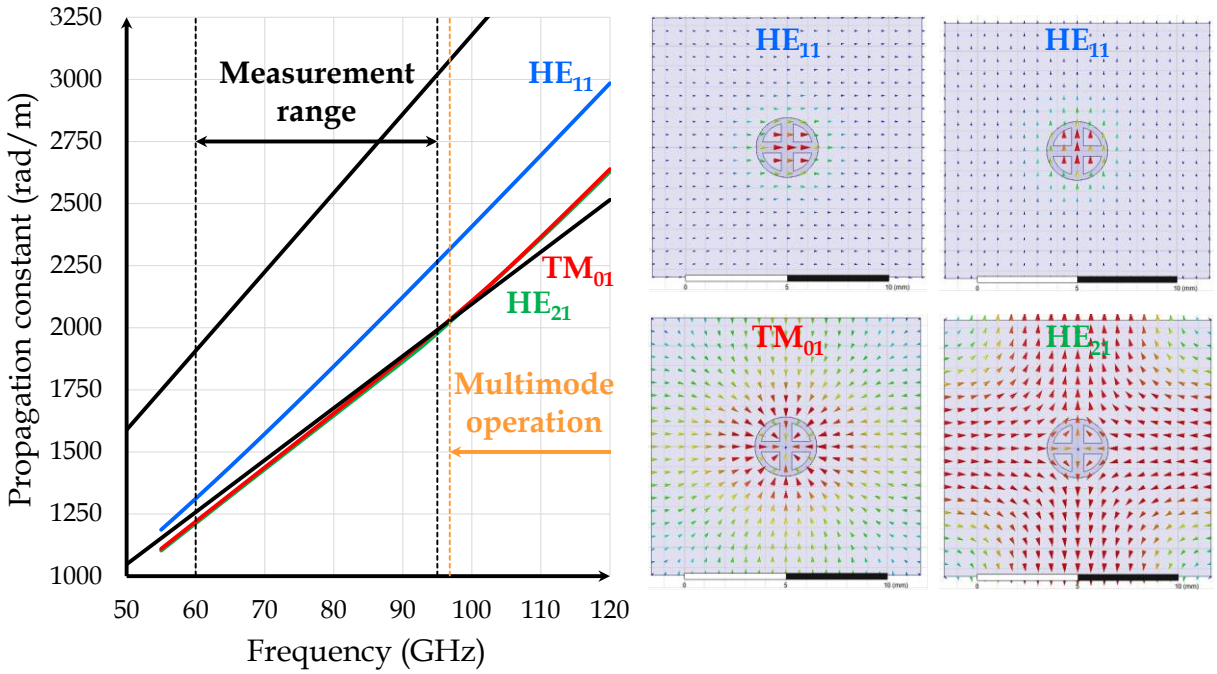

Figure 2-54: Simulated propagation constants (left) of the lowest order modes in the Magic Wheel design (Figure 2-53) and associated fields maps (right).

The fabricated prototype is presented in Figure 2-53. Because of additional design complexity causing manufacturing issues, the whole structure is made of PTFE instead of HDPE. Simulation results are given in Figure 2-54 and Figure 2-55 showing genuine single-mode operation in the measurement range. The dominant HE_{11} mode is characterized by an attenuation constant from 1.15 dB/m to 3.75 dB/m and a Poynting confinement factor ranging from 41 % to 80 %.

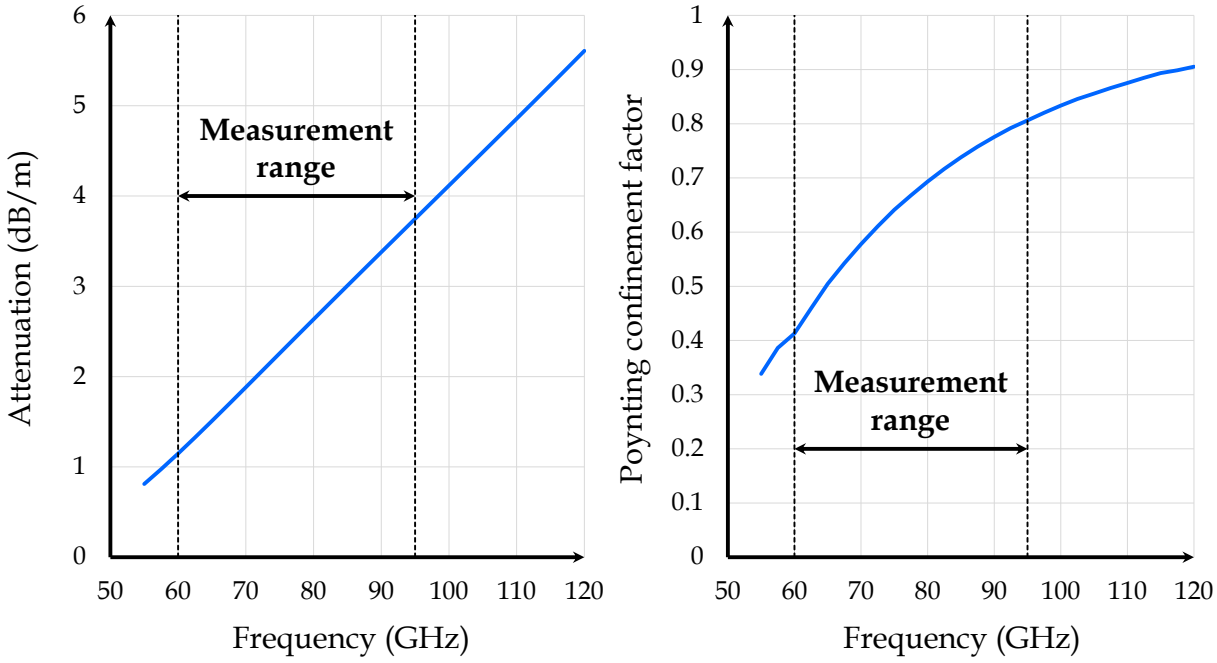

Figure 2-55: Attenuation (left) and Poynting confinement factor (right) of the dominant HE_{11} mode in Magic Wheel waveguide.

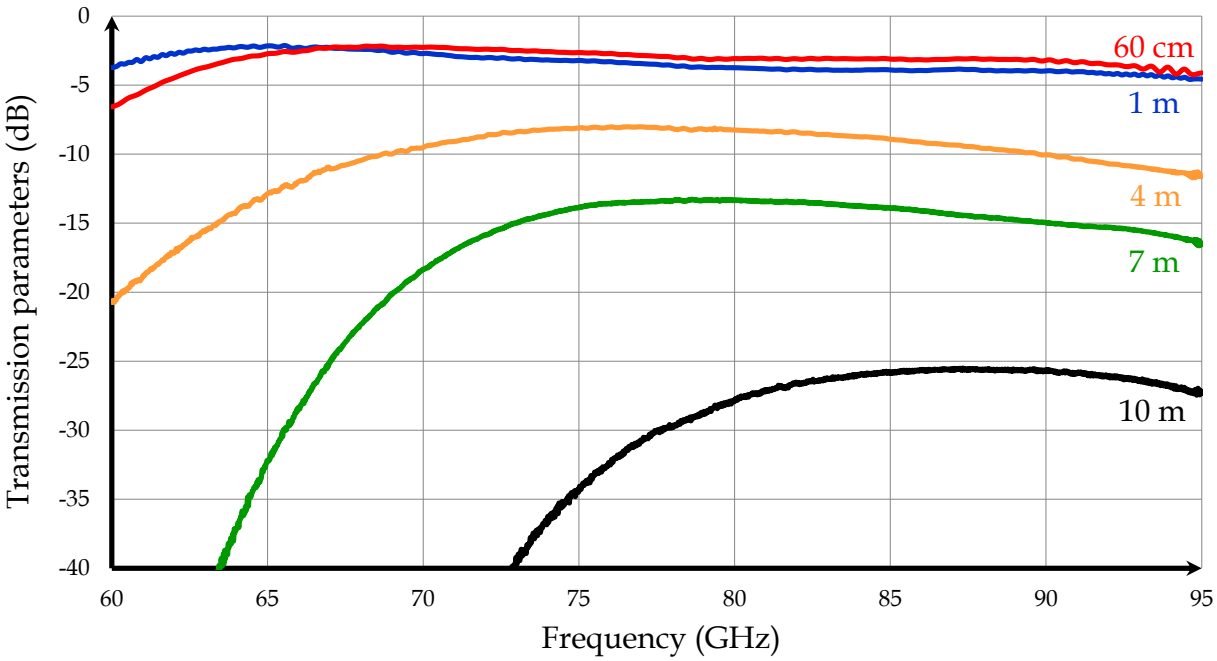

Figure 2-56: Gated transmission parameters of Magic Wheel waveguides for different lengths.

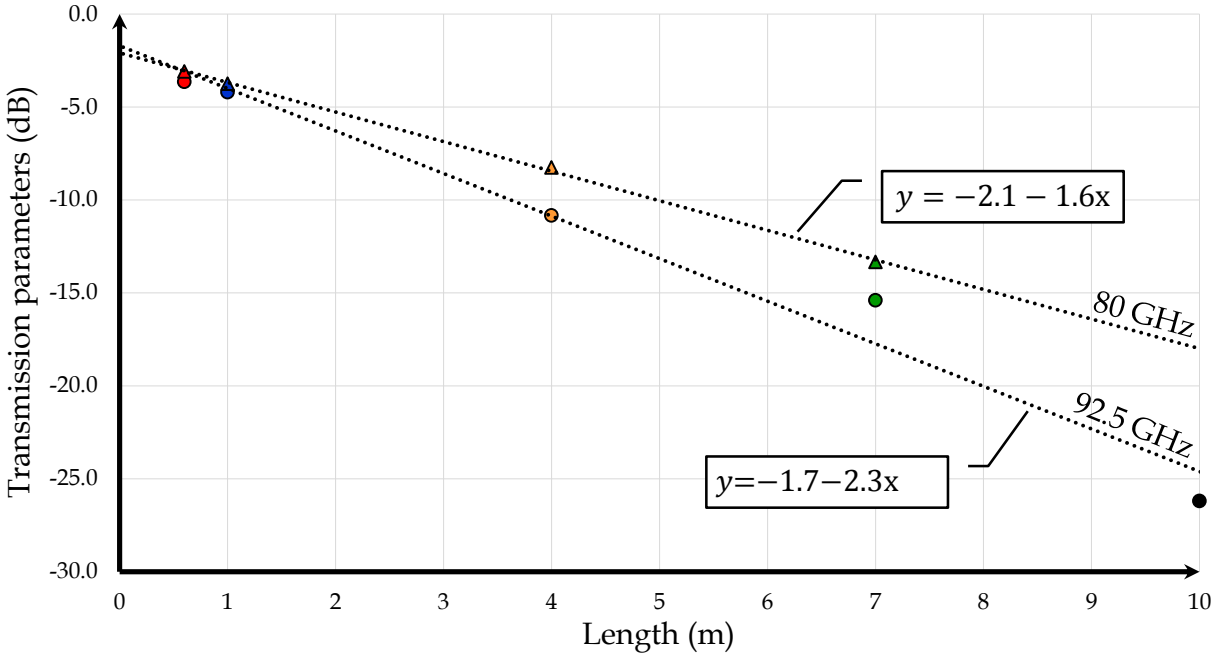

Figure 2-57: Extracted length dependency using Magic Wheel prototypes reported in Figure 2-56.

Figure 2-56 presents transmission parameters of Magic Wheel waveguides for variable sample lengths from 60 cm to 10 m. Contrary to MOREL 1 & 2, the length discrepancy is no longer visible except for the shortest sample at lower frequencies. This satisfying result allows for legitimate linear loss extraction (Figure 2-57). Attenuations of the order of 1.6 dB/m at 80 GHz and 2.3 dB/m at 92.5 GHz are obtained while coupler loss is approximately 1 dB per end. Two conclusions arise:

- Coupler loss is larger than simulated in section 2.6 but seems in-line with practical connector realizations at such frequencies. Manually tapered ends and moderate positioning precision might be responsible for this lower performance.

- Linear loss is lower than expected in simulation. This surprising result might be explained by inaccurate dielectric properties for the PTFE material. In fact, it has been shown in 2.4.2 that reported tan(δ) values for this material can be very different from one reference to another. Noticing that extracted linear loss "scales" as expected from 80 to 92.5 GHz ($\alpha_{92.5\ \mathrm{GHz}} \approx 1.4 \cdot \alpha_{80\ \mathrm{GHz}}$), this assumption is all the more credible.

However, as experienced before with other waveguides, this agreement is still very poor at lower frequencies. One more time, measurements clearly suggest a high-pass behavior instead of low-pass, as predicted theoretically. Generally speaking, for increasingly long waveguides, the low-pass characteristic becomes increasingly sharp and moves toward higher frequencies. Another loss mechanism having a different length dependency compared to attenuation might be at stake… Such additional losses obviously appear at lower frequencies, but neither at a specific frequency nor a specific frequency range. In fact, this phenomenon seems strongly correlated to lower Poynting confinement factors. To state it differently, the severe discrepancy observed between simulations and measurements may be not be the result of a fundamental incapacity to operate at ≈ 60 – 80 GHz but rather a practical consequence of limited Poynting confinement factor at these frequencies. In addition to the (simulated) material attenuation, we can assume that radiation occurs in practice because of inevitable bends and interferences with the environment. This important inference has been tested successfully in Appendix C, showing that sensitivity to bends is primarily impacted by low confinement.

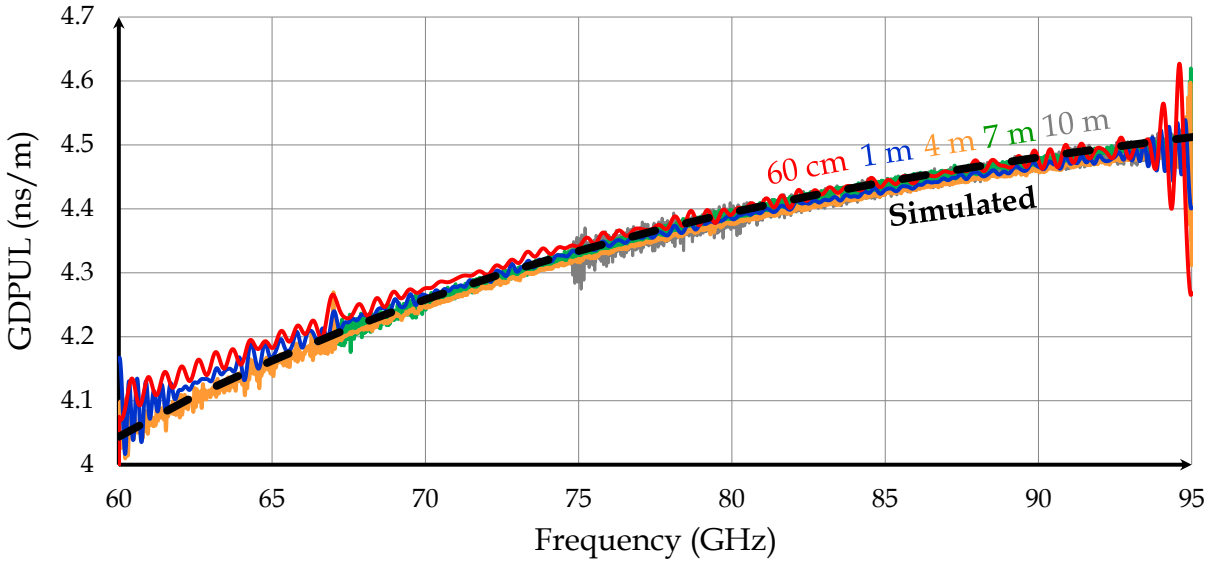

Figure 2-58: GDPUL for the Magic Wheel waveguide samples shown in Figure 2-56. Measurements (solid lines) are perfectly in-line with the simulation (dash line).

Group-delay should be investigated to complete the study. GDPUL measurements are compiled in Figure 2-58 and show excellent agreement with the simulation. This satisfying result noticeably extends to the whole measurement range contrary to measured attenuation, as reported earlier. Consequently, the simulation bench and the material dielectric constant are validated. Note that group-delay simulation is insensitive to dielectric losses.

This result also supports the extra loss explanation clarifying the difference between simulation and measurements. In fact, no particular resonance is visible in Figure 2-58 except at frequencies above ~ 93 GHz that may be due to the excitation of higher-order modes in the (loaded) WR-12 section of the couplers. If any resonance responsible for higher attenuation at lower frequencies would be present, it would affect group-delay significantly in Figure 2-58 and Figure 2-49. On the contrary, no additional phase change is induced by the practical

constraints affecting attenuation. Because of this singular conclusion, we can assume that radiation may be responsible for the observed additional losses.

Finally, we conclude this section with an investigation regarding sensitivity to external contact. Because the Magic Wheel original design was proposed as an attempt to reduce this drawback, comparative results with respect to MOREL 2 waveguide are presented in Figure 2-59. In the chosen test case, a 30 cm-long waveguide is pinched with two human fingers. Fingers position along the waveguide is roughly at equal distance of the two couplers although results were not found to be very dependent on a particular position. This perturbation causes a significant 10 - 15 dB degradation. In the same conditions, the MOREL 2 waveguide suffers from an 18 - 25 dB penalty. As expected, the Magic Wheel waveguide clearly exhibits improved robustness due to higher confinement. In the proposed test case, this improvement is ~10 dB. In order to increase robustness even more, a 1 mm-thick PTFE foam is introduced around the waveguides. According to Figure 2-59, the foam brings an additional 8 dB robustness to the Magic Wheel and 15 dB to the MOREL 2 one respectively, while still having very limited impact on the undisturbed transmission. Consequently, the foam-coated Magic Wheel design has only a 3 - 8 dB penalty, successfully paving the way to contact-insensitive waveguides. Note that degradation reduces quite linearly with increasing frequencies, which can be attributed to increasing confinement.

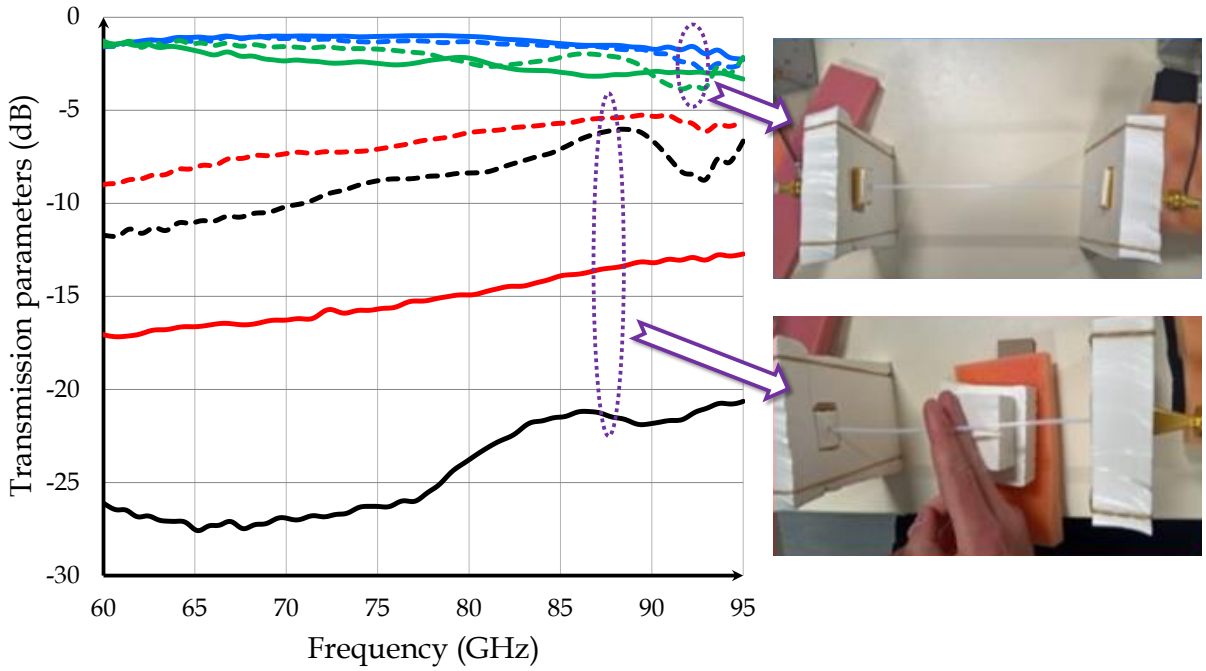

Figure 2-59: Compared transmissions of disturbed / undisturbed Magic Wheel waveguides (red / blue) with respect to disturbed / undisturbed MOREL 2 waveguides (black / green) respectively. Solid lines correspond to waveguides as fabricated while dotted lines represent waveguides surrounded by a 1 mm-thick PTFE foam.

2.8. Conclusions and Comparison with the State of the Art

After a brief historical review of both theoretical and practical developments in the context of waveguide communications, state-of-the art plastic waveguides have been investigated. The high potential of this technology, enabled by advanced CMOS technologies, appeared clearly through successful demonstrations up to almost 20 Gb/s. Low-loss propagation

(especially compared to free-space), low-cost manufacturing and robust positioning promising low cost assemblies, are the strongest advantages of this innovative solution. Leveraging on this potentiality to offer future communication products now requires a deeper understanding at both plastic waveguide and coupler levels.

In this work, propagation fundamentals in plastic waveguides have been presented first with a focus on single-mode operation and polarization description. Appropriate materials have been selected based on their dielectric properties and costs. Design parameters have been discussed to derive a rapid-prototyping methodology. Such a method may be particularly relevant in the context of versatile circuits to assess quickly the feasibility of a plastic waveguide solution at a given frequency.

The importance of couplers has also been highlighted. Their key role is to excite the plastic waveguide precisely so that mode selectivity, cross-polarization, bandwidth and insertion loss are then essential. Moreover, for long and low-loss waveguides, we have shown that improper transitions create detrimental ripples in the bandwidth. For the purpose of the measurements, a single polarization capable transition, based on a standard WR-12 waveguide horn antenna and tapered plastic waveguide ends, has been utilized. It has been simulated by means of an FEM tool showing excellent results for all the important metrics listed earlier. However, measurement results reported in this work obviously contradict this enthusiastic conclusion. While return loss is greater than 10 dB in the full E-band and insertion loss may be as low as ~ 1 dB, large amplitude ripples are observed indicating the presence of standing waves. To explain this large deviation compared to the simulation, practical difficulties with the precise and reproducible positioning of plastic waveguides in the foam-filled horns may be invocated. Manually tapered waveguide tips may additionally be blamed. Yet, it is still not clear how these discrepancies degrade excitation selectivity: are higher-order modes or/and orthogonal polarization modes excited in practice?

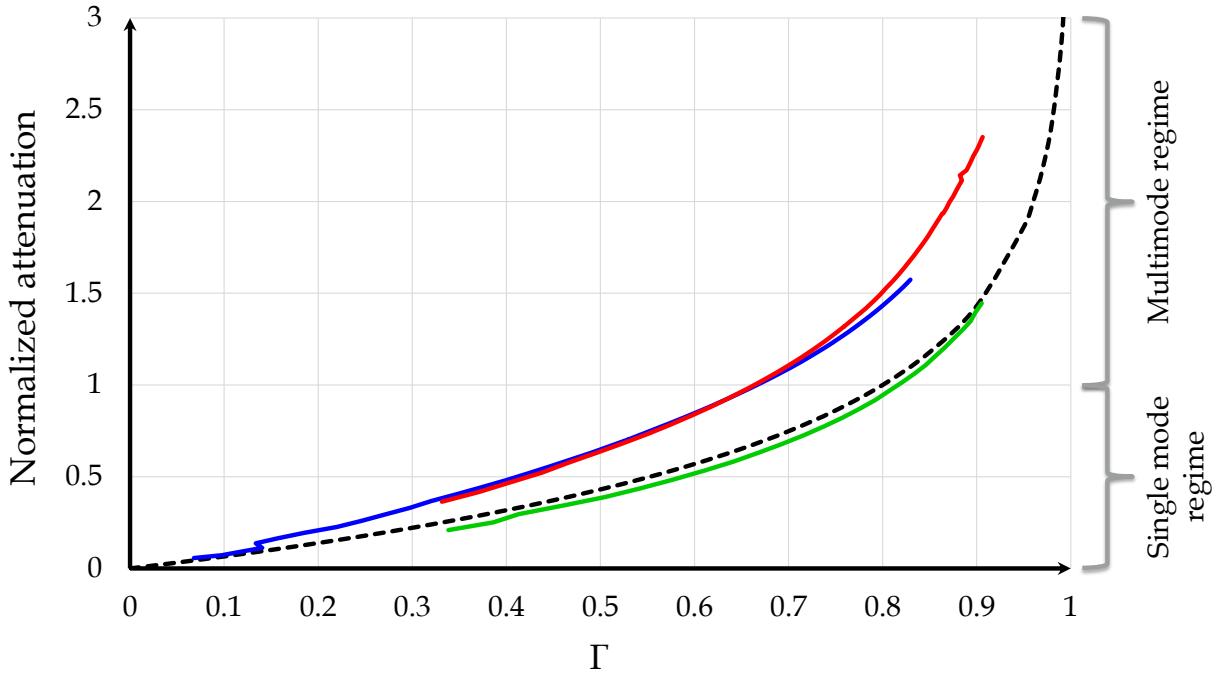

Figure 2-60: Simulated normalized attenuation (with respect to attenuation at maximum single-mode frequency) versus Poynting confinement. Black, blue and red lines correspond to solid HDPE core, MOREL 1 and MOREL 2 tubes (HDPE) respectively while the green line is related to the Magic Wheel waveguide design (PTFE).

Besides, based on the scarce details reported in the literature, the sensitivity to external contact has been described and the role of limited Poynting confinement factor as well as intrinsic limitations have been pointed out. To mitigate this detrimental effect without compromising mechanical reliability, an innovative design (Magic Wheel) has been proposed in this work. A shell is introduced around a cross-shape waveguide to prevent detrimental contact and maintain cladding conditions. The new design also features a single-mode operation capability with two orthogonal polarizations. Note that contrary to previously reported designs, these modes are symmetrical as well as polarization-maintained. Moreover, this design pushes further the common trade-off between confinement and single-mode operation. To illustrate this point, the different samples discussed in this work are compared in Figure 2-60. MOREL 1 and MOREL 2 tubular waveguides behave similarly especially in the single-mode regime with $\Gamma < 0.67$. The Magic Wheel clearly shows a superior confinement capability in this regime with $\Gamma < 0.82$ which is even slightly better than solid core waveguides. Naturally, as better confinement induces better immunity regarding external contact, the Magic Wheel waveguide exhibits ~10 dB higher robustness to fingers touching the waveguide compared with the highest confinement tubular waveguide (MOREL 2) in the 60 – 95 GHz frequency range. To push robustness further, foam coating should be considered. In practice, the foam-coated Magic Wheel effectively reduces sensitivity but the benefit compared to much simpler foam-coated tubes may be insufficient for cost-sensitive applications. Finally, Table 2-7 summarizes the comparison of the Magic Wheel design with respect to the State of the Art.

	[Fukuda, 2011]		[Tytgat, 2013]	[Kim, 2013]	[Volkaerts, 2015] [Van Thienen, 2016]		[Reynaert, 2017]		This Work			
Cross section	Rectangular		Rectangular	Tubular	Tubular		Cylindrical (foam-coated)		Magic Wheel		Magic Wheel (foam-coated)	
Ext. dimensions	8 mm x 1.1 mm		2.2 mm x 0.9 mm	Ø 3.2 mm	Ø 2 mm		Ø 6 mm		Ø 3 mm		Ø 5 mm	
Medium material	PS		PP	PTFE	PTFE		PTFE		PTFE		PTFE	
Freq. (GHz)	57	80	90 - 140	60	90	140	90	140	80	92.5	80	92.5
Attenuation (dB/m)	NC	NC	~ 1 - 3	~ 1.4	1.5	4.3	4	7.5	1.6	2.3	1.6*	2.3*
Dual-polarized	NO		NO	YES	YES		YES		YES		YES	
Polarization maintained	YES		YES	NO	NO		NO		YES		YES	
Single-mode operation	NO		YES	YES	YES	NO	YES**	NO**	YES		YES**	
Immunity to external contact	NO		NO	NO	NO		YES		Limited		Almost	

Table 2-7: State of the Art comparison of plastic waveguides.

(*) assuming foam is not responsible for additional loss, (**) assuming foam is made of pure air.

2.9. Perspectives

2.9.1. Orthogonal Polarization Modes Characterization

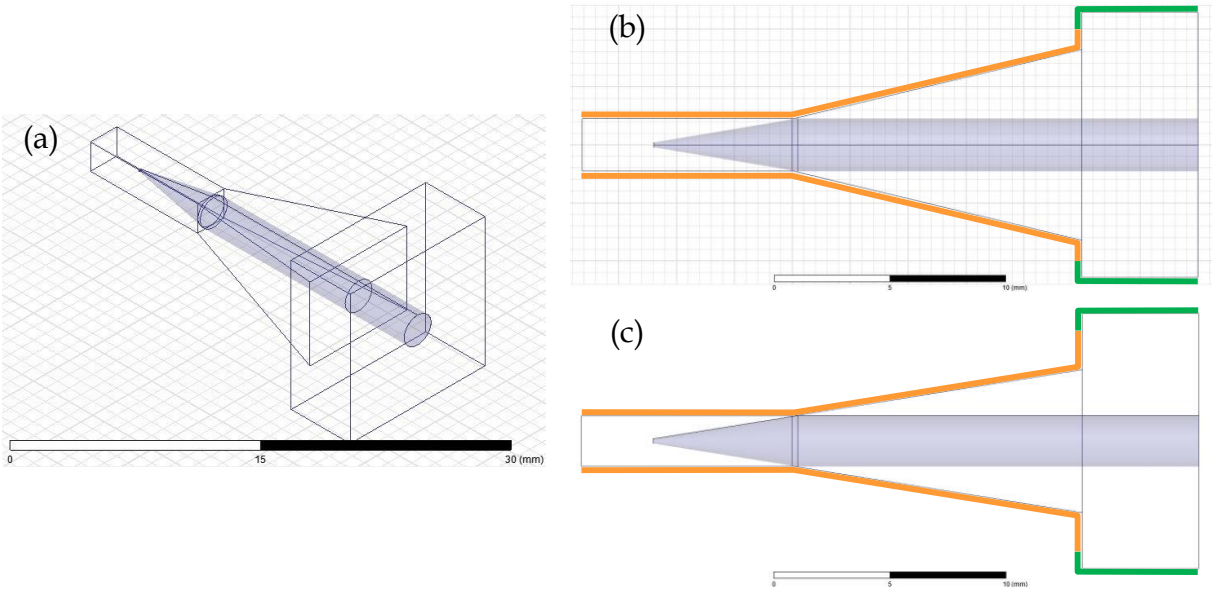

Figure 2-61: Description of a dual-polarization coupler between a square metallic waveguide and a conically tapered plastic waveguide (conductors not shown for visibility). An isometric view is presented in (a), a top view in (b) and a lateral view in (c). Orange lines indicate metallic conditions imposed by the horn while green lines indicate "radiation boundaries" around the "open" dielectric waveguide.

Following the previous discussion, and anticipating the developments in Chapter 3, the need to study further polarization is clear. Motivations are twofold: investigate the causes of practical discrepancies observed earlier and eventually offer an additional communication channel.

First, a dual-polarization coupler should be available. Considering the design presented in section 2.6, it is possible to realize such a transition easily. For example, in Figure 2-61, the WR-12 section has been replaced by a $\sqrt{2}/2$ smaller square section in order to maintain the same high cut-off frequency. Note that this frequency is actually ≈ 97 GHz to account for manufacturing tolerances so that the plastic waveguide is slightly larger than the metallic one, in opposition to Figure 2-17 where the comparison is made assuming the very same cut-off frequency.

The excitation of square (or alternatively cylindrical) waveguides is canonical and is typically realized thanks to Ortho-Mode Transducers (OMT). Several topologies propose variable trade-off between insertion loss, complexity, isolation and cross-polarization. Commercially available products can cover the full E-band with around 1 dB insertion loss, 40 dB isolation and 35 dB cross-polarization [**Sage, 2018**].

Nevertheless, the introduction of an additional mode at each end ideally advocates for an upgrade of the 2-port setup of Figure 2-44 to a 4-port setup. This modification is not benign at mmW frequencies because of terribly expensive equipment. Alternatively, 4-port measurements with only 2 measurement ports and 2 matched sections are feasible but are not

recommended in the context of potential sensitivity to waveguides positioning. In fact, it is worth noting that the coupler in Figure 2-61 does not bring any particular improvement to the practical plastic waveguide positioning issue. To address this particular item, plastic waveguide tips should no longer be realized manually but fabricated separately. These tips could be plugged at waveguide ends. Thin positioning fins may be added as well to increase reproducibility and robustness. To do so, the injection-molding process appears suitable.

Ultimately, polarization maintaining and isolation in the plastic waveguides should be studied. In this process, the Magic Wheel special design is likely to offer a noticeably better performance with respect to conventional designs having a symmetry of revolution (namely rods and tubes) thanks to clear polarization preferred directions.

2.9.2. Micro-structured Millimeter Wave Plastic Waveguides

Because of the inherent kinship between optical fibers and plastic waveguides (dedicated to mmW), the recent developments of the former may someday contribute to the development of the latter. Among them, micro-structured fibers are of particular interest.

In conventional fibers, the necessary index change is realized thanks to careful doping control between the core and the cladding (usually in silica) or with different index materials. A completely different process is involved in micro-structured fibers since only a single material is used in both core and cladding regions. However, to produce the index change, air holes are introduced in the cladding region to reduce the effective index surrounding the core. Even though no specific arrangement is needed, holes are typically placed periodically in 2D-patterns.

The density of holes of course controls the index change. Nevertheless, using clever dimensioning and positioning can actually offer performances that would be impossible to obtain in conventional fibers. In other words, microstructuring the fiber can be considered as an additional fiber design parameter to optimize optical non-linearities, increase bending tolerance or reduce temperature and radiation sensitivities [**Anscombe, 2011**]. Interestingly, the properties of such fibers are primarily governed by material structuring with reduced sensitivity to the material "bulk" properties, which is a characteristic commonly attributed to metamaterials.

As a subset of metamaterials, periodic arrangements of dielectric materials (or possibly metallic or semiconductor materials) are referred to as Photonic Crystals because of their ability to modify the propagation of EM waves in a similar way that crystalline "bulk" materials affect electron propagation. Photonic "band gaps" can then be created to block light propagation efficiently, just like semiconductor bandgaps operate with electric currents. Consequently, leveraging this property in the cladding region of an optical fiber appears as an attractive idea. Such a concept, giving birth to "holey" Photonic Crystal Fibers (PCF), is exemplified below in Figure 2-62 [**Limpert, 2004**] and Figure 2-63 (a) [**Cherif, 2009**]. Note that the core region can be interpreted as a defect line willfully introduced in the crystal so that propagation only occurs in this region. PCF can exhibit very unlikely properties like "endlessly single-mode" operation, meaning single-mode operation whatever the frequency, if designed appropriately (Figure 2-62 (c)). No matter the materials or their dimensions, this feature is clearly impossible in conventional fibers. In fact, this fortunate and unique effect in PCF is the result of a strong dependency of the effective index in the cladding region (see Figure 2-62 (b)).

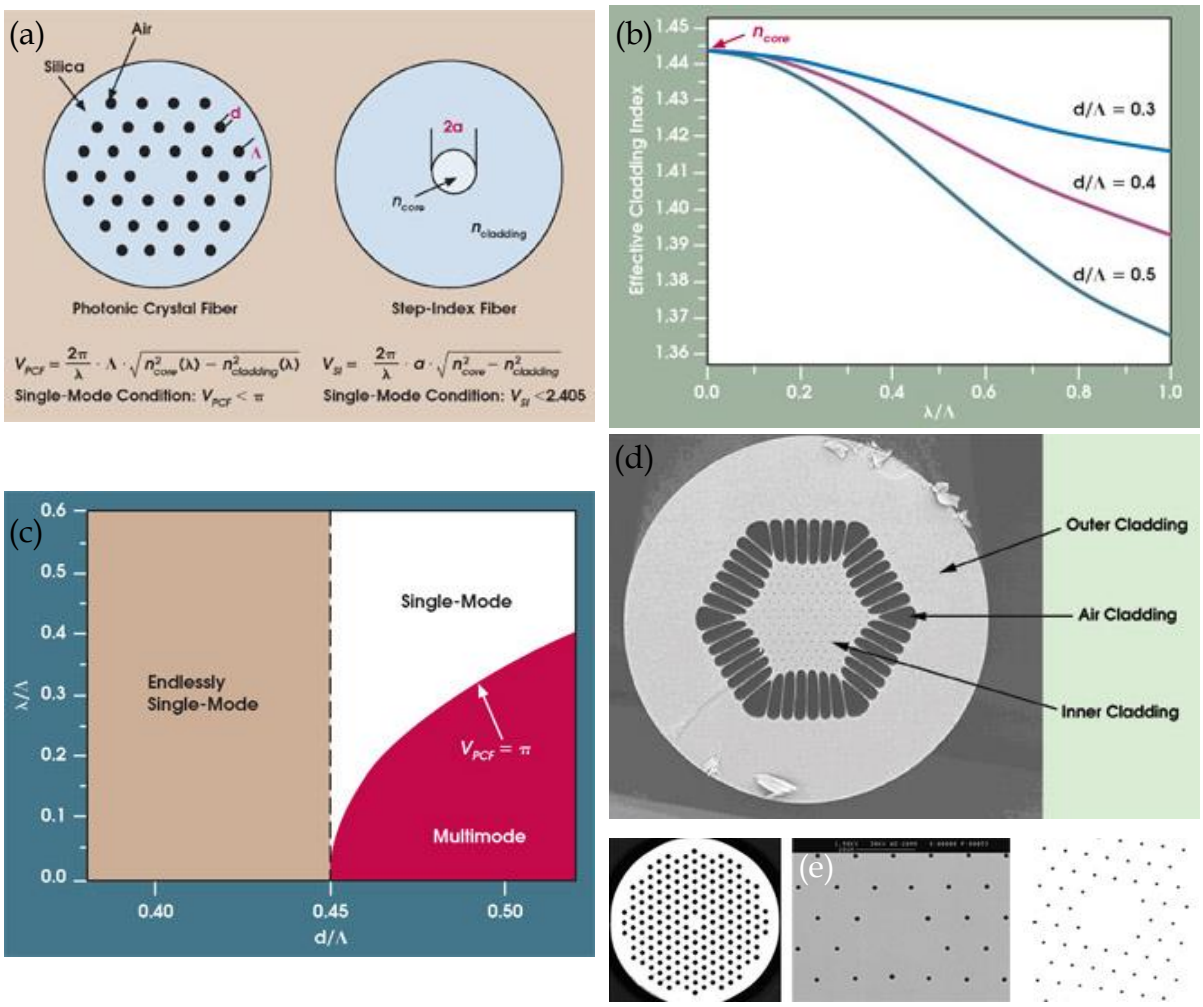

*Figure 2-62: Figures from **[Limpert, 2004]** showing the difference between conventional optical fibers and PCF (a), the wavelength dependent effective cladding index (b), the resulting "band-diagram" (c) and some examples of PCF with 1, 3 and 7 missing holes (d-e).*

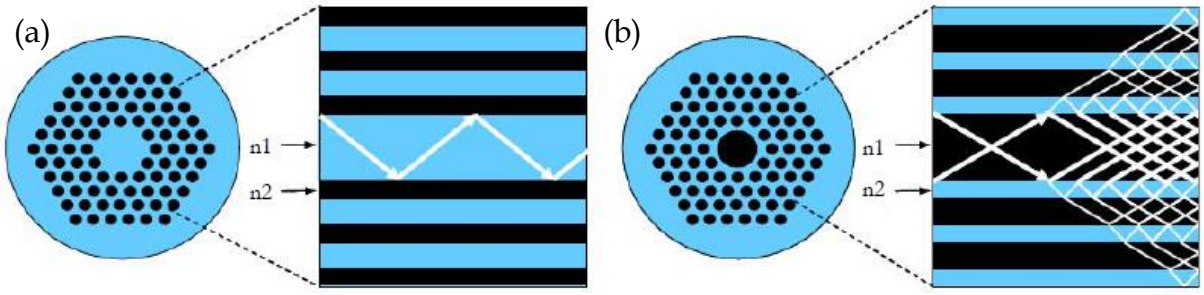

*Figure 2-63: "Holey" fibers leveraging total internal reflection (a) and "Hollow core" fibers featuring an equivalent Bragg mirror (b). Figures reproduced from **[Cherif, 2009]**.*

In semiconductors, pattern pitches (in Bravais lattices) are of the order of 0.5 nm. As regards Photonic Crystals, this dimension becomes $d/\lambda = d/\Lambda \cdot \Lambda/\lambda \approx 0.45 \cdot 1$ so that the pitch is roughly $\lambda/2$. Scaling this design to mmW wavelengths seems all the more feasible with silica… But what about conventional low-cost polymers?

Anyway, if possible, so-called Millimeter Wave Crystals Fibers could potentially disrupt the previously reported trade-off between single-mode operation and maximum Poynting confinement. However, as confinement increases so do losses. Attenuation minimization should then be investigated. While new materials, with specifically low loss at mmW, may be developed for such applications, this innovation path is not likely to offer significant

improvements and return on investment may be at risk. One the other hand, still looking at recent developments in the topics related to low loss optics, Photonic Crystals properties also enable propagation in "hollow core" fibers as illustrated from [**Cherif, 2009**]. In this case, the core index (air or appropriate gas) is clearly lower than the effective cladding index so that propagation no longer relies on total internal reflection as illustrated in Figure 2-63 (b). Light is actually confined at the center by the Photonic Crystals bandgap resulting from coherent reflections on the holes. In other words, this arrangement is similar to a Bragg mirror. Moreover, as most of the energy travels in the (lossless) hollow region, attenuation can be greatly reduced. This concept has already been applied with very limited complexity in the THz range with attenuation in the order of 0.1 – 1 dB/m (simulated) [**Lu, 2015**]. Once scaled at mmW, assuming that the Bragg mirror is thick enough, this concept could potentially disrupt attenuation / confinement / single-mode trade-offs.

References

[**3M, 2012**] Datasheet of 3M Active Optical Cable (AOC) Assemblies for QSFP+ to SFP+ Applications, available at http://multimedia.3m.com/mws/media/771907O/3mtm-active-optical-cable-aoc-assemblies.pdf

[**Afsar, 1985**] M. N. Afsar and K. J. Button. "Millimeter-Wave Dielectric Measurement of Materials," *Proceedings of the IEEE*, Vol. 73, No. 1, Jan. 1985.

[**Afsar, 1987**] M. N. Afsar. "Precision Millimeter-Wave Measurements of Complex Refractive index, Complex Dielectric Permittivity, and Loss Tangent of Common Polymers," *IEEE Transactions on Instrumentation and Measurement*, Vol. IM-36, No. 2, June 1987.

[**Anscombe, 2018**] N. Anscombe. "Photonic crystal pioneer," *Nature Photonics*, Vol. 5, pp. 464-465, Aug. 2011.

[**Balanis, 1969**] C. A. Balanis. "Measurement of dielectric constants and loss tangents at E-band using a Fabry-Perot Interferometer." NASA Technical Note, NASA TN D-5583, pp. 28-33, Dec. 1969.

[**Carson, 1936**] J. R. Carson, S. P. Mead, and S. A. Schelkunoff. "Hyperfrequency waveguides - mathematical theory," *Bell System Technical Journal*, Vol. 15, No. 310, 1936.

[**Cherif, 2009**] R. Cherif. "Etude des Effets Non-Linéaires dans les Fibres à Cristaux Photoniques," PhD thesis, Ecole Supérieure des Communications de Tunis, Tunisia, 2009.

[**Culshaw, 1962**] W. Culshaw and M. V. Anderson. "Measurement of permittivity and dielectric loss with a millimeter wave Fabry-Perot interferometer", *Proceedings of the IEE*, Part B, Suppl. 23, Vol. 109, pp. 820-826, 1962.

[**Dolatsha, 2013**] N. Dolatsha and A. Arbabian. "Dielectric Waveguide with Planar Multi-Mode Excitation for High Data-Rate Chip-to-Chip Interconnects," *Proceedings of the IEEE International Conference on Ubiquitous Wireless Broadband*, pp. 184-188, 2013.

[**Farnell, 2011**] Cat5e Cable Datasheet, available online at http://www.farnell.com/ datasheets/1311844.pdf (2011).

[**Fibercablesdirect, 2018**] OSx / OMx Datasheets, available online at https://fibercablesdirect.com (2018).

[**FrCustoms, 2017**] French Customs. "Polymers Prices in March 2017", France, 2017.

[**Friedsam, 1997**] G. L. Friedsam and E. M. Biebl. "Precision Free-Space Measurements of Complex Permittivity of Polymers in the W-Band," *IEEE Microwave Theory and Techniques Society Digest*, Vol. 3, pp. 1351-1354, 1997.

[**Fukuda, 2011**] S. Fukuda, Y. Hino, S. Ohashi, T. Takeda, H. Yamagishi, S. Shinke, K. Komori, M. Uno, Y. Akiyama, K. Kawasaki and A. Hajimiri. "A 12.5+12.5 Gb/s full-duplex plastic waveguide interconnect," *IEEE Journal of Solid-State Circuits*, Vol. 46, No. 12, pp 3113-3125, 2011.

[**Goubau, 1951**] G. Goubau. "Single conductor surface wave transmission lines," *Proceedings of the IRE*, Vol. 39, No. 619, 1951.

[**Harrington, 2000**] J. A. Harrington. "A review of IR Transmitting, Hollow Waveguides," *Fiber and Integrated Optics*, Vol. 19, No. 3, pp. 211-227, 2000.

[**Heaviside, 1893**] O. Heaviside. *Electromagnetic Theory*, Vol. 1, 1893. Reprinted by Dover, New York, 1950.

[**Hofmann, 2003**] A. Hofmann, E. Hörster, J. Weinzierl, L.-P. Schmidt, H. Brand. "Flexible Low-Loss Dielectric Waveguides for THz Frequencies with Transitions to Metal Waveguides," *Proceedings of the IEEE European Microwave Week*, pp. 955-958, 2003.

[**Hondros, 1910**] D. Hondros and P. Debye. "Elektromagnetische Wellen an dielektrischen Drähten," *Annalen der Physik*, Vol. 32, No. 465, 1910.

[**Kim, 2013**] Y. Kim, L. Nan, J. Cong and M-C. F. Chang. "High-speed mm-wave data-link based on hollow plastic cable and CMOS transceiver," *IEEE Microwave and Wireless Components Letters*, Vol. 23, No. 12, pp. 674-676, Dec. 2013.

[**Kogami, 2000**] Y. Kogami, H. Tamura, K. Matsumura. "Characterization of Low Loss Dielectric Materials in Millimeter Wave Region using a Whispering Gallery Mode Resonator," *Microwaves Radar and Wireless Communications*, Vol. 1, pp. 340-343, 2000.

[**Limpert, 2004**] J. Limpert, A. Liem, T. Schreiber, F. Röser, H. Zellmer and A. Tünnermann. "Scaling single-mode photonic crystal fiber lasers to kilowatts," *Photonics Spectra*, Vol. 38, No. 5, pp. 54-56, 2004.

[**Lu, 2015**] W. Lu, S. Lou and A. Argyros. "Investigation of Flexible Low-Loss Hollow-Core Fibres With Tube-Lattice Cladding for Terahertz Radiation," *IEEE Journal of Selected Topics in Quantum Electronics*, Vol. 22, No. 2, March / April 2016.

[**Maxwell, 1873**] J. C. Maxwell. *A Treatise on Electricity and Magnetism*, Vol. 1 & Vol. 2, Clarendon Press, Oxford, 1873.

[**Marcatili, 1969**] E. A. J. Marcatili. "Dielectric rectangular waveguide and directional couplers for integrated optics," *Bell System Technical Journal*, Vol. 48, No. 2071, 1969.

[**Microwaves101, 2015**] Waveguide Loss, available at https://www.microwaves101.com/encyclopedias/waveguide-loss (updated in Jan. 2015).

[**Nahin, 1988**] P. J. Nahin. *Oliver Heaviside: Sage in Solitude*, IEEE Press, New York, 1988.

[**Nickel, 2014**] H.-U. Nickel and J. Zovo. "Novel Flexible Dielectric Waveguide for Millimeter and Sub-Millimeter Frequencies – Design and Characterization," *Proceedings of the Automatic RF Techniques Group Conference*, Dec. 2014.

[**Packard, 1984**] K. S. Packard. "The Origin of Waveguides: A Case of Multiple Rediscovery," *IEEE Transactions on Microwave Theory and Techniques*, Vol. MTT-32, pp. 961–969, Sept. 1984.

[**Park, 2013**] K. Y. Park, N. Wiwatcharagoses, P. Chahal. "Wafer-level Integration of Micro-Lens for THz Focal Plane Array Application," *Electronic Components & Technology Conference*, pp. 1912-1919, 2013.

[**PlasticsEurope, 2018**] PlasticsEurope. "Plastics – the Facts 2017: An analysis of European plastics production, demand and waste data", available at https://plasticseurope.org, 2018.

[**Pozar, 2012**] D. M. Pozar. *Microwave Engineering*, Fourth edition, Wiley, 2012.

[**Rautio, 2010**] J. C. Rautio. "Twenty Three Years: The Acceptance of Maxwell's Equations," *Applied Computational Electromagnetics Society Journal*, Vol. 25, No. 12, Dec. 2010.

[**Rayleigh, 1897**] Lord Rayleigh. "On the Passage of Electric Waves through Tubes, or the Vibrations of Dielectric Cylinders," *Philosophical Magazine*, Vol. 43, pp. 125–132, 1897. Reprinted in Collected Papers, Cambridge University Press, Cambridge, 1903.

[**Reynaert, 2017**] P. Reynaert and Y. Zhang. "Polymer Waveguides as an Alternative to Optical and Copper High-Speed Communication," workshop presented at the *IEEE International Microwave Symposium*, June 2017.

[**Sage, 2018**] SAT-FE-12212-S1 E-Band Orthomode Transducer Datasheet, available at https://www.sagemillimeter.com (2018).

[**Shimabukuro, 1988**] F. Shimabukuro and C. Yeh. "Attenuation Measurement of Very Low Loss Dielectric Waveguides by the Cavity Resonator Method Applicable in the Millimeter/ Submillimeter Wavelength Range", *IEEE Microwave Theory and Techniques Transactions*, Vol. 36, No. 7, pp. 1160-1166, 1988.

[**Shimizu, 2002**] T. Shimizu, Y. Kobayashi. "Millimeter wave measurements of some low-loss dielectric plates by a novel cut-off circular waveguide method," *IEEE European Microwave Conference*, March 2002.

[**Southworth, 1962**] G. C. Southworth. "Survey and History of the Progress of the Microwave Arts," *Proceedings of the IRE Microwave Theory and Techniques*, pp. 1199-1206, May 1962.

[**Suzuki, 2008**] H. Suzuki, T. Kamijo. "Millimeter-Wave Measurement of Complex Permittivity by Perturbation Method Using Open Resonator", *IEEE Transactions on Instrumentation and Measurement*, Vol. 57, No. 12, Dec. 2008.

[**Teyssedre, 2010**] G. Teyssedre, L. Boudou. « Polymères et composites pour l'électrotechnique. » Techniques de l'Ingénieur, 2010.

[**Tytgat, 2013**] M. Tytgat and P. Reynaert. "A plastic waveguide receiver in 40nm CMOS with on-chip bondwire antenna," *Proceedings of the IEEE European Solid-State Circuits Conference*, pp. 335-338, 2013.

[**Voineau, 2018**] F. Voineau, C. Dehos, B. Martineau, M. Sié, M. Perchicot, N. H. Nguyen, A. Ghiotto and E. Kerhervé. "A 12 Gb/s 64QAM and OFDM compatible millimeter-wave communication link using a novel plastic waveguide design," *Proceedings of the IEEE Radio and Wireless Symposium*, pp. 250-252, 2018.

[**Van Thienen, 2016**] N. Van Thienen, Y. Zhang, M. De Wit and P. Reynaert. "An 18Gbps polymer microwave fiber (PMF) communication link in 40nm CMOS," *Proceedings of the IEEE European Solid-State Circuits Conference*, pp. 483-486, 2016.

[**Volkaerts, 2015**] W. Volkaerts, N. Van Thienen and P. Reynaert. "An FSK Plastic Waveguide Communication Link in 40nm CMOS," *Proceedings of the International Solid-State Circuits Conference*, pp. 178-180, 2015.

[**WikiCat6, 2018**] Cat6 cable Wikipedia page, available at https://fr.wikipedia.org/wiki/C%C3%A2ble_cat%C3%A9gorie_6 (2018).

[**WikiSMA, 2018**] SMA cable Wikipedia page, available at https://en.wikipedia.org/wiki/SMA_connector (2018).

[**Yeh, 2008**] C. Yeh and F. Shimabukuro. *The Essence of Dielectric Waveguides,* Springer, 2008.

[**Zahn, 1916**] H. Zahn. "Detection of electromagnetic waves along dielectric wires," *Annalen der Physik*, Vol. 49, No. 907, 1916.

[**Zhou, 2013**] P. Zhou, J. P. Y. Tsui, S. T. Chu, A. Taeb, E. Y.-B. Pun, and S. K. Chaudhuri. "Theoretical and Experimental Development of a Broadband Sub-millimeter Wave Rectangular Metallic to Dielectric Rod-Waveguide Adaptor," *IEEE Conference on Lasers and Electro-Optics Pacific Rim*, 2013.

[**Zhou, 2017**] P. Zhou, J. P. Y. Tsui, S. T. Chu, A. Taeb, E. Y.-B. Pun, S. K. Chaudhuri. "Design and Fabrication of a Broadband Millimeter Wave Rectangular-Metallic to Dielectric Rod-Waveguide Adaptor," *IEEE Transactions on Terahertz Science and Technology*, Vol. 7, No. 1, Jan. 2017.

Chapter 3

Building a Millimeter-wave System around the Channel

3.1. System Level Specifications

In the context depicted in Chapter 1, it clearly appeared that the potentials of plastic waveguide systems could be leveraged in multiple markets, which are already addressed by conventional copper cables or optical fibers. However, introducing such a disruptive technology is not benign from an industrial point of view. Although the similarities with optical fibers have been highlighted in Chapter 2, the huge wavelength scaling and radically different processing are likely to raise new industrial issues (while probably solve other ones). Because of this intermediate *Technology Readiness Level*, currently between two and four, we can assume that the developments of this technology will first focus on existing solutions or standards. Even if the introduction of dedicated standards would be more appropriate and / or optimized to plastic waveguides characteristics, replacing copper cables or optical fibers with proven business prospects is a much less risky approach from an economical point of view. With these preliminary economical and industrial conclusions in mind, the most relevant applications for plastic waveguides are presented in Figure 3-1.

The idea of replacing passive copper cables by systems containing a plastic waveguide channel as well as necessary mmW TRx at each end may seems troublesome. These latter actually need some energy to operate. However, in most cases, this point may not be a difficulty because host connectors usually have power delivery capabilities. Typically, a few Watts may be available and could be leveraged by the envisioned solution. In that sense, a plastic waveguide system is an active cable, meaning that the system has to take energy from its hosts in order to process transmitted signals according to the characteristics of its transmission channel. In fact, active cables are already found in Thunderbolt 1 and Thunderbolt 2 cables as well as in Direct Attach cables for datacenters applications. While signal processing in these latter solutions is realized in the analog or baseband domain, plastic waveguides demand dramatically different signals. To account for the high-pass or band-pass characteristics actually observed in plastic waveguides and reported in Chapter 2, a frequency transposition is required so that the information contained in transmitted signals is used to modulate a suitable mmW carrier frequency. These concepts will be detailed in section 3.2.

Note that, one more time, the analogy with optical fibers is natural since lasers also provide appropriate carriers for the transparency window (or bandwidth) of the fibers. Because of this common principle, the compatibility with applications dominated by optical solutions is even more apparent.

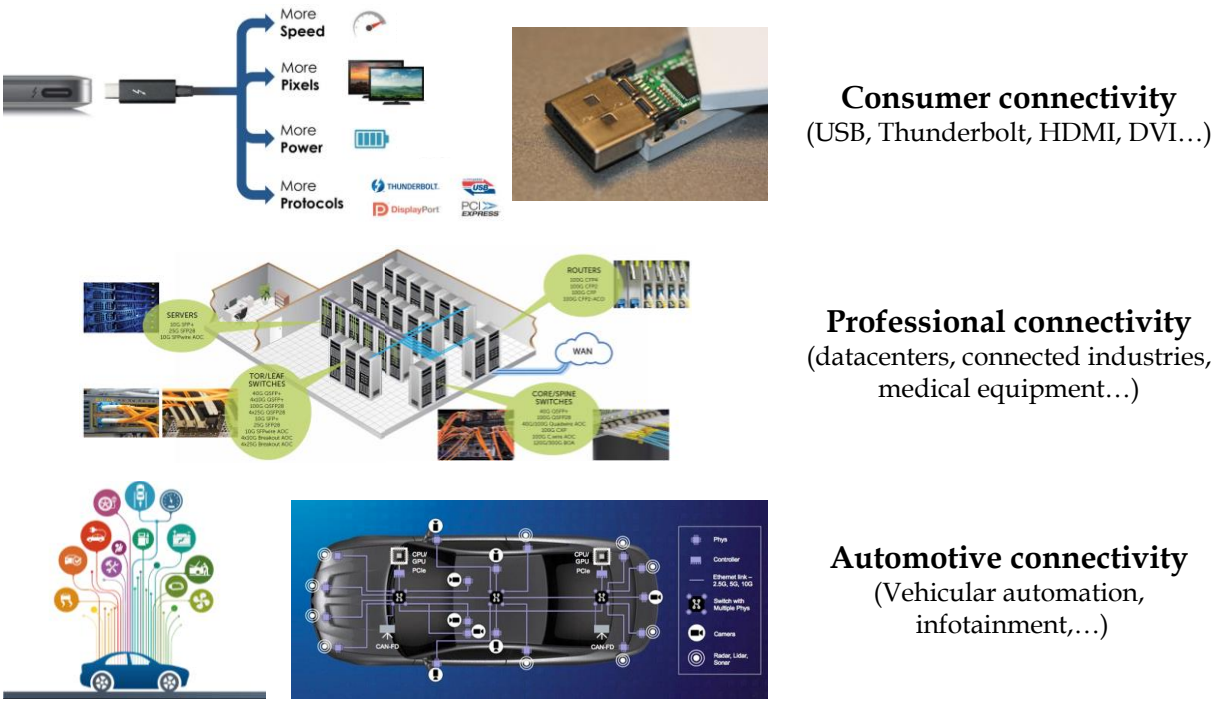

Figure 3-1: Plastic waveguides applications have been classified in three main categories.

To address successfully the variety of the markets presented in Figure 3-1, dedicated electrical interfaces should be integrated along with the mmW circuits. Implications are manifold. In addition to connector integration, specific digital IPs are to be integrated to mimic the response of a traditional connectivity, especially for the replacement of passive low-pass cables. Considering the mmW TRx, one can wonder whether it is possible to rationalize developments using the very same mmW IP in a "one size fits all" approach. An electrical performance analysis is proposed in Table 3-1 based on the most promising standards for each of the three identified segments.

Beginning with the consumer market, the widespread USB standard has been logically selected. The freshly released USB 3.2 standard defines four possible use cases to maximize data rates up to 10 Gb/s for the first generation and 20 Gb/s for the second one. Note that such data rates strongly limit maximum lengths to 2 m and 1 m respectively. As regards the professional market, there is no denying that it is dominated by datacenters applications. However, it is noticeably fragmented with a large variety of standards, each one being implemented using many different physical layers. In this context, 10GbE SFP+ DAC connectivity is already widely deployed for intra-rack connections and is therefore an immense opportunity. AOC solutions are still pre-existent competitors up to 100 m while *passive* DAC cables are low power but only cover distances up to 5 – 7 m. Besides, anticipating future bandwidth requirements, migration to QSFP+ 40GbE is possible in the long run. Currently, these high-speed standards are also mainly in use for inter-rack connectivity. With the same limitations, it is then relevant to address 40GbE QSFP+ DAC cables. Note that higher performance links (essentially 100 Gb/s and coming 400 Gb/s) have not been selected here because of inappropriate length X data rate products.

	Digital Interface & PHY layer		Data rate (per lane)	Parallel lanes	Operation	Length	Conso. (per end)
Consumer	USB 3.2	Gen 1x1	5 Gb/s	1	Full-duplex	≤ 2 m	NA
		Gen 1x2		2			
		Gen 2x1	10 Gb/s	1	Full-duplex	≤ 1 m	
		Gen 2x2		2			
Professional	10GbE	DAC	10 Gb/s	1	Full-duplex	≤ 5 - 7 m	< 1 mW
						≤ 15 m	≈ 100 mW
		AOC				≤ 100 m	≈ 250 mW
	40GbE	DAC	10 Gb/s	4	Full-duplex	≤ 7 m	< 20 mW
						≤ 15 m	< 1 W
		AOC				≤ 100 m	≈ 500 mW
Automotive	2.5GBase-T1		2.5 Gb/s	1	Full-duplex	≤ 15 m	NA
	5GBase-T1			2			
	10GBase-T1			4			

Table 3-1: Comparison of the most promising standards for consumer, professional and automotive markets.

Finally, the automotive market will transition from 1 Gb/s copper cables to higher data-rate solutions in the coming years to sustain increasingly more autonomous vehicles. This important market is looking for a cost-effective, lightweight, low-power and EMI-friendly connectivity. Because of these combined constraints, leveraging on conventional 10GbE solutions is not satisfying so that dedicated standards had to be introduced (2.5GBase-T1, 5GBase-T1, 10GBase-T1). Note that higher data rates rely on reduced baseband bandwidth for EMI constraints… at the expense of multiple lanes in parallel. For most point-to-point connections, 2.5 Gb/s is enough but higher throughputs would enable point-to-multipoint connections, thus saving weight and costs.

As a conclusion from Table 3-1, it should be possible to address the most promising applications with a unique mmW system based on plastic waveguide technology, which (ideal) specifications are given in Table 3-2. It is the purpose of this chapter to investigate the feasibility of such a system and to discuss system portioning while still mentioning relevant limitations based on the state of the art.

Data rate (per lane)	Parallel lanes	Operation	Length	Conso. (per end)	Energy efficiency
10 Gb/s	4	Full-duplex	≈ 15 m	≈ 500 mW	≈ 0.83 pJ/b/m

Table 3-2: Summary of the ideal performances of the mmW plastic waveguide system.

3.2. Millimeter-wave System Basics

In this section, millimeter-wave system basics are recalled so that the application to plastic waveguide systems will be proposed in the following section. In this work, the topic is simplified by focusing on digital communications, although other applications like radars or imagers are definitely possible. For the sack of simplicity, a digital clock (toggling between 0 and 1 deterministically) is first considered and is represented in Figure 3-2. This periodic signal can be decomposed in a Fourier series highlighting the time – frequency duality. The lower the frequency, the larger the spectral lobes. Note that, strictly speaking, the occupied bandwidth is infinite because of an infinite number of harmonics is actually required to obtain perfect square waveforms in the time-domain.

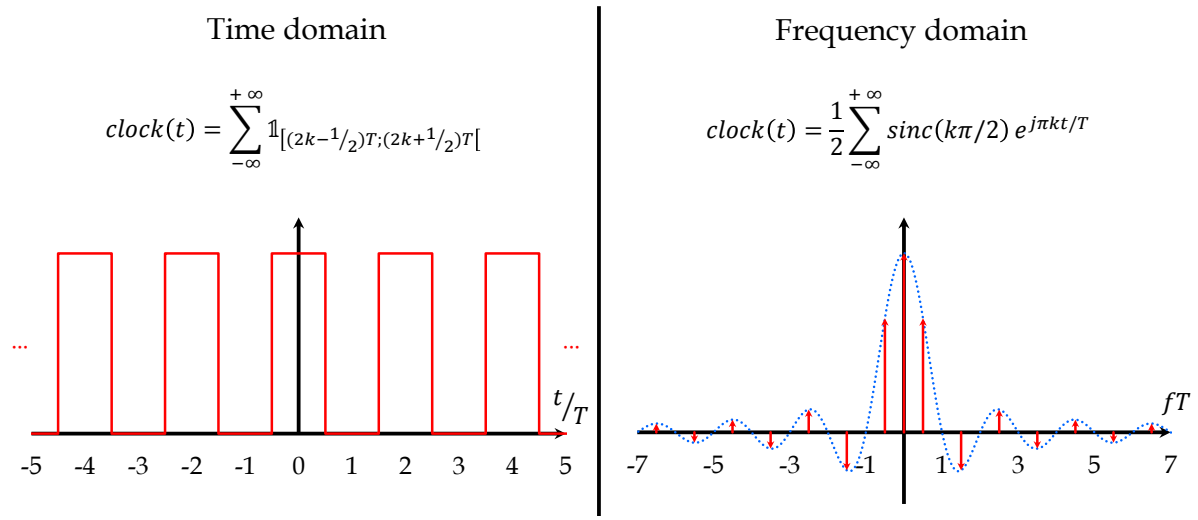

Figure 3-2: Time domain and frequency domain description of a 2T-periodic digital clock by means of Fourier series.

In practice, transmitting a clock as represented in Figure 3-2 is not a case of interest in a communication system since such a signal is purely deterministic. In other words, no information is carried inside such a signal. Instead, transmitted signals are random by nature (Figure 3-3). This important observation results in mathematical difficulties. First, Fourier series decomposition can no longer be used. Fourier transformation extends harmonic decomposition to aperiodic signals. These latter may be expressed as the sum (or integral) of a frequency continuum, as if the time periodicity was infinite. However, the direct computation of the Fourier transform of random signals is not straightforward. Moreover, a stationary random process like the signal in Figure 3-3 may not exhibit a finite energy as defined in Equation (3-1) so that Fourier transformation is not properly defined.

Energy associated to signal x $$E_x = \int_{-\infty}^{+\infty} |x(t)|^2 dt \qquad (3\text{-}1)$$

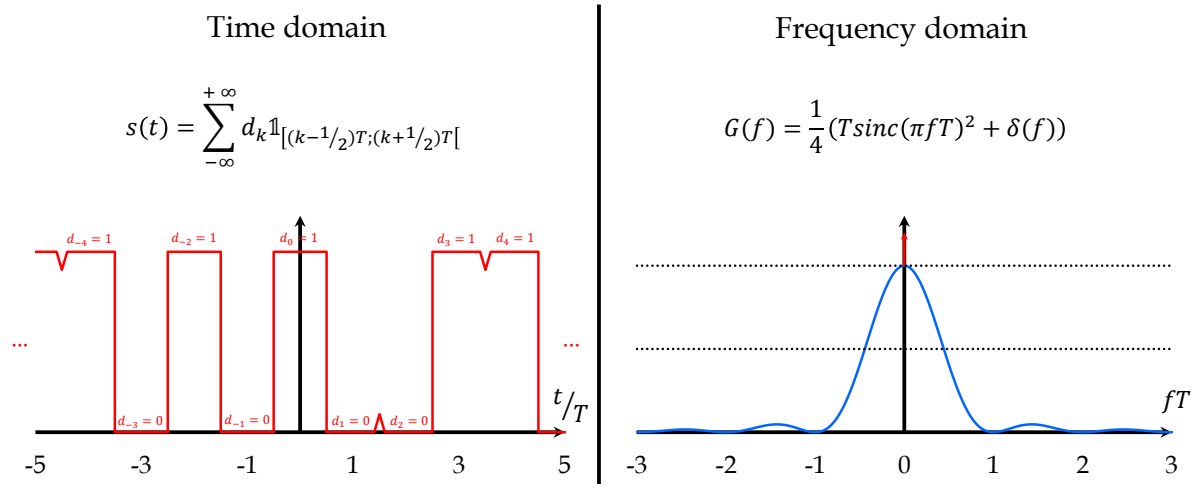

Figure 3-3: Time domain and frequency domain description of a random data sequence by means of Power Spectral Density.

To circumvent this issue, the concept of power spectral density (PSD) may be introduced. Practical random signals actually have a finite average power as defined by Equation (3-2) for periodic signals. It corresponds to the sum of the power carried by each harmonic thanks to Parseval's power conservation theorem. It is then a finite quantity for practical periodic signals as well as for aperiodic ones by considering an infinitely long period. Consequently, it is possible to introduce the PSD function to describe the distribution of the signal power in the frequency domain. Its integral over a given frequency range gives the amount of power in that range (Equation (3-3)). Note that the factor 2 accounts for positive and negative frequencies over which the PSD is evenly defined for real signals.

Average power associated to T-periodic signal x

$$P_x = \frac{1}{T}\int_T |x(t)|^2 dt \tag{3-2}$$

Signal power in the frequency range [f_1 ; f_2]

$$P_{band\ limited} = 2\int_{f_1}^{f_2} G(f)df \tag{3-3}$$

$$G(f) = \frac{1}{4}Tsinc(\pi fT)^2 + \frac{1}{4}\delta(f) \tag{3-4}$$

Under proper ergodicity and bits equal probability assumptions, one can show that the PSD of a stationary random data sequence is given by Equation (3-4) [**Glover, 1998**]. In Figure 3-3, the continuous nature of the PSD is noticeable while periodic signals were previously described by discrete harmonics. Note that the Dirac observed at DC is only caused by non-zero signal average. Strictly speaking, it is also clear that the overall spectral occupancy is not bounded. One more time, an infinite bandwidth is therefore necessary to obtain sharp transitions in the time domain. From Figure 3-3, PSD levels for frequencies beyond ± 1/T are obviously negligible. This result is consolidated quantitatively in Figure 3-4, suggesting that the use of a finite (…and much more physical) bandwidth is good *enough*. The conventional, but still arbitrary, bandwidth definition is given in Equation (3-5) with respect to the PSD maximum level (excluding Dirac contributions) and is referred to as the "-3 dB bandwidth". In the case of the signal presented in Figure 3-3, this bandwidth is computed in Equation (3-6).

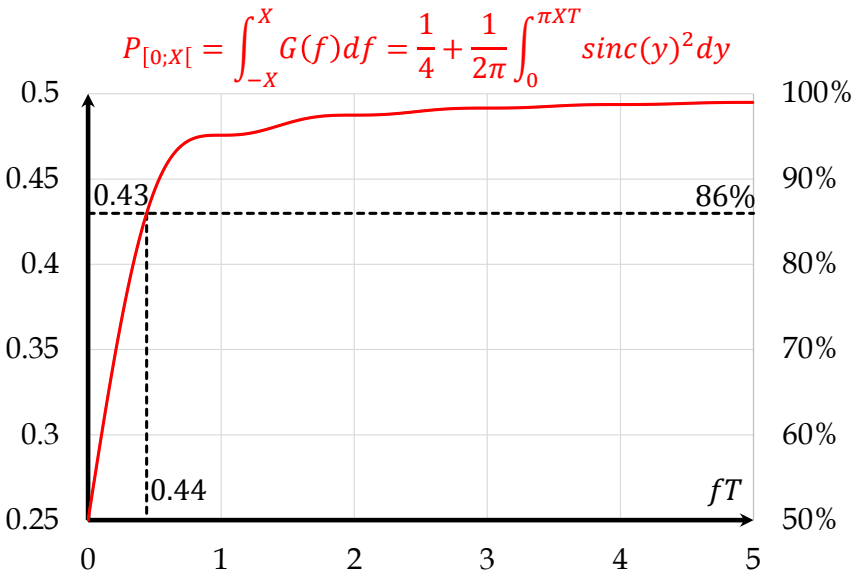

Figure 3-4: Integrated power (absolute value on the left and relative value on the right) as a function of the considered bandwidth. Note that the DC component of the spectrum represents 50% of the total signal power. Besides, the bandwidth defined in Equation (3-6) contains 86% of the total power.

-3 dB bandwidth

$$BW_{-3dB} = \max\left\{f, G(f) \geq \frac{\max G(f)}{2} = \frac{T}{8}\right\} \quad (3\text{-}5)$$

Stationary random data sequence bandwidth

$$sinc(\pi\, T\, BW_{-3dB}) = {}^{\sqrt{2}}/_{2} \Rightarrow BW_{-3dB} \approx \frac{0.44}{T} \quad (3\text{-}6)$$

Thanks to the bandwidth expression in Equation (3-6), the motivation to increase transmitted signals bandwidth in order to propagate higher data rates is evident. However, available baseband channels (mainly twisted pairs or coaxial cables) usually suffer from impractical attenuations at very high frequencies. The basic idea at the heart of any RF transmission is to move the entire signal spectrum to a much higher frequency region where relative signal occupancy is very small. In this manner, the discrepancies in the propagation channel can be mitigated and the absolute bandwidth can be enlarged.

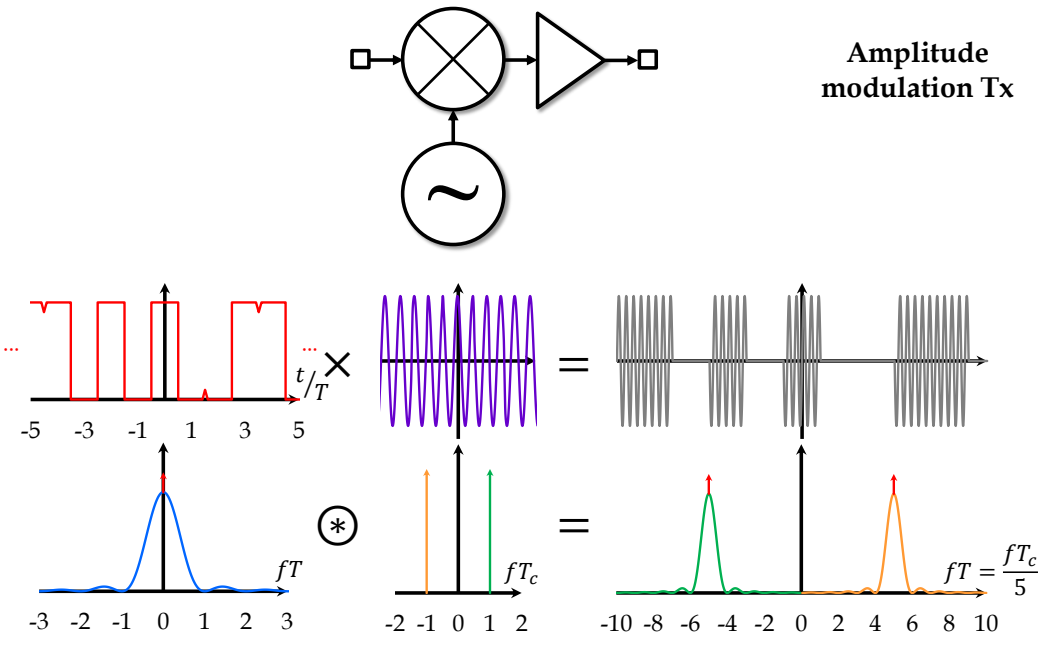

Figure 3-5: Representation of a basic amplitude modulation Tx.

In practice, a convenient way to convert signals from baseband to bandpass can be obtained by multiplying data with a high frequency (carrier) signal as illustrated in Figure 3-5. In fact, this modulation process is equivalent to a convolution in the frequency domain. Any RF communication system thus involves a Transmitter (Tx) circuit to modulate the carrier, although the complexity of some modulation techniques significantly differs from this basic example. However, amplitude modulated systems are quite common in mmW as discussed later. In that case, the resulting bandpass bandwidth is twice the baseband one (double side band).

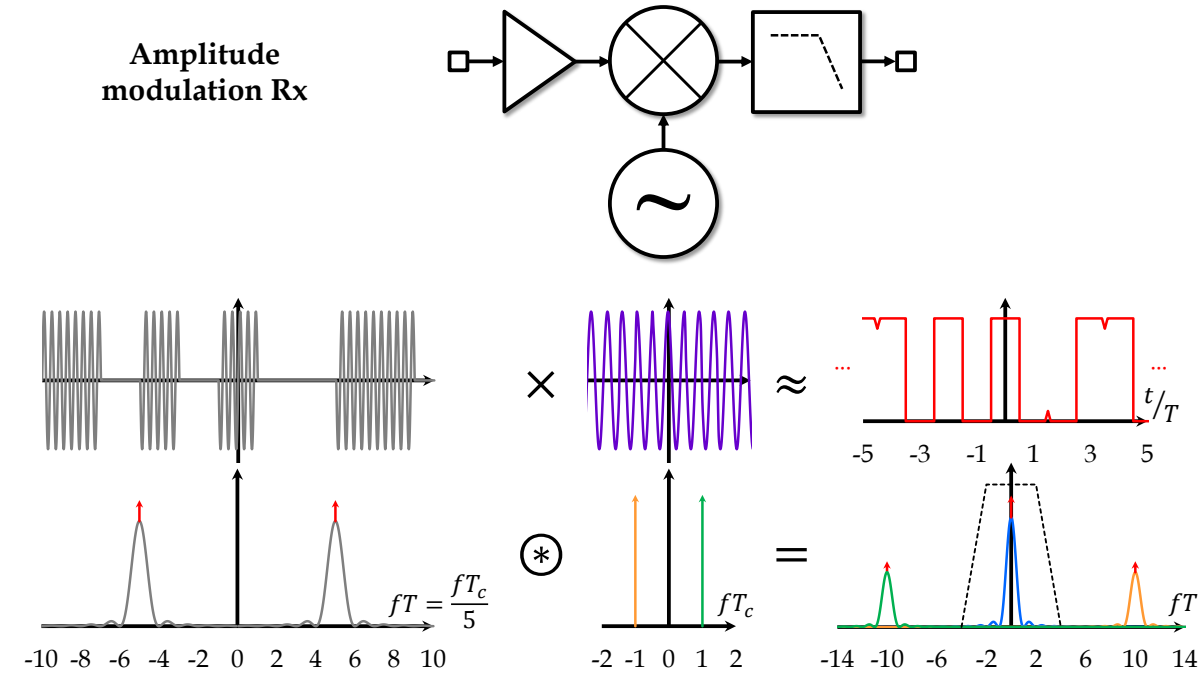

Figure 3-6: Representation of a basic amplitude demodulation Rx.

To recover baseband data from modulated signals, the modulation process should be inverted. In any RF system, this is the responsibility of the Receiver (Rx) circuit. To do so, a common Rx implementation also makes use of frequency convolution and low-pass filtering (Figure 3-6). However, this demodulation scheme assumes that a coherent copy of the carrier is available at Rx side (provided by the LO block). While carrier recovery or frequency synthesis are feasible at microwave, the difficulty of implementing this function increases dramatically at mmW due to higher power consumption and reduced noise performance. In practice, this reduces possible modulation / demodulation architectures.

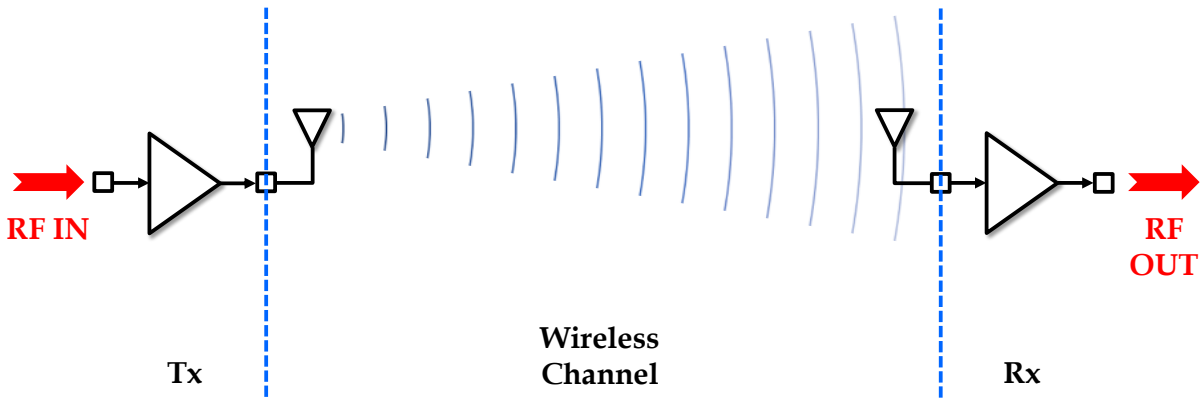

Figure 3-7: Wireless system interfacing Tx and Rx circuits thanks to antennas.

Finally, we conclude this review of fundamentals with a focus on the last part of the system, namely the channel. The vast majority of mmW systems (except those relying on plastic waveguides) are wireless. In this case, Tx and Rx antennas are used to communicate through the air, as described in Figure 3-7. From a system level point of view, the main characteristic of such a transmission is the loss introduced between the emitter and the receiver in Equation (3-7).

Friis transmission equation

$$P_{Rx\_dB} = P_{Tx\_dB} + G_{Tx\_dB} + G_{Rx\_dB} - FSPL_{dB} \quad (3\text{-}7)$$

Free Space Path Loss (FSPL)

$$FSPL_{dB} = 20\log\left(\frac{4\pi R}{\lambda}\right) \quad (3\text{-}8)$$

Fraunhofer distance

$$R_0 = 2\frac{D^2}{\lambda} \quad (3\text{-}9)$$

This relation is known as the Friis transmission equation and is based on several assumptions listed below:

- Line-of-sight propagation, so that no multipath is considered. This condition is typically satisfied in mmW systems because these frequencies are actually not reflected by the ionosphere (contrary to lower frequency counterparts). Their penetration through walls is also extremely weak. In addition to their important FSPL leading to negligible alternative paths, only a direct communication between Tx and Rx is therefore possible at mmW.
- The propagation distance, referred as to *R* in Equation (3-8), is supposed to be much longer than the cumulated far-field distances of the Tx and Rx antennas. For any antenna, this distance, also known as the Fraunhofer distance, is provided in Equation (3-9) where *D* is the largest dimension of the antenna. In other words, Equation (3-8) only applies in the far-field regime of both antennas. In practice, this point should be considered carefully at mmW frequencies since high-directivity antennas (typically > 20 dBi) are quite common but may exhibit Fraunhofer distances in the order of the meter or more.
- Antennas impedance mismatch are neglected.
- Polarization mismatch is neglected.
- No attenuation is considered in the channel. In fact, it should be clarified that the power loss in a free-space system has a twofold nature. The first loss cause is the "spherical dilution" (Equation (3-8)) because the power flow diminishes as $1/R^2$ in linear units. The term loss is ambiguous here since the power is not absolutely lost but only scattered in three dimensions. Theoretically, if the receiver antenna were able to capture it completely, it would result in zero loss. In practice, due to finite antenna gains, a power loss is still experienced between Tx and Rx which explains the use of this term. However, this effect can be mitigated by increasing the gain of any antenna in the system. The other loss mechanism at stack is medium attenuation resulting from molecular absorption. Unfortunately, and contrary to the precedent mechanism, the latter cannot be compensated by any means. It is illustrated in Figure 3-8 for through-air propagation that is a specifically relevant process at mmW frequencies. A strong correlation is observed between absorption peaks and molecular resonances in the

propagating medium. Although attenuation has an exponential dependency to distance (linear in dB/m), it should be noted that it is numerically very small even at the 60 GHz peak absorption.

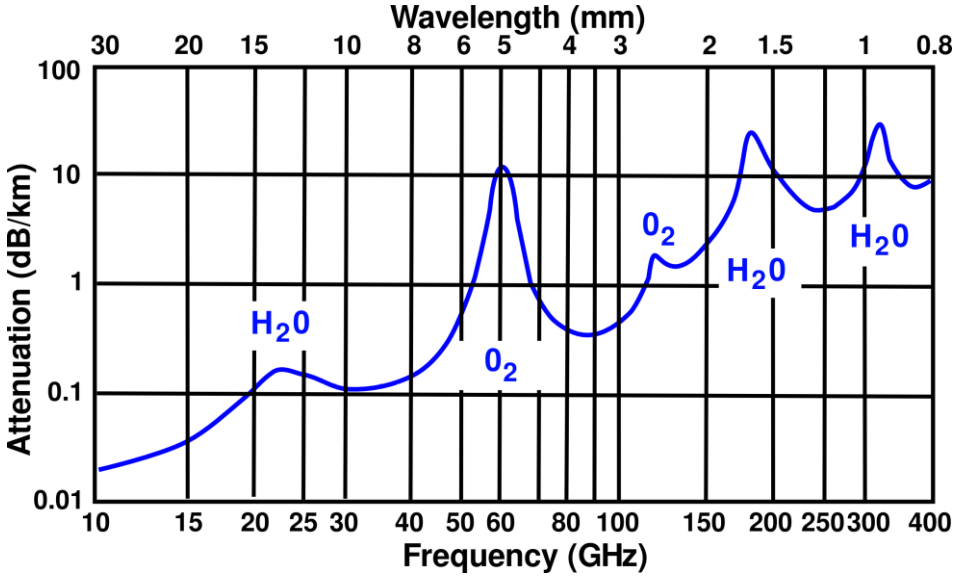

*Figure 3-8: Through-air attenuation measured at sea level from 10 to 400 GHz. Attenuation peaks are attributed to molecular resonances. Figure taken from [**TU-Berlin, 2015**].*

Following the discussion regarding the last assumption, FSPL obviously dominates for short distances (Figure 3-9) legitimating the assumption in Friis equation. Even for a 10 dB/km attenuation, it takes 100 m to induce a 1 dB additional loss while computed FSPL represents about 108 dB at 60 GHz. To go further, Figure 3-9 also shows the relevance of guiding the power in a low-loss medium waveguide in order to avoid spherical dilution and benefit from a much more favorable loss mechanism at lower distances. This basic idea is actually at the heart of any plastic waveguide system. Therefore, typical plastic waveguides attenuations (ranging from 1 to 5 dB/m) are interesting candidates for distances up to at least 20 m. **[Voineau, 2018]**

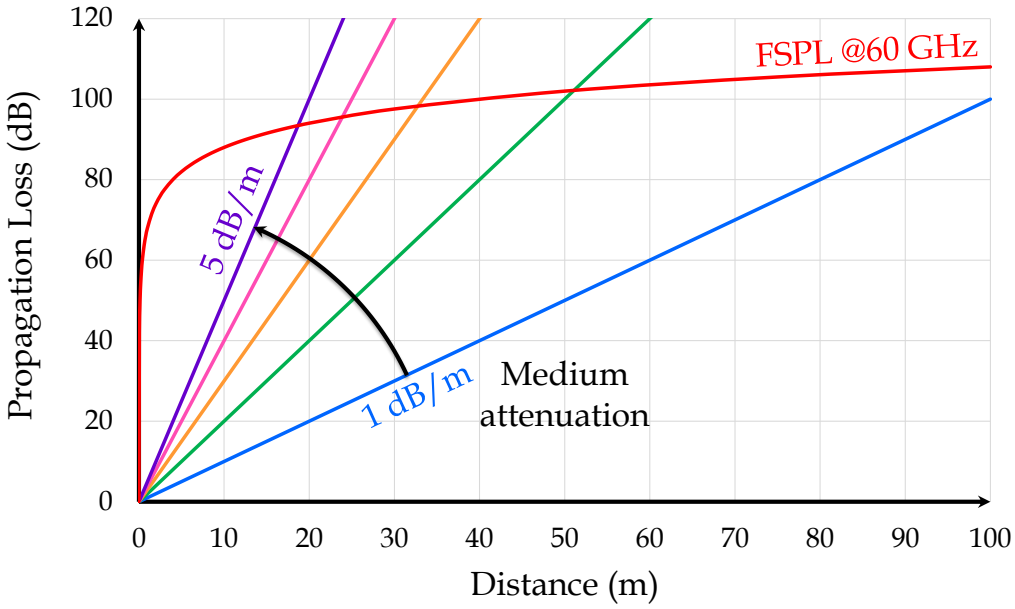

Figure 3-9: Comparison of propagation loss mechanisms. The FSPL is computed at 60 GHz (red) and shows a logarithmic increase while attenuation in dielectric medium is linear (blue, green, orange, rose and purple lines correspond to 1, 2, 3, 4 and 5 dB/m respectively).

3.3. Application to Plastic Waveguide Systems

Paradoxically, the most stringent constraints in a conventional wireless system are imposed by the simplest part of it, namely the channel. In fact, any RF emission is regulated to ensure good cohabitation of the numerous applications enabled by the EM spectrum. Moreover, it is important to guarantee interoperability between devices. Consequently, rigorous standards have been created for almost any application, defining carrier frequencies, bandwidths, Tx powers, ACLR, Rx sensitivity, etc. Ultimately, these specifications boil down to harsh design constraints on both Tx and Rx circuits which is believed to limit the achievable overall performance.

3.3.1. System Overview

In this context, introducing a dedicated low loss plastic waveguide channel makes sense. No specific standard currently addresses such communications. In addition, it has been shown in Chapter 2 that the waveguide properties can be tailored by several means. The resulting flexibility offers room for the design architect to build an efficient system.

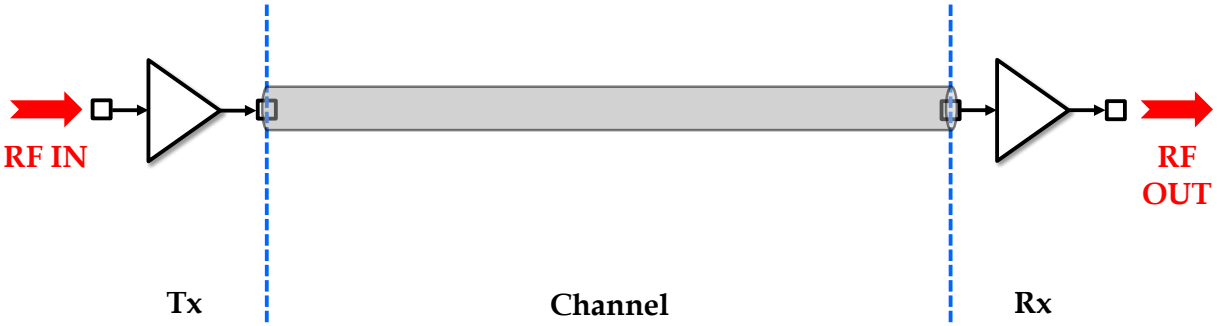

Figure 3-10: Wireline system interfacing Tx and Rx circuits through a plastic waveguide.

A schematic system overview is proposed in Figure 3-10. Note that a conventional RF/mmW architecture is used except that circuits are no longer coupled with antennas. Instead, the channel is composed of a plastic waveguide so that the Tx power travels in a one-dimensional bounded medium. Moreover, the power is coupled in and out the waveguide using dedicated couplers. To illustrate this functional schematic, Figure 3-11 presents a 3D representation of the global system, emphasizing the presence of the waveguide and the couplers. Note that it is only a suggestion so that other implementations may obviously be envisioned depending on applications. For example, the use of versatile circuits is likely to modify the appearance or the terminology of some system components (couplers may be used alternatively as directive antennas). In the following, the discussion focuses on the implementation of a dedicated system to comply with general specifications derived in section 3.1. The reasoning is exposed so that the reader may be able to adapt it according to its own application-dependent challenges.

To address the specifications summarized in Table 3-2, several system partitioning schemes are actually possible. The proposition in Figure 3-11 is primarily driven by the need to conserve the four input / output digital lanes (full duplex) in the system so that power-hungry serialization and deserialization are avoided. Another welcomed advantage is the reduced die area dedicated to digital interfaces, which may not be negligible. Moreover, a

40 Gb/s serialized data lane would either require an aggressive carrier frequency to support the bandwidth or a high-order modulation. None of these is satisfying from a power-efficiency point of view.

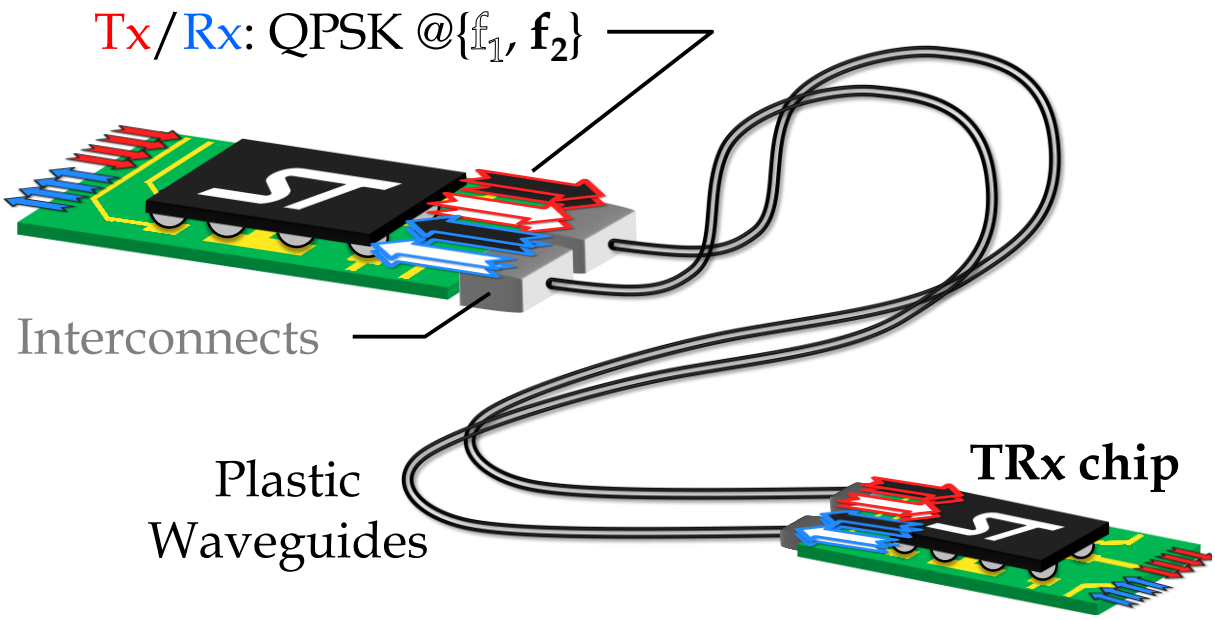

Figure 3-11: 3D overview of the proposed system based on plastic waveguides, illustrating the use of two QPSK-modulated frequency-multiplexed carriers per direction.

As a second motivation, the operating frequencies should be kept below about 100 GHz to benefit from comfortable design margins in advanced CMOS technologies. A multi-frequency architecture could be considered to fulfill this constraint. Nevertheless, this approach requires a very large overall bandwidth when taking into account mandatory guard bands between frequency bands of interest. Based on the results of section 3.2 for binary modulations, four carriers each modulated at a 10 Gb/s rate would require ≈ 4 x 8.8 GHz RF bandwidth (at least). Assuming roughly 5 GHz guard bands, such a system would require at least a 50 GHz bandwidth, which is obviously not feasible below 100 GHz.

Besides, in an attempt to contain circuit complexity and power consumption, low complexity modulations should be favored. In fact, there exists a strong trade-off between spectral efficiency and energy efficiency. This fundamental relation is illustrated and investigated further in Appendix D. Note that the QPSK modulation requires the same SNR compared to OOK while still offering a doubled data rate capability within the same bandwidth. What is more, the QPSK modulation can be considered as a superposition of two BPSK modulations in quadrature. Each I/Q signals may be modulated independently providing two parallel data lanes.

Synthesizing all the previously mentioned system constraints, the four 10 Gb/s modulated lanes may be cleverly realized thanks to QPSK signaling in combination to dual-band operation. From a circuit design point of view, this solution is a much more acceptable trade-off compared to 4-FSK or serialized 40 Gb/s. Meanwhile, from the waveguide point of view, the required bandwidth is still challenging especially for long waveguides (Chapter 2) for which inherent bends tend to reduce available bandwidth because of limited confinement. In this study, anticipating future developments of insensitive plastic waveguides, the channel bandwidth is supposed to be only limited by couplers bandwidth.

Finally, full-duplex operation can be addressed theoretically by leveraging waveguide orthogonal polarizations. However, practical difficulties of such an approach have been

highlighted in Chapter 2. Because of this lack of maturity, two parallel waveguides forming a bundle are used in Figure 3-11. Note that footprint and weight penalties are important so that the polarization approach is still a relevant one in the long-term.

3.3.2. Interconnects Challenges

As illustrated in Figure 3-11, interconnects play a central role in plastic waveguide systems. It is thus the purpose of this section to clarify their composition and discuss their associated challenges. Such a connector is proposed in Figure 3-12 using an intermediate WR-12 metallic waveguide section. Although it is not optimized, this latter essentially provides a standard to characterize the overall transition. In Figure 3-12 (b), a low-loss coupler design is presented based on a WR-12 waveguide and a conventional horn antenna, as recalled from Chapter 2. According to simulation results, its useful bandwidth may actually exceed the nominal WR-12 one (60 – 90 GHz). A range from 55 to 95 GHz is thus considered here. Nevertheless, the transition between a WR-12 metallic waveguide and a PCB transmission line (Figure 3-12 (a)) should be investigated as well, particularly in terms of bandwidth and insertion loss. In-band group-delay variations should also be studied for signal integrity purpose.

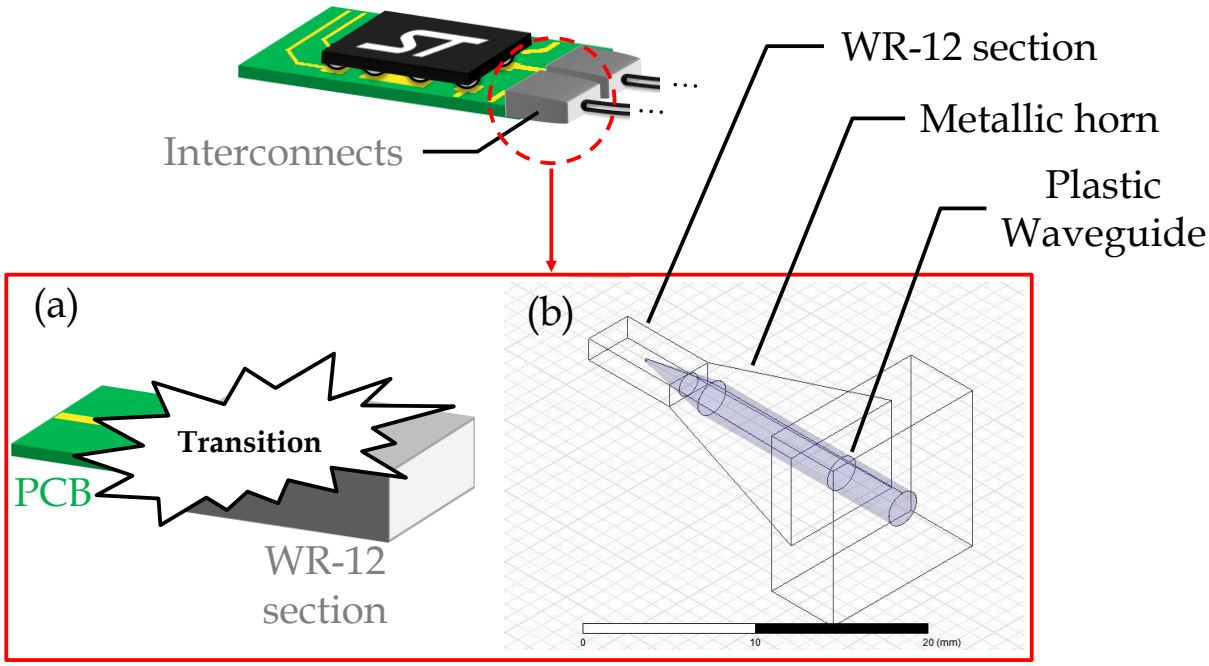

Figure 3-12: Proposed PCB to plastic waveguide connector composed of a large-band PCB to WR-12 transition (a) and a WR-12 to plastic waveguide transition (b). This latter is taken from Chapter 2.

In the following, metallic waveguides to PCB transitions are discussed. In the state of the art, such transitions can be classified in three main categories [**Voineau, 2017**]. The most popular one makes use of one or several resonators, usually implemented as patches (Figure 3-13 (a)). This family have been extensively investigated in [**Villegas, 1999**] [**Artemenko, 2011**] [**Fakharzadeh, 2015**] or [**Zhang, 2016**] among others. These designs typically exhibit low insertion losses (< 1 dB) and are usually very compact. Their resonant nature is still an issue when addressing large bandwidths so that none of the published designs in that category successfully covered the full E-band. Introducing an additional patch (Figure 3-13 (b)) is likely to broaden the bandwidth marginally, like in [**Zhang, 2016**], where reflection parameters are

lower than –10 dB from 70 to 87 GHz. This intrinsic limitation unfortunately comes with a detrimental group-delay behavior although this important metric is seldom reported in the literature.

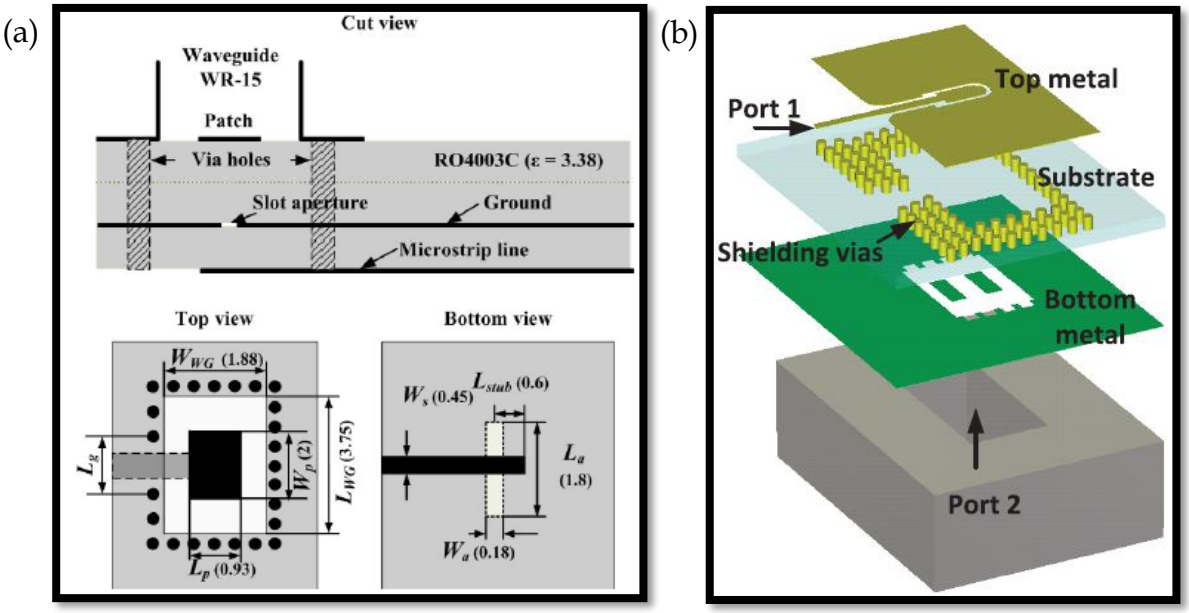

*Figure 3-13: Typical examples of patch-coupled PCB to waveguide transitions. (a) Slot aperture coupling as proposed in [**Artemenko, 2011**] and (b) double patch resonance reproduced from [**Zhang, 2016**].*

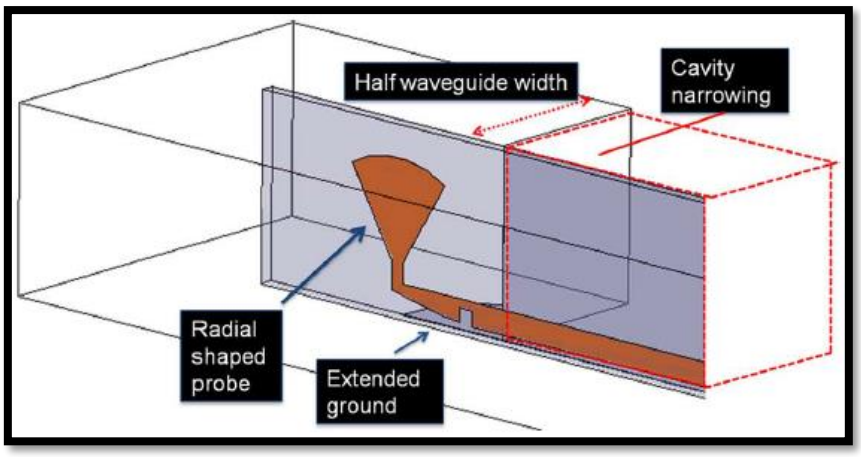

*Figure 3-14: Probe-coupled PCB to waveguide transition. The probe is placed at an appropriate distance from a "back-short" metallic wall to radiate inside the waveguide in the other direction. Illustration taken from [**Lou, 2008**].*

The second category similarly relies on a resonant process. As illustrated in Figure 3-14, a planar probe is introduced inside the waveguide at a particular distance from a "back-short" metallic wall. Although the concept can be successfully scaled up to 700 GHz [**Hurm, 2012**] as visible in Figure 3-15, it is also prone to be sensitive to manufacturing and positioning tolerances. As regards the bandwidth performance, achievable values are in the range of 30 – 40 % fractional bandwidth. It is much better than the first category while still being insufficient to cover the extended E-band. Moreover, resonating group delay characteristics in these structures is detrimental although it is also seldom reported.

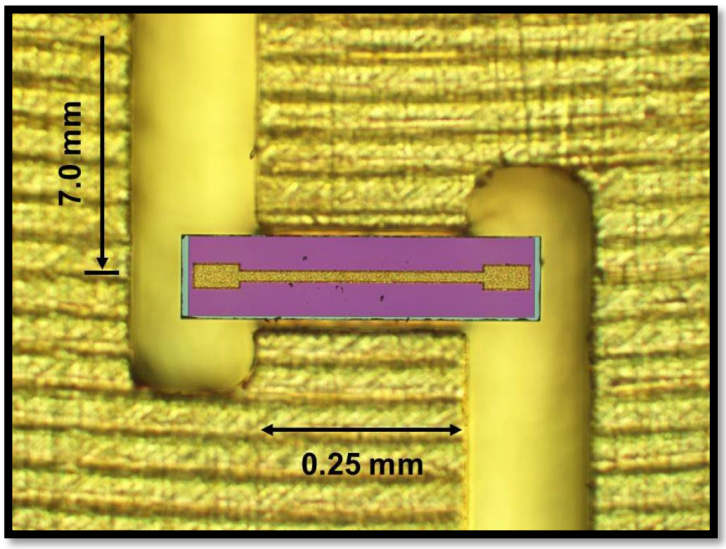

*Figure 3-15: GaAs chip to WR-1.5 waveguide transitions (back-to-back). The transition operates from 500 to 725 GHz [**Hurm, 2012**].*

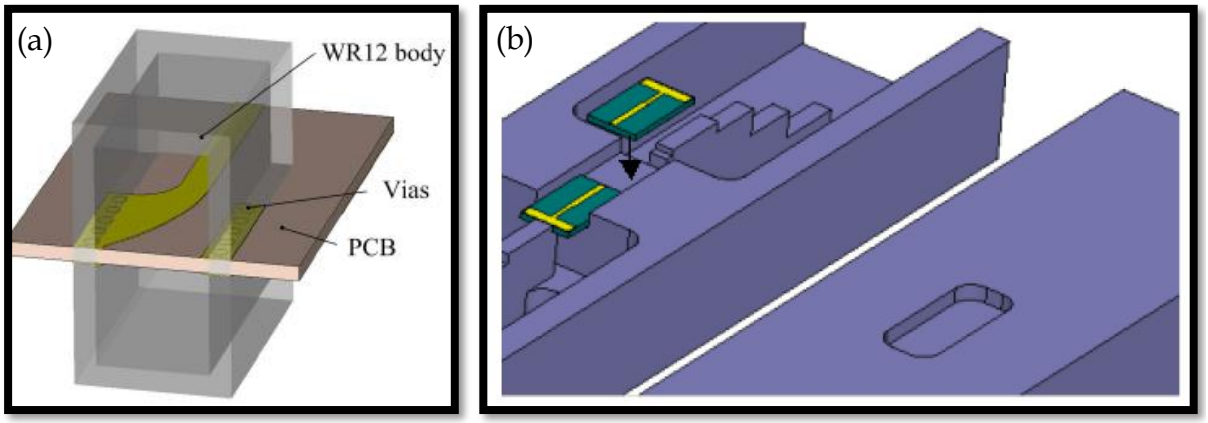

*Figure 3-16: Smooth PCB to waveguide transitions. (a) An antipodal fin-line design taken from [**Mozharovskiy, 2013**] and (b) a tapered-ridge waveguide design from [**Han, 2012**].*

Unlike the first and second transitions topologies, the last one gathers smooth impedance and fields matching transitions. The most popular designs in that category use fin-lines to realize a 90° E-field rotation at the center of the waveguide to match it with a microstrip line. This transition is illustrated in Figure 3-16 (a). At the expense of relaxed compactness, wideband operation is made possible. In [**Chuang, 2012**], a 5 GHz bandwidth from 8 GHz to 13 GHz is shown, largely exceeding the standard X-band (8.2 – 12.4 GHz). Moreover, return losses better than 15 dB are obtained. However, scaling these interesting properties at mmW is not so simple. Since waveguide dimensions drastically shrink faster with frequency than microstrip dimensions, the fin-line aperture gets narrower and narrower as targeted frequencies increase. Because the transition is more aggressive at longer wavelengths, a low-band limitation may appear. An illustration of this constraint can be found in [**Mozharovskiy, 2013**] where the tapered antipodal fin-line structure demonstrates a 66 – 90 GHz bandwidth.

Finally, it should be noted that an alternative concept based on ridged tapers is shown in [**Han, 2012**] covering the V-band (50 – 75 GHz), even though the reported design obviously suffers from manufacturability and positioning issues (Figure 3-16 (b)). Nevertheless, the *inline* line up is attractive. Besides, the use of ridges is twofold. First, they enable impedance matching from the 50 Ω microstrip line to the high-impedance waveguide. By concentrating

the power at the center of the waveguide, they also realize field matching, which is highly desirable due to very different heights between the PCB and the waveguide.

In spite of the aforementioned limitations, these results suggest that smooth impedance transitions are promising for wide bandwidth performance. Acceptable insertion loss in the order of 1 – 2 dB and non-resonating group-delay characteristics are expected.

3.3.3. Broadband Microstrip Line to Waveguide Transition

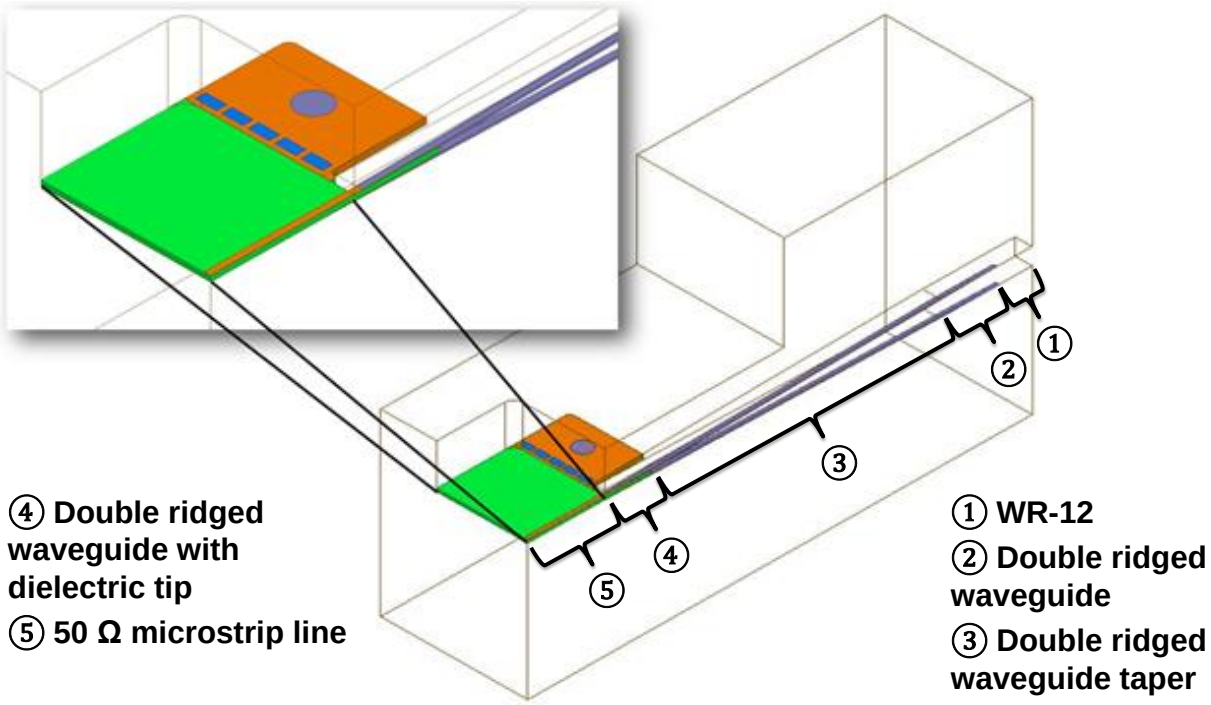

Figure 3-17: Isometric split-view of the proposed microstrip to WR-12 transition composed of a (green) PCB housed in a (transparent) metal case with (colored) double ridges. Inset view: zoom on the PCB region showing the dielectric tip.

Leveraging on the conclusions of previous sections, an innovative broadband transition targeting extended E band (from 55 to 95 GHz) is proposed in this work [**Voineau, 2017**]. Because this object is actually the halve of a transition from the PCB to the plastic waveguide, return losses better than 15 dB in the whole bandwidth are desired so that the global transition may not be limited.

As presented in Figure 3-17, the proposed transition is made of a PCB housed in a metal case that contains the WR-12 waveguide. The latter is composed of top and bottom parts shown in Figure 3-18. Dimensions are given in Table 3-3. From the WR-12 port visible at the right of Figure 3-17 and Figure 3-18, both parts contain a WR-12 section equally split between the parts (region 1), a WR-12 section with increasing double ridges (region 2) and a constant double ridged WR-12 section with tapered height (region 3). Top and bottom ridge width *s* is kept constant all along the transition. Note that only the bottom part ridge extends under the microstrip line access, thus making the structure slightly asymmetrical (Figure 3-20).

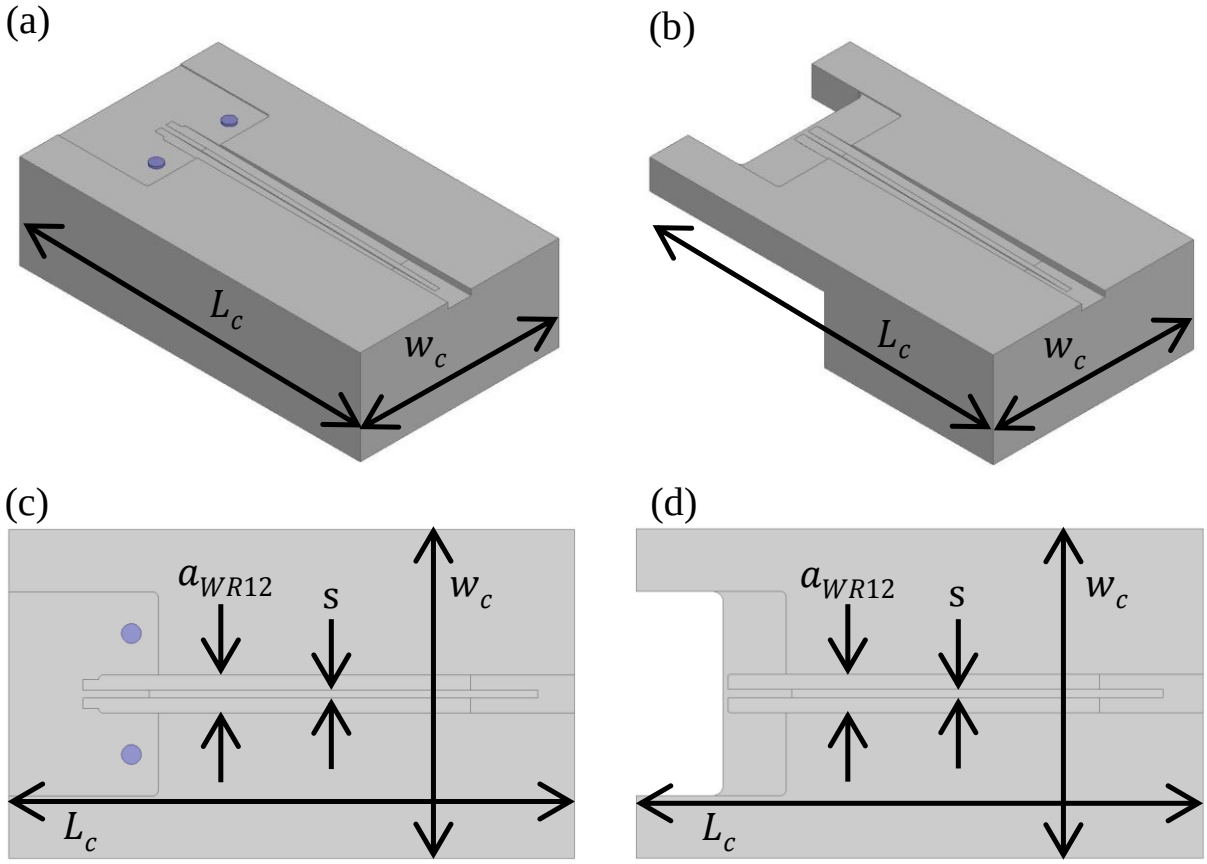

Figure 3-18: Different views of the proposed metal case made of top and bottom parts: (a) isometric view of bottom part, (b) isometric view of top part, (c) top view of bottom part, (d) top view of top part.

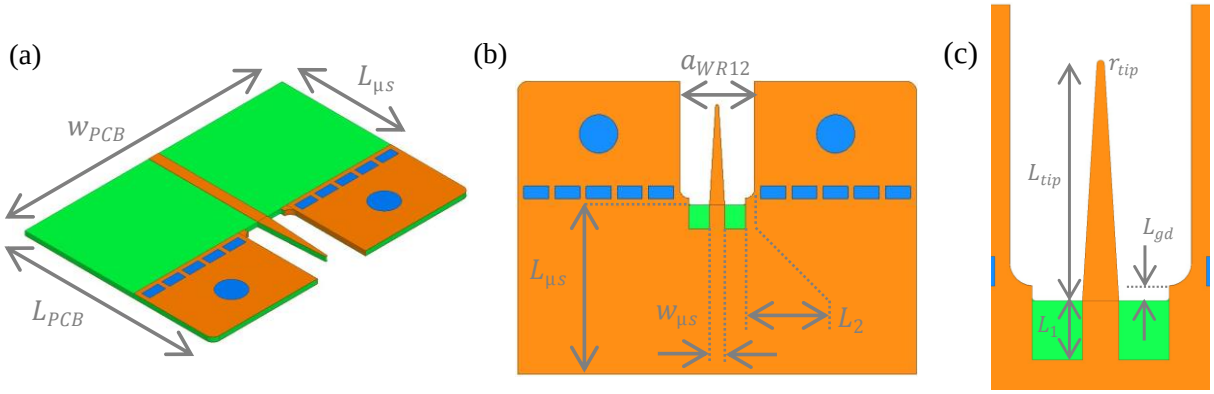

Figure 3-19: Different views of the proposed PCB showing bare dielectric areas (green), copper coated areas (orange) and metallized through vias (blue): (a) top isometric view, (b) bottom view, (c) zoom on bottom view.

A 254 µm-thick Rogers 6002 with ½ oz. (18 µm) copper conductors' thickness was chosen for the PCB implementation. Detailed views are given in Figure 3-19 with dimensions summarized in Table 3-3. From Figure 3-17 and Figure 3-19, it is clearly visible that a dielectric tip is machined in the PCB to be positioned at the center of the double ridged waveguide (region 4), thus ensuring mechanical stability and fields matching. Such a dielectric tip, as presented in [**Belenguer, 2014**], is preferred to avoid TE_{20} second mode excitation in the transition [**Parment, 2015**]. The end of the tip is rounded to account for the laser machining process tolerances (r_{tip}). Note that vertical sidewalls of the tip are not metallized while opposite sidewalls metallization is required to ensure TE_{10} mode propagation. Consequently, a guard distance L_{gd} between metallized / non-metallized sidewalls is added to maintain compatibility with standard manufacturing processes.

a_{WR12}	b_{WR12}	h_r	$L_{\mu s}$	L_1	L_2	L_{3_bottom}	L_{3_top}	L_c	L_{gd}
3.10	1.55	0.1	6.99	1.02	0.38	31.37	30.35	45.72	0.25
L_{PCB}	L_{tip}	L_{WR12}	r_{tip}	s	t_{PCB}	$w_{\mu s}$	w_c	w_{PCB}	--
12.06	4.11	8.38	0.05	0.64	0.29	0.61	26.67	16.51	--

Table 3-3: Summary of dimensions [in millimeters] for the proposed microstrip line to waveguide transition.

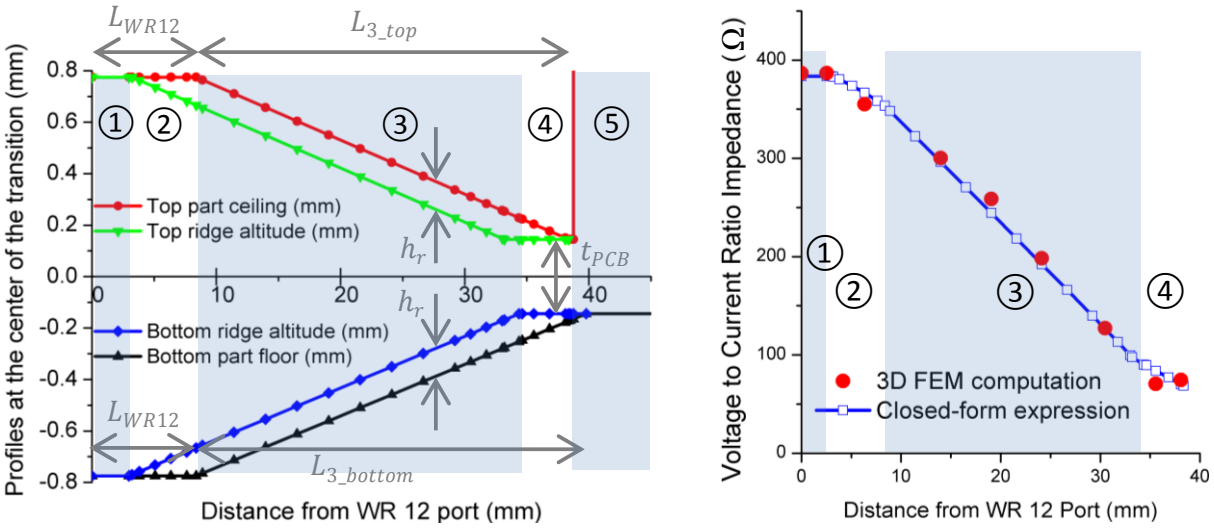

Figure 3-20: On the left, profiles in the metal housing for top (positive values) and bottom (negative values) parts are presented. On the right, the impedance is simulated at 75 GHz along the section and it is compared with theoretical results.

The impedance is approximated in the middle of the double-ridged section based on the theory developed in **[Hoefer, 1982]**. As impedance is ambiguous, the same voltage-to-current ratio definition is also applied here. The relative change in capacitance should be modified to account for partial dielectric loading at a given point of the transition as follows in Equation (3-10). In this equation, a is the waveguide width, b is the waveguide height, s is the ridge width, d is the distance between ridges, w_{diel} is the dielectric material width and ε_r is the material relative dielectric permittivity.

Relative change in capacitance

$$\frac{\Delta C}{C} = \left[\frac{(\varepsilon_r - 1)w_{diel}}{d} + \frac{s}{d}\right]\frac{2b}{a-s} \tag{3-10}$$

Finally, the modified cutoff wavelength λ_c^{diel} is derived in Equation (3-11) to determine the impedance **[Hoefer, 1982]**.

$$\frac{b}{\lambda_c^{diel}} = \frac{b}{2(a-s)}\left[1 + \frac{4}{\pi}\left(1 + 0.2\sqrt{\frac{b}{a-s}}\right)\frac{b}{a-s}\ln\csc\frac{\pi}{2}\frac{d}{b} + \left(2.45 + 0.2\frac{s}{a}\right)\frac{\Delta C}{2C}\right]^{-1/2} \tag{3-11}$$

Figure 3-20 (right) presents the resulting impedance along the transition at the center band frequency of 75 GHz and shows good agreement with 3D FEM simulation. Even if most of impedance transformation actually occurs in the tapered ridged waveguide section (region 3),

the partially loaded section (region 4) further helps in continuously matching the high WR-12 impedance to the low microstrip one.

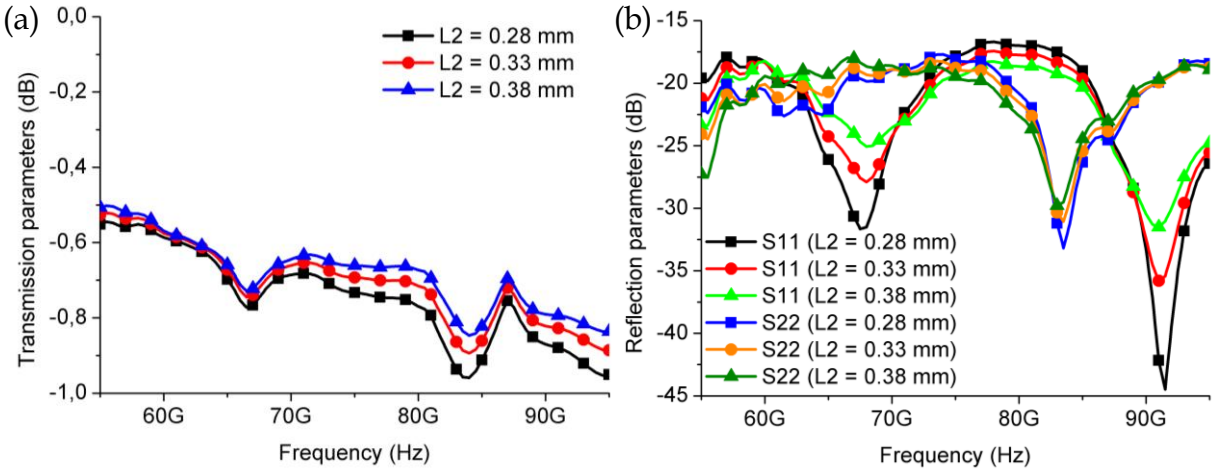

Figure 3-21: Simulated impact on S-parameters of an over-etching on L_2 design variable. (a) Transmission and (b) reflection parameters. Port 1 and port 2 correspond to the microstrip line and WR-12 waveguide respectively.

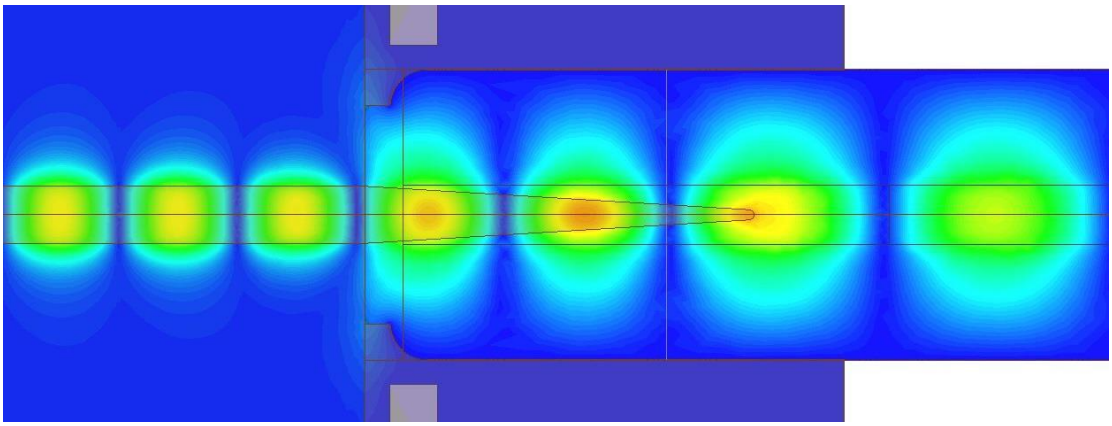

Figure 3-22: E-field magnitude simulated at 75 GHz around the dielectric tip confirming TE_{10} operation only.

In the design, the length L_2 is responsible for a "back-short effect" that was carefully optimized by means of 3D FEM simulations. However, as laser manufacturing is prone to over-etching, the impact of a shorter L_2 has also been investigated in Figure 3-21. A usual tolerance of 100 µm was found to have no significant impact on S-parameters, confirming robust behavior. For L_2 nominal value, simulated insertion loss is between 0.5 – 0.84 dB (Figure 3-21 (a)) while reflection loss is at least 18 dB and is kept below 20 dB in most of the targeted 55 - 95 GHz band (Figure 3-21 (b)). Moreover, the E-field magnitude computed at 75 GHz confirms that only TE_{10} propagation occurs in the transition (Figure 3-22) thanks to the cumulative effects of the dielectric tip and the ridges that all contribute in concentrating the energy at the center of the section.

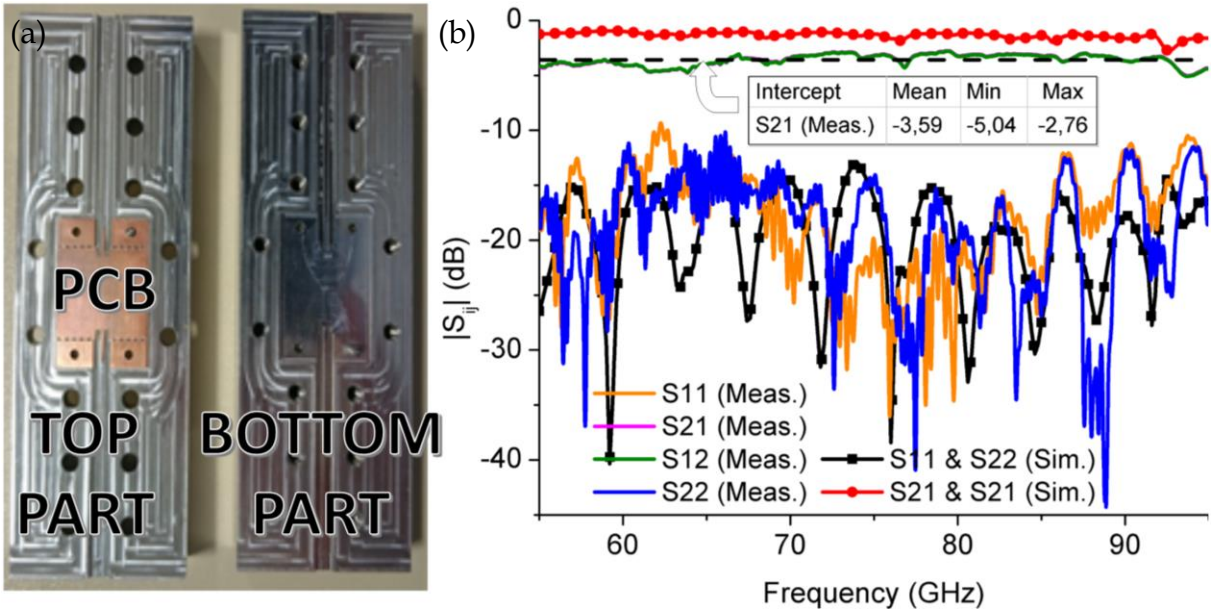

Figure 3-23: Back-to-back transitions: (a) fabricated prototype with PCB ground plane visible, and (b) measured and simulated S-parameters.

For measurement purposes, the VNA was calibrated from 55 to 67 GHz and from 67 to 95 GHz with mmW extenders to confirm that the concept operates beyond the E-band. Figure 3-23 (a) shows the photo of the fabricated back-to-back transitions while simulated and measured S-parameters are presented in Figure 3-23 (b). The minimum and maximum insertion loss are respectively 2.76 dB and 5.04 dB. Average insertion loss is 3.59 dB leading to 1.8 dB for a single transition, which includes a 7 mm-long microstrip line. Return losses exceed 10 dB in the band, with good agreement with simulation results. Note that, in spite of a symmetrical back-to-back configuration, measured reflection parameters are slightly different. This is likely due to mechanical tolerances in the PCB and case manufacturing. These latter were actually confirmed by microscope and profilometer measurements. In addition with roughness and frequency dependence of dielectric properties (not taken into account in the simulation), they could also explain higher than expected insertion loss.

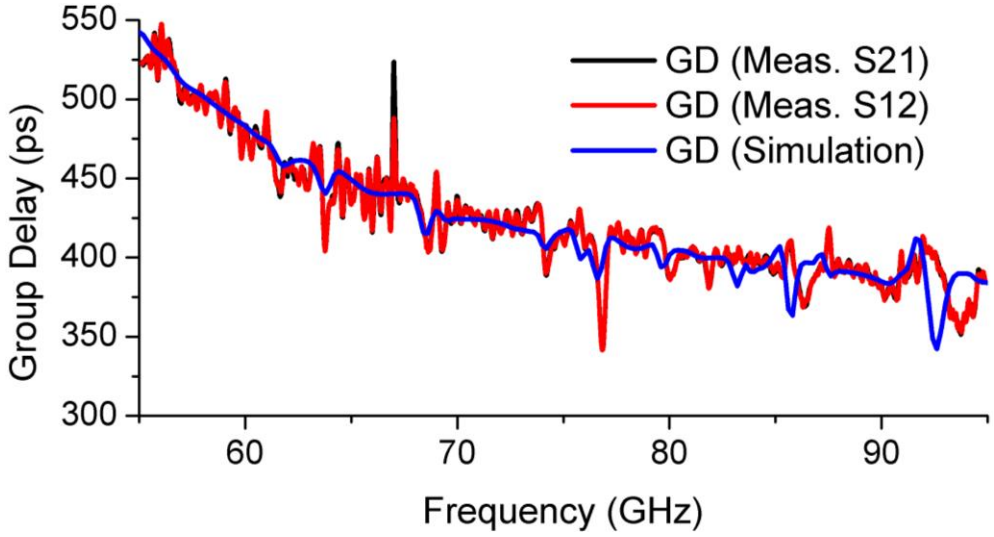

Figure 3-24: Measured and simulated group delays of back-to-back transitions.

To complete the investigation, group delay measurement was also performed in order to highlight further the wideband operation (Figure 3-24). A very good agreement with simulation is observed. As expected, the designed transition leads to a slowly varying group

delay that is far more desirable than resonant characteristics for wideband applications. Note that the major deviation observed at 67 GHz is actually a measurement artifact. In fact, mmW extenders take over above 67 GHz is responsible for a significant phase discontinuity that is difficult to calibrate in practice.

3.3.4. Comparison with the State of the Art

In section 3.3.3, a 55 to 95 GHz microstrip line to WR-12 transition based on a dielectric tip and a tapered double-ridged waveguide intermediate section is proposed to realize smooth impedance matching. According to Table 3-4, this innovative transition concept achieves the widest bandwidth ever reported around 75 GHz (center of the E-band) resulting in more than 50 % fractional bandwidth. A back-to-back transition was fabricated and measured to confirm the wideband operation with moderate average insertion loss (1.8 dB) as well as non-resonant group delay characteristics. Despite the importance of this metric for high-data rate communications, a simulation vs. measurement comparison is reported for the first time. Beyond the context of this study, the proposed concept could easily comply with double or single ridged waveguide standards.

	[**Artemenko, 2011**]	[**Mozharov-skiy, 2013**]	[**Fakhar-zadeh, 2015**]	[**Zhang, 2016**]	This work [**Voineau, 2017**]
Topology	Coupled patch reson.	Fin-line	Coupled patch reson.	Coupled patch reson. (x2)	**Double ridge & dielectric tip**
$S_{xx} < -15$ dB (simulated)	55 – 64 GHz [15 %]	68 – 90 GHz [28 %]	59 – 67 GHz [13%]	71 – 86 GHz [19 %]	**55 – 95 GHz [53 %]**
S_{xy} (simulated)	0.4 – 0.8 dB	0.4 – 0.6 dB	< 0.2 dB	< 0.5 dB	**0.5 – 0.9 dB**
S_{xy} (measured)	≈ 1.8 dB	0.9 – 1.5 dB	0.4 – 0.8 dB	1.3 dB @ 77 GHz	**1.4 – 2.5 dB**
Microstrip line length	15 mm	5 mm	N.A. (CPW)	10 mm (on alumina)	**7 mm**

Table 3-4: State of the art comparison of PCB transmission lines to waveguide transitions.

3.4. Link Budget Analysis

In Figure 3-25, the link budget of the system is presented. For the sack of simplicity, attenuation in the (plastic waveguide) channel is supposed to be constant. Based on the simulation results presented in Chapter 2, a value of 2 dB/m is assumed here, although we have already shown that attenuation increases with frequency. Additionally, the practical consequences of limited confinement, especially for long waveguides, are likely to induce large losses at low frequencies depending on environmental conditions, bending, etc.

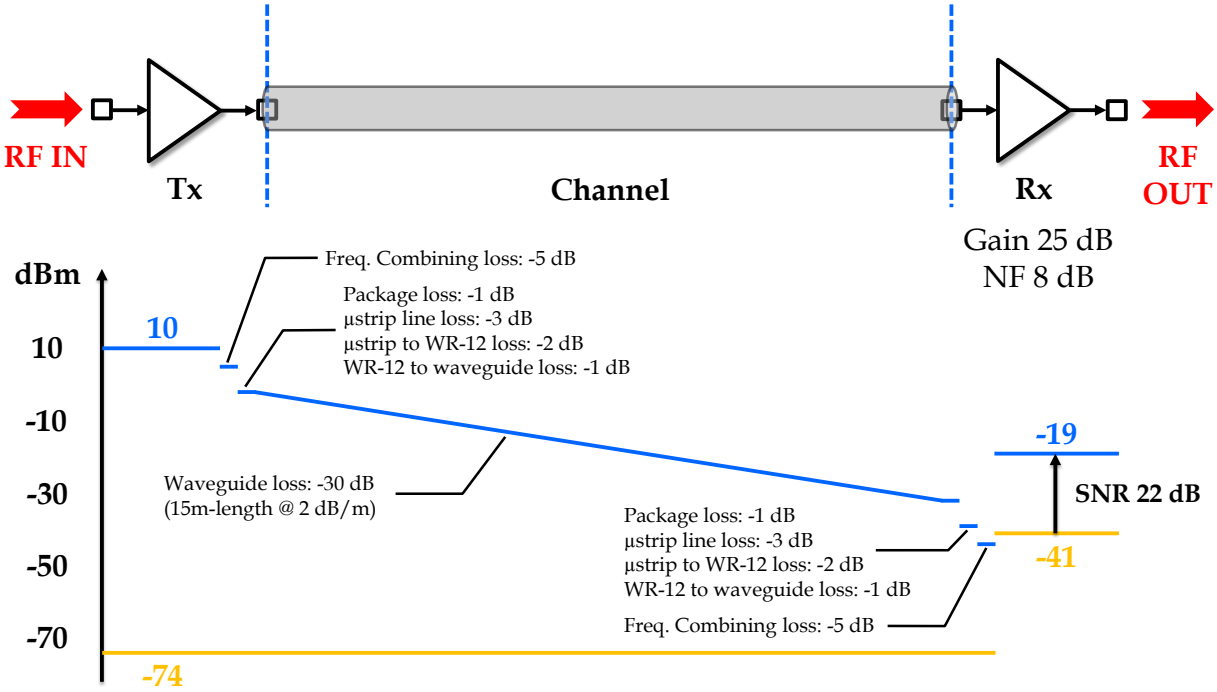

Figure 3-25: Link budget of the proposed system exhibiting a SNR of 22 dB.

Regarding the Tx power, 10 dBm is considered in the PA output plane. However, combining two frequency bands on-chip is costly and results in a 5 dB loss (justified in Chapter 4). Moreover, the RF path up to the plastic waveguide is likely to create roughly a 7 dB additional insertion loss. Symmetrical losses are also expected at the Rx side. Note that global interconnects loss is 24 dB which is comparable to the waveguide loss budget (30 dB).

At the Rx input, the noise power spectral density is given by Equation (3-12). Assuming a 10 GHz bandwidth, the noise power is then derived from Equation (3-13). Finally, the Rx output noise is computed in equation (3-14). This system leads to a SNR of 22 dB, exceeding the minimum 13.93 dB required for QPSK demodulation at BER < 10^{-12} (Appendix D). The link margin is then around 8 dB.

Noise Power Spectral Density

$$N_0 = k_B T \approx -174 \text{ dBm/Hz} \tag{3-12}$$

Noise Power

$$N = BN_0 \approx -74 \text{ dBm} \tag{3-13}$$

Output Noise Power

$$N_{Rx} = N + G_{Rx} + NF_{Rx} \approx -74 + 25 + 8 = -41 \text{ dBm} \tag{3-14}$$

The above reasoning is useful to derive the maximum link length. This limit is the consequence of limited or constrained available energy in the system. It is illustrated in Figure 3-26 (data rate versus length plot) by a vertical green line. In this graph, a data rate boundary is also visible in blue, which results from bandwidth limitations at channel (plastic waveguide) and circuit levels. In fact, whatever the considered length, limited bandwidth clamps the maximum achievable data rate. Another limitation may finally be caused by intramodal dispersion, a phenomenon that is also known as chromatic dispersion in optics. As presented in Chapter 2, this phenomenon is responsible for frequency-dependent Group Delay Per Unit Length (GDPUL) within the channel, potentially causing significant signal distortions like pulse broadening and ultimately symbol errors.

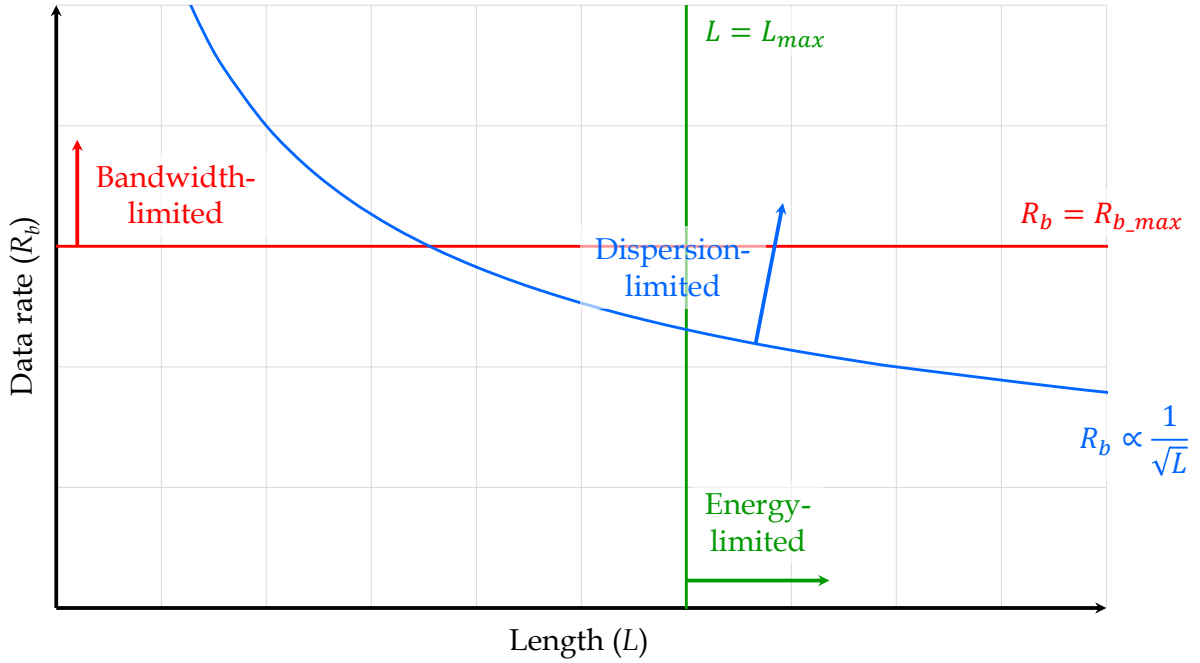

Figure 3-26: Illustration of data rate and length limitations potentially encountered in plastic waveguide systems.

As a first-order approximation, one can consider that GDPUL dispersion evolves linearly as a function of the required bandwidth B (Equation (3-15)). Therefore, the group delay dispersion is expressed in Equation (3-16) for a given length L. This quantity should be limited to avoid the detrimental effects evocated previously. A symbol period duration is proposed as an approximate limit in Equation (3-17) although this arbitrary bound should be consolidated with further system-level simulations. Combining Equations (3-17) and (3-18), the dispersion-limited regime is derived in Equation (3-19) where η is the spectral efficiency of the considered modulation. The noticeable inversed square root length-dependency of this regime is illustrated in Figure 3-26 (blue curve). As expected, Equation (3-19) indicates that this regime may be avoided by considering low-dispersion waveguides, but also high-order modulation schemes.

GDPUL dispersion

$$\Delta GDPUL = \frac{\Delta\tau_u}{\Delta f} B \tag{3-15}$$

GD dispersion

$$\Delta GD = \frac{\Delta\tau_u}{\Delta f} B\, L \tag{3-16}$$

$$\Delta GD < T_s = \frac{1}{R_s} \tag{3-17}$$

$$R_b = \eta\, R_s = \eta\, B \tag{3-18}$$

Dispersion-limited regime

$$R_b > \frac{\eta}{\sqrt{\frac{\Delta\tau_u}{\Delta f} L}} \tag{3-19}$$

Even though the above-mentioned limitations should be fully taken into taken at system-level depending on requirements, it is still worth noting that none of them is specific to plastic waveguide systems. Similar limits are actually found in optic systems as well, and system portioning is realized accordingly.

3.5. Analysis of Millimeter-wave QPSK Modulators and Demodulators

Considering QPSK modulators first, two approaches may be followed to realize such a function. The most typical one rely on mixers, e.g. Gilbert cells, which perform algebraic multiplication of the baseband data with the RF carrier. Note that such a modulator architecture is not particular to QPSK, but is actually suitable for any type of QAM although linearity constraints on the mixer may be drastically higher. With the same limitations in mind, it is also compatible with pulse-shaped data. Although this clever design topology is popular and poses no major problem, a simpler passive architecture may still be used for the specific purpose of QPSK operation. In fact, the combination of two BPSK signals in quadrature with respect to each other results in a QPSK signal. Furthermore, as BPSK can be easily implemented in the context of pseudo-differential circuits in a phase-reversal manner, the overall function may be realized both simply and power-efficiently. Therefore, it appears that practical realizations of QPSK modulators exhibit moderate complexity with acceptable performance. Note that silicon implementation of the latter approach based on quadrature BPSK combination is presented in Chapter 4 along with validation measurements.

On the other hand, the increased complexity of the QPSK compared to OOK is particularly significant at the receiver side. Although OOK coherent demodulation (Figure 3-6) is possible, well-known non-coherent implementations are usually preferred thus avoiding complex and power-consuming carrier recovery circuits and/or PLL. In fact, whatever the modulation scheme, the issue is the availability of a Tx carrier replica in the Rx circuit. In order to demodulate properly, this replica should oscillate at exactly the same frequency at any time. Not only the average oscillating frequencies should be equal but Tx carrier synthesis imperfections should be mimicked as well, including instantaneous phase noise, phase or frequency drifts induced by PVT variations, etc. Note that this practical difficulty is frequently alleviated in most publications [**Carpenter, 2016**] [**Tokgoz, 2016**] [**Tokgoz, 2018**] thanks to shared local oscillator (LO) although it is definitely not a case of practical interest.

Like OOK, QPSK may also be demodulated in a non-coherent fashion. It is the objective of section 3.5 to compare QPSK demodulation techniques and highlight their principal limitations.

3.5.1. Canonical Demodulation of *M*-ary PSK Constellations

As a first approximation, QSPK is a special case of *M*-ary PSK where *M* equals four as illustrated in Figure 3-27. For any integer *M*, it appears that the signal raised to the power of *M* is data independent and contains the M^{th} carrier harmonic. This result clearly suggests that it is possible to recover the carrier simply by multiplying *M* copies of the modulated signal and using appropriate frequency division by *M*.

Although the complexity increases significantly for large *M* values, this techniques is especially simple for QPSK (*M* = 4) because the signal should only be doubled two times, and then frequency-divided by four. The low block count is therefore attractive.

However, circuits operating at four times the carrier frequency still represent a technological challenge. In fact, even the most advanced CMOS processes, such as 28 nm CMOS FD-SOI presented in Chapter 4, only offer $f_{max} \approx$ 300 GHz, which theoretically sets a

maximum recoverable carrier frequency at $^{300}/_{4} \approx 75$ GHz. This value is likely to be an upper bound as practical design constraints make it difficult to operate at frequencies close to f_{max}. Nevertheless, future technological progress may one day make this technique suitable to demodulate targeted E-band frequencies.

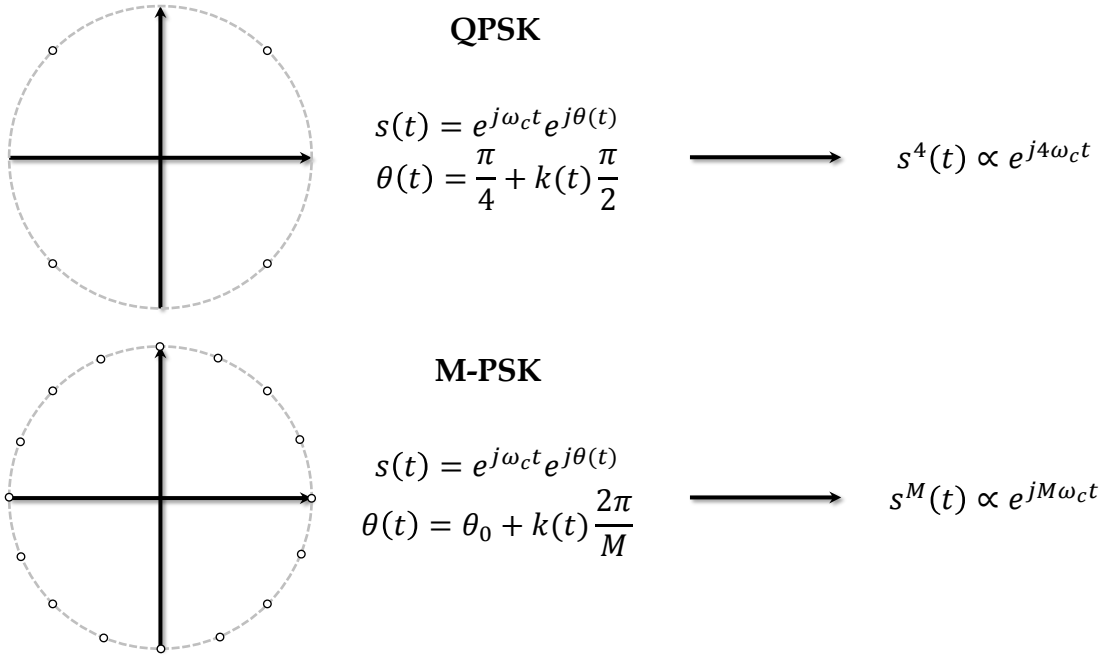

Figure 3-27: Constellations of QPSK and M-ary PSK and associated invariants.

3.5.2. D-QPSK Demodulation Using Time-Delay Comparison

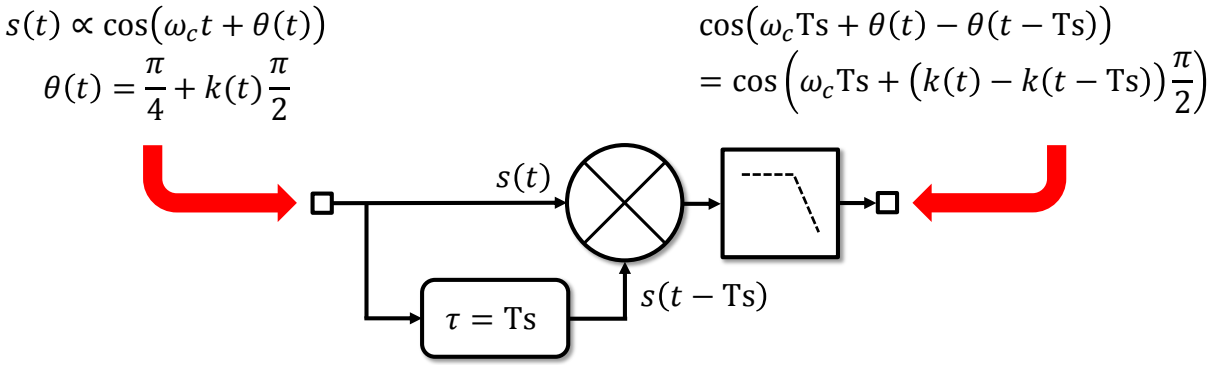

Figure 3-28: Conceptual schematic of D-QPSK non-coherent demodulation based on time delay.

Differential QPSK (D-QPSK) is a slightly modified form of QPSK in which the data are encoded at symbol transitions, instead of symbol phases. In other words, absolute symbol phases are no longer meaningful, only symbol phase changes contain data. This minor modification thus affects both Tx and Rx circuits. For the latter, each demodulated symbol is to be compared to its predecessor in a recursive way. Note that D-QPSK can be implemented relying on coherent demodulation without any particular benefits.

A non-coherent technique is still possible and has the advantage of theoretically much reduced complexity. While symbol phases are compared in the Rx baseband domain in a coherent demodulator, they are compared in the Rx bandpass (RF) domain in a non-coherent

one. This concept is illustrated in Figure 3-28. It is noticeable that a one-symbol delayed replica of the modulated signal is necessary to provide the carrier reference and perform phase change tracking continuously. Consequently, the practical difficulty of this demodulation scheme is the creation of a time-delay in the RF path. In [**Takahashi, 2010**], D-QPSK is successfully applied at 120 GHz and it is recalled that a long transmission line effectively acts as an accurate delay circuit. However, generating time delays in the order of a few hundreds of picoseconds (for multi-gigabits signaling) actually requires incredibly long lines of a few tens of millimeters… In addition to impractical area consumption, such lines would induce a very large insertion loss that should be compensated by amplification means. In [**Takahashi, 2010**], a transmission line with periodic shunt capacitor loads is proposed to reduce line length down to 10 mm for a 200 ps time delay. In spite of a 2.5x length reduction, simulated insertion loss of the modified line still reaches 18 dB.

Finally, another limitation of D-QPSK non-coherent demodulation is related to data rate flexibility. Because the time delay directly equals the symbol time, the system can only demodulate at a fixed symbol rate. Operating in a given data rate range would actually require continuous tuning of the delay introduced in the circuit. This feature is obviously not accessible, particularly if the delay is implemented with transmission lines.

3.5.3. Carrier and Data Recovery with a Costas Loop

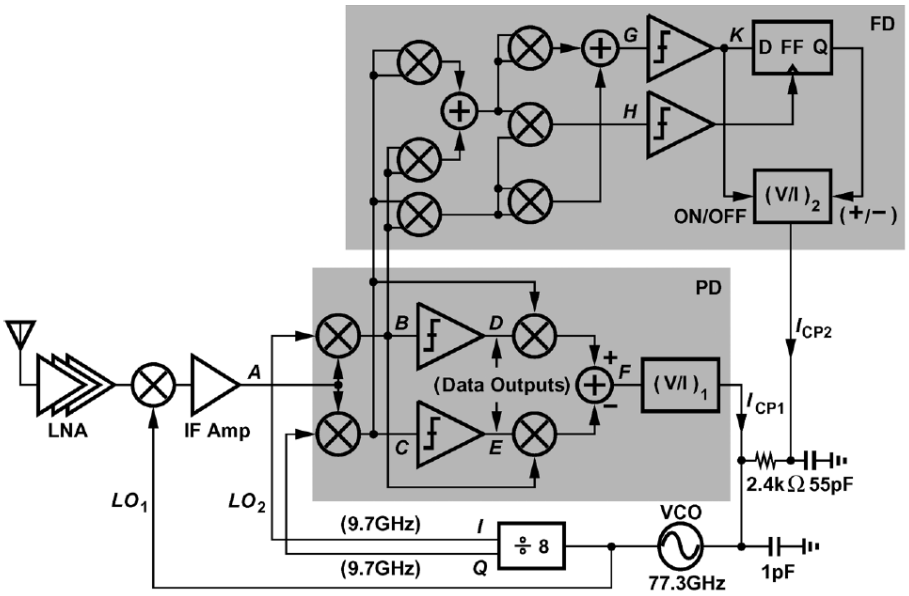

*Figure 3-29: Illustration taken from [**Huang, 2011**] of a mmW Costas Loop QPSK demodulator, containing a frequency locking loop (FD) and a phase locking loop (PD).*

The Costas loop is a carrier recovery circuit capable of both frequency and phase locking. Interestingly, when a phase-modulated RF signal is applied at its input, the phase variations imposed by the data are tracked so that monitoring the phase errors in the loop actually gives a direct access to demodulated data. Although this technique is more common at lower frequencies, a mmW implementation of the Costas Loop is proposed in [**Huang, 2011**] to address W-band communications (Figure 3-29).

Although the Costas loop architecture is clever, the implementation suffers from high block count causing large chip area and high power consumption. In [**Huang, 2011**], the latter

is mitigated by operating at a 9.7 GHz intermediate frequency at the expense of lower available bandwidth. The resulting maximum data rate is then limited to only a few Gb/s. In addition, the recovery mechanism is sensitive to identical consecutive symbols patterns (later referred to as ICSP) as reported in Figure 3-30. Even though data encoding is a well-known and efficient solution for alleviating such issues, it comes with a further effective data rate reduction.

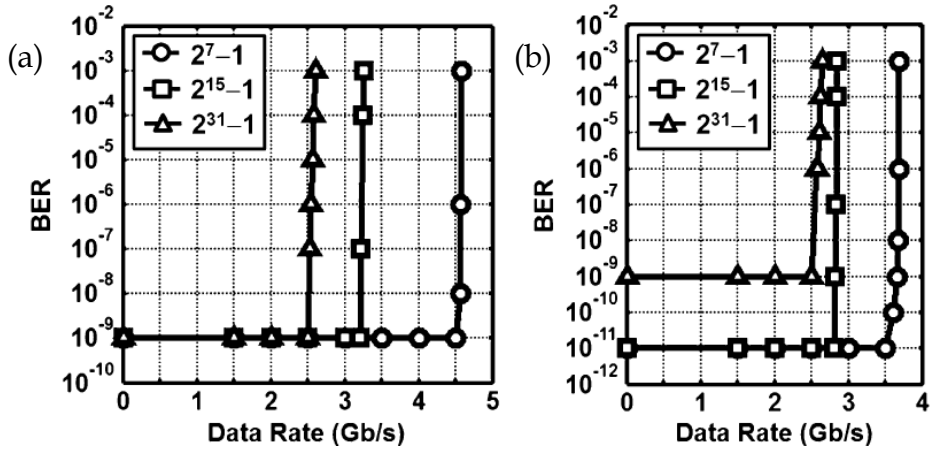

Figure 3-30: Demodulation sensitivity to PRBS length in BPSK (a) and QPSK (b) Costas loops from ***[Huang, 2011]****.*

3.5.4. Limitations Summary of Millimeter-wave QPSK Demodulators

Table 3-5 summarizes the above discussion regarding mmW QPSK demodulators. It is noticeable that no technique currently satisfies all the necessary constraints of a high data rate circuit with moderate area and power consumption. Consequently, an alternative demodulation scheme is proposed in this work, which favorably features high data rate capability with limited complexity to enable low power operation with reduced chip area. This solution is presented in the following section 3.6.

	Advantages ☺	**Disadvantages ☹**	**Remarks**
Frequency Quadrupling	• **Low block count**	• **Operation at 4x $f_{carrier}$**	Not currently feasible in CMOS technologies
Non-coherent D-QPSK	• **Small complexity overhead** • **Low block count**	• **Time delay circuit** • **Fixed data rate**	Transmission-line based delay circuits are too bulky and lossy
Costas Loop	• **Capability to operate at an intermediate frequency**	• **Large block count** • **Sensitivity to ICSP**	Large area and high consumption needed

Table 3-5: Millimeter-wave QPSK demodulation techniques summary.

3.6. ILO Based Demodulation for High-Speed QPSK Systems

This section aims at presenting an innovative phase demodulator technique based on an Injection Lock Oscillator (ILO). Theoretical basics are recalled first so that the underlying demodulation concept can be introduced in the time-domain as well as in the frequency domain. The operation is then illustrated during a one-symbol duration to highlight some limitations. Finally, the architecture is numerically simulated over long bit sequences and performance is discussed.

3.6.1. ILO Theoretical Basics

An ILO is the combination of an oscillator and an injection circuit. In some cases, denoted locking conditions, a particular relation appears between the oscillator phase and the injected signal one. If one considers the injected signal phase as an input and the oscillator phase as an output, the ILO transfer function can be derived in the phase domain. The study of this function dates back to [**Adler, 1946**]. It was primarily dedicated to explain the locking mechanisms observed in LC oscillators. Another derivation was later proposed in [**Razavi, 2003**] in the slightly different context of injection pulling, which brings an additional insightful understanding of this very complex non-linear phenomenon.

Since then, ILO theory has been widely investigated. The unique properties of this block have made it a very interesting component in frequency dividers, frequency multipliers or PLL alternatives due to small power and area requirements [**Dunwell, 2013**]. Moreover, the ILO phase tracking capability enables efficient phase noise translation from the input (reference) injected signal to the output oscillator signal. Consequently, ILO phase noise characteristics are usually very attractive. Note that injected signal frequency may although significantly differs from the output one. In that case, the interaction between input and output signals occurs thanks to harmonic or sub-harmonic coupling. For example, this effect makes it possible to realize high ratio frequency multipliers while still benefiting from the favorable phase noise of the low frequency input signal [**Jany, 2014**].

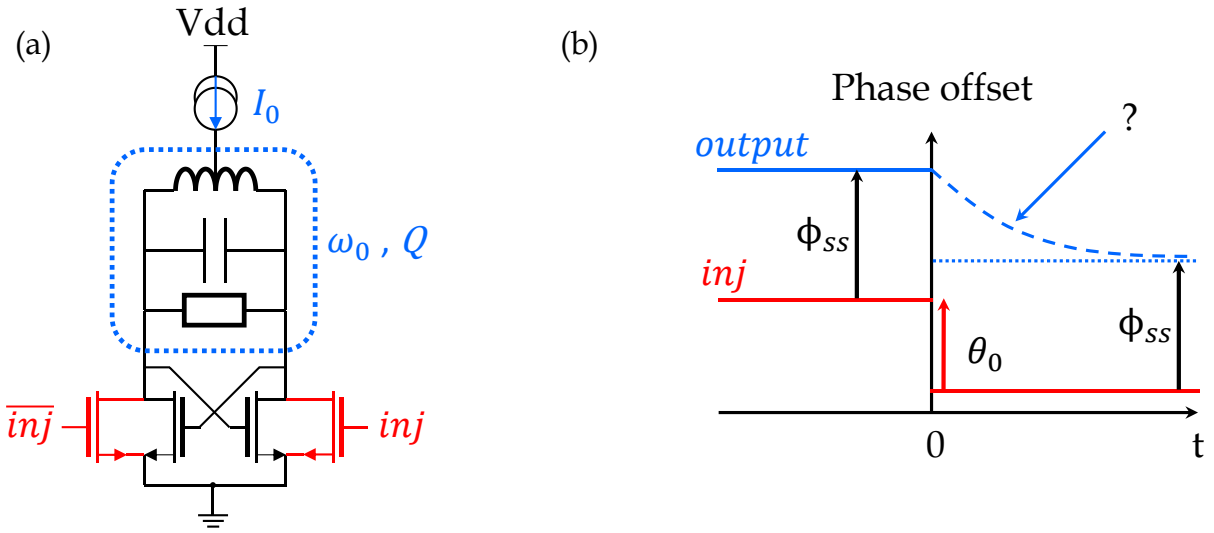

Figure 3-31: ILO schematic made of a LC-tank (a) and time-domain illustration of the phase locking process (b).

In this section, ILO theoretical basics are reviewed to provide comprehensive foundations. However, to focus on the essence of this block, some derivation details are assumed but most of them may be found in [**Adler, 1946**] or [**Razavi, 2003**]. Figure 3-31 recalls the canonical circuit schematic of an ILO and illustrates the injection locking process. Provided that locking conditions are satisfied (derived later), the oscillator is assumed to oscillate at the same frequency as the injected signal (fundamental injection), although a (possibly time-dependent) phase offset φ may exist as defined in Equation (3-22).

Injected signal $$s_{inj} \propto \cos\left(\omega_{inj}t + \theta_{inj}(t)\right) \quad (3\text{-}20)$$

Output signal $$s_{out} \propto \cos\left(\omega_{inj}t + \theta_{out}(t)\right) \quad (3\text{-}21)$$

Phase offset $$\varphi(t) = \theta_{out}(t) - \theta_{inj}(t) \quad (3\text{-}22)$$

As expected from a "locking process", the output phase should follow any phase variation from the input. In other words, if the injected signal experiences a θ_0 phase reduction, the output one should experience a similar θ_0 reduction. However, such a phase change is not instantaneous (contrary to the considered input phase change) and it is actually the purpose of Adler's equation [**Adler, 1946**] to describe this evolution in the time-domain. Therefore, it takes the form of a system of differential equations in Equation (3-23) whose solution is the phase offset φ. Note that such an equation is valid only under the assumptions summarized in Equations (3-25) - (3-27).

Adler's equation $$\begin{cases} \varphi(0) = \varphi_0 \\ \dfrac{d\varphi}{dt} = \left(\omega_0 - \omega_{inj}\right) - \omega_L \sin\left(\varphi(t)\right) \end{cases} \quad (3\text{-}23)$$

Half locking range $$\omega_L = \frac{\omega_0}{2Q}\frac{I_{inj}}{I_0} \quad (3\text{-}24)$$

$$\left|\omega_0 - \omega_{inj}\right| \ll \frac{\omega_0}{Q} \quad (3\text{-}25)$$

$$T' \ll \frac{1}{\omega_0 - \omega_{inj}} \quad (3\text{-}26)$$

$$\frac{I_{inj}}{I_0} \ll 1 \quad (3\text{-}27)$$

The obvious similarity with classical mechanical systems like pendulum inspires a representation in the phase space. From Figure 3-32 (a), it is clear that the system has periodic solutions and admits two steady-state solutions in the range $]-\pi, \pi]$ given by Equations (3-28) and (3-29). However, only ϕ_{ss} is stable according to Figure 3-32 (a). This important result confirms the desired phase locking mechanism since the output phase always tends to recover its initial phase offset with respect to the input. It should be mentioned that Equation (3-28) is only defined for $\left|\frac{\omega_0 - \omega_{inj}}{\omega_L}\right| \leq 1$ which sets the locking range expressed in Equation (3-30).

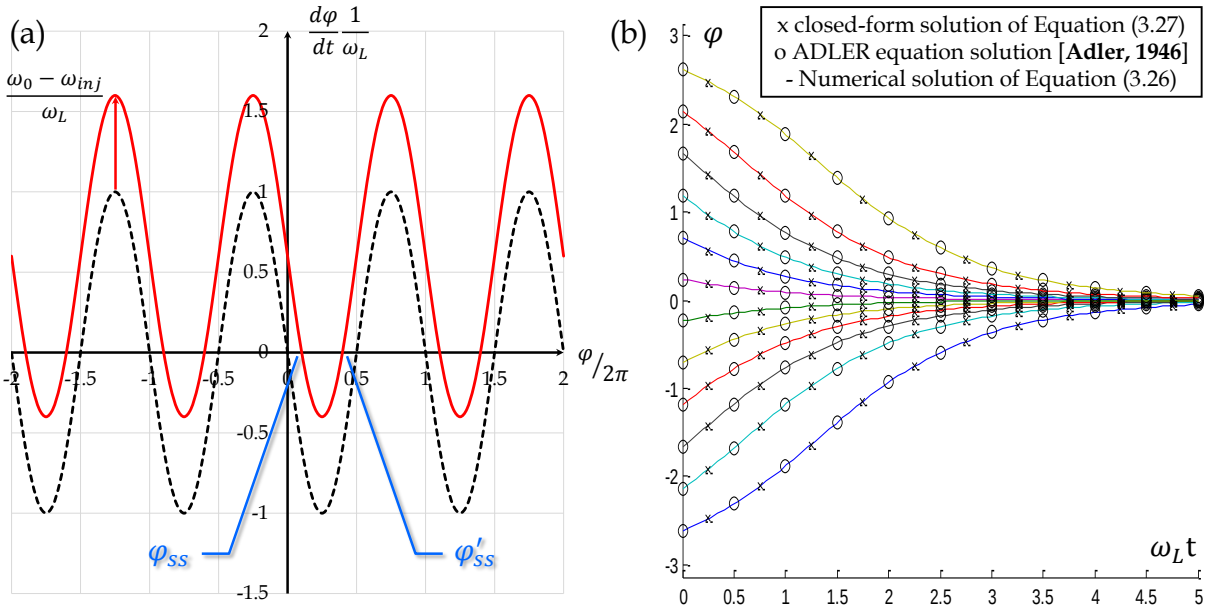

Figure 3-32: Representations of Adler's equation. (a) Phase space and (b) time-domain evolutions (assuming $\phi_{ss} = 0$). In this latter, solutions obtained with different methods are compared showing perfect agreement with each other.

Stable steady-state solution
$$\phi_{ss} = \text{asin}\left(\frac{\omega_0 - \omega_{inj}}{\omega_L}\right) \quad (3\text{-}28)$$

Unstable steady-state solution
$$\phi'_{ss} = \pi - \phi_{ss} \quad (3\text{-}29)$$

Locking range condition
$$\omega_0 - \omega_L \leq \omega_{inj} \leq \omega_0 + \omega_L \quad (3\text{-}30)$$

Adler's equation alternative form
$$\begin{cases} \varphi(0) = \varphi_0 \\ \frac{d\varphi}{dt} = \omega_L\left(\sin\phi_{ss} - \sin\varphi(t)\right) \end{cases} \quad (3\text{-}31)$$

Closed-form solution assuming $\phi_{ss} = 0$
$$\varphi(t) = 2\,\text{atan}\left(\tan\left(\frac{\varphi_0}{2}\right)e^{-\omega_L t}\right) \quad (3\text{-}32)$$

Another form of Adler's equation is proposed in Equation (3-31). Assuming that injection occurs at the free-running frequency ($\phi_{ss} = 0$), it is possible to derive a very simple closed-form expression of φ (Equation (3-32)). This solution is plotted in the time-domain for different initial conditions in Figure 3-32 (b) and the closed-form expression is compared to a numerical solution computed from Equation (3-31) showing excellent agreement.

In the literature, the locking time, or locking speed, received a lot of attention because of crucial importance in associated designs. The demodulation concept proposed in this work in section 3.6.2 is no exception so that we also need to investigate this fundamental property analytically. Design and implementation constraints resulting from the analysis will be discussed later in section 3.6.4.

It should be mentioned first that convergence in the system of Equation (3-31) is asymptotical. In other words, perfect phase locking only occurs after an infinite time as illustrated in the particular case of Figure 3-32 (b). Consequently, we define in Equation (3-33) a convergence criterion associated with a corresponding convergence time $\tau_{X(\%)}$. When X = 100 %, the phase offset equals 100 % of its initial value so that $\tau_{100\%}$ is always equal to

zero. On the opposite, at $X = 0$ % the system has completely lost the memory of the initial phase offset value which corresponds to asymptotic convergence ($\tau_{0\%} = +\infty$). For intermediate values of X, the phase offset linearly lies between initial and final values and $\tau_{X(\%)}$ is finite. Depending on application requirements, one can consider that locking is achieved at $\tau_{10\%}, \tau_{1\%}, \tau_{0.1\%}$, etc. Combining Equations (3-32) and (3-33), an analytical expression of $\tau_{X(\%)}$ is derived in Equation (3-34) in the particular case of free-running frequency injection. For a given convergence value, Figure 3-33 (b) clearly illustrates the convergence time dependence as regards the initial phase offset. In short, the larger the initial phase deviation, the longer it takes to reach the convergence, as visible in Figure 3-33 (a). Note that all derived expressions make use of dimensionless quantities $\omega_L t$ or $\omega_L \tau$. It indicates that the half-locking range ω_L also plays a significant role in setting the locking speed.

Convergence criterion

$$\begin{aligned}\varphi\left(\tau_{X(\%)}\right) &= \varphi(t \to \infty) + X(\%) \cdot (\varphi(0) - \varphi(t \to \infty)) \\ &= X(\%)\,\varphi_0 + \left(1 - X(\%)\right)\phi_{ss}\end{aligned} \tag{3-33}$$

Convergence time assuming $\phi_{ss} = 0$

$$\omega_L \tau_{X(\%)} = \ln\left(\frac{\tan\left(\frac{\varphi_0}{2}\right)}{\tan\left(X(\%) \cdot \frac{\varphi_0}{2}\right)}\right) \tag{3-34}$$

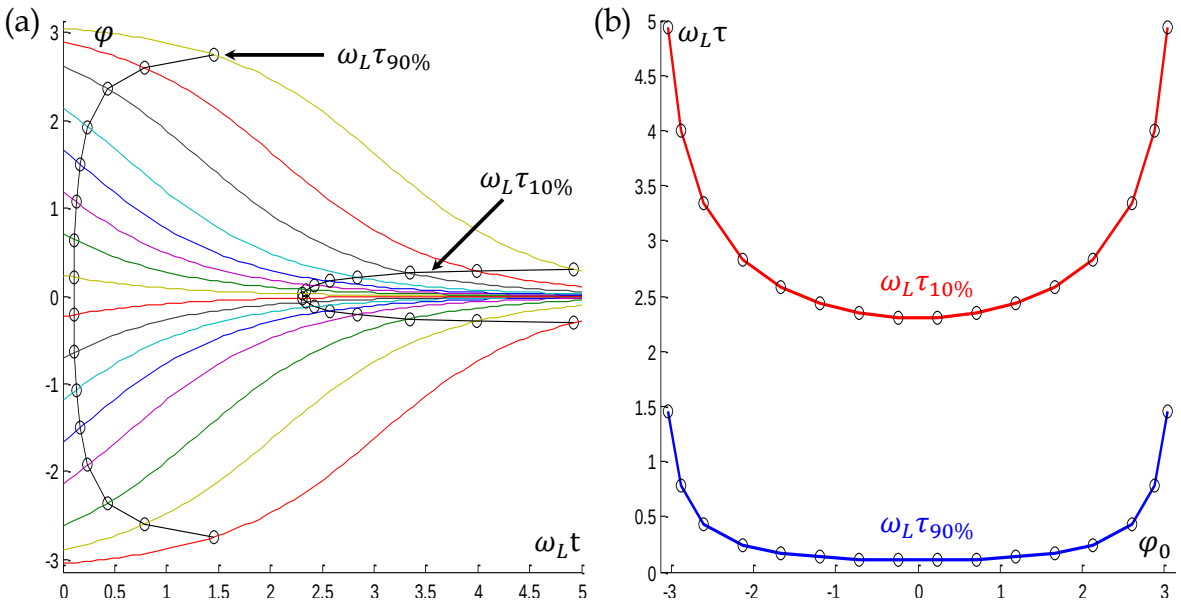

Figure 3-33: Time-domain evolution of the solution of Adler's equation (a) and associated convergence times plotted as a function of initial phase offset (b). Injection at the free-running frequency is considered in both plots.

Finally, these primary conclusions need to be discussed in the more general case ($\phi_{ss} \neq 0$). While a convergence definition is given in Equation (3-33) without any loss of generality, the mathematical complexity of Equation (3-31) makes it difficult to generalize them easily to any ϕ_{ss} situation. To do so a general solution $\varphi(t)$ should be derived analytically, making it possible to invert Equation (3-33). Thus, an expression of the convergence time is obtained, enabling previous conclusions to be generalized.

A commonly admitted solution of Equation (3-31) is reported in Equation (3-35) [**Jany, 2014**]. This expression makes use of an integration constant t_0 homogenous to a time quantity, which should be computed at $t = 0$ in Equation (3-35) and related to $\varphi(0)$. In spite of the moderate complexity of this equation, the opacity introduced by the time-constant does

not help in understanding the essence of the locking behavior and the relevant parameters involved in that mechanism. Moreover, it appears after a closer look at Equation (3-35) that it is in fact not defined for $\phi_{ss} = 0$ as the denominator equals zero. Such a singular phenomenon may be overcome if the numerator also equals zero (it is an indeterminate form). On the contrary, the numerator seems finite and different from zero, thus eliminating a possible continuous extension. This remark is all the more troublesome that an analytical solution actually exists in that case, and is readily available in Equation (3-32). To eliminate the apparent paradox, it should be considered that the integration constant t_0 strongly varies with ϕ_{ss} as well.

$$\exists t_0 \in \mathbb{R}^+ \mid$$

Adler's equation general solution

$$\varphi(t) = 2\,\mathrm{atan}\left(\frac{1 - \cos\phi_{ss}\tanh\left(\frac{\omega_L}{2}(t - t_0)\cos\phi_{ss}\right)}{\sin\phi_{ss}}\right) \tag{3-35}$$

$$\varphi(t) = 2\,\mathrm{atan}\left(\tan\left(\frac{\phi_{SS}}{2}\right) + \frac{2}{\tan(\phi_{SS}) + \lambda(\varphi_0, \phi_{SS})e^{\omega_L\cos(\phi_{SS})t}}\right) \tag{3-36}$$

$$\lambda(\varphi_0, \phi_{SS}) = \frac{2}{\tan\left(\frac{\varphi_0}{2}\right) - \tan\left(\frac{\phi_{SS}}{2}\right)} - \tan(\phi_{SS}) \tag{3-37}$$

In order to investigate further the locking dynamics, an alternative closed-form solution of the most general Adler's equation is necessary. In the context of this work, such an analytical expression is successfully derived in Equation (3-36). The complete mathematical proof is provided in Appendix E. As expected, it is also shown that Equations (3-35) and (3-36) are equivalent for $\phi_{ss} \neq 0$. However, the superiority of Equation (3-36) is really revealed for $\phi_{ss} = 0$ since a direct substitution straightforwardly leads to Equation (3-32) without any pathological phenomenon to be resolved. Note that the quantity defined in Equation (3-37) has nothing to do with the previous integration constant t_0. Moreover, its dependence with respect to both φ_0 and ϕ_{SS} parameters is extremely clear. In addition, it is always a finite quantity…except in the absence of perturbation ($\varphi_0 = \phi_{SS}$) where it becomes infinite so that $\varphi(t)$ remains at ϕ_{SS} (as expected in such a trivial situation).

Finally, the desired closed-form expression of the convergence time is derived in Equation (3-39) thanks to the combination of Equations (3-33), (3-36) and (3-38). The dependence to φ_0 and ϕ_{SS} is not straightforward and is exemplified in Figure 3-34. Nevertheless, it is confirmed that the half-locking range ω_L linearly contributes to the locking speed. Besides, it is furthermore noticed that the phase offset $\varphi(t)$ has a high-pass behavior. This holds because, for any input phase step $\theta_{inj}(t \geq 0) - \theta_{inj}(t < 0)$, provoking a similar phase offset step $\Delta\varphi$ so that $\varphi_0 = \phi_{ss} + \Delta\varphi$, the ILO system always manages to get back to its original phase offset condition and converges asymptotically to ϕ_{ss}. By definition, this implies that the output phase $\theta_{out}(t)$ converges to $\phi_{ss} + \theta_{inj}(t \geq 0) = \theta_{out}(t < 0) + \theta_{inj}(t \geq 0) - \theta_{inj}(t < 0)$ as well. It is therefore very clear that the ILO output phase $\theta_{out}(t)$ mimics the input phase variations acting as a particular kind of (non-linear) low-pass phase filter. What is more, this low-pass dynamics and associated time constants are the same as previously described for $\varphi(t)$, justifying the in-depth investigation of this quantity.

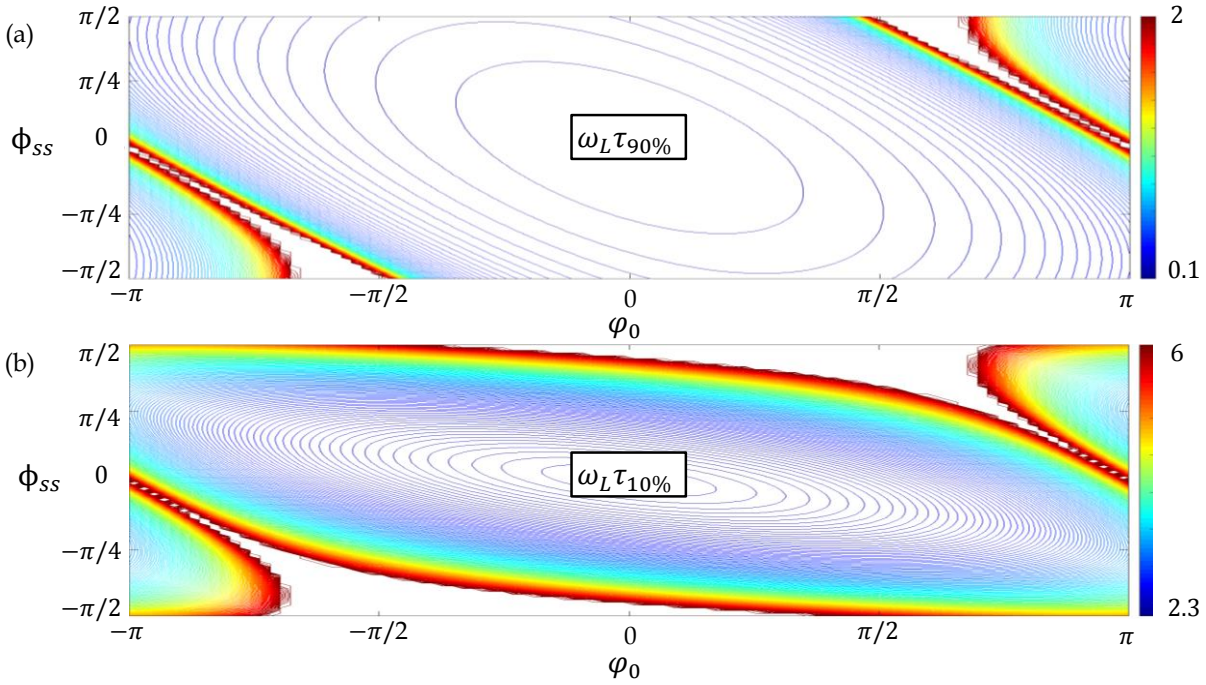

Figure 3-34: Numerical simulations of convergence times for (a) $\omega_L\tau_{90\%}$ and (b) $\omega_L\tau_{10\%}$ of as a function of the initial and final phase offsets φ_0 and ϕ_{ss}. All contour steps are 0.02.

$$\varphi_X = \varphi\left(\tau_{X(\%)}\right) = X(\%)\,\varphi_0 + \left(1 - X(\%)\right)\phi_{ss} \tag{3-38}$$

General case convergence time

$$\omega_L\tau_{X\%}\cos(\phi_{SS}) = \ln\left(\frac{\frac{2}{\tan\left(\frac{\varphi_X}{2}\right)-\tan\left(\frac{\phi_{SS}}{2}\right)}-\tan(\phi_{SS})}{\frac{2}{\tan\left(\frac{\varphi_0}{2}\right)-\tan\left(\frac{\phi_{SS}}{2}\right)}-\tan(\phi_{SS})}\right) \tag{3-39}$$

3.6.2. ILO Demodulation Concept: Frequency-domain Presentation

Interestingly, most of the publications related to injection-locking focus on the steady-state (phase-locked) regime. On the contrary, this work mainly leverages on the transient regime occurring just a moment after the initial phase offset step. The proposed QPSK demodulation architecture is presented in Figure 3-35. At a first glance, it is composed of a variable-gain LNA, an ILO (fundamental injection), a phase-shifter, an I/Q mixer and some basic digital / analog feedback controls. Therefore, the resulting low block count can potentially be very attractive in terms of area and power requirements.

At the heart of this concept is the assumption that the ILO locking range is much smaller compared to the incoming QPSK RF signal bandwidth, as illustrated in Figure 3-36. Hence, the ILO output is likely to be *unlocked* at any time. In this configuration, the ILO is actually used as a low-pass phase filter to recover the (unmodulated) Tx carrier. Assuming that the latter lies inside the ILO locking range, the produced carrier replica can theoretically track "low-frequency" changes. This ability is very important in order to compensate inherent PVT-induced phase or frequency drifts at Tx side. Moreover, it may even be possible to have a free-running Tx LO if the locking range is chosen large enough.

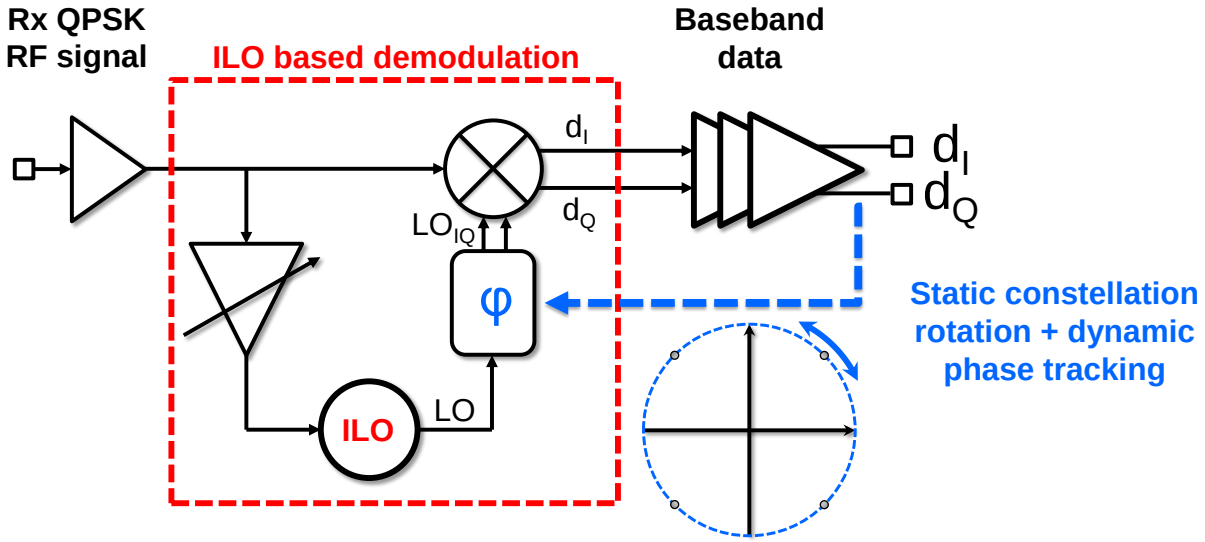

Figure 3-35: Schematic of the proposed ILO based QPSK demodulation architecture, featuring a variable-gain LNA, an ILO, a phase-shifter, an I/Q mixer and feedback loop for static and dynamic absolute phase compensation.

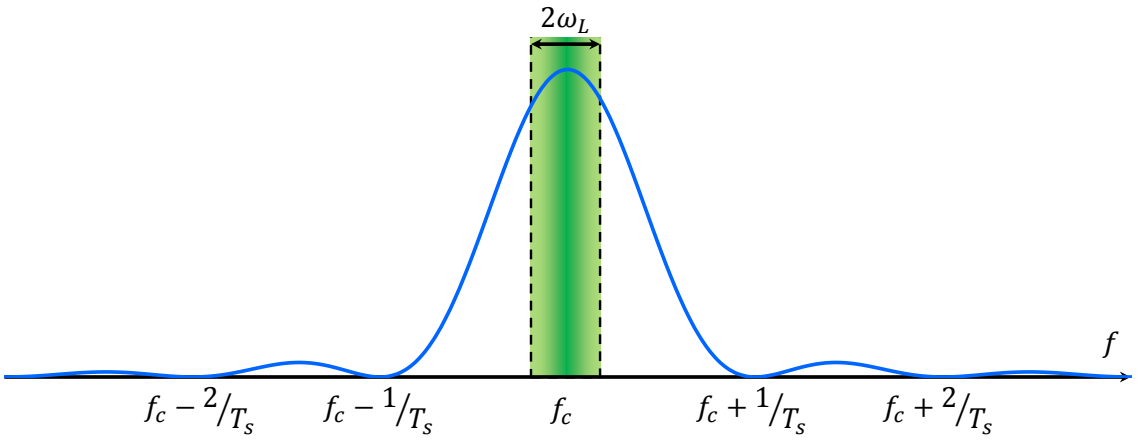

Figure 3-36: The occupied bandwidth of the incoming modulated signal (blue) largely exceeds the locking range of the ILO (green).

However, a difficulty may appear as the data rate and occupied RF bandwidth diminish. In that case, the previous fundamental assumption no longer holds and the ILO output spectra may gradually look like the input one. In other words, ILO phase filtering is expected to be less and less efficient as data rate decreases, resulting in a poorer carrier recovery. According to Equation (3-24), it is although possible to tune the locking range by tuning the current ratio $\frac{I_{inj}}{I_0}$. It is actually the purpose of the variable-gain LNA.

However, if the locking range becomes too small, it may no longer be able to compensate for the drifts evocated here. In that case, this sets a data rate lower bound under which the proposed architecture no longer operates correctly. Fortunately, this architecture also features an alternative amplitude demodulation capability. Considering an OOK RF signal (instead of QPSK) in the context of low spectrum occupancy, the ILO mainly operates in the locked regime…as long as an RF power is applied at its input. Consequently, self-mixing occurs during one-symbols, issuing one-values in the baseband. On the contrary, noise is mixed to the free-running ILO frequency during zero-symbols, thus causing zero-values in the baseband. In short, the proposed demodulation architecture can handle both OOK and QPSK at low and high data rates respectively. Its favorable versatility enables continuous data rate scaling.

3.6.3. Demodulation Illustration in the Time-domain

In this section, QPSK demodulation is investigated in the time-domain using the convergence formalism and results derived in section 3.6.1. Moreover, in section 3.6.2, locking range is assumed much smaller than the occupied signal bandwidth. This fundamental assumption transposes in the time-domain so that symbol time is much smaller than ILO convergence time constant. In other words, the ILO is always in the *unlocked* regime as symbols are not long enough to let it converge. This concept is illustrated in Figure 3-37.

For $t < 0$, ILO phase offset is such that $\varphi(t < 0) = \phi_{ss}$ (steady-state regime). The first symbol to be demodulated is received at time $t = 0$. It causes an initial phase offset step that the system immediately starts to compensate by modifying ILO output phase. Note that demodulated data are directly an image of the ILO phase offset, making it the relevant quantity to focus on. It should be noted as well that a demodulation error slightly grows during symbol demodulation because of ILO convergence. In the light of this observation, the aforementioned design assumption clearly makes sense in order to minimize demodulation errors.

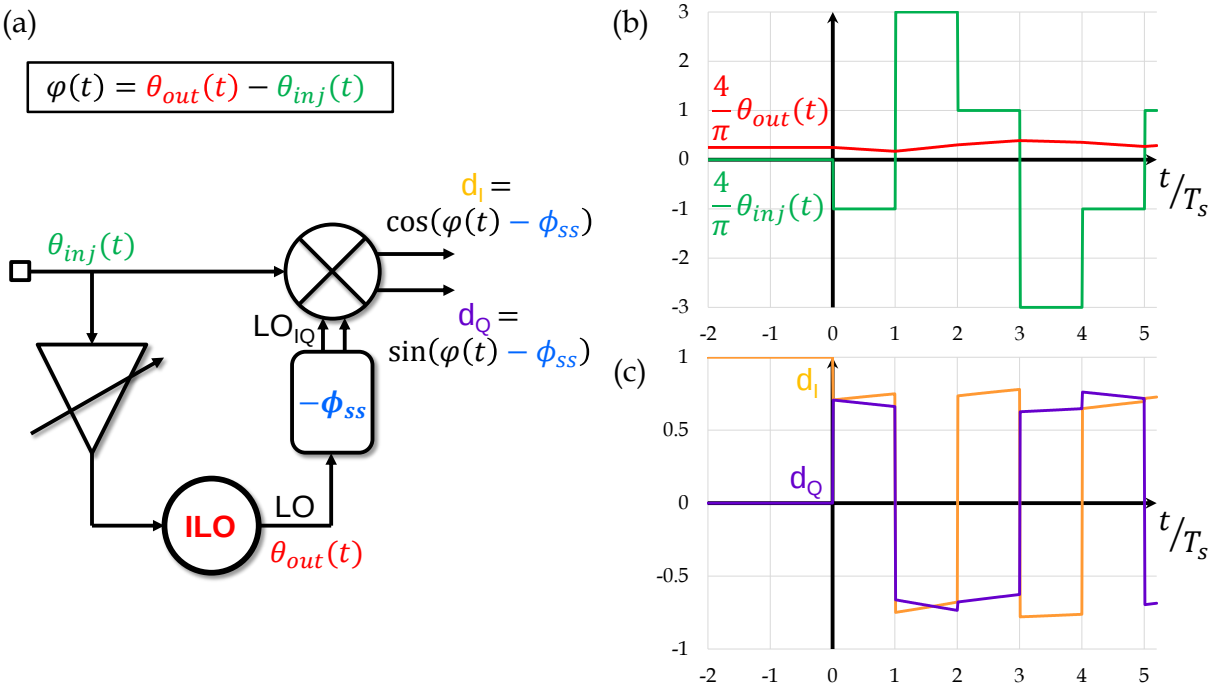

Figure 3-37: Illustration of the demodulation operation in the time domain for a random symbol sequence and arbitrary design parameters. (a) Schematic and relevant node designations, (b) injected and output phases, (c) demodulated data on I/Q paths.

After the first symbol, the received modulated signal creates a second phase offset. A new convergence limit is thus introduced for the output phase. However, the starting point is different from the previous steady-state condition. In fact, it now depends on both first symbol value and output phase state reached during the first symbol. Note that an ILO with almost infinite locking time would be of particular interest in this context because the error introduced by the end of symbols would be negligible. On the contrary, finite locking times are susceptible to create non-negligible phase errors that may also propagate from symbol to symbol causing detrimental SNR reduction or bit errors. Fortunately, these errors interact with each other constructively as well as destructively. Assuming equal symbol probabilities and taking into

account the balanced distribution of phases in the QPSK modulation, demodulation errors are statistically canceled for long-enough symbol sequences.

3.6.4. Design Considerations

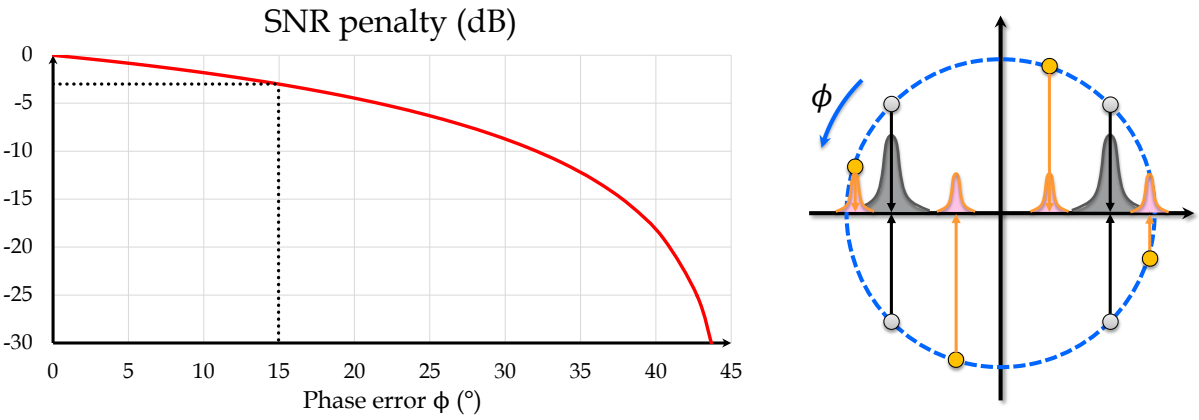

Figure 3-38: SNR penalty as a function of the constellation rotation angle.

In this section, the limitations mentioned earlier are discussed quantitatively and realistic implementation in integrated CMOS technologies is envisioned.

First, it is noticed that demodulations errors evocated in section 3.6.3 are not bound although the mathematical expected value is zero. In other words, large error excursions are actually possible. In that case, the recovered carrier frequency suffers from a parasitic (time-dependent) phase offset ϕ. The resulting SNR penalty is derived in Equation (3-40) as if the QPSK constellation were rotated with the same angle ϕ (Figure 3-38).

SNR penalty (dB) $10\log(1-\sin 2|\phi|)$ (3-40)

Large demodulation errors caused by ILO convergence are likely to be particularly prominent in the case of long ICSP. In that specific case, after an initial phase offset step, the input phase is kept constant for a long time. This situation is actually the one described by Adler's Equation in section 3.6.1 for which it has been shown that the phase offset $\varphi(t)$ eventually loses memory of the initial phase offset step that is to say the data. Therefore, long ICSP should be eliminated by design. Note that such sequences are also avoided in classical amplitude modulated systems because they tend to disturb threshold positioning. In such systems, encoding is an efficient way to break wide ICSP. Because of the versatility of the proposed architecture, which combines OOK and QPSK to enable large data rate scaling, this choice is relevant. Considering 8b/10b encoding, ICSP are limited to only six symbols. According to Figure 3-38, if the SNR penalty is to be kept below 3 dB, the recovered carrier phase drift should not excess 15° by the end of the 6th symbol.

Remembering convergence definitions given in Equations (3-33) and (3-38), convergence criterion are computed through Equations (3-41) - (3-43) and results are summarized in Table 3-6. Associated time constants are plotted in Figure 3-39 as a function of the steady-state phase offset. Whatever the steady-state configuration, the longest ICSP (= 6Ts for 8b/10b) should not last more than the smallest convergence time, that is to say roughly $^{0.126}/_{\omega_L}$.

However, it is possible to relax this duration to about $^{0.2}/_{\omega_L}$ by limiting possible steady-state configurations, as expressed in Equation (3-44).

$$\varphi(\tau_{X\%}) = \varphi_0 X(\%) + \big(1 - X(\%)\big)\phi_{SS} = \varphi_0 \pm 15° \tag{3-41}$$

$$\varphi_0 \cong \phi_{SS} + \Delta\varphi \tag{3-42}$$

$$X(\%) = 1 - \frac{15°}{|\Delta\varphi|} \tag{3-43}$$

$$-0.4\frac{\pi}{2} \leq \phi_{SS} \leq 0.4\frac{\pi}{2} \tag{3-44}$$

$\Delta\varphi$	-180°	-90°	90°	180°
X	≈ 92 %	≈ 83 %	≈ 83 %	≈ 92 %

Table 3-6: QPSK convergence criterion assuming a 3 dB SNR penalty.

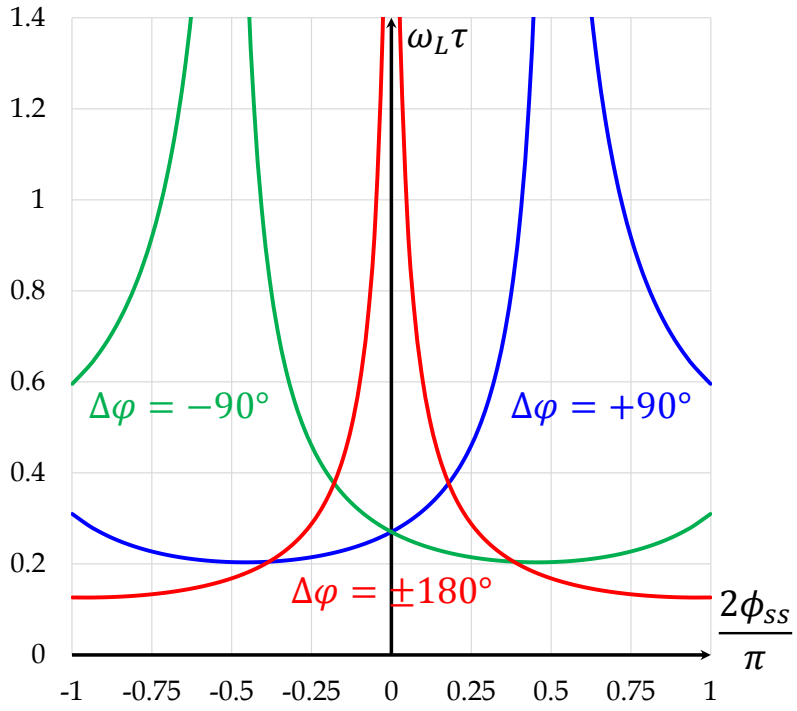

Figure 3-39: Convergence time constants associated to QPSK phase changes as a function of steady-state phase offset.

Depending on the lowest desired data rate, ILO design parameters ω_L and $\frac{I_{inj}}{I_0}$ can be computed thanks to Equations (3-45) and (3-47) respectively. Adler's equation assumptions are also verified in Equations (3-47) - (3-49). Finally, Equation (3-46) is interpreted as the required Tx/Rx alignment, directly leading to Equation (3-50). Unfortunately, an alignment inferior to 12 MHz (≈ 160 ppm) seems at least very difficult to guarantee across all PVT corners with current CMOS technologies, if not simply impossible... An order of magnitude should be gained on this design constraint to ensure both feasibility and reliability.

Assuming $R_s \geq 4$ GS/s

$$\omega_L \tau \geq 0.2 \rightarrow \omega_L \leq \frac{0.2}{6T_s} \approx 2\pi \ 21 \text{ MHz} \quad (3\text{-}45)$$

$$|\omega_0 - \omega_{inj}| \lesssim 2\pi \cdot 12 \text{ MHz} \quad (3\text{-}46)$$

Assuming $\omega_0 \approx 75$ GHz and $Q \approx 7$

$$\frac{I_{inj}}{I_0} = 2Q\frac{\omega_L}{\omega_0} \approx \frac{1}{250} \ll 1 \quad (3\text{-}47)$$

$$|\omega_0 - \omega_{inj}| \ll \frac{\omega_0}{Q} \approx 2\pi \cdot \frac{75}{7}\text{GHz} \quad (3\text{-}48)$$

$$|\omega_0 - \omega_{inj}| \leq \omega_L \quad (3\text{-}49)$$

Tx / Rx alignment

$$|f_{Tx} - f_{Rx}| \leq 12 \text{ MHz} \quad (3\text{-}50)$$

3.7. Demonstration at 60 GHz

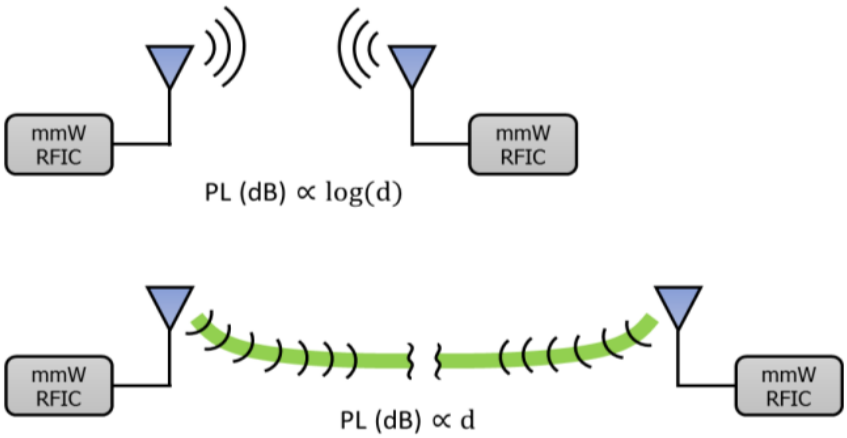

Figure 3-40: Versatile millimeter-wave propagation using the same transceivers: wireless for short ranges (top) and guided through plastic waveguides for longer ranges (bottom).

Finally, a basic mmW plastic waveguide demonstration is presented to close the system level discussions of this Chapter. In the context of mmW plastic waveguide systems, low spectral efficiency modulations, mainly OOK and 2-FSK, have received tremendous attention. This trend is logical as the waveguide has a large bandwidth capability that can be traded for energy efficiency. However, in the context of versatile transceivers, higher-order modulation schemes are needed to maintain high data rates in the wireless mode. In the *wired* mode, the system benefits from the favorable plastic waveguide propagation characteristics, resulting in better Rx SNR, to extend link distance (Figure 3-40), reduce Tx output power and/or increase modulation order for higher bit rate. In any case, the carrier frequency and occupied bandwidth of transmitted signals are likely to remain roughly the same. It is indeed believed that plastic waveguides may offer an additional feature to circuits primarily dedicated to wireless communications. To do so, only minor circuit modifications are expected for both economic reasons (low cost driven applications) and technical reasons (some design constraints are actually relaxed). An alternative versatile system would feature two very different operating modes, each one being optimized for wired or wireless constraints. Such a dual-mode implementation would certainly be very complex and expensive. Therefore, turning wireless transceivers into versatile ones seems the most pragmatic approach.

However, the plastic waveguide capability to transmit "wireless-oriented" high order modulation signals (possibly OFDM signals) should be demonstrated. In this work, such a demonstration carried out by combining the Magic Wheel plastic waveguide already

presented in Chapter 2 [**Voineau, 2018**] as well as a 60 GHz transceiver published in [**Siligaris, 2011**] with 64QAM and OFDM capabilities. Multiple views of the setup are provided in Figure 3-41. An AWG is used to feed the Tx chip with pseudo-random bit patterns. Tx RF output is first interfaced to a V-connector and a WR-15 horn antenna in which the plastic waveguide is introduced and maintained at the center thanks to a low loss foam. The other end of the waveguide is then positioned in front of the receiver antenna (reported on a BGA). It is similarly maintained ~ 1 mm away not to disturb the antenna resonance by a foam material. Manual alignment was sufficient to achieve a 4 Gb/s communication over a 4 m distance thus quadrupling the wireless range.

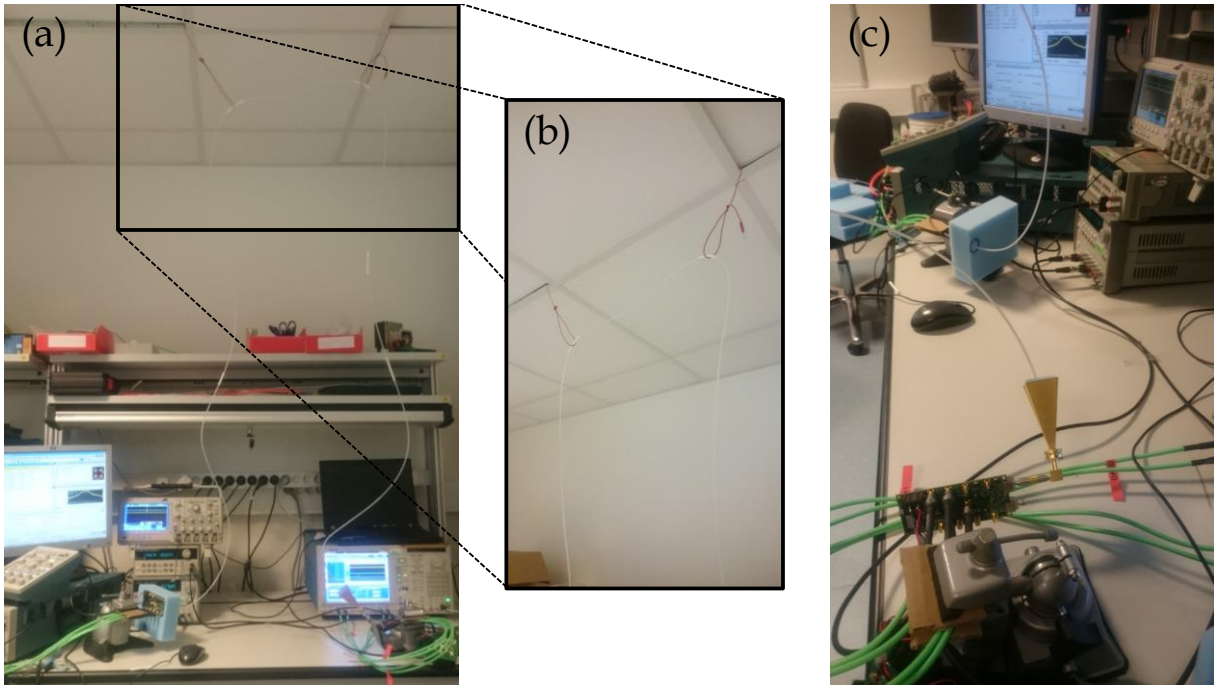

Figure 3-41: Demonstration of a 4 m link with modulated signals. Face view of the setup (a), waveguide fixation on the ceiling (b) and side view of the setup (c).

	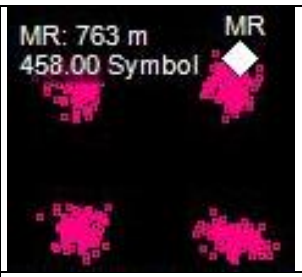		
Modulation	**QPSK** (Tx + Rx)	**16QAM** (Tx)	**64QAM** (Tx)
Data rate	4 Gb/s	8 Gb/s	12 Gb/s
EVM_{RMS}	17.0 %	6.4 %	11.2 %

Table 3-7: Link performance summary for different modulations (Magic Wheel – 4 m). Note that QPSK is achieved using both Tx and Rx circuits while 16QAM and 64QAM are obtained with the Tx and a real-time oscilloscope as a demodulator.

By replacing the Rx chip with a Tektronix DPO77002SX 70 GHz 200 GS/s real-time oscilloscope performing direct demodulation, it is possible to increase modulation order to 16QAM and 64QAM while still guarantying good EVM, as summarized in Table 3-7. Note that scope demodulation clearly improves EVM in comparison with the Rx circuit. Measurements

on the same sample also show successful 16QAM OFDM signals transmission with SNR superior to 20 dB (Figure 3-42).

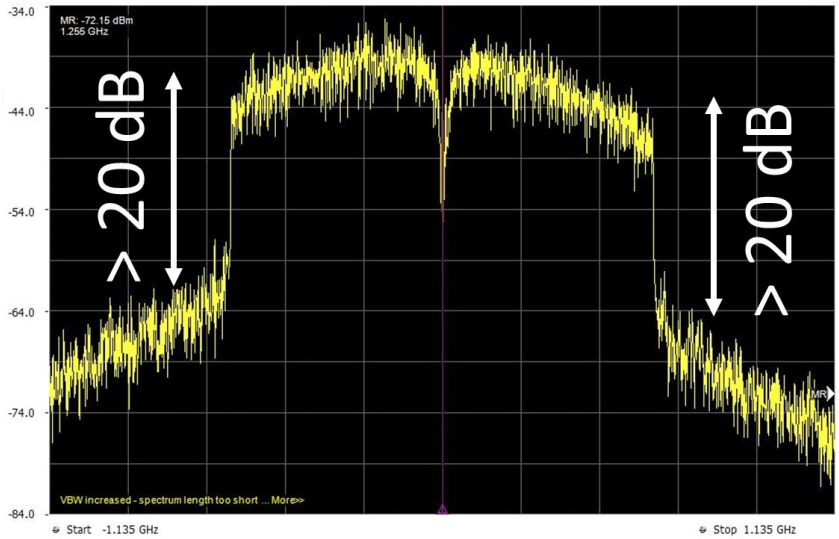

Figure 3-42: Measured OFDM after propagation in a 4 m-long Magic Wheel plastic waveguide showing 16QAM capability (SNR > 20 dB).

Although further investigation is necessary to quantify modulated signals distortions, this demonstration clearly confirms plastic waveguide capability to transmit high order modulations, up to at least 64QAM, including OFDM signaling. This important result paves the way to high-speed and versatile millimeter-wave systems in which plastic waveguides are key enablers. Finally, the performance of this versatile system is compared with the state of the art in Appendix F. Interestingly, this work reports the highest FoM as defined in Equation (3-51).

$$\text{FoM} = \frac{\text{Data Rate x Link Distance}}{\text{Carrier Frequency}} \ [\text{m x b}] \qquad (3\text{-}51)$$

3.8. Conclusions

In this Chapter, most promising applications have been discussed first in order to derive basic system level specifications. To address most of them, including 40 GbE applications, a single channel with a very large bandwidth is neither required nor desired. Consequently, a dual-frequency architecture is proposed in addition to QPSK thus providing 4x10 Gb/s channels in the E-band. Full duplex has also been identified as another important specification. In this work, it is addressed thanks to two parallel waveguides (one per direction) although polarization duplexing still represents an attractive solution in spite of its lack of maturity (Chapter 2).

A major contribution of this Chapter regards interconnects bandwidth improvement, as the proposed architecture requires a bandwidth in excess of 30 GHz, extending beyond E-band. From Chapter 2, it has been shown that the transition from a plastic waveguide to a WR-12 metallic waveguide may not really limit the bandwidth. However, a suitable transition from a WR-12 waveguide to a PCB microstrip line was missing. An innovative structure has been presented in this work leveraging on a dielectric tip machined in the PCB, which is inserted in a tapered double-ridge waveguide section. This transition realizes a smooth impedance and

fields matching and results in a 55 – 95 GHz bandwidth with return losses exceeding 15 dB. Moreover, it exhibits a non-resonant group-delay characteristic, which is particularly desirable for high-speed communications. By pushing further the bandwidth / compactness trade-off, this work reaches more than 50 % fractional bandwidth, almost improving the state of the art by a factor of two.

Another challenge raised by the proposed system architecture is related to QPSK demodulation. While QPSK modulation may be implemented easily at Tx side, the demodulation process at Rx is much harder. On the one hand, coherent QPSK demodulation techniques usually rely on carrier recovery circuits, but their operation at mmW tends to be very power hungry. On the other hand, some non-coherent ones, like non-coherent D-QPSK, offer reduced consumption capability. Nevertheless, their limitations have been clearly highlighted. Therefore, none of these techniques really comply with the low power, high data rate and low area requirements of this work. An innovative ILO based demodulation technique has been introduced with the potential to meet these needs. Additionally, this technique features both OOK and QPSK compatibility for low and high data rates respectively. Contrary to most designs leveraging on ILO, this concept operates in the transient regime and actually behaves with a low pass transfer function in the phase domain. This characteristic has been illustrated from the famous Adler's equation but it should be noted that conventional analytical solutions in the transient regime of interest were impractical. For feasibility assessment, an alternative closed-form expression is proposed to ease convergence analysis and remove mathematical difficulties encountered with the previous solution. Hence, after qualitative descriptions in both frequency and time domains, the concept has been discussed quantitatively and challenged regarding its integration in CMOS technologies. It appeared that extremely narrow locking ranges as well as unrealistic Tx / Rx frequency alignments are necessary because of limited available quality factors at mmW.

Ultimately, a versatile demonstration is described by combining a wireless transceiver and a plastic waveguide. It should be mentioned that none of them were originally designed for that purpose. In fact, the transceiver has been designed many years before the realization of this demonstrator and actually targets WiGig applications in the 60 GHz unlicensed band. As regards the plastic waveguide, it targets the E-band that is to say above 60 GHz. Nevertheless, its confinement ability increases with frequency, making it ideal for frequencies around 90 GHz at which it is still single-mode (Chapter 2). In spite of these apparent discrepancies, this successful demonstration highlights the great versatility potential of mmW plastic waveguides and sheds a different light on the system level discussion.

3.9. Perspectives

3.9.1. Low Loss Interconnects

The new microstrip line to WR-12 waveguide transition developed in this work has an attractive bandwidth but there is still some room for improvement as regards its insertion loss and compactness. In Figure 3-20, the transition length from the double ridge waveguide to the standard WR-12 one represents most of the overall transition length. By eliminating the intermediate WR-12 section in the PCB to plastic waveguide transition, significant length reduction could be obtained along with reduced insertion loss. Moreover, the low return losses

previously reported may not be compromised in such a transition, as the impedance in ridge waveguides is lower than in conventional rectangular waveguides. Ridge waveguide to plastic waveguide transition thus exhibits a much more favorable impedance change.

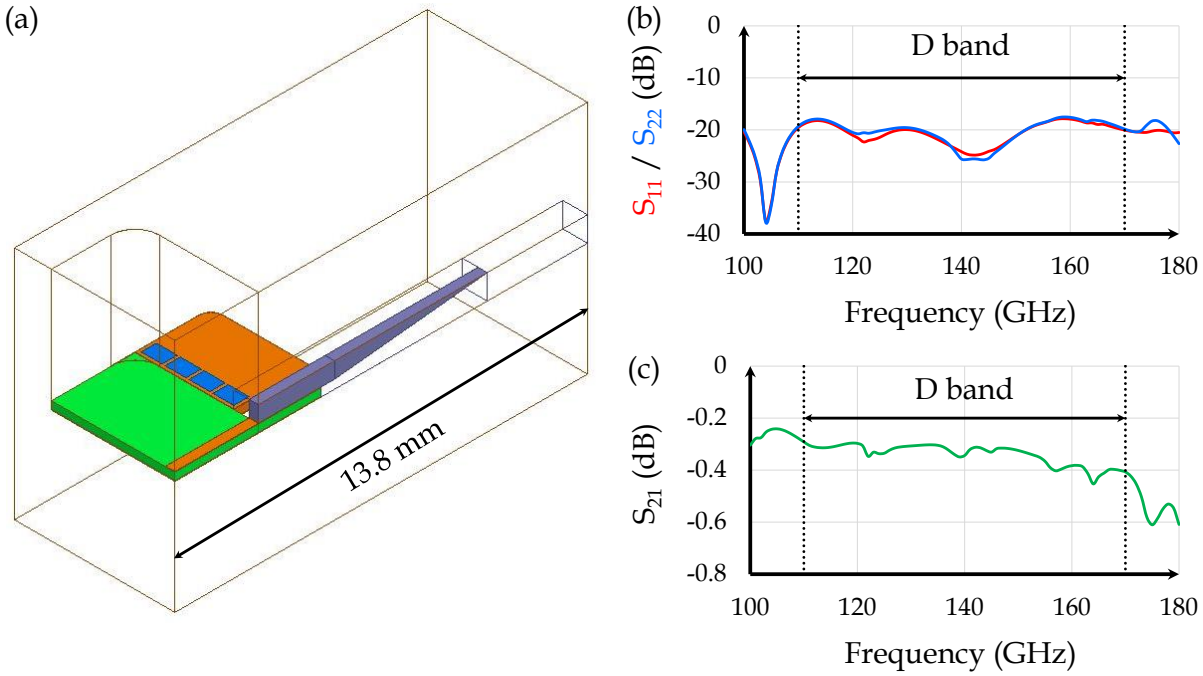

Figure 3-43: Single ridge waveguide to PCB transition in D band. (a) 3D view (transparent metal case for clarity), (b) simulated reflection parameters and (c) transmission parameters. Port 1 and Port 2 are assigned to the microstrip and the WR-6 sides respectively.

Looking further, the development of a dedicated plastic waveguide connector will be strongly impacted by the perspectives already described in Chapter 2. However, the development of PCB to rectangular waveguide transitions is a widespread research topic extending well beyond plastic waveguide interconnects. In fact, the proposed concept can be applied easily to higher frequencies leveraging on significant waveguide reduction. As the PCB thickness remain the same, the transition from ridge waveguide to rectangular waveguide is minimized and insertion loss may be lowered. In addition, a given dielectric tip length results in a smoother transition with respect to the reduced wavelength, potentially improving return losses further. In Figure 3-43, an application in D band (110 – 170 GHz) is proposed as a preliminary result. Because of reduced waveguide dimensions, single ridge waveguides are more appropriate than double ridge ones with a drastically decreased transition length. Moreover, the manufacturability is improved while still offering excellent return and insertion losses, as shown in Figure 3-43 (b) and Figure 3-43 (c) respectively.

3.9.2. ILO Based Demodulation Further Investigations and Improvements

In this Chapter, an innovative demodulation technique is proposed with theoretical benefits in terms of low block count, low power consumption as well as OOK and QPSK compatibility. Primary design considerations still suggest that the concept suffers from implementation issues and actually requires impractical design parameters. However, a further study is necessary in order to assess the real benefits and drawbacks of this

architecture. The following sections draw interesting perspectives that may significantly mitigate these previous conclusions.

3.9.2.1. Pulse Shaping Impact

The theoretical derivations and the resulting harsh design specifications obtained in section 3.6 assume that input modulated signals are perfectly "square" modulated. In other words, phase transitions are abrupt and thus occur instantaneously. In practice, such signals are clearly impossible, as they would in fact require an infinite bandwidth (section 3.2). Because all amplification stages in the system (as well as the plastic waveguide) have finite bandwidths, the overall bandwidth is even more limited. Consequently, practical phase transitions may not be abrupt at all. In the context of high-speed digital modulation, each rise and fall times may represent up to ~ 30 % of the symbol duration. Neglecting them is therefore an excessively simplifying hypothesis. ILO phase convergence times should be reconsidered accordingly.

This consideration obviously highlights the presence of inexorable pulse shaping. Assuming that the system is described with a sufficient degree of knowledge, complementary pulse shaping may also be introduced willfully to optimize demodulation performance. This approach is attractive since it could balance practical design complexity between Tx / Rx. For example, introducing intermediate phase states during rise and fall times could mitigate the rapid convergence issue caused by long ICSP. Favorably relaxed design constraints could be expected. This effect is observed in Figure 3-44 (a), where a trapezoidal pulse shape is approximated by a staircase function so that the numerical derivations obtained in section 3.6.1 may still be considered. Note that the trapezoidal pulse accumulates less phase deviation at the end of the symbol Figure 3-44 (b).

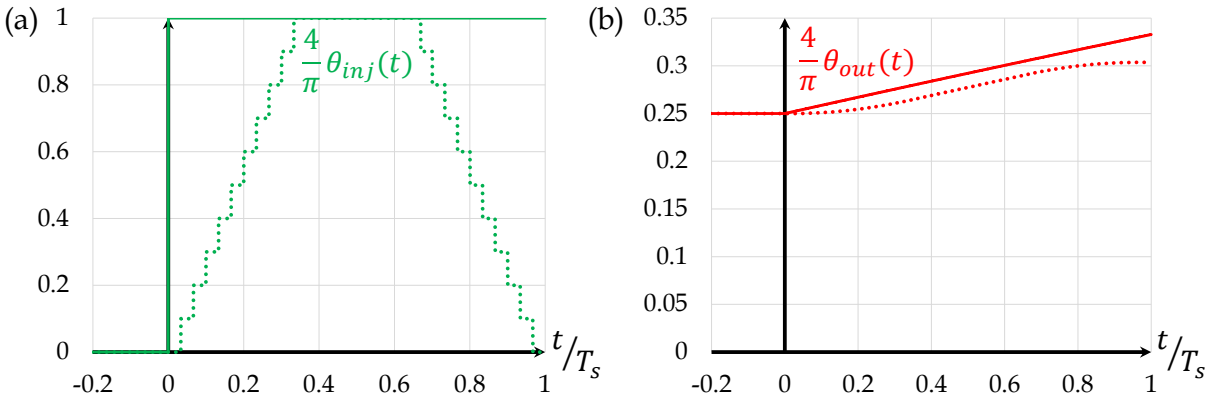

Figure 3-44: Comparison of two different pulse shapes. Solid lanes are related to perfect "square" modulation while dashed lines correspond to a trapezoidal approximation. (a) input and (b) output phases are given.

3.9.2.2. Feedback loop

In the schematic of Figure 3-35, a phase-shifter is necessary to compensate for the steady state phase offset introduced by the ILO. It has been shown that this quantity is a function of the difference between injected and free-running frequencies as well as the locking range. Because all these quantities can suffer from important PVT dispersions, the phase shifter dynamic should ideally cover 0°-180°. As regards phase resolution, Figure 3-38 provides valuable insights to conclude that at least four control bits are required to limit SNR degradation below 3 dB. In short, a high-resolution phase shifter with large dynamic should be implemented.

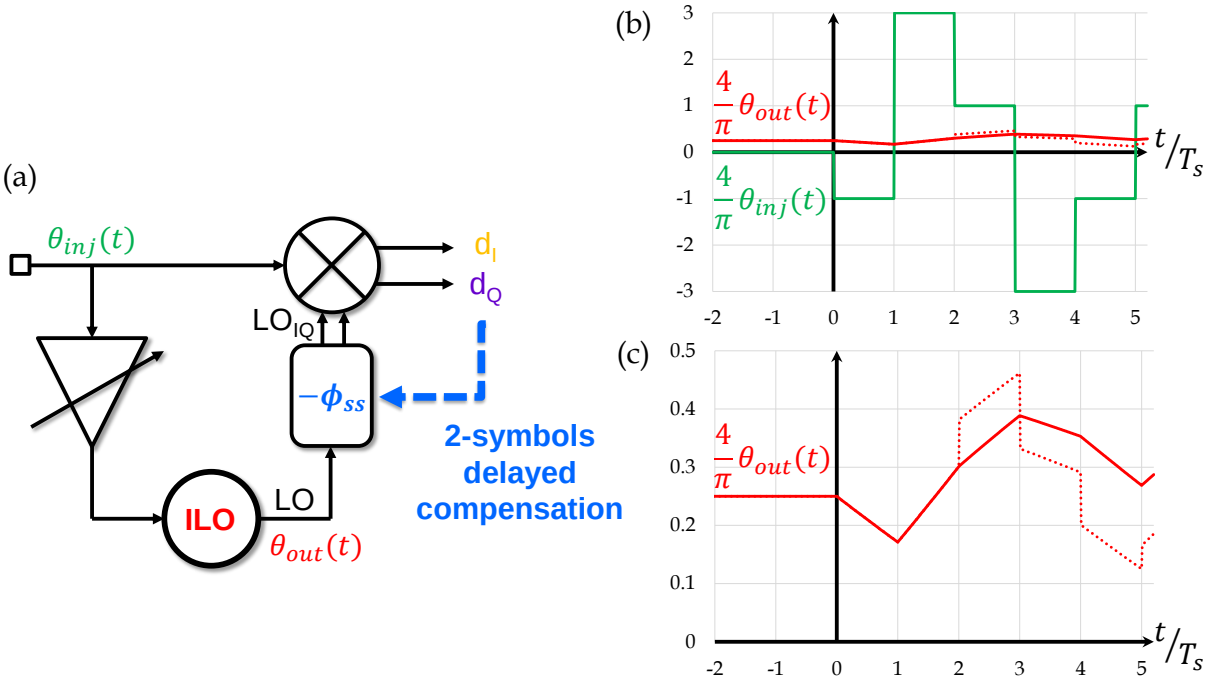

Figure 3-45: Data-assisted demodulation scheme (dashed line) is compared to normal demodulation (solid line) assuming that compensation occurs with a two symbol-time delay. (a) schematic, (b) injected and output phases over time, (c) output phase close-up view.

Moreover, phase shifting angle may be modified dynamically according to PVT variations. Even though only slowly varying processes are concerned here compared to typical symbol times and data-induced demodulation errors, the existence of such a dynamic control seems an attractive solution to compensate also the detrimental ILO convergence. Leveraging on demodulated data too, several correction schemes are clearly possible, but the latency of such feedback correction loops seems critical. In fact, demodulation errors can grow very rapidly, especially in the case of long ICSP, so that compensation angles should be introduced with short latency (shorter than a few symbol times). Otherwise, the design constraints imposed by maximum duration ICSP are not relaxed and over-compensation risks grow. Starting again from the example of Figure 3-37, two-symbol delayed data-assisted demodulation is illustrated in Figure 3-45. Note that over-compensation is clearly visible in this example. In spite of much better robustness as regards ICSP (worst case), this data-assisted demodulation scheme is likely to recover a poorer carrier on average.

References

[**Adler, 1946**] R. Adler. "A study of locking phenomena in oscillators," *Proceedings of the IRE*, Vol. 34, No. 6, pp. 351–357, 1946.

[**Artemenko, 2011**] A. Artemenko, A. Maltsev, R. Maslennikov, A. Sevastyanov, V. Ssorin. "Design of wideband waveguide to microstrip transition for 60 GHz frequency band," *Proceedings of the European Microwave Conference*, pp. 838-841, 2011.

[**Belenguer, 2014**] A. Belenguer, A L. Borja, H. Esteban, V. E. Boria. "Novel empty substrate integrated waveguide for high-performance microwave integrated circuits," *IEEE Transactions on Microwave Theory and Techniques*, Vol. 62, No. 4, pp. 832–839, April 2014.

[**Carpenter, 2016**] S. Carpenter, D. Nopchinda, M. Abbasi, Z. S. He, M. Bao, T. Eriksson and H. Zirath. "A D-band 48-Gbit/s 64-QAM/QPSK direct-conversion I/Q transceiver chipset," *IEEE Transactions on Microwave Theory and Techniques*, Vol. 64, No. 4, April 2016.

[**Chuang, 2012**] J.-K. Chuang, R.-Y. Fang, and C.-L. Wang. "Compact and broadband microstrip-to-waveguide transition using antisymmetric tapered probes," *Electronic Letters*, Vol. 48, No. 6, pp. 332-333, March 2012.

[**Dunwell, 2013**] D. Dunwell and A. C. Carusone. "Modeling oscillator injection locking using the phase domain response," *IEEE Transactions on Circuits and Systems I*, Vol. 60, No. 11, pp. 2823-2833, Nov. 2013.

[**Fakharzadeh, 2015**] M. Fakharzadeh and S. Jafarlou. "A broadband low-loss 60 GHz die to rectangular waveguide transition," *IEEE Microwave and Wireless Components Letters*, Vol. 25, No. 6, pp. 370-372, June 2015.

[**Fukuda, 2011**] S. Fukuda, Y. Hino, S. Ohashi, T. Takeda, H. Yamagishi, S. Shinke, K. Komori, M. Uno, Y. Akiyama, K. Kawasaki and A. Hajimiri . "A 12.5+12.5 Gb/s full-duplex plastic waveguide interconnect," *IEEE Journal of Solid-State Circuits*, Vol. 46, No. 12, pp. 3113-3125, 2011.

[**Han, 2012**] K. Y. Han and C.-K. Pao. "A V-band waveguide to microstrip inline transition," *Proceedings of the IEEE International Microwave Symposium,* pp. 1–3, 2012.

[**Hoefer, 1982**] W. J. R. Hoefer and M. N. Burton. "Closed-formed expressions for the parameters of finned and ridged waveguides," *IEEE Transactions on Microwave Theory and Techniques*, Vol. 30, No. 12, pp. 2190-2194, Dec. 1982.

[**Huang, 2011**] S.-J. Huang, Y.-C. Yeh, H. Wang, P.-N. Chen, J. Lee. "W-Band BPSK and QPSK transceivers with Costas-loop carrier recovery in 65-nm CMOS technology," *IEEE Journal of Solid-State Circuits*, Vol. 46, No. 12, pp 3033-3046, Dec. 2011.

[**Hurm, 2012**] V. Hurm, A. Tessmann, H. Massler, A. Leuther, M. Riessle, M. Zink, M. Schlechtweg, and O. Ambacher. "GaAs microstrip-to-waveguide transition operating in the WR-1.5 waveguide band (500-750 GHz)," *Proceedings of the Asian Pacific Microwave Conference,* pp. 145-147, 2012.

[**Jany, 2014**] C. Jany. "Conception et étude d'une synthèse de fréquence innovante en technologies CMOS avancées pour les applications en bande de fréquence millimétriques," PhD Thesis, Grenoble University, France, 2014.

[**Kim, 2013**] Y. Kim, L. Nan, J. Cong and M.-C. F. Chang. "High-speed mm-wave data-link based on hollow plastic cable and CMOS transceiver," *IEEE Microwave and Wireless Components Letters*, Vol. 23, No. 12, pp. 674-676, Dec. 2013.

[**Lou, 2008**] Y. Lou, C. H. Chan, and Q. Xue. "An in-line waveguide-to-microstrip transition using radial-shaped probe," *IEEE Microwave and Wireless Components Letters*, Vol. 18, No. 5, pp. 311-313, 2008.

[**Mozharovskiy, 2013**] A. Mozharovskiy, A. Artemenko, V. Ssorin, R. Maslennikov, A. Sevastyanov. "Wideband tapered antipodal fin-line waveguide-to-microstrip transition for E-band applications," *Proceedings of IEEE European Microwave Conference*, pp. 1187-1190, Oct. 2013.

[**Parment, 2015**] F. Parment, A. Ghiotto, T.-P. Vuong, J.-M. Duchamp and K. Wu. "Air-filled substrate integrated waveguide for low-loss and high power-handling millimeter-wave substrate integrated circuits," *IEEE Transactions on Microwave Theory and Techniques*, Vol. 63, No. 4, pp. 1228–1238, April 2015.

[**Razavi, 2003**] B. Razavi. "A study of injection pulling and locking in oscillators," *Proceedings of IEEE Custom Integrated Circuits Conference*, pp. 305-312, 2003.

[**Siligaris, 2011**] A. Siligaris et al. "A 65-nm CMOS fully integrated transceiver module for 60-GHz wireless HD applications," *IEEE Journal of Solid-State Circuits*, Vol. 46, No. 12, pp 3005-3017, 2011.

[**Takahashi, 2010**] H. Takahashi, T. Kosugi, A. Hirata, K. Murata and N. Kukutsu. "10-Gbit/s quadrature phase-shift-keying modulator and demodulator for 120-GHz-band wireless links," *IEEE Transactions on Microwave Theory and Techniques*, Vol. 58, No. 12, pp. 4072-4078, Dec. 2010.

[**Tokgoz, 2016**] K. K. Tokgoz, S. Maki, S. Kawai, N. Nagashima, J. Emmei, M. Dome, H. Kato, J. Pang, Y. Kawano, T. Suzuki, T. Iwai, Y. Seo, K. Lim, S. Sato, L Ning, K. Nakata, K. Okada, A. Matsuzawa. "A 56Gb/s W-band CMOS wireless transceiver," *IEEE International Solid-State Circuits Conference*, pp. 242-243, Feb. 2016.

[**Tokgoz, 2018**] K. K. Tokgoz, S. Maki, J. Pang, N. Nagashima, I. Abdo, S. Kawai, T. Fujimura, Y. Kawano, T. Suzuki, T. Iwai, K. Okada, A. Matsuzawa. "A 120Gb/s 16QAM CMOS millimeter-wave wireless transceiver," *IEEE International Solid-State Circuits Conference*, pp. 168-169, Feb. 2018.

[**TU-Berlin, 2015**] Neighbor discovery and tracking in mm-wave networks, TU-Berlin, 2015. [Online] available at https://www.tkn.tu-berlin.de/fileadmin/_processed_/a/a7/csm_mm_ Wave_Networks_1_d2c7ee19b2.png.

[**Tytgat, 2013**] M. Tytgat and P. Reynaert. "A plastic waveguide receiver in 40nm CMOS with on-chip bondwire antenna," *Proceedings of the European Solid-State Circuits Conference*, pp. 335-338, 2013.

[**Van Thienen, 2016**] N. Van Thienen, Y. Zhang, M. De Wit and P. Reynaert. "An 18Gbps polymer microwave fiber (PMF) communication link in 40nm CMOS," *Proceedings of the European Solid-State Circuits Conference*, pp. 483-486, 2016.

[**Villegas, 1999**] F. J. Villegas, D. I. Stones, and H. A. Hung. "A novel waveguide-to-microstrip transition for millimeter-wave module applications," *IEEE Transactions on Microwave Theory and Techniques*, Vol. 47, No. 1, pp. 48-55, Jan. 1999.

[**Voineau, 2017**] F. Voineau, A. Ghiotto, E. Kerhervé, M. Sié and B. Martineau. "Broadband 55 – 95 GHz microstrip to waveguide transition based on a dielectric tip and a tapered double-ridged waveguide section," *IEEE International Microwave Symposium,* pp. 723-726, 2017.

[**Voineau, 2018**] F. Voineau, C. Dehos, B. Martineau, M. Sié, M. Perchicot, N. H. Nguyen, A. Ghiotto and E. Kerhervé. "A 12 Gb/s 64QAM and OFDM compatible millimeter-wave communication link using a novel plastic waveguide design," *Proceedings of the IEEE Radio and Wireless Symposium*, pp. 250-252, 2018.

[**Volkaerts, 2015**] W. Volkaerts, N. Van Thienen and P. Reynaert. "An FSK plastic waveguide communication link in 40nm CMOS," *Proceedings of the IEEE International Solid-State Circuits Conference*, pp. 178-180, 2015.

[**Zhang, 2016**] Y. Zhang, D. Zhao and P. Reynaert. "A flip-chip packaging design with waveguide output on single-layer alumina board for E-band applications," *IEEE Transactions on Microwave Theory and Techniques*, Vol. 64, No. 4, pp. 1255-1264, Apr. 2016.

Chapter 4

Designing a Millimeter-wave RFIC Targeting Multi-Gigabit Operation

4.1. Transmitter Architecture

Following the system level specifications discussed in Chapter 3, the implementation of the dual-band QPSK transmitter is now investigated in Chapter 4. An overall schematic is presented in Figure 4-1. While both chains are quite similar and relatively classical, it should be mentioned that the novelty of this architecture is the presence of shared input reference and output pins. In other words, an integrated hybrid coupler designed at 16.7 GHz is used as a power divider at the input and another hybrid coupler designed at 75 GHz is used as a power combiner at the output. The choice of an integrated hybrid coupler to realize these functions is mainly motivated by the feasibility of strong and wideband isolation characteristics. Their detailed characteristics are given in sections 4.4 and 4.8.

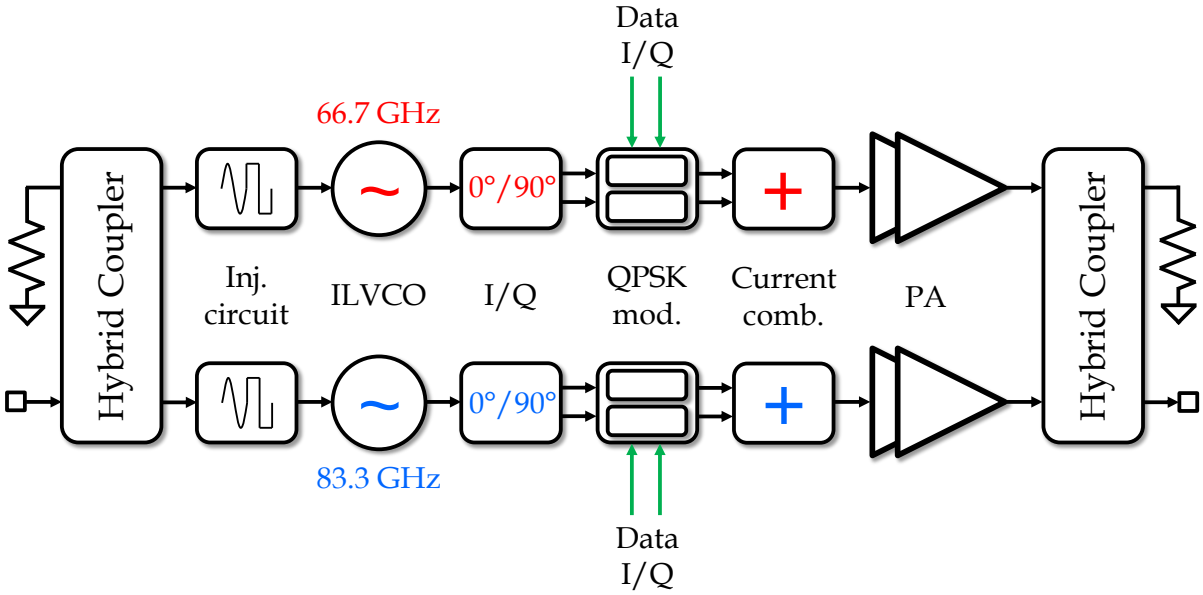

Figure 4-1: Overall schematic of the proposed dual-band QPSK transmitter.

Note that 66.7 GHz and 83.3 GHz operating frequencies as well as the 16.7 GHz input reference frequency have been chosen carefully. Indeed, to benefit from the developments presented earlier, operating bands should be centered around 75 GHz (middle of the E-band). Moreover, the input reference frequency, which is a common sub-multiple of the two operating frequencies, is chosen between 15 and 20 GHz since reasonable frequency multiplication ratios (< 7 - 8) are desired and signal synthesis circuits typically report good performance in this frequency range. Even though the integration of such circuits is beyond the scope of this work, it would be necessary in the context of an advanced future demonstrator. This constraint has thus been taken into account for frequency planning although the signal is actually delivered by an external generator. The exact derivation of the frequency plan is given in Appendix G, showing that the proposed solution is actually the only one satisfying the above conditions.

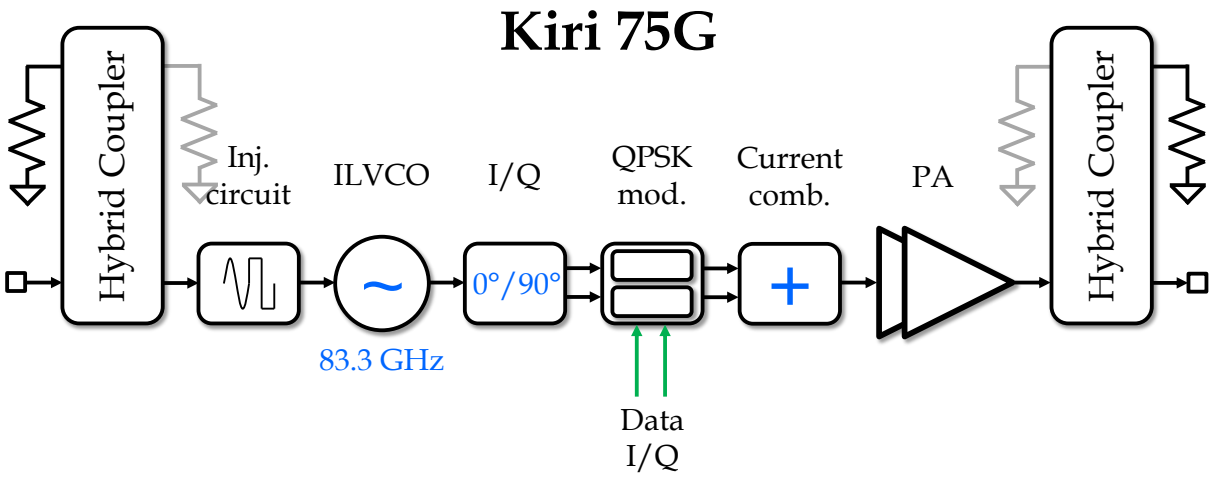

Figure 4-2: Overall schematic of the realized 83.3 GHz QPSK transmitter.

Unfortunately, the dual band QPSK architecture described in Figure 4-1 has not been designed completely because of limited time-frame. A single-band QPSK chain has been designed instead, as visible in Figure 4-2, with all the necessary functions. The highest band has been chosen to validate frequency locking with the most aggressive frequency multiplication ratio while input / output hybrids are terminated by matched loads. It is the purpose of this Chapter to present the design of each block briefly. After a short presentation of the technology from both front-end and back-end points of view, the oscillator is firstly described. Then, the injection circuit (including the input hybrid coupler), which is only used in the case of injection-locking operation, is discussed. Next, quadrature signal generation, QPSK modulation, current combination, power amplification and the output hybrid coupler are presented sequentially. Finally, validation measurements are shown.

4.2. Overview of STMicroelectronics 28 nm CMOS FD-SOI Technology and Comparison with the State of the Art

In this section, the technology used for circuit implementation is discussed briefly. It is the 28 nm CMOS FD-SOI node offered by STMicroelectronics. Interestingly, this technology benefits from an additional design flexibility at transistor level because of the introduction of a "back-gate" allowing a large body-biasing dynamic. Moreover, both reverse and forward body biasing are possible. Although this unique feature has not been used in this work, additional information may be found in multiple sources [**Larie, 2015**] [**Cathelin, 2017**].

On top of solid front-end and back-end of line performances suitable for mmW operation, the choice of this technology is in fact mainly motivated by integration compatibility with high-speed and low-power digital circuits at relatively low costs. Meanwhile, 28 nm FD-SOI high frequency capability is studied in the following sections.

4.2.1. Front End of Line Performance

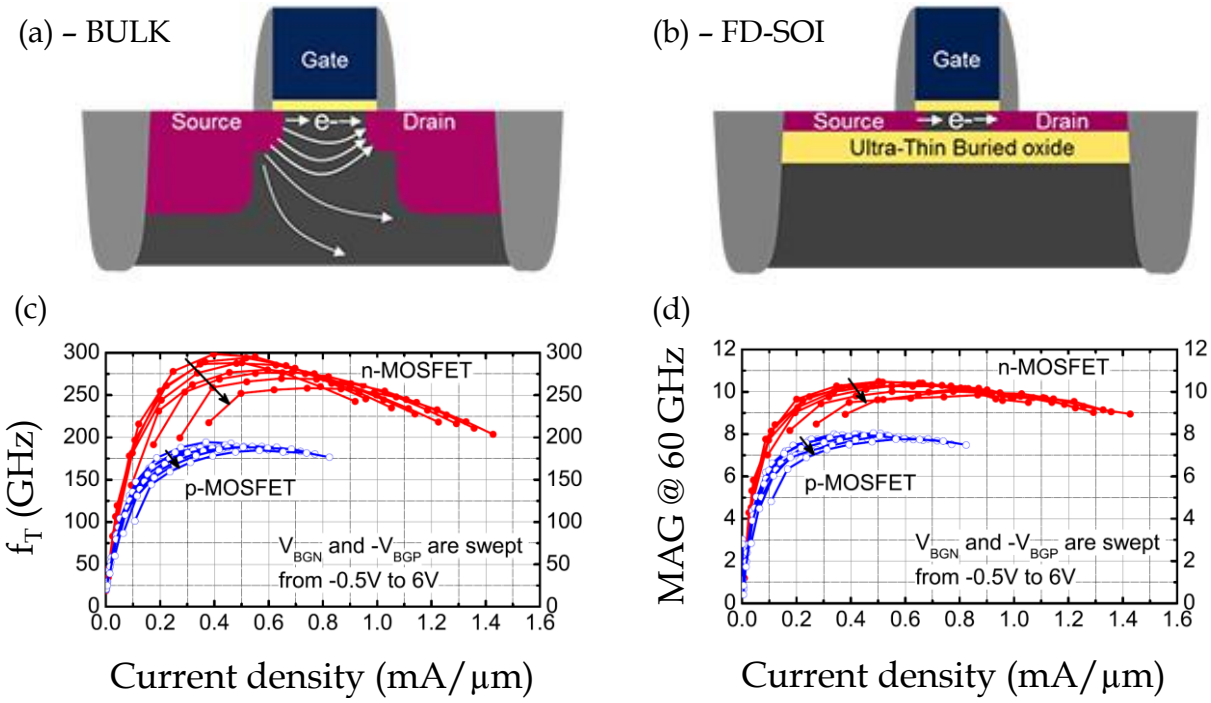

Figure 4-3: Superior FD-SOI transistor performance. Cross-section comparative view of a Bulk transistor (a) and a FD-SOI transistor (b) respectively. Transition frequency f_T (c) and Maximum Available Gain at 60 GHz (d) as measured in 28 nm FD-SOI (including full back-end of line parasitics). Data reproduced from ***[Shopov, 2014]****.*

Figure 4-3 (a) and Figure 4-3 (b) present a cross-section comparative view of a FD-SOI transistor with respect to a traditional Bulk one. The introduction of a Buried Oxide layer enhances the electrostatic control of the channel and reduces source-drain parasitic capacitance. Consequently, peak transition frequency (f_T) and peak maximum oscillation frequency (f_{max}) in excess of 300 GHz have been demonstrated in **[Cathelin, 2017]**. In Figure 4-3 (c), the f_T is also investigated as a function of applied body biasing. It shows that optimum performance can be tuned to higher current densities, which is especially interesting in the design of high-frequency power amplifiers. Maximum Available Gain (MAG) is measured at 60 GHz in Figure 4-3 (d) in similar conditions. While peak MAG remain close to 10 dB, corresponding current densities also move to higher values, which is very desirable. Such a very high frequency capability makes this technology node a very suitable choice for mmW circuit design.

Comparing these intrinsic performances to other technology nodes is very insightful. In Figure 4-4 (a) and Figure 4-4 (b), it is worth noting that RF CMOS technologies can compete with Silicon-Germanium Heterojunction Bipolar Transistors (SiGe HBT) and Indium-Phosphide (InP) HBT at the expense of more aggressive lithography processes. The use of SiGe HBT or InP HBT thus makes sense for RF purposes. However, the integration of high-speed

digital functions at low cost (which is an important key success factor as mentioned earlier) is not satisfying. Besides, advanced CMOS technologies have the potential to meet all these needs. In this context, the 28 nm FD-SOI node clearly offers best-in-class performances among the CMOS devices thanks to a reduced gate length. In addition, pushing the reduction further seems attractive when considering the linear regressions in Figure 4-4, as even higher performances may be expected.

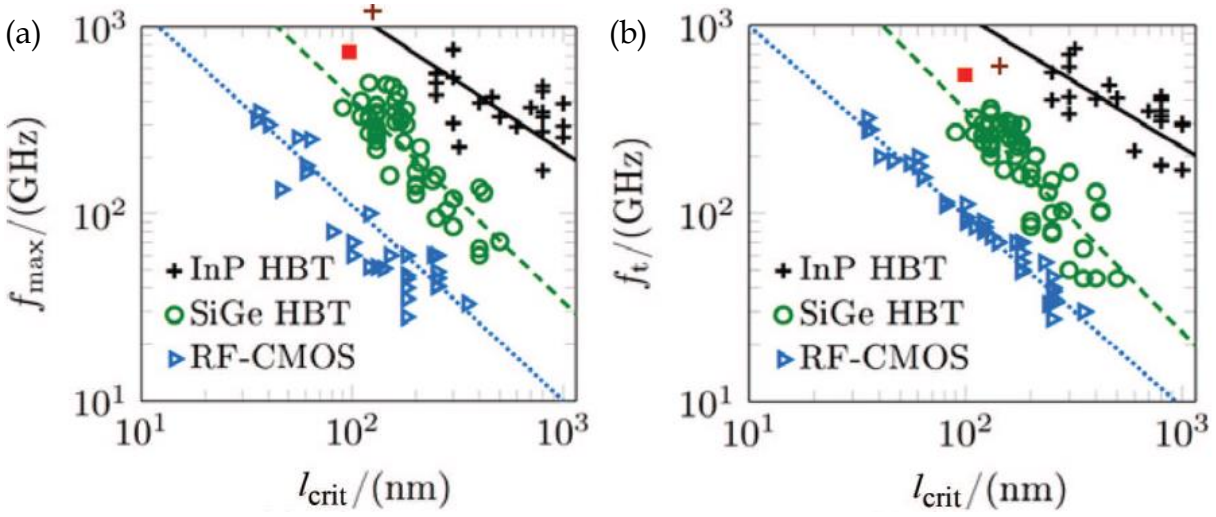

Figure 4-4: Summary of peak f_T (a) and f_{max} (b) for different technological processes as a function of the critical lithography dimension (i.e., emitter width or channel length). Note that red squares represent the results of the DOTSEVEN project (SiGe HBT), while the brown crosses are the best InP HBT data available. Figures reproduced from ***[Rinaldi, 2018]****.*

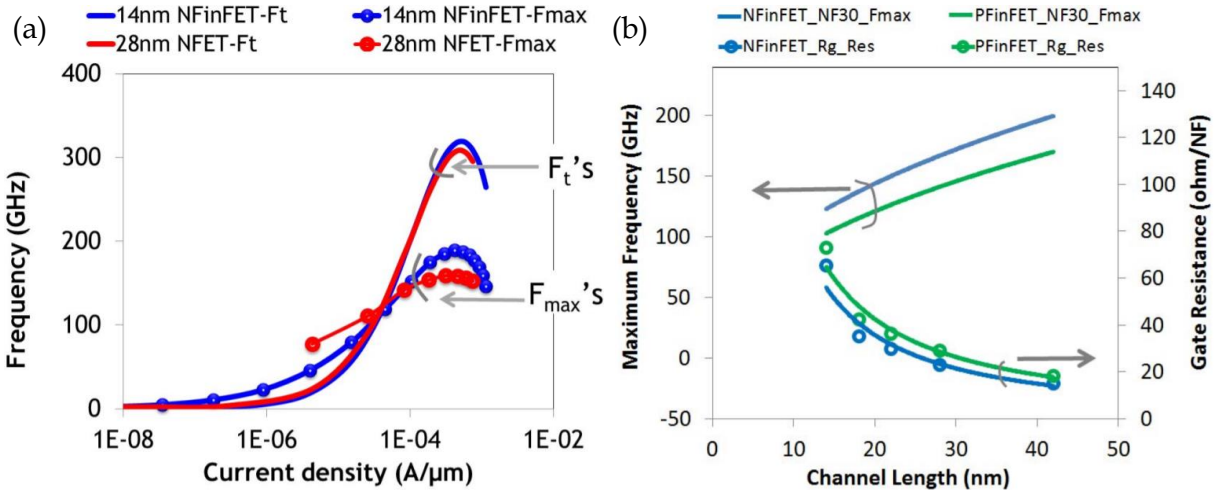

Figure 4-5: FinFET high-frequency behavior investigation. (a) f_T and f_{max} comparisons between the 28 nm (planar) and 14 nm (FinFET) technologies. (b) f_{max} and gate resistance evolution as a function of the channel length in the 14 nm FinFET process. Figures reproduced from ***[Singh, 2018]****.*

However, starting from the 22 nm node, the CMOS industry has actually moved from planar to 3D structures named FinFET. Mainly driven by improved digital performances and favorable area scaling, this topology unfortunately suffers from disappointing performances from the RF / mmW point of view, as illustrated in Figure 4-5 (a). In this figure, it is clear on both f_T and f_{max} metrics that rather limited progress is actually offered to the RF designer. Among other parasitics resulting from the FinFET architecture, Figure 4-5 (b) shows that detrimental gate resistances are responsible for significant f_{max} reduction, especially at lower channel lengths. Furthermore, the power dissipation capability, which is an important metric for most power amplifiers, is very constrained too because FinFET channels have a large

thermal isolation from the substrate. To sum up, the 28 nm CMOS FD-SOI node has been selected as an excellent traded-off for both digital and RF / mmW performances as well as fabrication costs.

4.2.2. Back End of Line Performance

Although FEOL performance is critical for the design of efficient mmW circuits, Back End of Line (BEOL) contribution is also significant. The ability to design high quality factors passive devices like transmission lines, inductors, transformers or baluns is in fact related to many technology parameters including the number of metal layers, their thicknesses, the total dielectric thickness and the substrate conductivity. In Figure 4-6, the most advanced standard processes from STMicroelectronics are compared qualitatively. Interestingly, the BEOL of the 28 nm FD-SOI node features two thick copper metal layers (≈ 1 µm) similar to those on CMOS 40 nm and 65 nm processes but singularly offers a thicker Aluminum Cap layer than previous nodes. Initially introduced to meet stringent mechanical rules (copper pillar assembly), this metal layer has also good RF characteristics because of low resistance and low parasitic capacitance. Besides, the comparison the BiCMOS 55 nm technology, which is fully dedicated to high-frequency applications, is instructive. Indeed, the presence of an additional very thick-copper layer (≈ 3 µm), far from the substrate, can also be leveraged for the design of low-loss mmW passive devices.

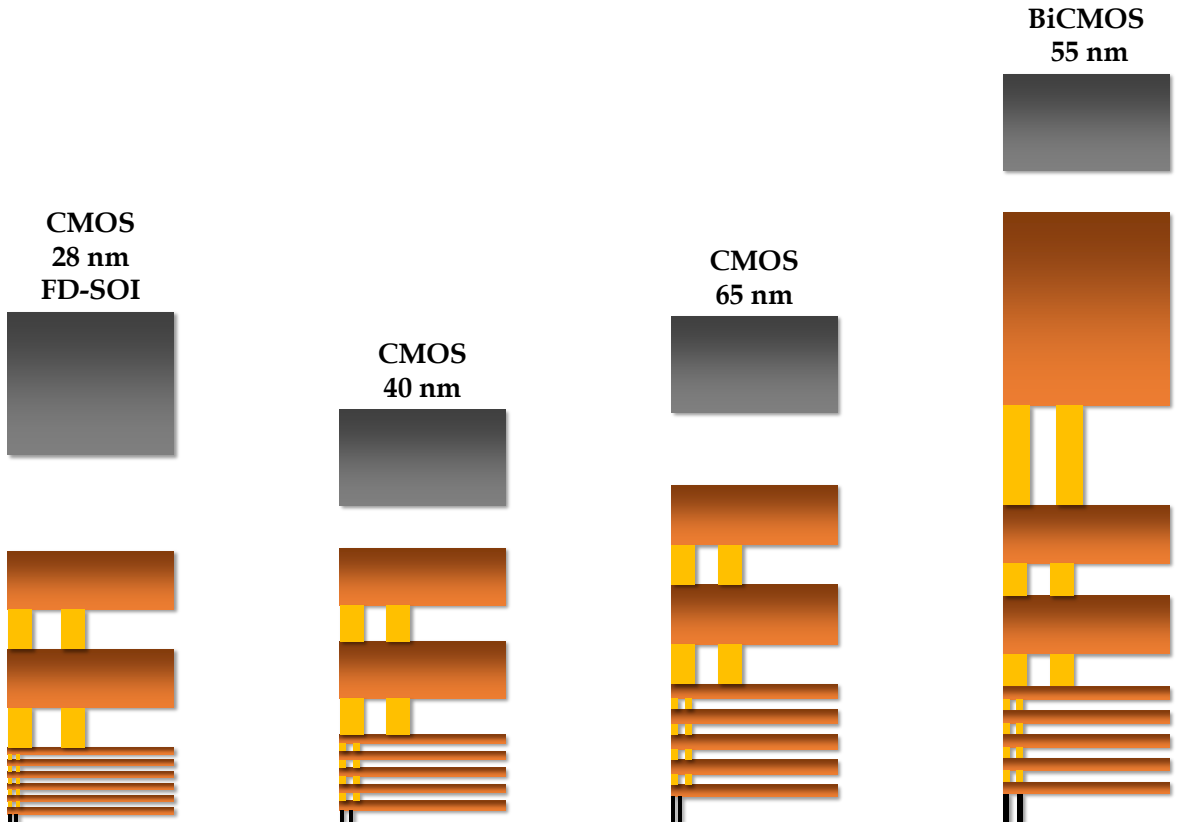

Figure 4-6: BEOL stacks comparison for advanced technology nodes available from STMicroelectronics (standard processes).

In order to provide insights on high-frequency capabilities of the previously evocated technologies, 50 Ω microstrip lines have been designed and simulated with Momentum. As an example, the simulation model used in 28 nm FD-SOI is shown in Figure 4-7 (a) while

attenuation results are summarized in Figure 4-7 (b). Due to its very high stack, BiCMOS 50 Ω microstrip is much larger, clearly exhibiting a superior performance. Nevertheless, advanced CMOS nodes show very acceptable results, especially as regards the CMOS FD-SOI one, with attenuations lower than 0.9 dB/mm. Although it is definitely not an exhaustive investigation, this school-case study highlights the mmW capability of the selected CMOS 28 nm FD-SOI.

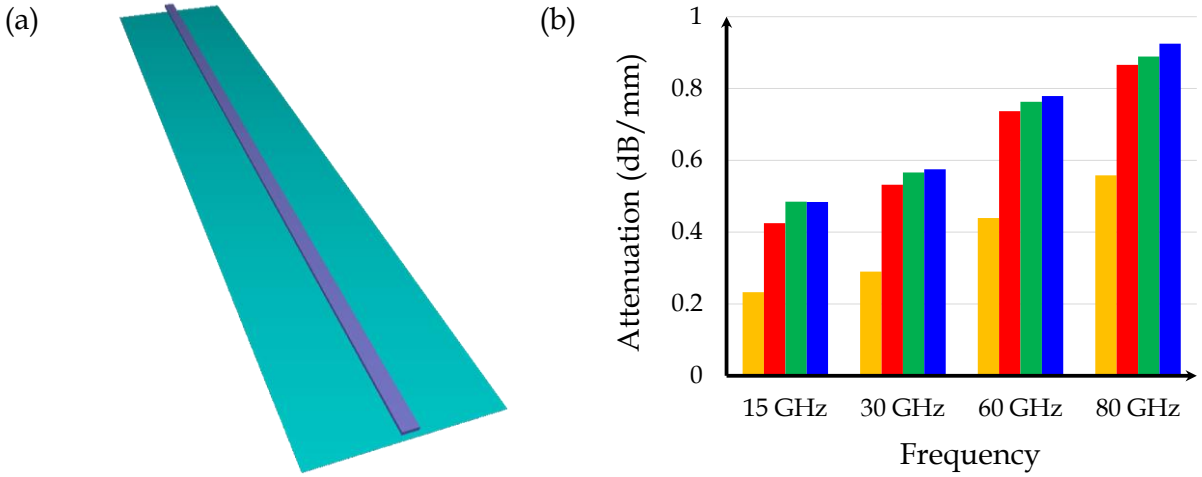

Figure 4-7: Transmission lines simulations for different technology nodes. (a) simulation model and (b) simulated attenuations. Orange, red, green and blue refer to BiCMOS 55 nm, CMOS 28 nm FD-SOI, CMOS 40 nm and CMOS 65 nm respectively.

4.3. Low Power Oscillator

The schematic of the realized ILO is shown in Figure 4-8 and is illustrated in Figure 4-9. The L-C tank is made of a transformer in addition to a 4-bit switched capacitors bank. All passive devices have been carefully designed using EM simulation tools, including capacitors and accesses of the bank. While MIM capacitors typically offer good capacitance density with high quality factors, they require additional process steps that increase manufacturing costs. In contrast, MOM capacitors are directly made in the BEOL (no extra cost) at the expense of larger required areas. In our case, as only reasonable capacitance values are needed to achieve a large tuning range (≈ 10%), plate MOM capacitors have been designed. To compensate for manufacturing variability as well as EM simulation inaccuracy, the switched capacitors bank has four tuning bits.

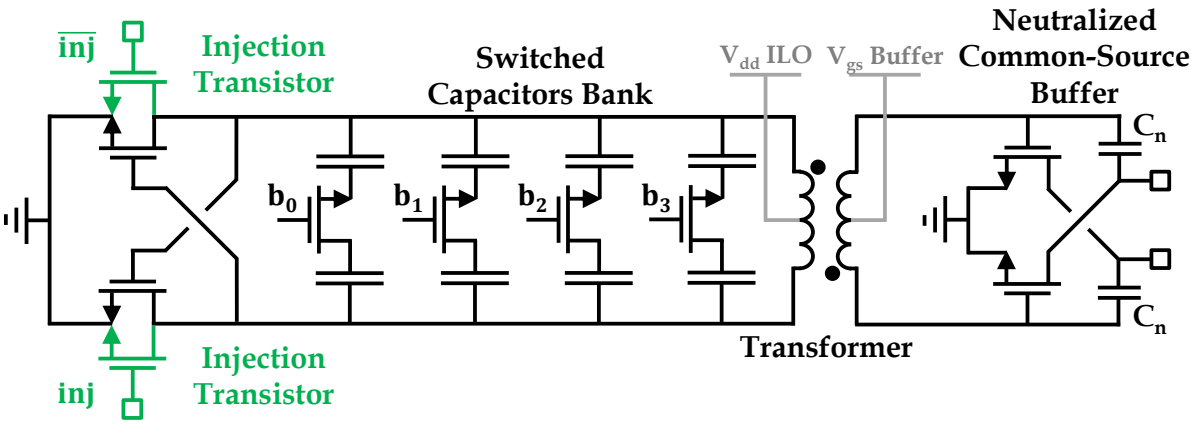

Figure 4-8: Schematic of the realized Injection-Locked Oscillator featuring four tuning bits (biasing components not shown).

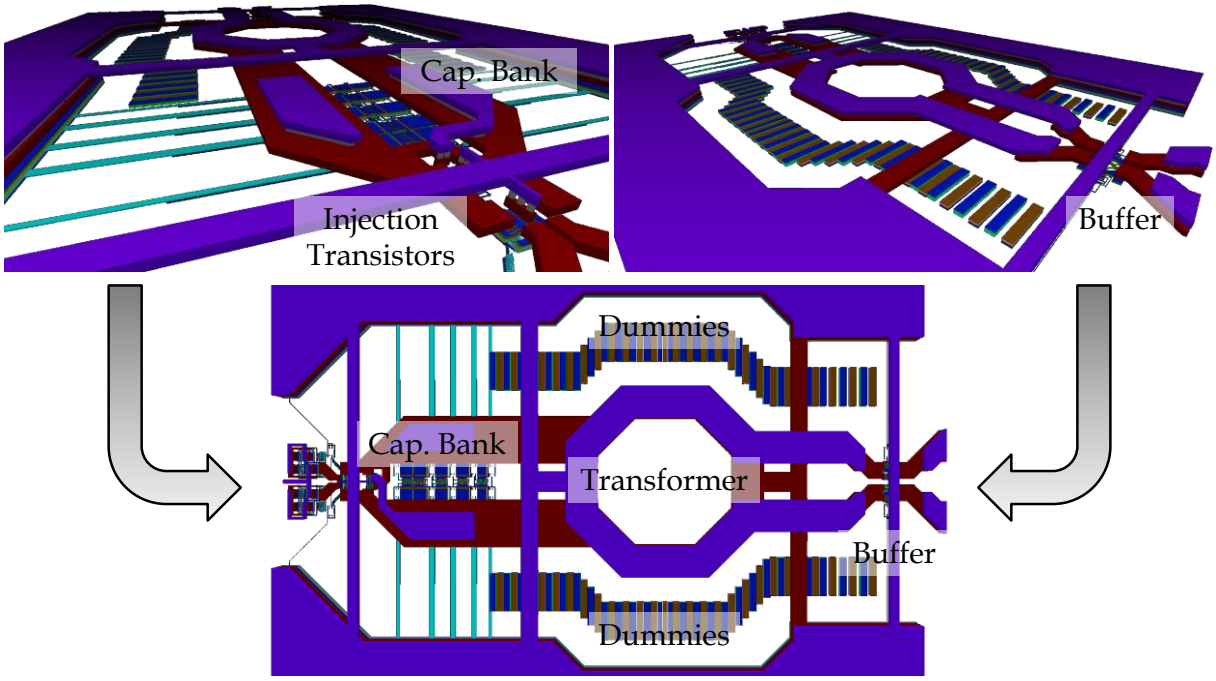

Figure 4-9: Different layout views of the realized ILO.

Note that metal densities have been carefully optimized to comply with stringent technology rules. In order to minimize additional parasitics introduced by automated tiling generation, metal densities have been satisfied manually. Ground plane spacing is maximized while still satisfying top metal layers densities. Consequently, no "Dummies" are required for these metals. However, as the transformer does not include any thin layer metals, long and thin shapes (bars) are placed around the structure to compensate for metal absence (Figure 4-9). These shapes are preferred to avoid Eddy currents, which would otherwise alter transformer operation. Moreover, their position (outside the transformer) is likely to induce minimal perturbation. A staggered layout is also proposed to reduce capacitive couplings between bars. Finally, it should be noted that such a layout might not be optimized in terms of detrimental couplings reduction and densities homogeneity. However, such a manual configuration has the great advantage of being compatible with EM simulation tools contrary to automated tiling. In other words, manual tiling is potentially worst but introduced degradation can be quantified by simulation while the complexity of automated tiling is clearly out of reach.

	Injection	**Oscillator**	**Switches**				**Buffer**
			b_0	b_1	b_2	b_3	
Transistors widths (µm)	2x 12.3	2x 12.3	2x 12.3	12.3	12.3	12.3	2x 12.3
Transistors Lengths (nm)	30	30	30	30	30	30	30

Biasing and supply voltages	
V_{dd} ILO	500 m
V_{gs} Buffer	500 m
V_{dd} Buffer	850 m

Table 4-1: ILO transistors sizing and associated biasing and supply voltages.

Transistor sizes and biasing conditions are summarized in Table 4-1. It is worth noting that supply voltages are well below 1 V (nominal value of this technology). In fact, V_{dd} ILO is chosen at 500 mV to reduce consumption and free-running noise. Reliability is of primary interest as regards V_{dd} Buffer, because the transistors output impedance is high, which causes large voltage swings. Furthermore, as an output power of around 0 dBm was targeted, V_{dd} is fixed to 850 mV. Oscillation frequencies are presented in Figure 4-10 showing around 7 GHz tuning capability roughly centered at 83 GHz in both injected and free-running modes.

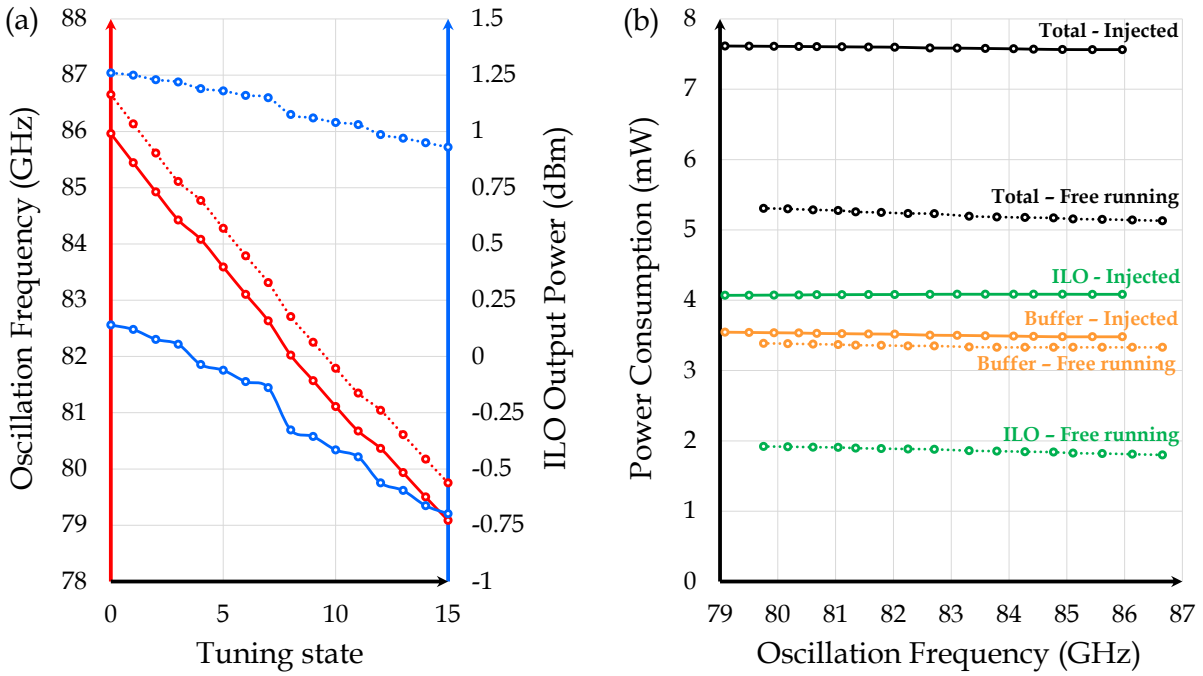

Figure 4-10: Simulated ILO main electrical metrics. (a) Oscillation frequency and output power for all 4-bit tuning states in free-running (dot) and injected (solid) modes. (b) Detailed ILO power consumption as a function of the oscillation frequency.

4.4. Injection Circuit for Locked Operation

The injection circuit is composed of an input balun, a Differential Vertical Hybrid Coupler (DVHC) and a large differential inverter (Figure 4-11). The balun realizes single-to-differential conversion. On the differential side, a 150 fF MOM capacitor (C_{tune}) is used to decrease the resonant frequency and lower the balun area requirement (Figure 4-12). Moreover, taking into account the parasitic capacitance of the input signal pad (C_{PAD}), such a resonant network achieves a wideband impedance matching as illustrated in Figure 4-13. Note that a 70 Ω differential impedance is considered at the DVHC port. In such a configuration, a wideband power transfer is also obtained. From Figure 4-13, minimum insertion loss is 0.95 dB at 16.7 GHz and the -3 dB-bandwidth exceeds the 9 – 35 GHz range, ensuring good circuit robustness.

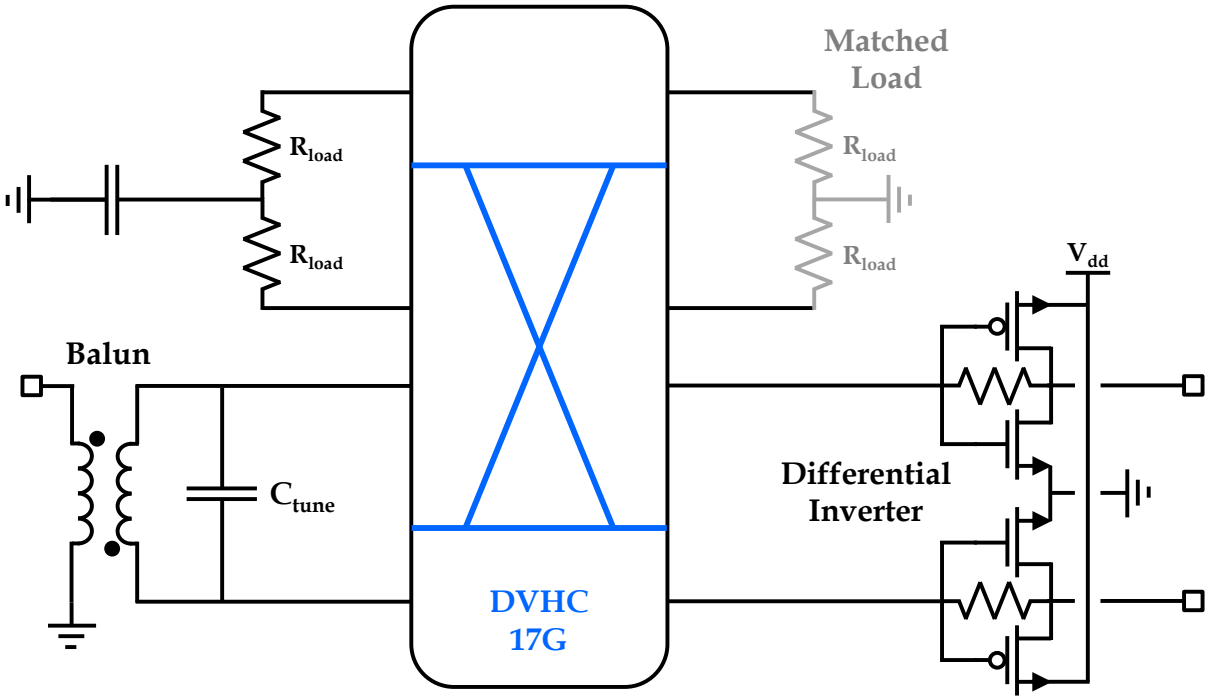

Figure 4-11: Schematic of the realized injection circuit.

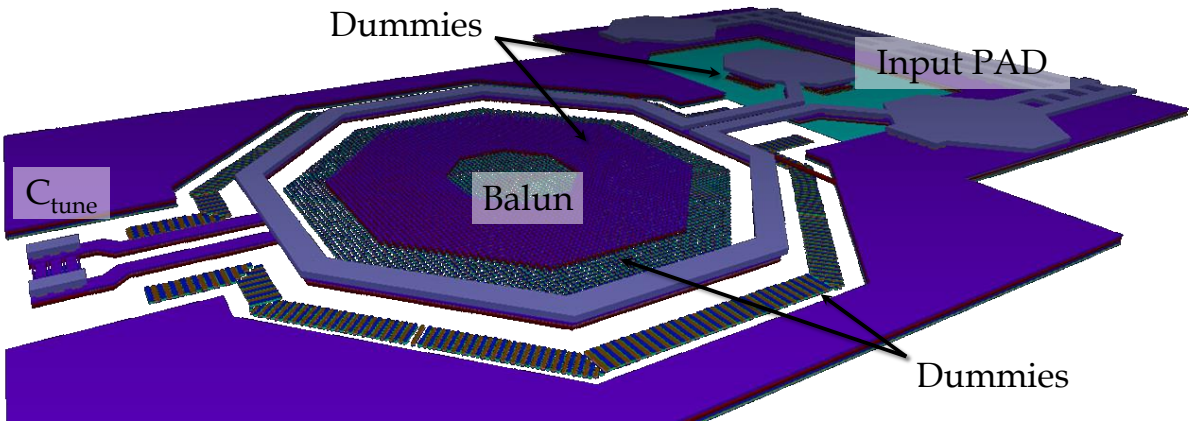

Figure 4-12: Layout view of the realized 17 GHz input matching circuit.

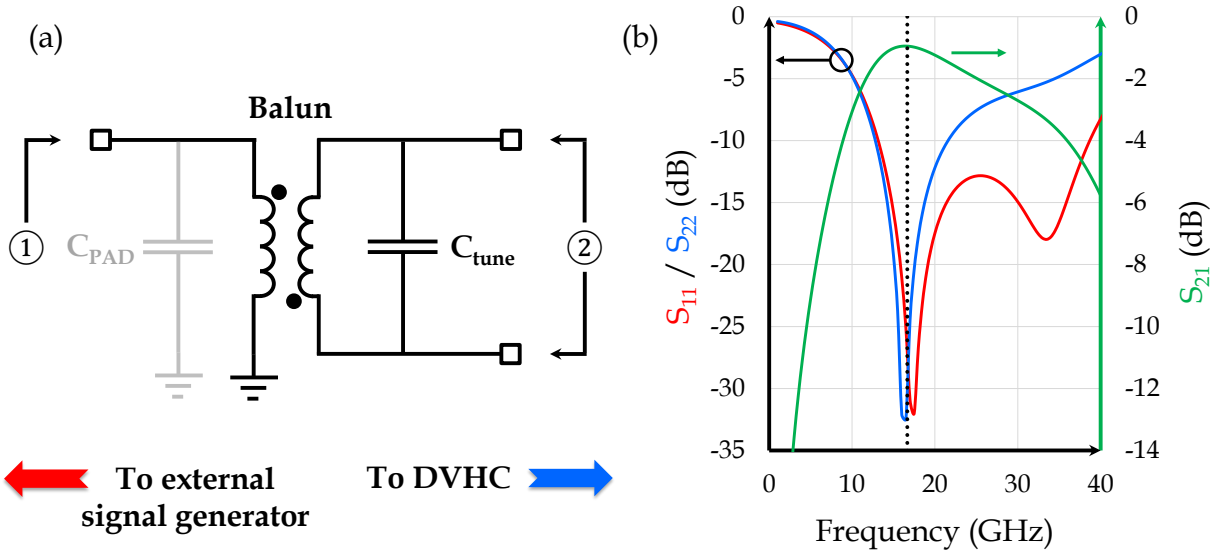

Figure 4-13: Simulated input matching circuit. (a) Equivalent matching network and (b) simulated S-parameters.

The DVHC is centered at around 17 GHz to allow good power division of the reference signal. For simplicity reasons, it features the same topology as developed for the output DVHC, which is centered at around 75 GHz (section 0). From Figure 4-14, the same metal density strategy as described in section 4.3 has been enforced. However, it was not possible to simulate all thin metal bars due to excessive complexity. Therefore, simulation results presented in Figure 4-15 only take into account central dummies in between the magnetically coupled differential lines and the ground walls surrounding the structure. From this latter figure, it is very clear that a very wideband behavior is obtained. In fact, return losses are larger than 20 dB from 0 to 35 GHz. Moreover, a rather large-band power division occurs around 17 GHz where a 0.67 dB insertion loss is simulated in addition of the 3-dB power split. Isolation between CPL and OUT ports is close to 30 dB at the desired frequency and it exhibits a wideband characteristic as well. On top of a differential by-design topology, such a large and robust isolation feature is the main motivation to choose this topology. Additionally, the realized DVHC core length equals 894 µm (Figure 4-14). Taking into account the technology shrink (x0.9) and BEOL equivalent dielectric permittivity (≈ 4), this length represents only 0.09 λ which make it a very compact structure.

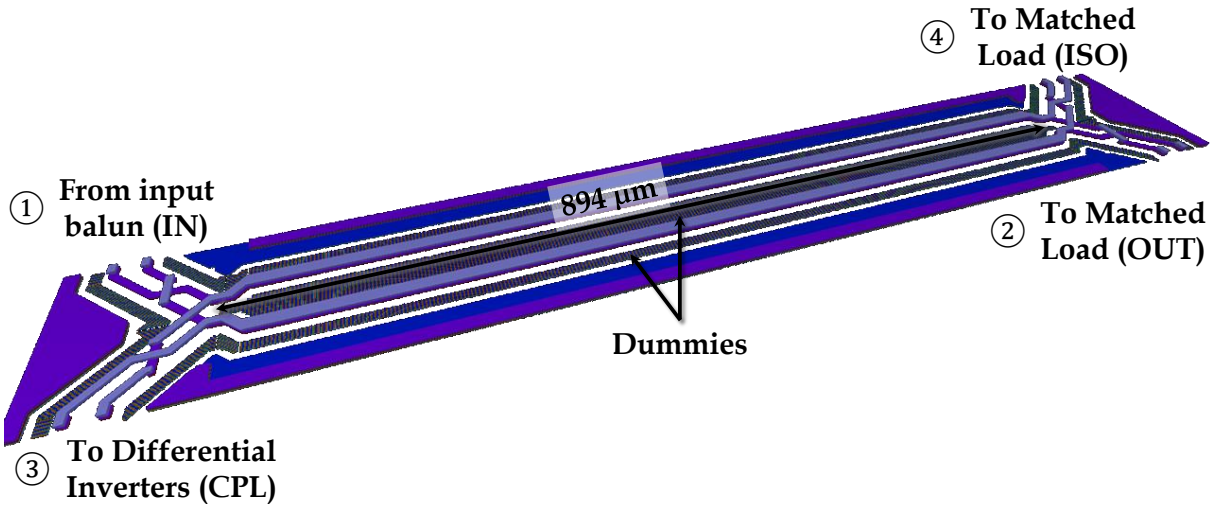

Figure 4-14: Layout view of the realized 17 GHz DVHC.

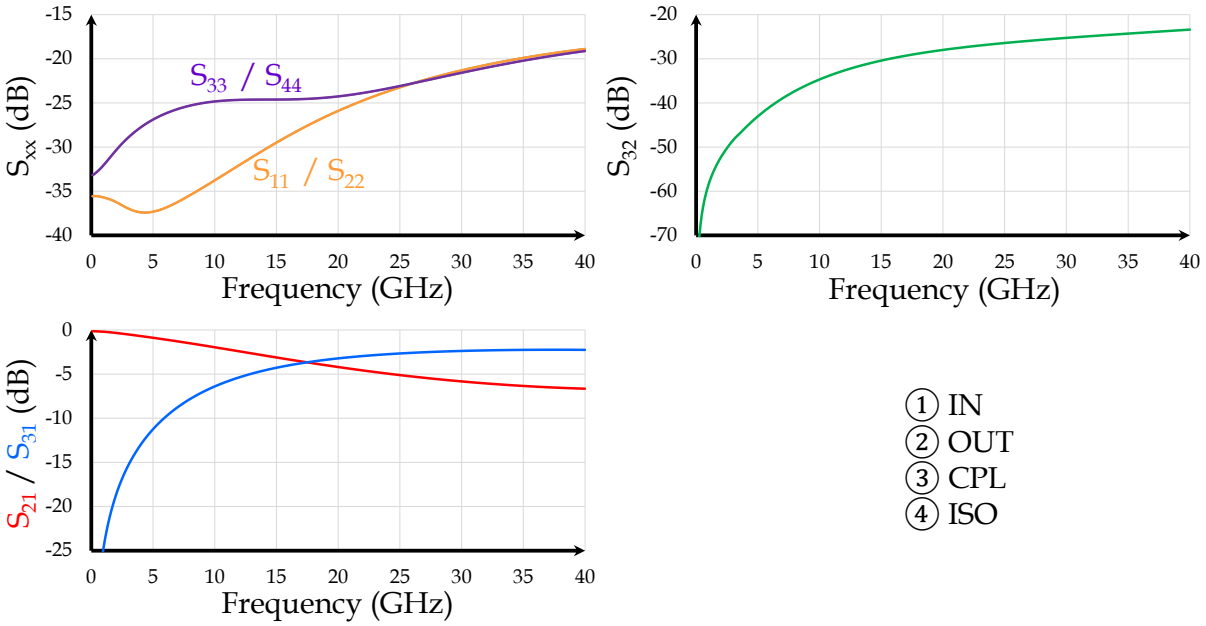

Figure 4-15: Simulation results of the 17 GHz DVHC.

Finally, a large inverter cell turns the pure sinusoidal reference into square-like signals then generating the necessary harmonics for the ILO. This block therefore relies on non-linear characteristics of inverters to generate a rich harmonic content. Note that a large feedback-resistance (10.7 kΩ) is used in this design (Figure 4-16 (a)) to ensure inverters self-polarization. Unfortunately, introducing a feedback resistance usually results in inverter gain linearization, which is obviously not desired here. Considering a -8 dBm constant input power on a single-ended inverter, Figure 4-16 (b) clearly shows that fifth harmonic generation as well as power consumption are improved for larger feedback resistances. Consequently, a large 10.7 kΩ resistance is implemented.

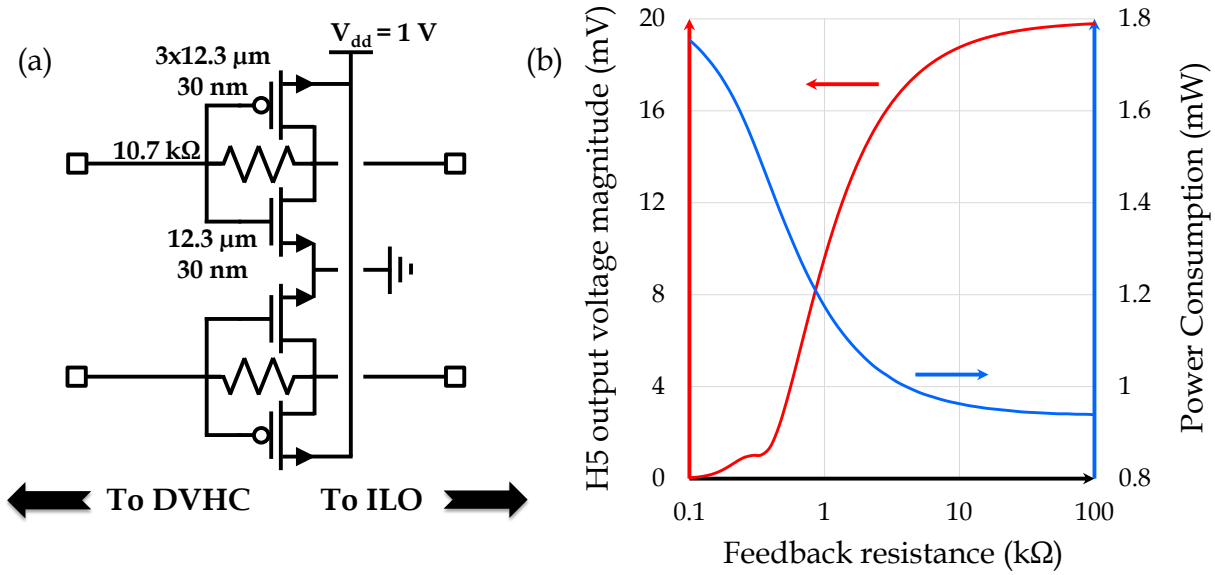

Figure 4-16: Resistance-feedback inverter design. (a) Realized differential inverters and (b) simulated impact of the resistance feedback on the generation of the fifth harmonic at 83.33 GHz and the power consumption (considering a single-ended feedback inverter).

4.5. Quadrature Signal Generation

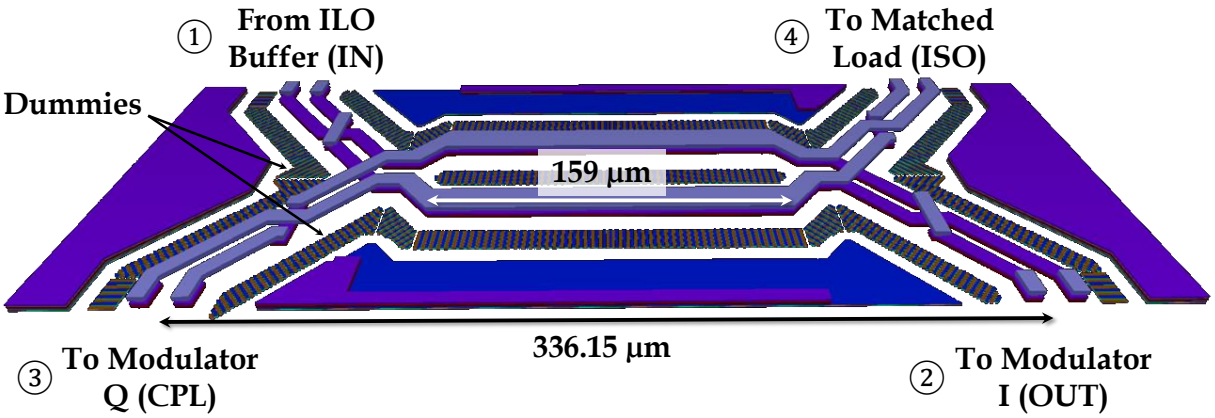

Figure 4-17: Layout view of the realized 83 GHz DVHC used as a quadrature signal generator.

Leveraging on the versatility of this component, a DVHC is implemented in this section to generate quadrature signals from the ILO as presented in Figure 4-17. In this context, the amplitude imbalance and the phase offset as well as the outputs isolation are essential figures of merit. Corresponding simulation results are shown in Figure 4-18. From this figure, it is clear that this design achieves accurate and wideband quadrature signals. Although the

coupler is perfectly balanced only at 83.1 GHz, it features a large frequency range from 72.4 to 96.2 GHz where the amplitude imbalance is lower than 1 dB, which represents more than 28 % fractional bandwidth.

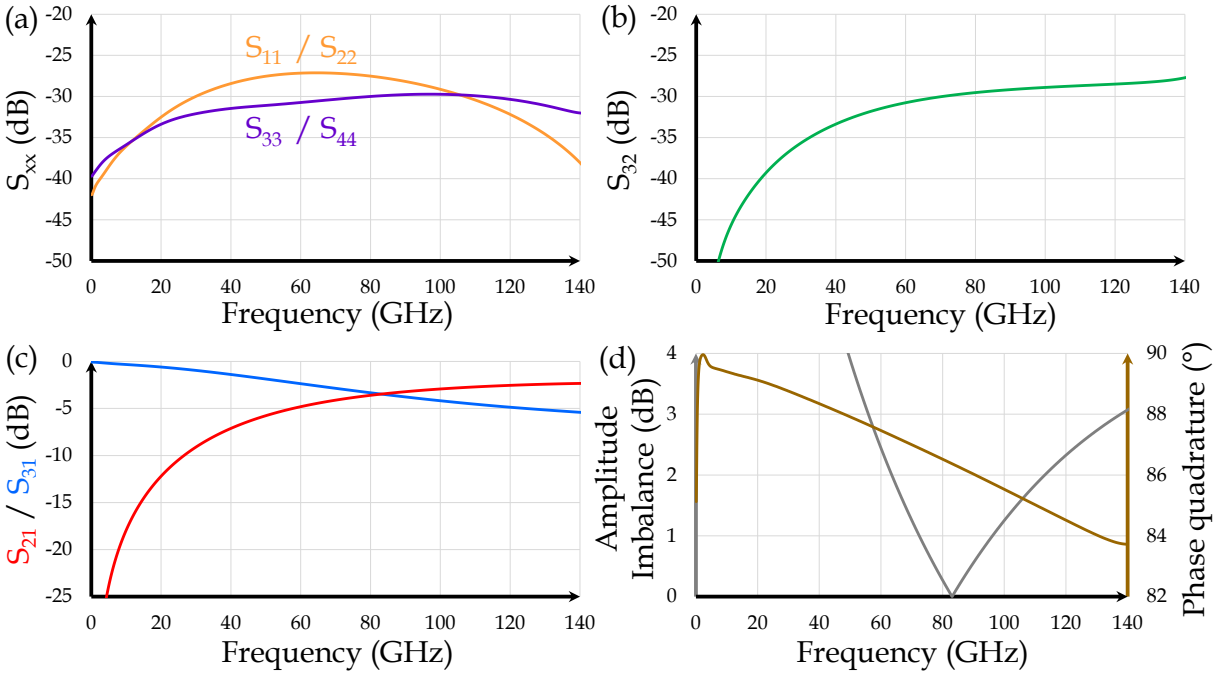

Figure 4-18: Simulation results of the realized quadrature signal generation implemented thanks to an appropriately scaled DVHC: (a) reflection parameters, (b) outputs isolation, (c) transmission parameters, (d) amplitude imbalance (grey) and phase quadrature (brown). For simplicity, all ports are loaded by 70 Ω differential loads and dummies are not simulated. Port numbers are taken from Figure 4-17.

In this frequency range, phase quadrature remains very close to 90° (86.37° at 83.1 GHz) and only shows 1.2° variation thus exhibiting a weakly frequency-dependent behavior that is very desirable for robust quadrature synthesis. In addition, both wideband and strong reflection losses along with an isolation in the order of 30 dB are obtained assuming 70 Ω ports impedance. Finally, the simulated insertion loss at 83.1 GHz is only 0.47 dB on top of the 3 dB power split.

Considering all these metrics together, it appears that the overall performance of the designed DVHC for quadrature signals generation are excellent. What is more, Figure 4-17 indicates that the function is realized in a very compact layout. In this implementation, the length of the accesses are not negligible so that the total coupler length is 336.15 µm. Taking into account the technology shrink (x0.9) and BEOL equivalent dielectric permittivity (≈ 4), this length represents only 0.17 λ which make it a very compact structure, especially compared to conventional branch line couplers based on 0.25 λ transmission lines.

4.6. QPSK Modulator

Contrary to most common implementations relying on double-balanced Gilbert cell mixers, the proposed QPSK modulator is a passive structure and results in a much more straightforward design. It is mainly composed of two pairs of differential switches interfacing with each I/Q signal path. They operate in a phase-reversal manner as illustrated in

Figure 4-19 (a). From this figure, four 24.6 µm-wide transistors are necessary to achieve low insertion loss (1 dB simulated at 83.3 GHz) and high power compression (7 dBm). Note that such a design actually benefits from self-neutralization since blocked transistors neutralize source / drain parasitic capacitors and therefore increase linearity. However, this advantage comes at the unobvious expense of a transistor width trade-off, so that insertion loss no longer reduces while transistors width increases. Similarly, forward body biasing results in worst insertion losses as transistors conductance has wider dynamics in blocked states (subthreshold regime) compared to passing states (saturation regime), and then causes signal cancelation.

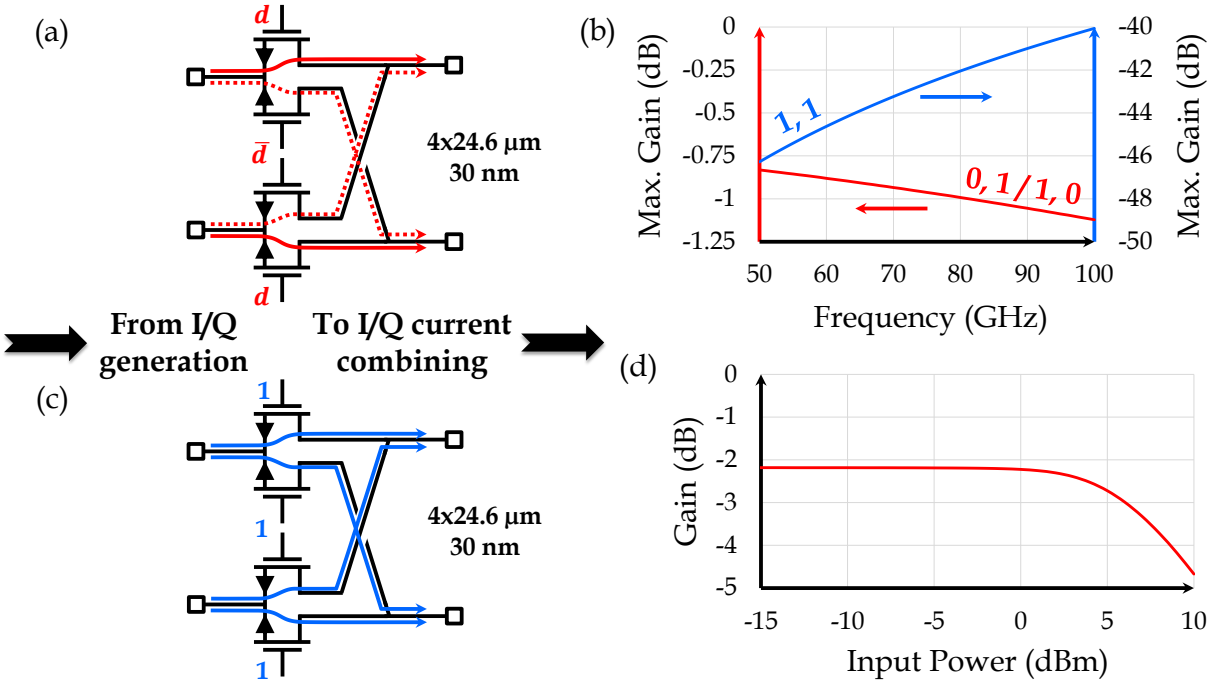

Figure 4-19: Realized QPSK modulator. The proposed schematic allows phase reversal operation (a) as well as strong amplitude cancellation (c) depending on applied voltages. Simulated maximum gain versus frequency for these two operating modes are shown in (b). In (d), gain compression at 83.3 GHz is visible above 0 dBm, assuming a 70 Ω differential input impedance and an optimum output load impedance. All simulations include full-layout parasitics.

Leveraging on this remark, an alternative mode is proposed in Figure 4-19 (c), in which all transistors gates are set to 1 V causing strong attenuation due to signal destructive interference. In practice, since simulated maximum gain is less than -40 dB in Figure 4-19 (b), actual attenuation assuming practical impedances may be even lower. Consequently, a very large isolation is possible (> 40 dB) making this design an excellent candidate for OOK as well. Although an OOK alternative mode would totally make sense in the frame of the innovative QPSK demodulation discussed in Chapter 3, it has unfortunately not been implemented in this work because of time limitations.

With the conditions of this alternative mode in mind, and coming back to the original phase-reversal mode, a careful attention should then be paid on accurately balanced gate controls to avoid any signal attenuation during transition times. In Figure 4-20, it is shown that all gate accesses are routed coming from the same point (at the bottom left) for simplicity. Hence, path length compensation has been implemented to ensure synchronized gates switching. In addition, a metal shield wraps the signals all around up to biasing resistors to avoid undesired couplings.

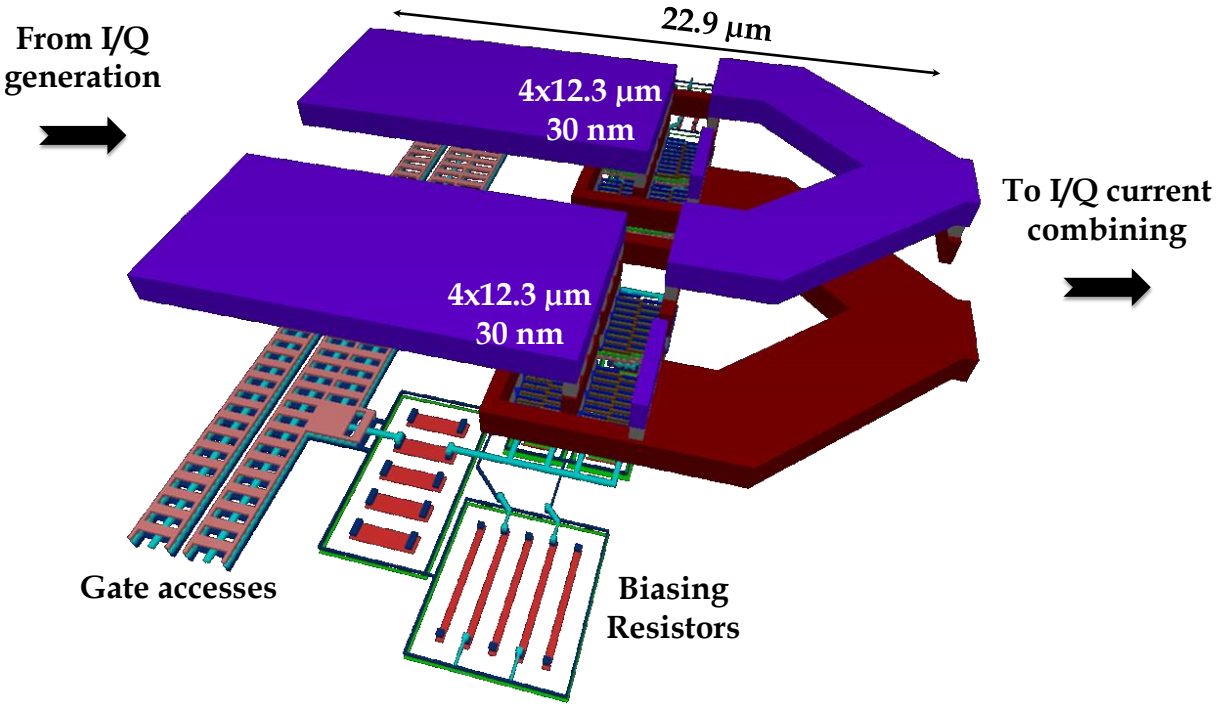

Figure 4-20: Layout of the realized modulator, including top metal accesses. Note that transistors are split for symmetry reasons.

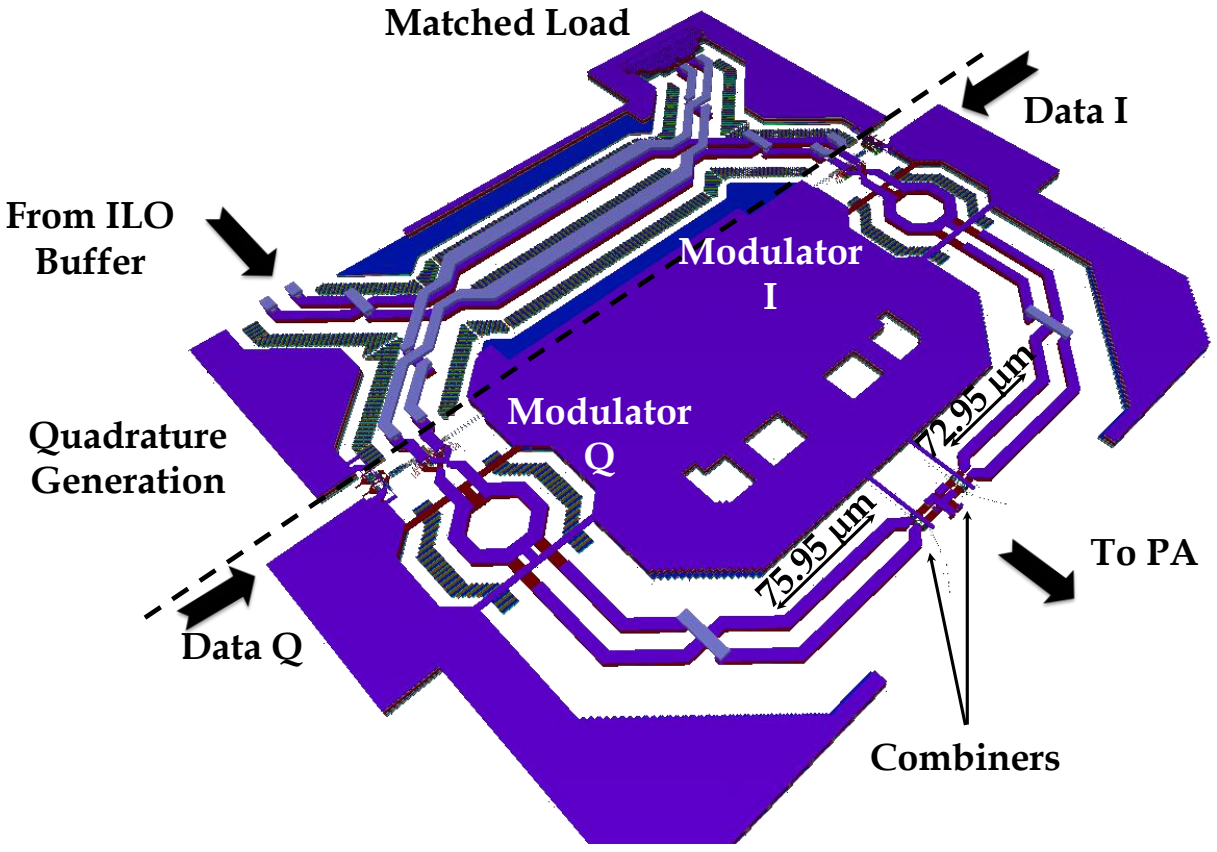

Figure 4-21: Overall layout view of the realized quadrature signal generation and QPSK modulator.

Modulated I/Q signals are finally current-combined using two differential neutralized common-source amplifiers. Note that a transformer and a long inductive path are willfully introduced between these blocks to ensure proper impedance matching and amplifiers biasing. Moreover, I/Q path lengths are adapted to compensate for non-ideal quadrature generation (3.6° phase error), so that the Q path is 3-µm longer than the I path (Figure 4-21).

Strictly speaking, tuning this inductive path also comes with impedance modification. In fact, the impedance presented at OUT and CPL ports of the DVHC may be slightly different resulting in an I/Q amplitude imbalance instead of phase error. In Figure 4-22, the modulator robustness to impedance mismatch is investigated through load-pull simulations. Negligible amplitude imbalance is actually obtained.

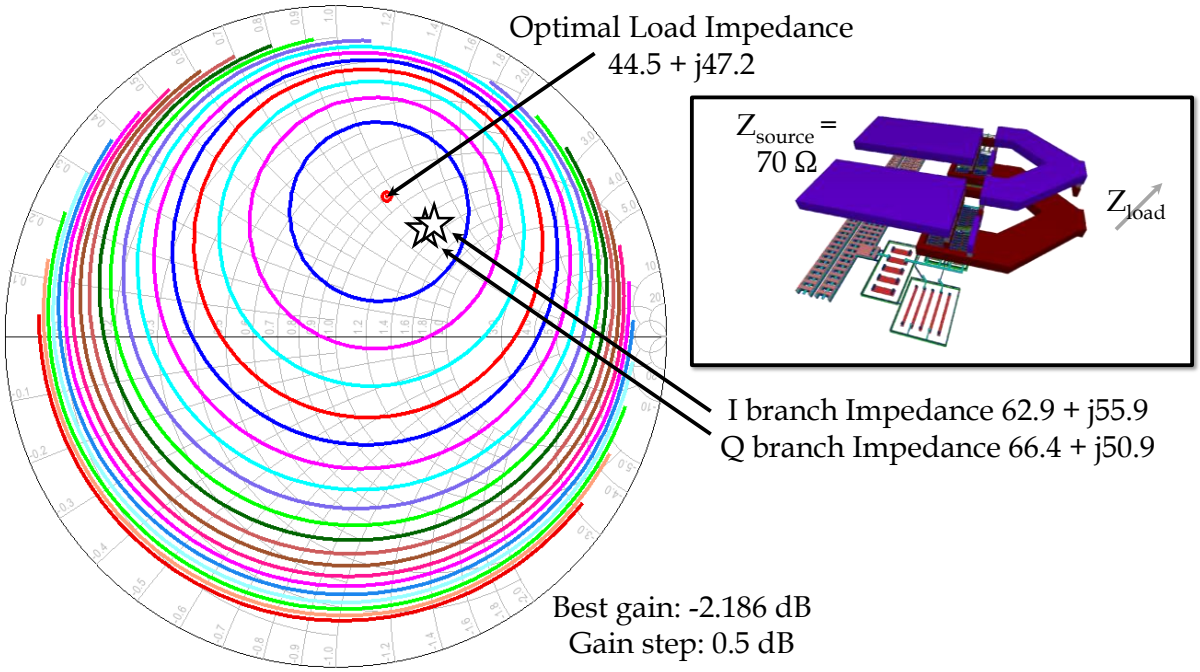

Figure 4-22: Modulator Load-Pull analysis at 83.33 GHz showing large output matching tolerance.

4.7. Low Power and High Efficiency Power Amplifier

In the low-power context described earlier, the linearity / efficiency trade-off usually encountered in the design of power amplifiers (PA) has been circumvented here. Because of the QPSK constant envelope feature, energy efficiency can actually be favored at the expense of degraded linearity. Consequently, operation at peak Power Added Efficiency (PAE) is desired.

Figure 4-23 presents the schematic of the realized PA. A 2-stage neutralized common-source amplifier topology is proposed to meet the high efficiency and moderate output power requirements. Integrated transformers are used to realize both impedance matching as well as transistors biasing and power supply through center-taps. Note that biasing and supply voltages between the driver and the power stages are chosen equal to rationalize the number of inputs / outputs (I/O). Nominal supply voltages are set to V_{dd} Power = V_{dd} Driver = 850 mV so that signal excursions on output drains are limited to ≈ 2x V_{dd} ≈ 1.6 V for reliability. Biasing conditions (V_{gs} Power = V_{gs} Driver = 500 mV) ensure full class A operation to benefit from high peak PAE at high output power (≈ 9 dBm), as illustrated in Figure 4-24. In such a configuration, it is clear that the PA operates non-linearly well above the compression.

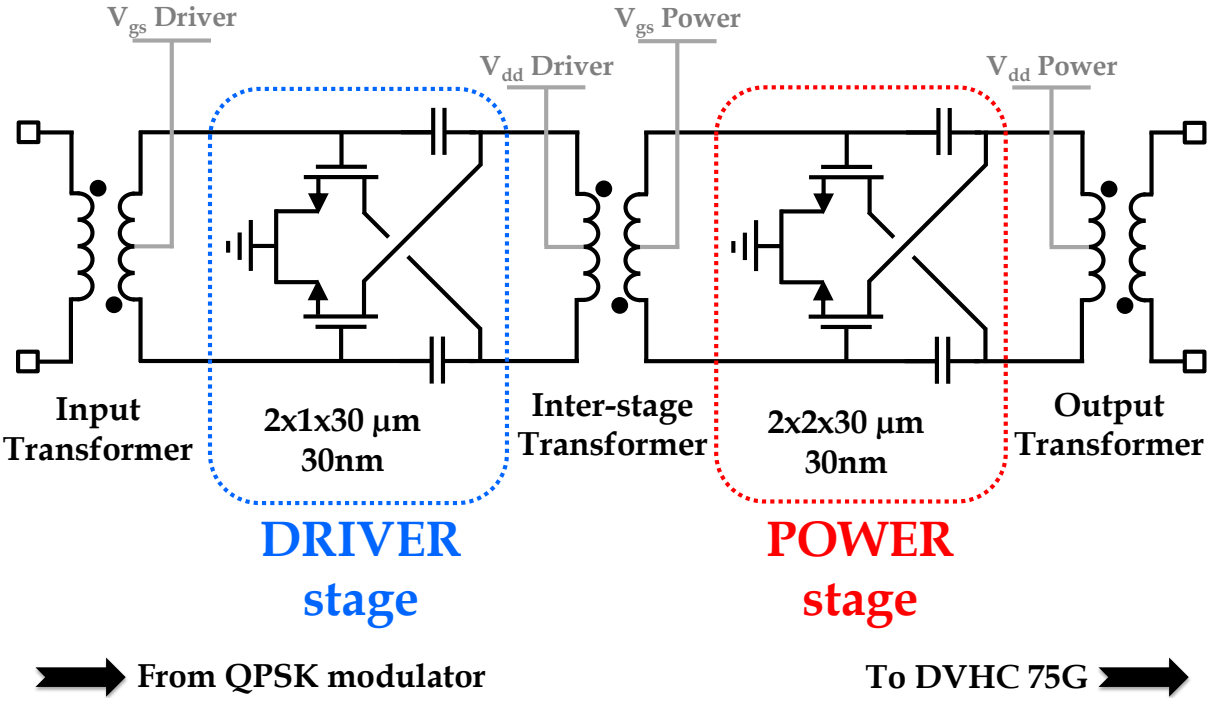

Figure 4-23: Realized PA schematic made of two neutralized common-source stages and integrated transformers. Biasing and supply voltages are fed by center-taps. Decoupling capacitances and biasing resistances not shown for clarity.

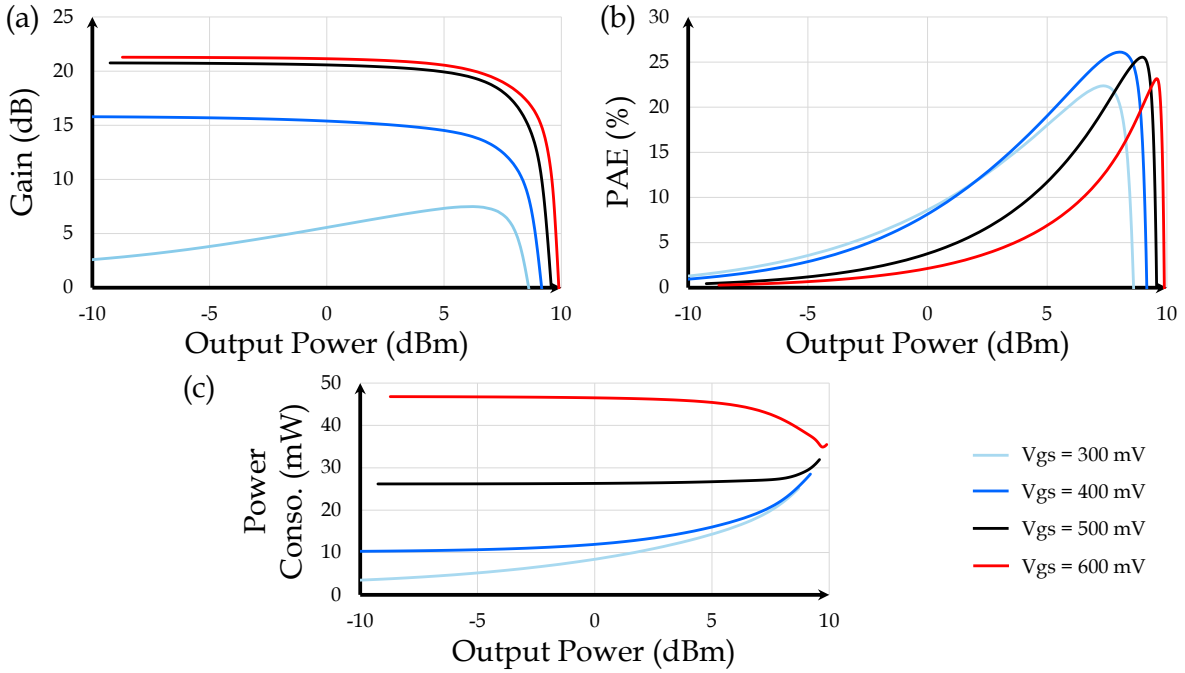

Figure 4-24: Harmonic Balance simulations of the realized PA plotted with respect to the output power for different biasing conditions at 83.3 GHz. (a) Gain, (b) PAE and (c) Total power consumption.

Consequently, a linear analysis based on simulated S-parameters is of limited interest, except for the small-signal stability validation presented in Figure 4-25. From these simulation results, we can conclude that the circuit is unconditionally stable from 60 to 100 GHz. By exploring lower and higher frequencies, it is actually possible to demonstrate the unconditional stability of the PA whatever the considered frequency.

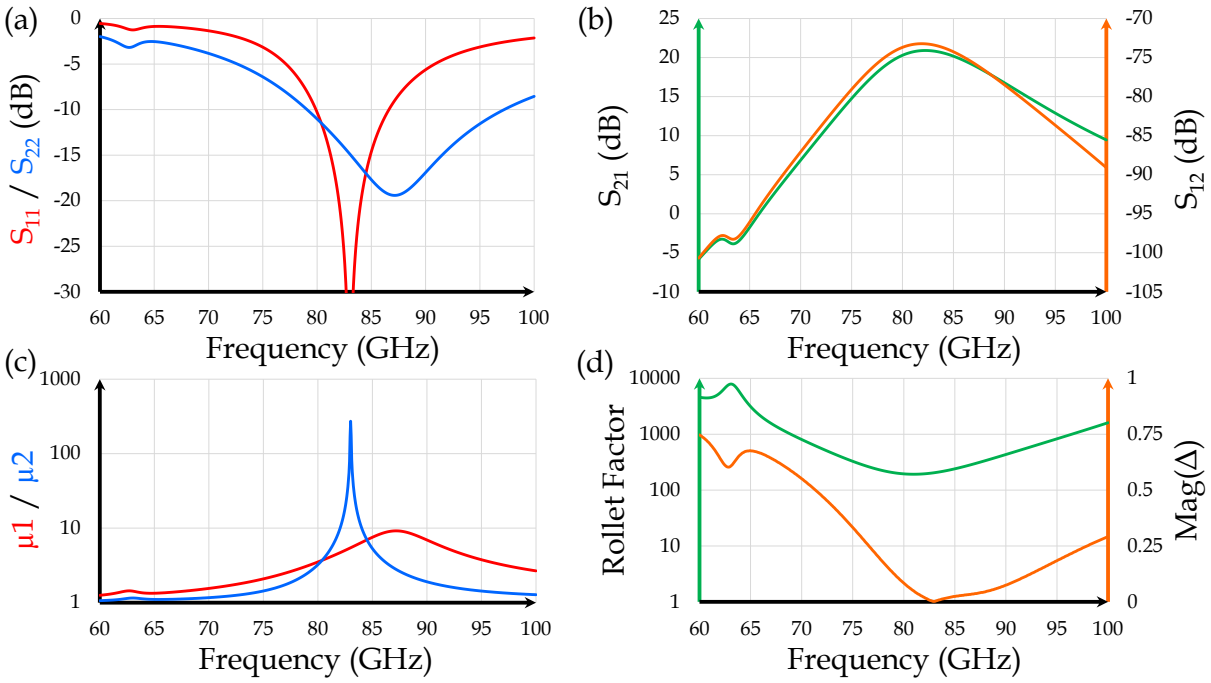

Figure 4-25: S-parameters analysis of the realized PA. (a) Reflection parameters, (b) gain and reverse isolation, (c) Edwards-Sinsky parameters and (d) Rollet factor and magnitude of the S-matrix determinant.

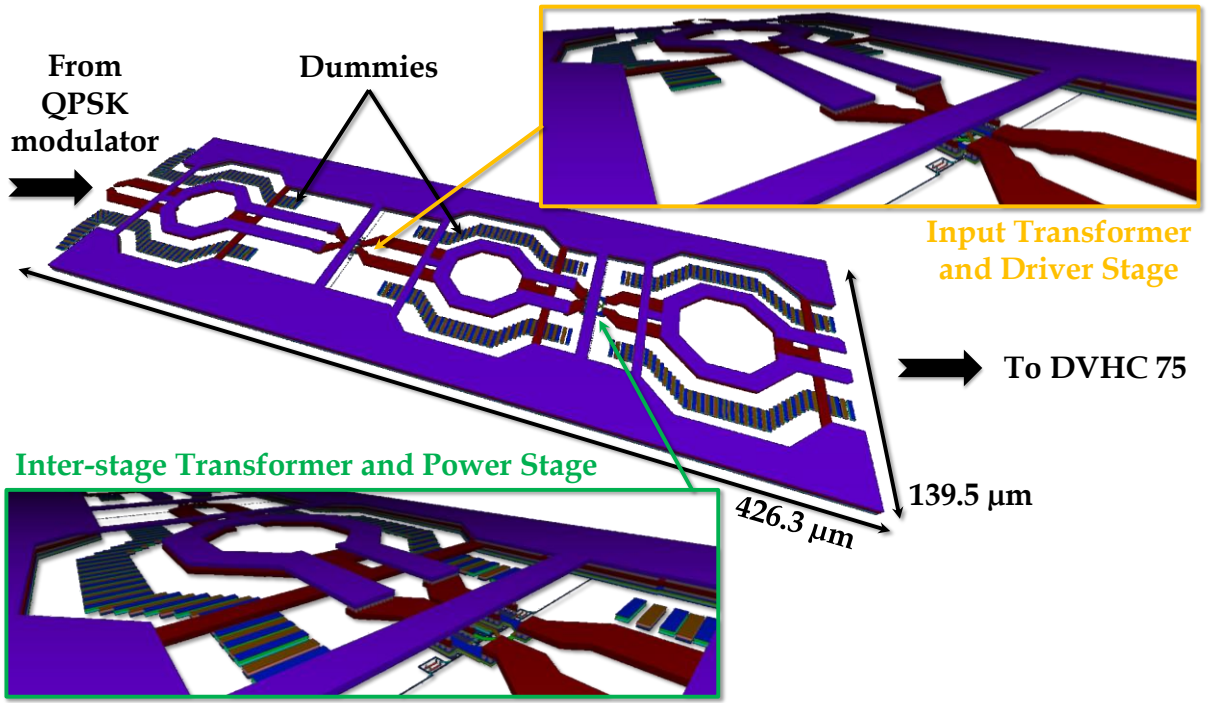

Figure 4-26: Layout of the realized PA with inset views of the driver and power stages.

Finally, the layout is presented in Figure 4-26. One more time, stringent metal density rules have been satisfied by including thin dummy bars outside the transformers to avoid metal tiling inside the transformers. The influence of such dummies has been simulated with EM tools (using Momentum simulator) but negligible impact was found. This reassuring result may be the consequence of strong confinements obtained in stacked transformers in combination of an appropriately wide spacing between the dummies and the windings (7 μm).

4.8. Dual Band Combiner using a Differential Vertical Hybrid Coupler

As stated at the very beginning of this Chapter, the main novelty of the realized transmitter architecture is related to the combination of two frequency bands leading to a single output pin. The DVHC topology (already presented in other building blocks contexts) was originally developed for that specific purpose because good isolation, low insertion losses and wideband port matching were strongly desired.

Contrary to large area consuming structures composed of two parallel single-ended hybrids [**Shi, 2013**], the DVHC actually supports differential operation by-design without suffering from additional routing penalty. Moreover, it can be implemented in a much more compact layout than conventional (differential) branch-line couplers based on quarter-wavelengths. Although a slow-wave version was proposed in [**Vahdati, 2015**] to reduce area requirements, branch-line implementations remain bulky and have high insertion losses.

Another transformer-based topology was recently published in [**Wan, 2017**] leveraging vertical magnetic coupling between two folded transformers. The resulting layout is very compact and achieves only 0.3 dB insertion loss at 25 GHz. Nevertheless, the introduced inter-winding parasitic capacitance is detrimental at higher frequencies.

In parallel, the concept of coupled-lines hybrid couplers was successfully revisited in [**Moret, 2017**]. Note that the topology is single-ended but parallelizing two structures is not easy and results in severe detrimental couplings at higher frequencies.

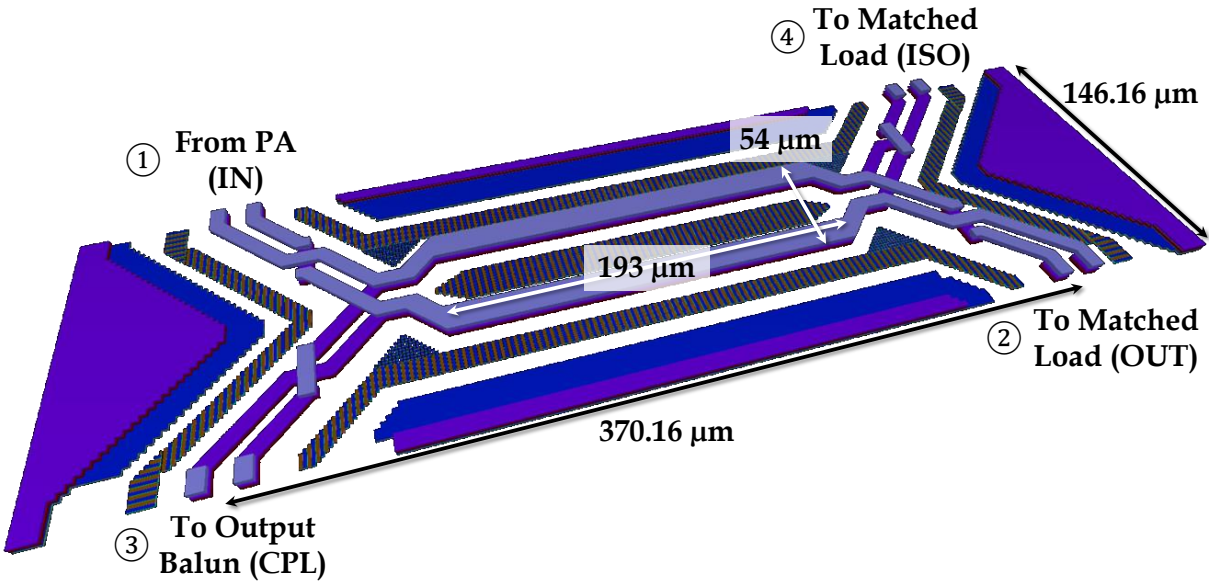

Figure 4-27: Layout view of the realized 75 GHz center frequency DVHC.

As presented in Figure 4-27, the proposed DVHC concept relies on two magnetically coupled differential transmission lines. Since vertical coupling offers better confinement at millimeter-wave frequencies, thus minimizing substrate losses and parasitic couplings, this layout is more desirable than a lateral coupling used in [**Moret, 2017**]. Replacing transmission lines by folded transformers, the same discussion also applies for the implementation in [**Wan, 2017**]. The DVHC design is also very compact. In the context of this work where a 75 GHz center frequency is needed, the core area is only 193 µm x 54 µm ($\approx \lambda/10 \times \lambda/40$) although line width was set to the maximum allowed value (12 µm). This design choice actually results in low insertion loss in addition with a favorable characteristic impedance close to 70 Ω on all 4 ports (Figure 4-28 (a)).

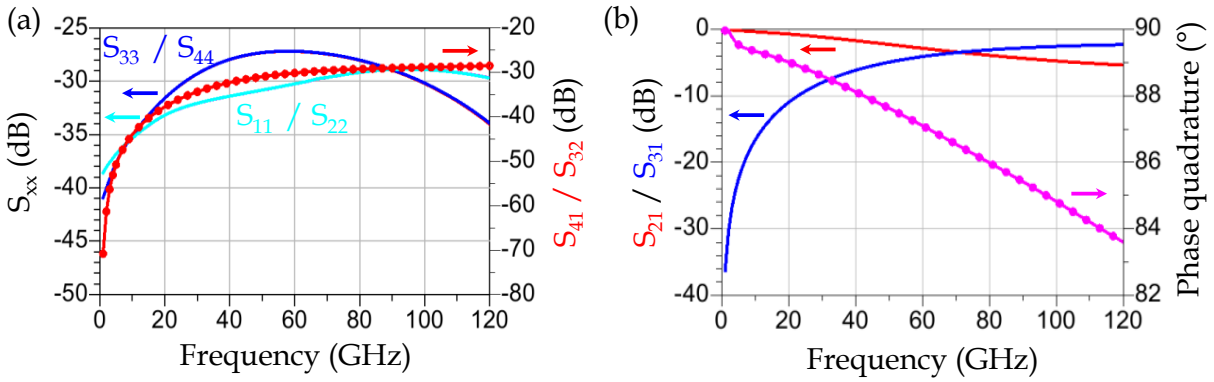

Figure 4-28: Simulation results of the realized DVHC centered at 75 GHz assuming 70 Ω differential impedance on all 4 ports. (a) Reflection and isolation parameters, and (b) transmission parameters and phase quadrature.

References	**[Shi, 2013]**	**[Wan, 2017]**	**[Moret, 2017]**	**This Work [Voineau, 2018]**
Frequency (GHz)	54 - 67	20 – 30	25 – 35 (*)	62 – 83 (*)
Phase error (°)	≤ 3	0 ± 1	3.7 ± 1 (*)	3.5 ± 0.5 (*)
Amplitude Imbalance (dB)	0.8 (*)	1.5	1 (*)	1 (*)
Insertion Loss (dB)	2 (*)	0.3	0.62 (*)	0.5 (*)
Area (µm x µm) (**)	2 x 60 x 65	170 x 130	NC	174 x 49
Process	40 nm	90 nm	28 nm FD-SOI	28 nm FD-SOI

(*) simulation, (**) on-silicon dimensions (post-shrink)

Table 4-2: DVHC Performance comparison with state-of-the-art mmW hybrid couplers.

A wideband isolation (between through and coupled ports) close to 30 dB with insertion loss of only 0.5 dB at 75 GHz is obtained. Note that careful design optimization of DVHC accesses is key to obtain weak frequency-dependent phase quadrature (Figure 4-28 (b)) along with stable characteristic impedances (Figure 4-28 (a)). For that latter reason, differential accesses are length compensated with under-path or upper-path even though phase quadrature is not a figure of merit here. Finally, the achieved performance of the designed DVHC is summarized in Table 4-2 and compared to the literature. Because of the four-port nature of hybrid couplers and inherent measurement complexity at mmW, most of reported works are only simulation results. Nevertheless, assuming a 1 dB maximum amplitude imbalance, the DVHC design clearly offers the widest bandwidth for a very small insertion loss. Note that in this specific context of frequency combining, such a wideband balanced amplitude range is not of interest since a sharp low band / high band transition would actually be preferred.

Anyway, these promising results have been demonstrated successfully, although indirectly, in **[Voineau, 2018].**

4.9. Optimized Low Capacitance RF Pads for Wideband Applications

Finally, the design of low capacitance RF pads is discussed in this section. In a mmW framework, it should be mentioned first that traditional wire bonds can't be considered anymore because of their unacceptable parasitic inductance (typically in the order of 100 pH – 1 nH). Consequently, only flip-chip assemblies are relevant for this application. However, conventional shielded RF pad, as illustrated in Figure 4-29 (a), exhibits at least ≈ 30 fF parasitic capacitance once implemented in the 28 nm CMOS FD-SOI 8ML technology (considering the most aggressive FC44S flip-chip pad class). Such a capacitance value is significant and should be either minimized by appropriate layout changes or/and canceled out using inductive elements to create a resonance at the considered frequency.

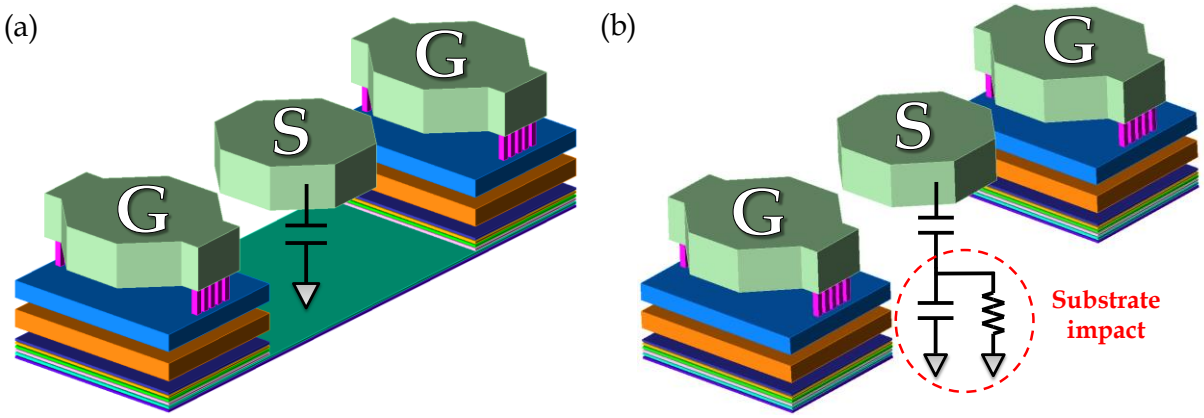

Figure 4-29: Layout of (a) shielded and (b) unshielded RF pads compatible with standard FC44S 100 µm-pitch assembly rules in 28 nm CMOS FD-SOI. Z-scale x10 for visibility.

In this work, a low capacitance RF pad has been designed for bandwidth requirements and is shown in Figure 4-29 (b). In this latter implementation, the underneath ground-to-ground connection has been removed, revealing the substrate that is therefore responsible for a different equivalent circuit. The resulting parasitic capacitance is thus frequency-dependent and features a much lower quality factor. In practice, ground pads are still connected by a full-stack metal path, which bypasses the signal pad (not shown here), to avoid ground discrepancy. Nevertheless, this connection is responsible for a significant capacitance increase and has to be taken into account during simulations. Similarly, stringent metal densities related to flip-chip mechanical constraints are also taken into account. Doing so, Momentum simulation results reveal that the parasitic capacitance is reduced by more than 50 % down to ≈ 15 fF at 75 GHz.

The motivation to reduce parasitic capacitance is justified further from an impedance matching bandwidth point of view. In Figure 4-30 (a), the typical configuration associating a balun and a pad parasitic capacitance C_{PAD} is recalled. Considering only $k \approx 0.8$ as the only source of non-ideality, the odd mode analysis is derived in Figure 4-30 (b). To simplify the discussion and focus on first order effects, an ideal transformer ($k = 1$) is considered in Figure 4-30 (c).

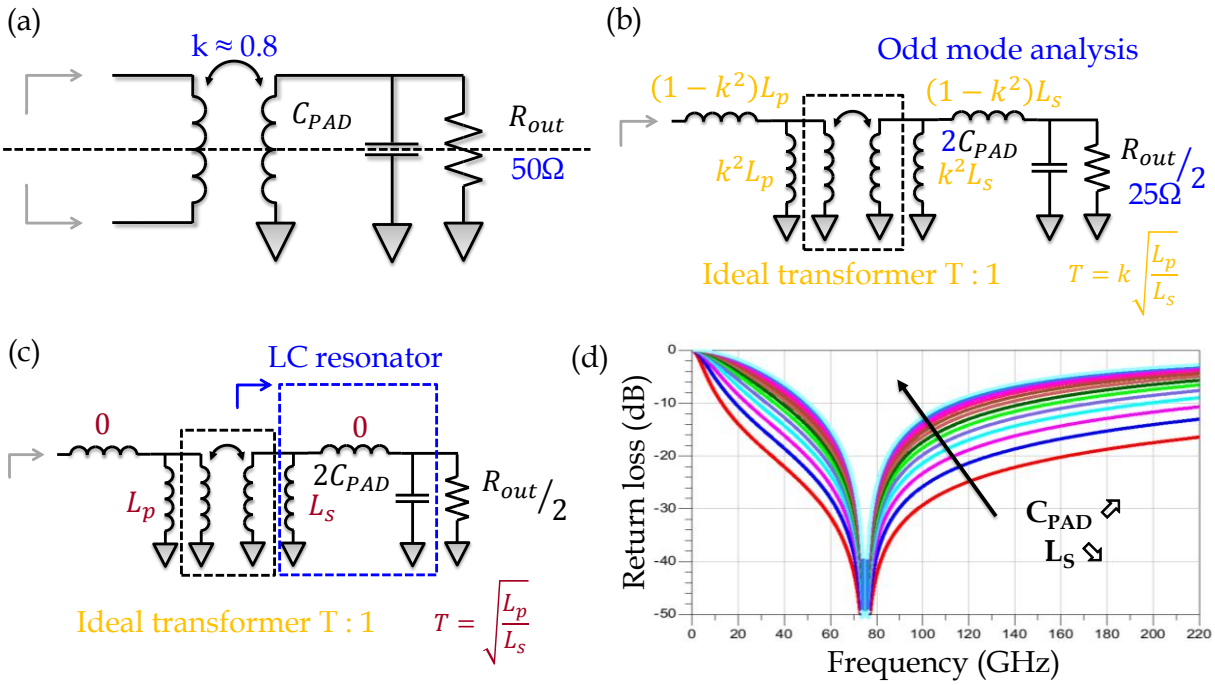

Figure 4-30: Impedance matching bandwidth analysis. (a) Typical use-case of a non-ideal balun with a pad parasitic capacitance, (b) odd mode analysis, (c) simplified analysis assuming an ideal transformer (k = 1) and (d) return loss as seen from the transformer to the LC resonator for different (C_{PAD}, L_S) couples.

In Figure 4-30 (d), the return loss of the output network (LC resonator + resistive load) is investigated at 75 GHz for several capacitance values from 10 fF to 70 fF. Although there always exists an inductance value to resonate with any capacitance value, it is clear that the impedance matching bandwidth reduces when C_{PAD} increases. From this simplified circuit analysis, we can conclude that minimizing C_{PAD} is of primary interest in order to achieve broadband impedance matching.

In the remaining section, the output balun is presented and, as a central part of the resonant network, the obtained bandwidth is investigated. On one hand, the layout of the balun is composed of two stacked windings as visible in Figure 4-31 (a) to benefit from maximum coupling factor (k > 0.8) at around 75 GHz (Figure 4-31 (b)), thus allowing enlarged bandwidth [**Long, 2000**]. On the other hand, the choice of a 65 µm-side square shape allows slight quality factor reduction (Figure 4-31 (c)) and favors broadly resonant operation. Note that in spite of different trace widths (6 µm for the differential winding made of the 2 thick copper layers and 10 µm for the single-ended winding only made of the aluminum layer), both windings exhibit a similar 100 pH inductance.

The balun is finally completed on the differential side with a custom 44 fF MOM capacitor C_{MOM} in parallel. An overview of the entire matching network is presented in Figure 4-32 (a). The insertion and reflection parameters of this network are provided in Figure 4-32 (d) and (b) respectively in order to illustrate further the significant bandwidth achieved from 40.2 GHz to 104.7 GHz, which represents an 89 % fractional bandwidth. Moreover, such a frequency range can successfully carry a dual-band modulation scheme at 66.7 GHz and 83.3 GHz with 10 GHz bandwidth for each carrier, so that the realized output network ensures no bandwidth bottleneck.

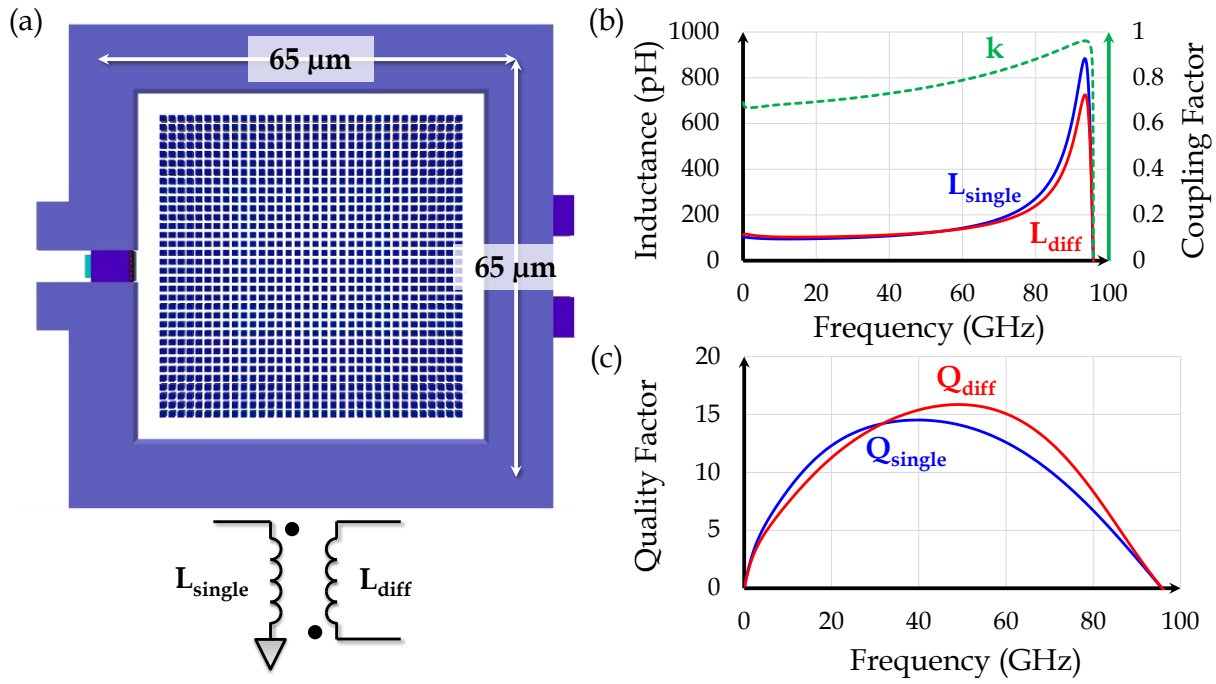

Figure 4-31: Output balun overview. (a) Layout top view, (b) primary and secondary inductances as well as the coupling factor, (c) primary and secondary quality factors.

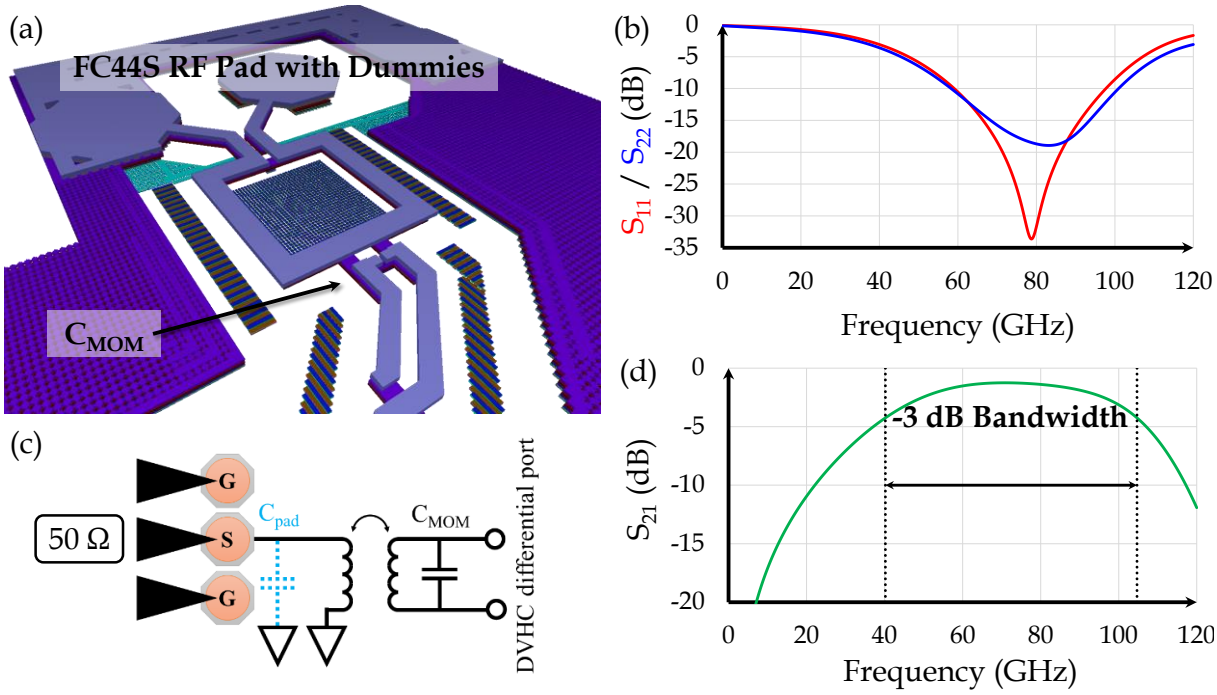

Figure 4-32: Output matching network bandwidth simulation. (a) Layout overview, (b) reflection parameters, (c) equivalent circuit and (d) transmission parameter. Port 1 and Port 2 correspond to the 70 Ω differential DVHC port and the 50 Ω single-ended output port respectively.

4.10. Measurement Results

In this section, the measurement of the realized mmW transmitter is discussed. First, preliminary S-parameters measurements regarding the output DVHC are presented. Next, the measurement setup is described and encountered difficulties are explained. Then, injection-

locking measurements are presented validating the wide locking range as well as the low noise operation capabilities. Finally, the circuit has been tested successfully with high-speed digital signals thanks to a real-time oscilloscope to perform direct demodulation and derive an Error Vector Modulation (EVM) specification.

4.10.1. Preliminary Validation of the DVHC Component

In this work, a first circuit has been realized using the 28 nm CMOS FD-SOI technology in order to validate the proper operation of the DVHC component discussed all along this Chapter. Because of its particular importance, the 75 GHz output DVHC has been selected.

The four-port intrinsic nature of the DVHC advocates for full four-port measurements as well. Unfortunately, the design is too small to allow it without long parasitic accesses. For this reason, two test structures are two-port measured with other ports being internally matched by 70 Ω (2x35 Ω pseudo-differential) resistive loads. The impedance transformation and differential to single-ended conversion are realized with very same output matching network as discussed in section 4.9. Therefore, presented results in Figure 4-33 are not de-embedded, thus including the significant contribution of matching networks (RF pads included) in terms of insertion loss and impedance mismatch. Nevertheless, good agreement is still obtained with simulation, clearly validating the DVHC concept in the E-band. Measurements were repeated on several dies (5 shown here) with excellent repeatability and no visible die-to-die dispersion.

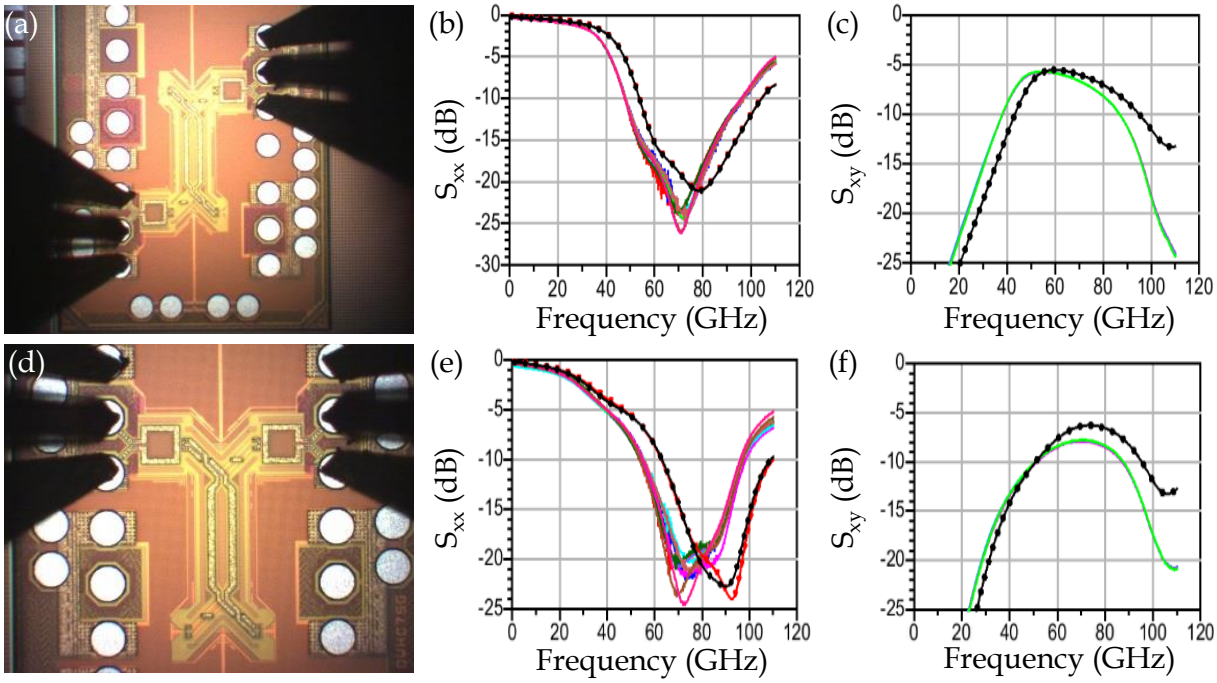

Figure 4-33: DVHC validation measurements. (a) Through configuration circuit view, and associated (b) reflection and (c) transmission parameters. (d) Coupled configuration circuit view, and associated (b) reflection and (c) transmission parameters. Measurements (solid lines - 5 measured dies) are compared to Momentum simulations (dotted lines).

4.10.2. Measurement Setup

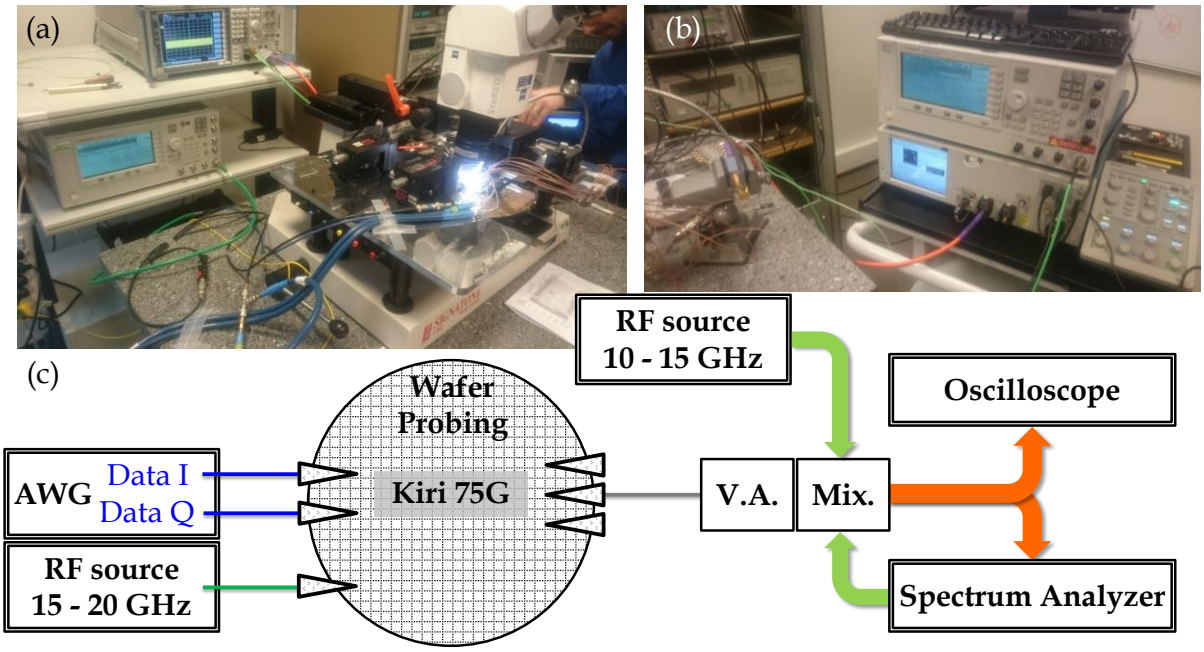

Figure 4-34: Illustration of the measurement setup. (a) Probe station seen from the left side, (b) right side view and (c) schematic view of the setup. V.A. and Mix. stand for variable attenuator and harmonic (down-converter) mixer respectively.

The measurement setup is presented in Figure 4-34. On the left, an Agilent E8257D signal generator delivers a reference signal which 5th harmonic allows injection-locking operation. Additionally, modulated data are provided by a Tektronix AWG 7122C Arbitrary Waveform Generator (AWG). On the right, the circuit output signal is down-converted thanks to a Rohde & Schwarz FS Z-75 harmonic mixer. This mixer requires an external oscillation signal that is delivered either by another Agilent E8257D signal generator for modulated signals measurements or, alternatively, by the Rohde & Schwarz FSUP 50 Spectrum Analyzer used for locking range and noise measurements. In the case of modulated signals, the down-converted output is visualized using a Tektronix DPO77002SX 70 GHz 200 GS/s real-time oscilloscope, which also performs direct demodulation.

The main limitation of this setup is the harmonic mixer that is actually used out of its specification range (50 – 75 GHz). Therefore, large (typically 23 dB at 75 GHz [**R&S, 2017**]) but unspecified insertion losses are introduced in the setup that prevents accurate power calibration in the chip output plane. Moreover, a programmable attenuator may be used because the mixer 1-dB compression point is rated at – 6 dBm at the RF input [**R&S, 2017**]. In most cases, the attenuation value has been set at ≈ 0 dB for maximum signal amplitude at the expense of probable higher distortions. Finally, the IF mixer port has a very limited bandwidth from 5 MHz to 3.2 GHz [**R&S, 2017**] which is definitely not suitable for high-speed signals.

With all these limitations in mind, the circuit characterization is reported in the following sections.

4.10.3. Injection Locking Measurements

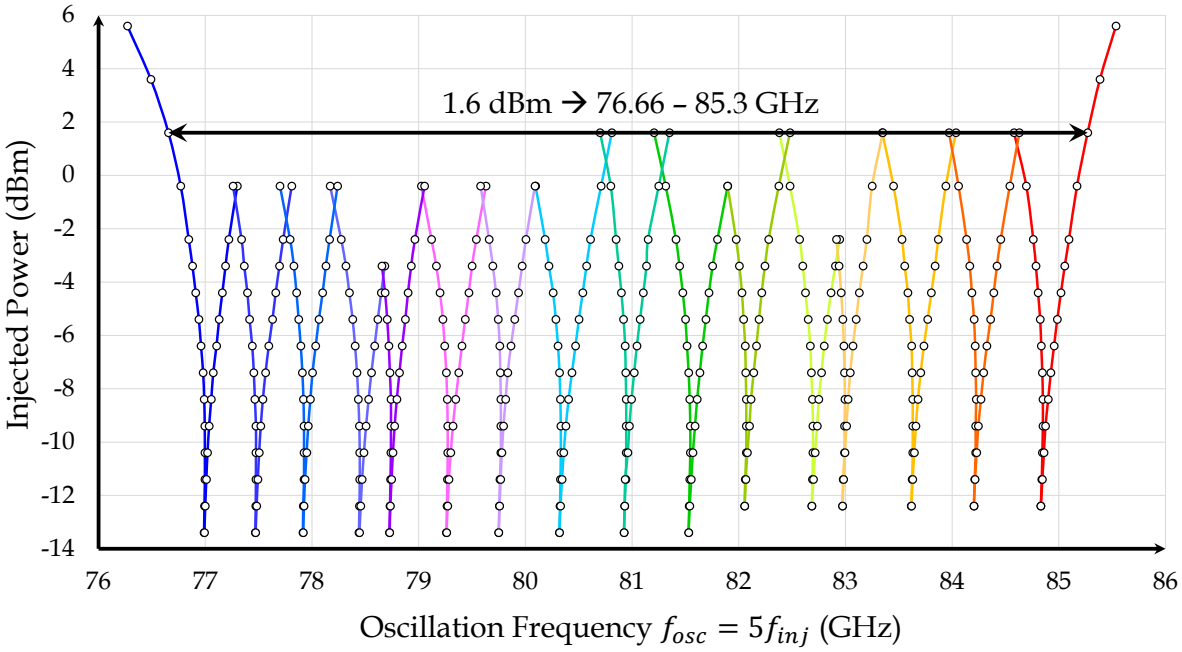

Figure 4-35: Locking range measurements for the $2^4 = 16$ configurations of the Kiri 75G circuit.

Although free-running operation has been validated as well, operation in the locked regime is of particular interest to allow precise frequency tuning with reduced phase noise. Locking range measurements are reported in Figure 4-35. Characteristic V-shape curves are obtained for every possible state of the 4-bit IL-VCO. A continuous locking range, defined by the overlap of all elementary locking ranges, is demonstrated for a minimum injected power of 1.6 dBm. It covers almost 9 GHz from 76.66 GHz to 85.3 GHz, representing 10.7 % of the center frequency. Note that injected power has been de-embedded and is given in the chip input plane.

Considering an injected power higher than 5.6 dBm, it was even possible to demonstrate a continuous locking range when using only the three most significant bits of the IL-VCO. The least significant bit of the IL-VCO then permits a 4 dB input power requirement reduction. Interestingly, locking ranges overlap is better at lower frequencies, which can be explained by lower tank quality factors.

In Figure 4-36, the phase noise is measured at 77 GHz and compared to the phase noise of the input reference signal. As expected from the theory, the resulting phase noise is mainly a copy of the input one. Consequently, a -124.2 dBc/Hz phase noise at 1 MHz offset is measured. Visible spurs were unfortunately captured during the acquisition, but there blinking nature observed during the measurements advocates for an artifact origin. On the contrary, a real phase noise degradation is observed at offset frequencies lower than 50 kHz. Such a degradation might be explained by the choice of a voltage polarization of the VCO instead of a conventional current polarization. While this latter suffers from degraded oscillation amplitude (theoretically leading to a worsened phase noise), it is still more robust to ground perturbations induced by other blocks sharing the same ground net.

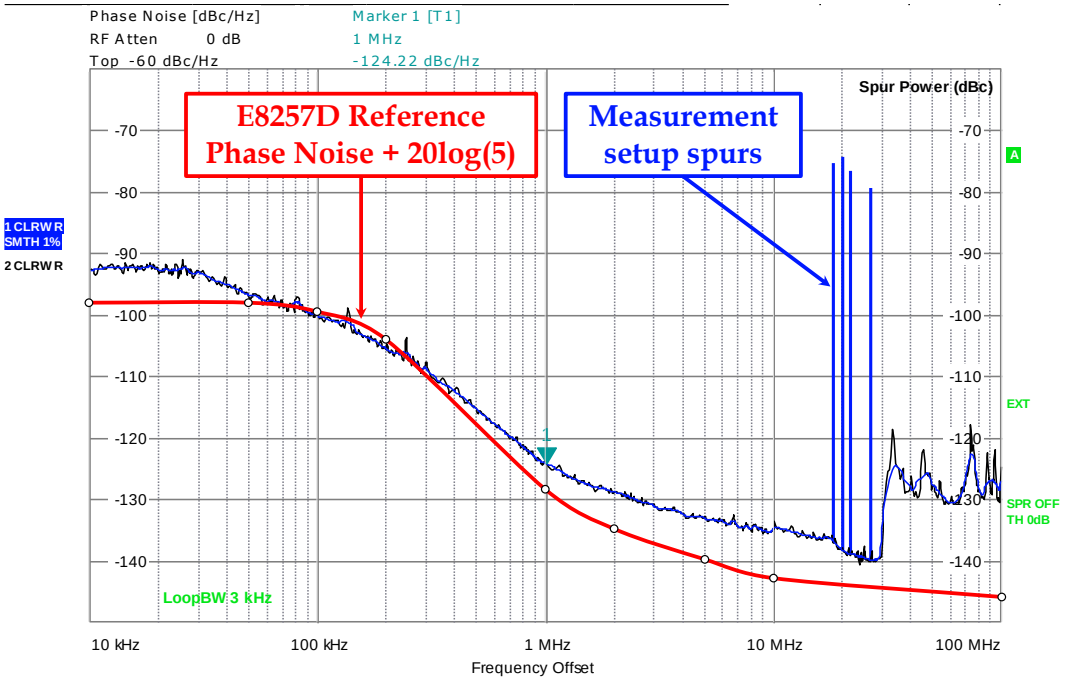

Figure 4-36: Measured phase noise at 77 GHz (blue) in the injection-locked regime compared to the 15.4 GHz reference phase noise (red – scaled to 77 GHz) from the E8257D signal generator.

4.10.4. Modulated Signals Measurements

In Figure 4-37 and Figure 4-38, pseudo-random bit patterns are applied on digital inputs to validate the ability to transmit QPSK signals. In the first case, the down-converted spectrum is very characteristic at only 100 MS/s (Figure 4-37). Demodulated constellation exhibits a 6.5 % EVM (RMS). Moreover, a 2.65° phase error and 4.6% magnitude error are obtained. Although these values should be considered carefully due to the use of low-complexity equalization and direct demodulation algorithms limitations, we can still conclude that QPSK is properly realized thus validating the design methodology presented earlier in this Chapter.

Going further and increasing the data rate, we were actually able to demodulate a 4.5 GS/s signal even though it is clear from Figure 4-38 that spectrum distortions are extremely important. Increased complexity equalization is used to mitigate this effect. However, a very high 33.6 % EVM (RMS) is obtained which corresponds to a $\approx 1.3\ 10^{-5}$ Bit Error Rate (BER).

One more time, it should be mentioned that these results are not de-embedded and fully take into account measurement artifacts and distortions. As regards high-speed data transmission, it seems that the performance is not primarily limited by the circuit. On the contrary, the contribution of the sharp low-pass behavior of the harmonic mixer at IF port was found to be a major limitation.

This observation is additionally supported in Figure 4-39 and Figure 4-40 in which a BPSK is considered by duplicating data on both I/Q channels. The same bandwidth limitation is visible at high symbol rates in Figure 4-39. Nevertheless, we were actually able to demodulate a 5.5 GS/s clock-signal (deterministic state changes at a 2.75 GHz frequency) as reported in Figure 4-40 with an improved EVM. It clearly confirms the high-speed capability of the circuit and the overall bandwidth limitation. Note that the demodulation algorithm was not able to demodulate clocks above 5.5 GS/s because of the mixer spurs having a much higher intensity.

Figure 4-37: QPSK demodulation at 100 MS/s.

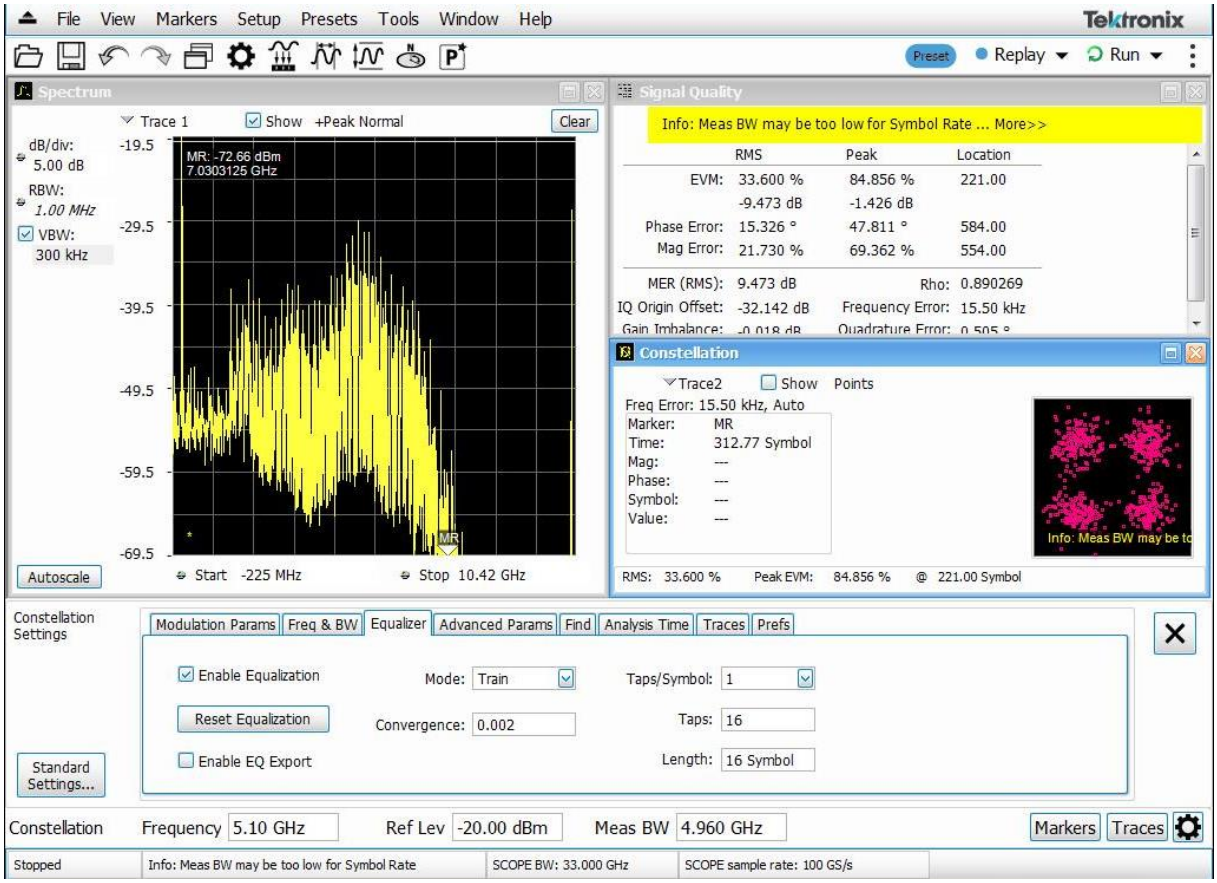

Figure 4-38: QPSK demodulation at 4.5 GS/s.

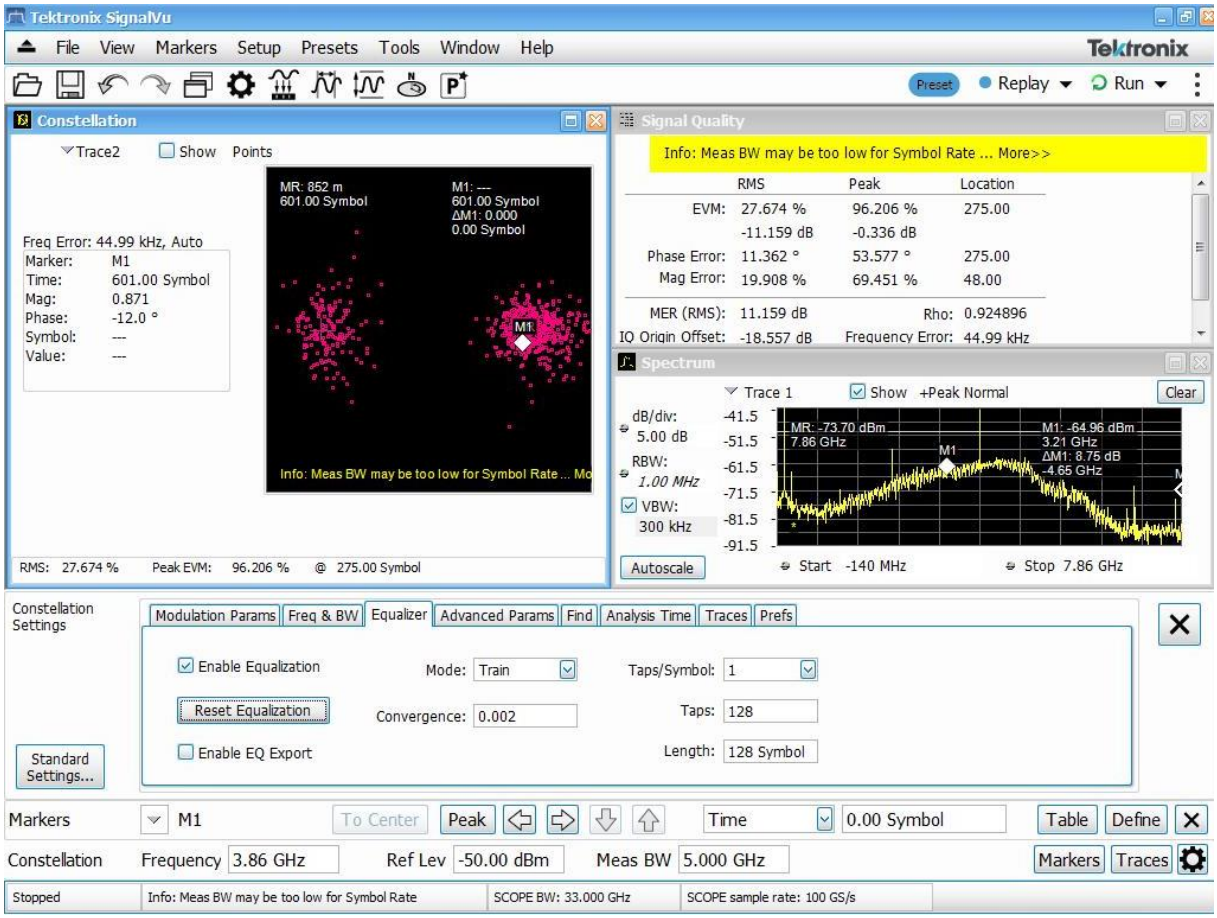

Figure 4-39: BPSK demodulation at 4 GS/s.

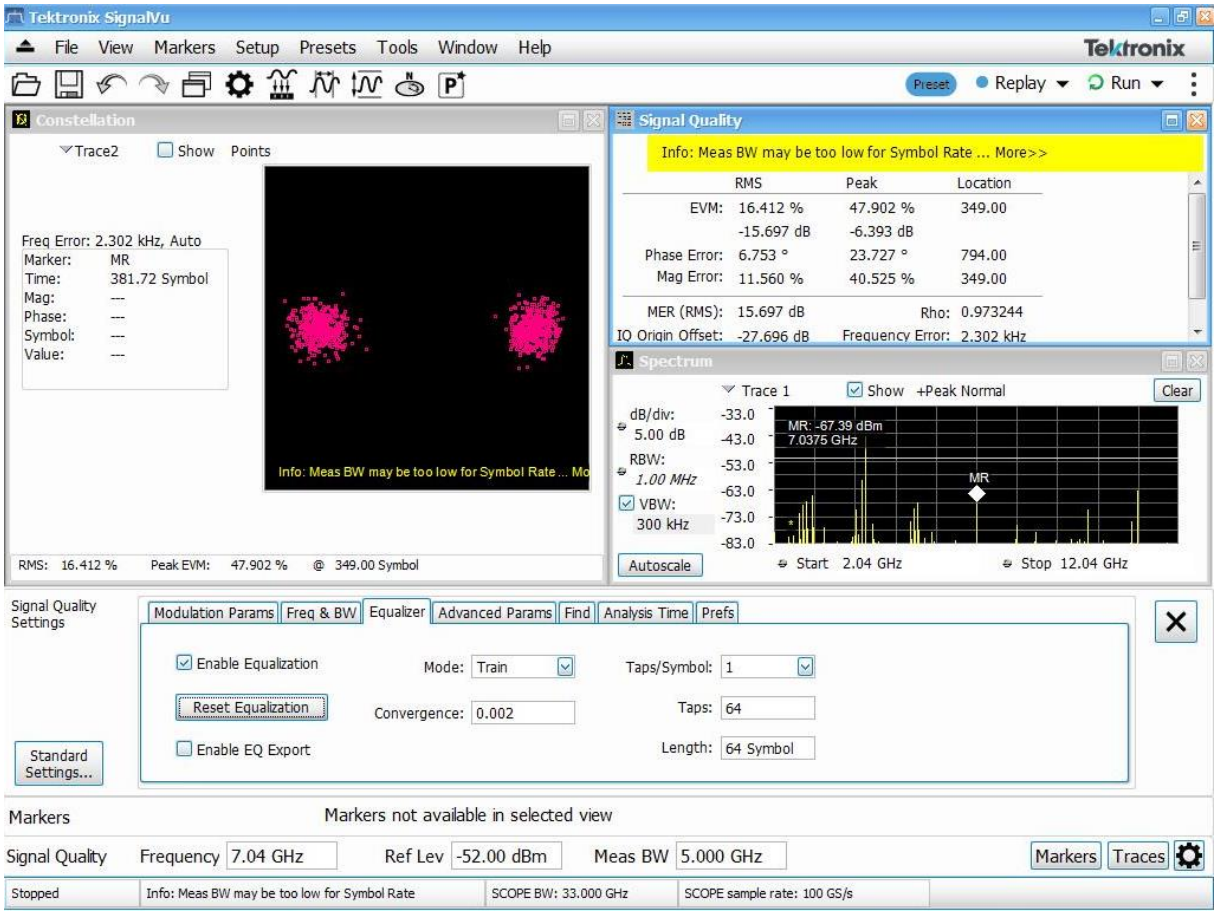

Figure 4-40: BPSK demodulation of a 5.5 GS/s clock signal.

4.11. Conclusions and Comparison with State-of-the-Art Realizations

In conclusion, the design of a dual-band transmitter circuit operating in mmW bands has been discussed in this Chapter. While each chain may be designed assuming moderate complexity, the novelty at both architecture and design levels is the use of an integrated hybrid coupler. In fact, such a component benefits from a strong and wideband isolation, which enables power division at the input of a common reference signal as well as power combination at the output so that modulated signals may finally share the same output pin.

The design of a mmW transmitter chain using the 28 nm CMOS FD-SOI technology has been presented. Although only the high-band transmitter has been fabricated in the frame of this work, the realized Kiri 75G circuit embeds the input and output hybrid couplers. These 17 GHz and 75 GHz couplers are based on the DVHC topology introduced in this Chapter as a significant innovative contribution. This topology is found to be easily scalable for a given mmW frequency with superior isolation features and very weakly frequency-dependent port impedance thus allowing wideband and simple impedance matching. Moreover, intrinsic attenuation in the order of only 0.5 – 0.7 dB are possible. This design can also be used as a quadrature signal generator as demonstrated successfully in this work with a third 83 GHz counterpart. Most importantly, all these interesting characteristics are feasible in a very compact silicon area much smaller than conventional quarter-wavelength based designs like branch-line couplers. The differential design and the choice of a vertical coupling significantly reduce the risk of detrimental couplings. Keep-out areas may then be favorably minimized.

Another contribution of this work is the development of low-capacitance mmW pads complying with the stringent flip-chip assembly rules of the 28 nm CMOS FD-SOI technology. While traditional shielded pads have ≈ 30 fF parasitic capacitance, the proposed un-shielded version exhibits only ≈ 15 fF (≈ 11 fF measured) which represents a valuable enhancement. It has actually be shown that the lower the parasitic pad capacitance, the larger the achievable bandwidth. Consequently, a broadband output matching network has been designed with ≈ 90 % fractional bandwidth that largely exceeds the targeted E-band. The feasibility of the proposed dual-band architecture is therefore validated since no prohibitive bandwidth bottleneck appears at the circuit output.

Finally, the realized Kiri 75G circuit has been characterized in spite of measurement difficulties encountered at such high frequencies. Interestingly, an on-chip fifth harmonic generator allows a wide locking range capability of around 11 % fractional bandwidth. Additionally, the injection-locking mechanism involved here results in a very low phase noise at only a fraction of the power consumption of traditional PLL. Moreover, QPSK has been demonstrated successfully up to 4.5 GS/s, which is equivalent to 9 Gb/s, although the characterization was actually limited by measurement capabilities. In Table 4-3, the performance of the circuit is compared to state-of-the-art realizations. It should be noted that the reported designs suffer from significantly low output powers. This results from the superior power capability of the 28 nm CMOS FD-SOI technology at mmW frequencies as well as a design choice to deliver much higher output signals (in agreement with the link budget presented in Chapter 3). Furthermore, the proposed combining technique relying on a passive DVHC enables power combining of the signals after energy-efficient (non-linear) amplification. On the contrary, signal combination before the PA in [**Tokgoz, 2016**] and [**Tokgoz, 2018**] then requires linear and less-efficient amplification.

	[Tanaka, 2012]	[Tokgoz, 2016]	[Tokgoz, 2018]	This Work
CMOS Process Node	40 nm	65 nm	65 nm	28 nm FD-SOI
Core Area (mm²)	0.42	< 6	3.2	0.585 (only 1 Tx)
P_{DC} (mW)	Tx: 52 Rx: 85	Tx: 260 Rx: 300	Tx: 120 Rx: 160	Tx: 74.25** Rx: NA
Tx Pout (dBm)	-1.3*	-8.4	-1.9	6***
Frequency (GHz)	49 – 65* 72 – 88*	71 – 84 86 – 99	70 – 87.5 87.5 – 105	60 – 75 (potentially) 75 – 90
Reference Frequency (GHz)	57 + 80	34	35	15.25 – 17.1
Frequency Combining Technique	Impedance Transformation	Resistive Feedback Buffers Combining	Resistive Feedback Buffers Combining	DVHC
Data Rate (modulation)	30 Gb/s (OOK)	56 Gb/s (16QAM)	60 Gb/s (QPSK) 120 Gb/s (16QAM)	> 2x 9 Gb/s (QPSK)

*estimated **digital buffers excluded ***simulation results

Table 4-3: Circuit comparison with state-of-the-art realizations featuring wideband mmW frequencies combining (only on-chip CMOS considered).

4.12. Perspectives

Enhancement perspectives are proposed in the following sections. It is clear that incremental improvements are obviously possible, like for example optimized baseband circuitry, better VCO polarization or the use of several inverter stages in the injection circuit. However, the discussion focusses on disruptive ideas that could significantly improve the circuit and make it closer to an industrial product.

4.12.1. Dual-Band Implementation and Integration of the External Signal Reference

As mentioned earlier, the low-band transmitter chain centered at 66.7 GHz has not been implemented in the Kiri 75G circuit and it is therefore an obvious enhancement perspective. Moreover, the low-complexity architecture of each transmitter allows easy blocks reuse. Integrated transformers should then be re-sized accordingly leading to mainly similar performances between the two chains. The only exception is related to the injection strategy as the low-band chain is supposed to be locked on the fourth (even) harmonic of the reference signal while the realized high-band transmitter is locked on the fifth (odd) harmonic. Primary simulations indicate that the proposed inverter-based harmonic generator only delivers odd harmonics content which is thus unsuitable. Consequently, this block should probably be replaced by a conventional quadrupler.

Additionally, external synthesis currently delivered by an external equipment should be integrated. Conventional PLL are typically well suited for such an application because passive components like inductors and varactors have good quality factors in the range 10 – 20 GHz

leading to favorable phase noise and low power consumption. Alternatively, state-of-the-art signal synthesis based on Periodically Repeated Oscillations Train (PROT) may be considered for reduced area and power requirements [**Jany, 2015**].

4.12.2. Serial Interface Integration and EVM Calibration

The measured circuit suffered from a large number of I/O, including many static polarizations, which turned wafer probing into an impractical and chancy task. To ease characterization of a future circuit, a serial interface could be implemented along with appropriate resolution Digital to Analog Converter (DAC). Benefiting from the digital interface, the number of polarization controls can be increased virtually so that any block could be polarization optimally. Moreover, the body-biasing feature of the FD-SOI technology could be leveraged for fine polarization tuning while almost all back-gate controls had to be tied to ground in the Kiri 75G circuit to limit the number of I/O.

At the same time, the additional OOK operating mode could be implemented easily thanks to the inherent compatibility of the proposed modulator architecture. Only modulator commands should then be modified accordingly.

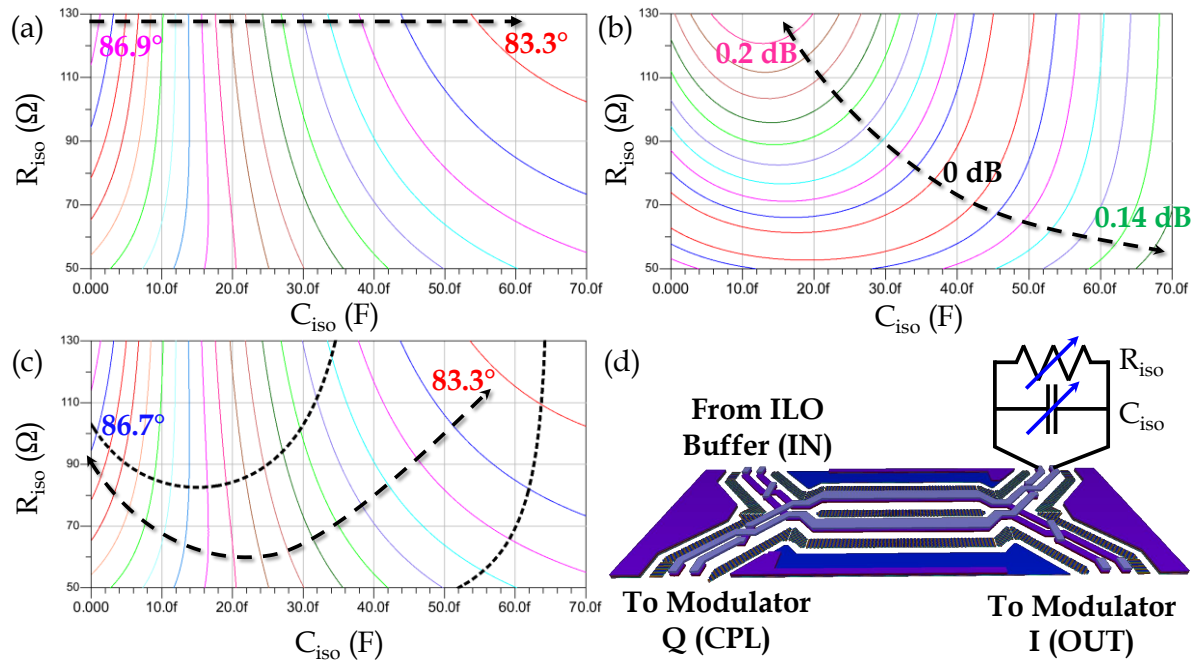

Figure 4-41: Simulation of a variable load on the ISO port of the 83 GHz DVHC as presented in Figure 4-17. (a) Phase quadrature contour plots with a 0.2° step, (b) amplitude imbalance contour plots with a 0.02 dB step, (c) phase quadrature contour plots (colored) with a 0.2° step and delimited 0 – 0.1 dB amplitude imbalance area (black), (d) schematic illustration of the modulated load on the ISO port. All simulations are carried out at 83 GHz assuming a 70 Ω differential impedance on other ports.

Finally, more controls could also enable interesting EVM calibration. To do so, both phase and amplitude quadrature should be tunable. In Figure 4-41 (d), a variable R-C load is introduced at ISO port. Such a load may be easily implemented using capacitors and resistors banks. A very accurate phase offset trimming is therefore possible (Figure 4-41 (a)) with negligible impact on amplitude imbalance (Figure 4-41 (b)). Quantitatively, it is possible to modify the phase quadrature at 83 GHz from 86.7° to 83.3° while still limiting the amplitude

imbalance degradation to only 0.1 dB, as visible in Figure 4-41 (c). Note that this result is achieved using reasonable values of resistors and capacitors, which is important for both feasibility and process variation tolerances.

As regards amplitude calibration, gate biasing and back-gate body-biasing of the I/Q current combiners could be adjusted for coarse and fine amplitude tuning respectively. Consequently, a global EVM calibration scheme may be implemented.

4.12.3. Versatile Multi-Modulation Compliancy

Among the many benefits of implementing a digital serial interface, the easy introduction of an OOK compliancy has been presented previously. Addressing additional modulation schemes may still present an advantage in terms of system versatility. In this section, a slight modification of the modulator schematic is proposed to comply with higher-order modulations without compromising circuit simplicity. To do so, switch transistors in Figure 4-42 (b) are actually segmented and controlled independently. Taking low-complexity digital circuitry for granted, multi-level amplitude modulation is enabled by proper control of destructive interferences induced in the RF path. The resulting Pulse Amplitude Modulation (PAM) could be valuable. Furthermore, if two quadrature paths are combined as realized in our demonstrator, Quadrature Amplitude Modulation (QAM) becomes possible as well. Note that circuit complexity increase (from Figure 4-42 (a) to Figure 4-42 (b)) is quite modest compared to potential benefits.

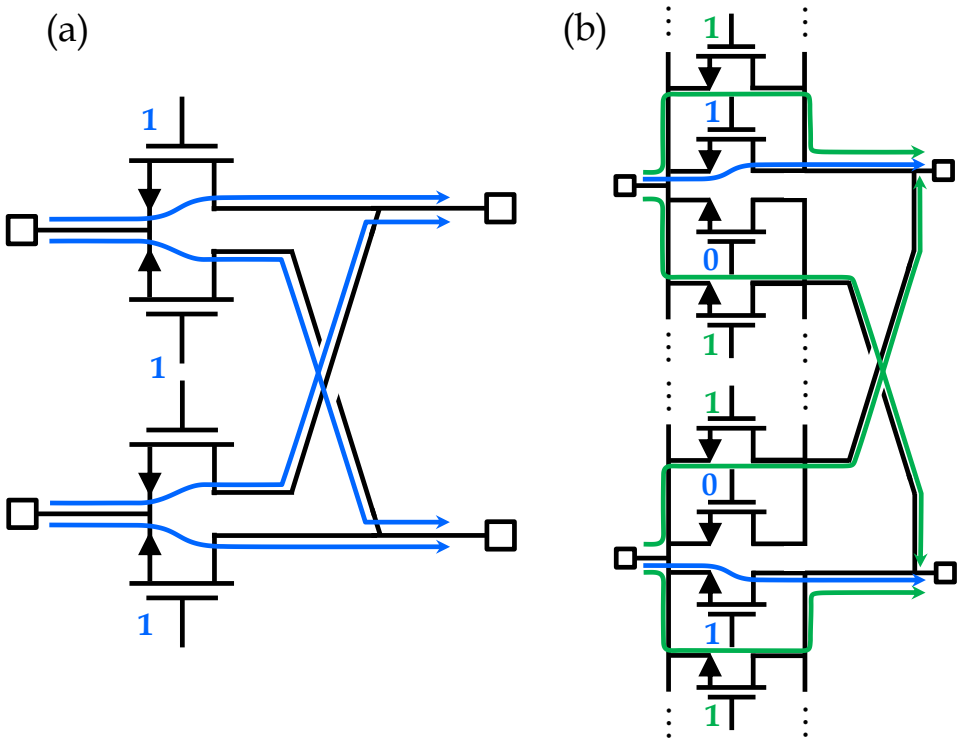

Figure 4-42: Segmented gates modulator. (a) OOK capable modulator and (b) PAM capable alternative design.

Finally, leveraging on the dual band architecture synchronized by means of a common reference signal as proposed in this work, in addition to the OOK capability in each branch, a wideband FSK scheme is also achievable (Figure 4-44). In fact, large-band frequency modulations usually exhibit enhanced robustness to noise and distortions because of strong

non-linearities in FSK demodulation processes [**McCune, 2010**]. For that reason, such a scheme could be valuable for long-range plastic waveguides applications for which conventional modulations may be impractical due to limited available powers at Tx level.

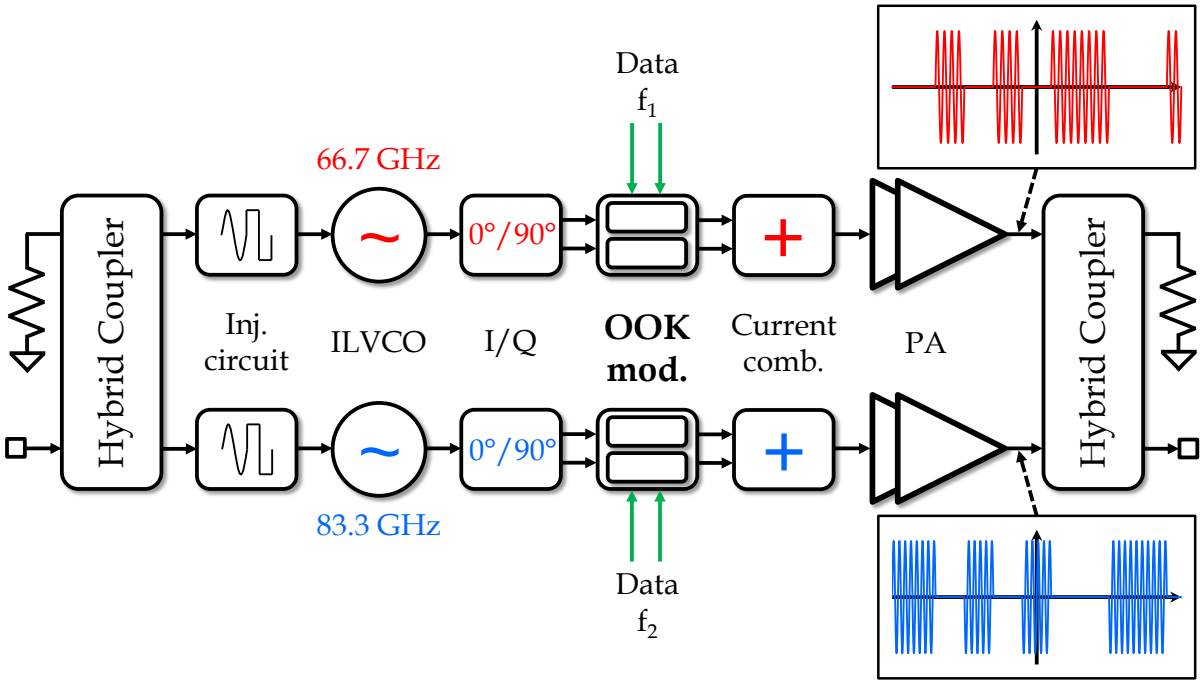

Figure 4-43: Schematic of a possible wideband FSK configuration relying on the proposed synchronized dual band architecture.

4.12.4. Dual Polarization Investigation

The dual-band combining capability of the proposed architecture comes at the expense of a rough 3 dB output loss penalty, which significantly affects the system energy efficiency. However, it should be mentioned that the considered loss is actually the result of a power division. While half of the signal power is effectively directed to the output, the other half is actually dissipated in a matched (resistive) load on the ISO port. With this observation in mind comes the idea of using the ISO port as a second output that could be combined off-chip in order to avoid the 3 dB loss.

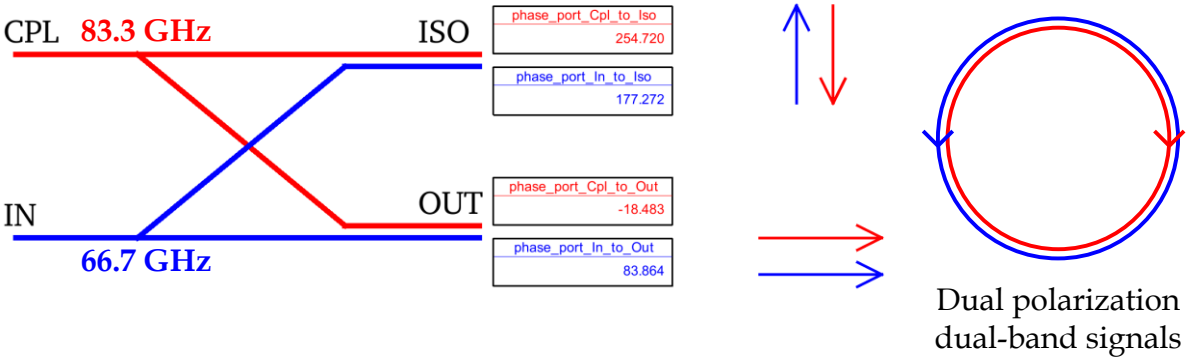

Figure 4-44: Illustration of a circular polarization excitation scheme using a hybrid coupler. The 75 GHz DVHC is proposed in this case (simulation results).

This idea is even more appealing when remembering that hybrid couplers are typically used in circular polarization excitation schemes. Therefore, Figure 4-44 presents a dual polarization and dual-band excitation scheme that leverages ISO port as a secondary output in quadrature. However, this concept assumes sufficient polarization control in the plastic waveguide channel as well as in the PCB to waveguide transition. As evocated in Chapter 3, this point is still a research topic but it is clear that, once a fully polarization-controlled plastic waveguide link will be available, circular polarization will draw a particular attention (due to rotational immunity) and the proposed DVHC will thus gain another advantage.

References

[**Cathelin, 2017**] A. Cathelin. "Fully depleted silicon on insulator devices CMOS: The 28-nm node is the perfect technology for analog, RF, mmW, and mixed-signal system-on-chip integration," *IEEE Solid-State Circuits Magazine*, pp. 18–26, Fall 2017.

[**Jany, 2015**] C. Jany, A. Siligaris, J. L. Gonzales-Jimenez, P. Vincent, P. Ferrari. "A programmable frequency multiplier-by-29 architecture for millimeter wave applications," *IEEE Journal of Solid-State Circuits*, Vol. 50, No. 7, July 2015.

[**Larie, 2015**] A. Larie, É. Kerhervé, B. Martineau, L. Vogt, D. Belot. "A 60GHz 28nm UTBB FD-SOI CMOS reconfigurable power amplifier with 21% PAE, 18.2dBm P1dB and 74mW PDC," *IEEE International Solid-State Circuits Conference*, pp. 48-50, Feb. 2015.

[**Long, 2000**] J. R. Long. "Monolithic transformers for silicon RF IC design," *IEEE Journal of Solid-State Circuits*, Vol. 35, No. 9, pp. 1368-1382, Sept. 2000.

[**McCune, 2010**] E. McCune. "Digital frequency modulation" in *Practical Digital Wireless Signals*, 1st edition, Cambridge University Press, pp. 124-159, 2010.

[**Moret, 2017**] B. Moret, V. Knopik, É. Kerhervé. "A 28GHz self-contained power amplifier for 5G applications in 28nm FD-SOI CMOS," *IEEE Latin America Symposium on Circuits and Systems*, pp. 1-4, Feb. 2017.

[**R&S, 2017**] Rohde & Schwarz. "R&S®FS-Z75 harmonic mixer specifications," available online at www.rohde-schwarz.com, 2017.

[**Rinaldi, 2018**] N. Rinaldi and M. Schröter. *Silicon-Germanium Heterojunction Bipolar Transistors for mm-Wave Systems: Technology, Modeling and Circuit Applications*. River Publishers, pp. 310, 2018.

[**Shi, 2013**] Q. Shi, K. Vaesen, B. Parvais, G. Mangraviti, P. Wambacq. "A 54-69.3 GHz dual-band VCO with differential hybrid coupler for quadrature generation," *IEEE Asian Solid-State Circuits Conference*, pp. 325-328, Nov. 2013.

[**Shopov, 2014**] S. Shopov and S. P. Voinigescu. "Characterization of the high frequency performance of 28-nm UTBB FDSOI MOSFETs as a function of backgate bias," *IEEE Compound Semiconductor Integrated Circuit Symposium*, pp. 1-4, 2014.

[**Singh, 2018**] J. Singh, J. Ciavatti, K. Sundaram, J. S. Wong, A. Bandyopadhyay, X. Zhang, S. Li, A. Bellaouar, J. Watts, J. G. Lee, and S. B. Samavedam. "14-nm FinFET Technology for analog and RF applications," *IEEE Transactions on Electron Devices*, Vol. 85, No. 1, pp. 31-37, 2018.

[**Tanaka, 2012**] Y. Tanaka, Y. Hino, Y. Okada, T. Takeda, S. Ohashi, H. Yamagishi, K. Kawasaki, A. Hajimiri. "A versatile multi-modality serial link," *IEEE Solid-State Circuits Conference*, pp. 332-333, Feb. 2012.

[**Tokgoz, 2016**] K. K. Tokgoz, S. Maki, S. Kawai, N. Nagashima, J. Emmei, M. Dome, H. Kato, J. Pang, Y. Kawano, T. Suzuki, T. Iwai, Y. Seo, K. Lim, S. Sato, L Ning, K. Nakata, K. Okada, A. Matsuzawa. "A 56Gb/s W-band CMOS wireless transceiver," *IEEE Solid-State Circuits Conference*, pp. 242-243, Feb. 2016.

[**Tokgoz, 2018**] K. K. Tokgoz, S. Maki, J. Pang, N. Nagashima, I. Abdo, S. Kawai, T. Fujimura, Y. Kawano, T. Suzuki, T. Iwai, K. Okada, A. Matsuzawa. "A 120Gb/s 16QAM CMOS millimeter-wave wireless transceiver," *IEEE Solid-State Circuits Conference*, pp. 168-169, Feb. 2018.

[**Vahdati, 2015**] A. Vahdati, D. Parveg, M. Varonen, M. Kärkkäinen, D. Karaca, K. A. I. Halonen. "A 100-GHz phase shifter in 28-nm CMOS FDSOI", *IEEE European Microwave Conference*, pp. 112-115, Sept. 2015.

[**Voineau, 2018**] F. Voineau, B. Martineau, M. Sié, A. Ghiotto, E. Kerhervé. "A Differential Vertical Hybrid Coupler and Low Capacitance RF Pads for Millimeter-Wave Applications in 28 nm CMOS FDSOI," *IEEE Topical Meeting on Silicon Monolithic Integrated Circuits in RF Systems*, pp. 57-59, Jan. 2018.

[**Wan, 2017**] J. Wan, Z. Chen, Q. An, and X. Wang. "A truly balanced Q-band CMOS frequency doubler based on hybrid quadrature coupler," *IEEE Microwave and Wireless Components Letters*, Vol. 27, No. 2, pp. 165-167, Fev. 2017.

Chapter 5

Conclusions

5.1 Summary and Contributions

In this work, various contributions to the development of plastic waveguide systems have been presented in order to pave the way to innovative high-speed and low-cost communication links. The theory of waveguides has been recalled in Chapter 2 and has been illustrated with many EM simulations. These results confirmed the low attenuation characteristics promises of such media, as reported earlier in the literature. However, and beyond the analogy with optical waveguides, limited confinement properties have been extensively discussed. This phenomenon was confirmed in practice and was actually found to be a major limitation, especially at lower frequencies. For that reason, an innovative plastic waveguide design was proposed, manufactured, characterized and it successfully demonstrated a superior confinement capability. Although there is still a lot to be done on this topic to obtain an environment insensitive channel with no attenuation penalty, this work opened a new research area by considering the plastic waveguide section as an additional design parameter.

Integrating this channel in a communication system obviously raised system level discussions gathered in Chapter 3. Large bandwidth requirements led to the development of a broadband PCB to rectangular waveguide transition in E band. Besides, a dual-band QPSK system architecture was proposed to favor a much easier digital interface with current envisioned applications. Compared to plastic waveguide systems that were commonly suggested, reduced-bandwidth RF channels mitigate attenuation and group-delay variations, enabling longer distances and / or higher data rates potentially. However, Chapter 3 also highlighted the difficulties encountered when demodulating QPSK signals at the receiver side. Benefiting from evident low power and low area requirements advantages, an innovative ILO based demodulation technique has been presented and discussed. For the purpose of a very simple analysis, an alternative closed-form solution of Adler's equation has been derived. Unfortunately, first numerical results showed unrealistic integration in CMOS technologies due to impractically narrow locking ranges and too tight Tx / Rx frequency alignments. Nevertheless, it was also shown that infinitely sharp phase transitions, as considered in this investigation, are both non-physical and pessimistic in this context, suggesting further studies.

Finally, Chapter 4 presented the design and realization of a mmW transmitter in a commercially available 28 nm CMOS FD-SOI node from STMicroelectronics. As a circuit dedicated to plastic waveguide communications, its specifications were guided by the high speed, low power and low cost context described all along this work. To deal with the

important bandwidth requirement imposed by the dual-band architecture on the circuit output, an innovative on-chip combining technique has been proposed relying on an integrated hybrid coupler. This design block has been successfully revisited through the introduction of the DVHC at 75 GHz, resulting in particularly broadband, low loss and strong isolation properties. On top of enabling a large output matching, the DVHC concept was also proven scalable from 17 GHz to 83 GHz without limitations, including accurate quadrature generation. In addition of this significant design contribution, optimized low capacitance mmW pads in 28 nm CMOS FD-SOI have been proposed while still maintaining compatibility with harsh flip-chip assembly rules for future package integration. Moreover, a mmW QPSK transmitter has been designed and demonstrated up to 9 Gb/s despite measurement limitations. Interestingly, the circuit internal oscillator can operate either in a free-running regime at lower consumption or in an injection-lock regime delivering very low phase noise. In the locked state, an external ≈ 16 GHz reference signal is needed that could be easily integrated in future circuit developments.

5.2 Future Work

This work main objective was finally to increase the maturity level of plastic waveguides underlying technologies (considering both the waveguide and mmW circuits) in order to speed up the transfer to preliminary industrial demonstrations. Consequently, since the early researches on plastic waveguides communications at STMicroelectronics in mid-2014, a long path has been drawn. The excessive enthusiasm regarding plastic waveguides properties which was initially triggered by the publication of very appealing results, has now turned into a more realistic vision as fundamental limitations such as limited confinement, bending sensitivity or chromatic dispersion, were predicted, demonstrated and quantified. In that sense, it is clear that the progress is important for both the academic community as well as the industry. Initial promises to deliver multi tens of Gb/s over a few tens of meters currently seem out of reach for many years to go, restraining first potential applications to moderate length links with data rates in the order of a few Gb/s.

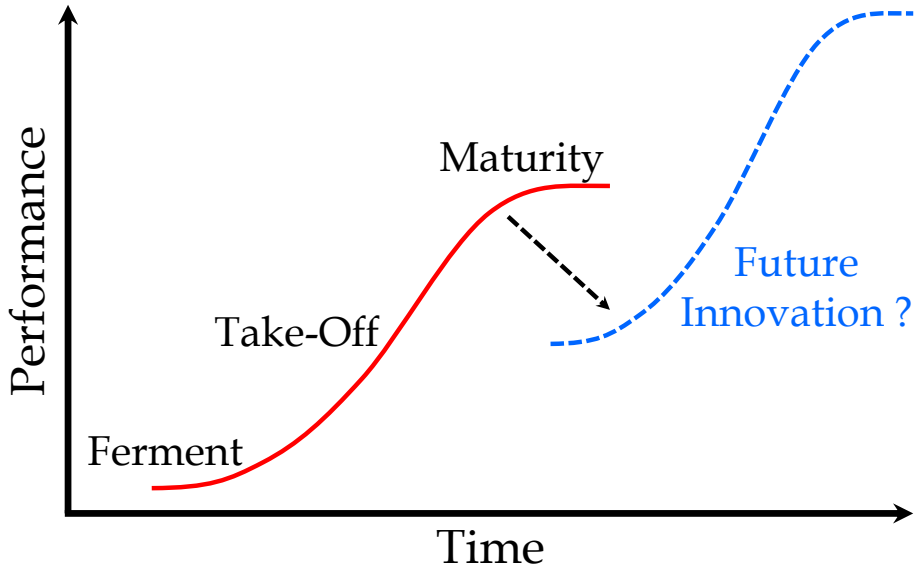

Figure 5-1: Typical S-curves describing usual innovation cycles.

It is still worth noticing that plastic waveguide performance evolution over time is qualitatively similar to any other technology, following a notable trend that is well known as the S-curve (Figure 5-1). Innovation is therefore the key to overcome limitations that appeared after the "take-off" period. Specifically, since the plastic waveguide technology clearly benefits from an obvious low cost advantage, it makes it a nice to have one because of a still promising performance / cost trade-off in the long-term. For that reason, it is believed that developments should be pursued through further investigations at waveguide and connector levels as well as more and more advanced demonstrations. In an attempt to identify possible technology enablers on different time scales, perspectives have been detailed at the end of each chapter of this thesis, considering both incremental and disruptive ideas.

5.3 List of Publications

This work has led to the following publications:

- F. Voineau, R. Pilard, B. Martineau, M. Sié, A. Ghiotto, E. Kerhervé. "Conception d'un guide d'ondes en plastique pour le transfert de données à haut-débit et bas coût aux fréquences millimétriques," Proceedings of the XIXth Journées Nationales Microondes (JNM), Bordeaux, June 2015.
- F. Voineau, A. Ghiotto, B. Martineau, M. Sié, E. Kerhervé. "Transition ligne micro-ruban / guide d'ondes de 55 à 95 GHz par l'ajout d'une pointe diélectrique et d'une section à double moulure," Proceedings of the XXth Journées Nationales Microondes (JNM), Saint-Malo, May 2017.
- F. Voineau, A. Ghiotto, E. Kerhervé, M. Sié, B. Martineau. "Broadband 55 – 95 GHz Microstrip to Waveguide Transition Based on a Dielectric Tip and a Tapered Double-Ridged Waveguide Section," IEEE International Microwave Symposium (IMS), pp. 723-726, June 2017.
- F. Voineau, B. Martineau, M. Sié, A. Ghiotto, E. Kerhervé. "A Differential Vertical Hybrid Coupler and Low Capacitance RF Pads for Millimeter-Wave Applications in 28 nm CMOS FDSOI," 18th IEEE Topical Meeting on Silicon Monolithic Integrated Circuits in RF Systems (SiRF), pp. 57-59, Jan. 2018.
- F. Voineau, C. Dehos, B. Martineau, M. Sié, M. Perchicot, N. H. Nguyen, A. Ghiotto, E. Kerhervé. "A 12 Gb/s 64QAM and OFDM Compatible Millimeter-Wave Communication Link Using a Novel Plastic Waveguide Design," IEEE Radio and Wireless (RWS), pp. 250-252, Jan. 2018.
- F. Voineau, A. Ghiotto, E. Kerhervé. Patent reference WO2017191409A1. "Ensemble pour la propagation d'ondes dans la gamme de fréquences comprises entre 1 GHz et 10 THz," Deposited on May, 3rd 2016.

Appendix A

Foam-coated Waveguide Study

The purpose of this Appendix is to provide additional information about plastic waveguide sensitivity to external contacts. Since the guiding mechanism in such waveguides actually relies on the interface between two dielectric materials, EM fields extend outside the structure so that a part of the carried energy effectively travels outside the *core* area that is to say in the *cladding* region. This situation leads to the definition of Poynting confinement factor that is therefore strictly inferior to 1, as explained in Chapter 2. However, it should be noted that this energy is "bound" to the core and may not be radiated. It should not be considered as a loss as long as…any perturbations are introduced, modifying the canonical propagation conditions. Such disturbances may be caused by a non-negligible bending of the waveguide (see Appendix C) or the presence of an undesirable dielectric / metallic material positioned near the waveguide. This latter configuration is typically encountered if the user touches the waveguide or if it is deposited on a table.

To illustrate this latter issue concretely, the foam-coated waveguide presented in [**Reynaert, 2017**] is simulated by means of a Finite Elements Method (FEM) solver. It is composed of a Ø 2 mm diameter PTFE waveguide coated by a 6 mm outer diameter foam. Unfortunately, dielectric properties of the materials used in this assembly are not reported. For the purpose of this investigation, we consider that the PTFE material is almost lossless ($\varepsilon_r = 2.1$, $\tan(\delta) = 10^{-6}$) so that simulated losses could be directly attributed to perturbation losses. Regarding the foam, we consider as a fair approximation that it is made of pure air. In that sense, it is not different from the air box enclosing the simulation. In the following, it is verified that the foam efficiently immunize the waveguide from detrimental contacts by simply preventing too close perturbations. Moreover, the foam thickness is swept to challenge its benefit with respect to the enlarged cross-sectional area penalty.

First, one may wonder about the (undisturbed) propagation constants of the waveguide. It is indeed overmoded beyond 109.4 GHz (Equation (A-1)), which is theoretically an unfavorable configuration for the application reported in [**Reynaert, 2017**] at around 120 GHz. Consequently, we can wonder whether this dimensioning is made on purpose or in a rather opportunistic way. Note that no explanations are actually delivered to make a decision. Nevertheless, two raisons may still explain this choice. Although higher order modes are able to propagate at 120 GHz in theory, their low confinement could make them very sensitive to practical propagation conditions (e.g. bends). We can therefore presume that they could be only responsible for additional (radiation induced) losses. One may consider this waveguide

as practically single-mode slightly above 110 GHz, but this explanation is definitely not sufficient to allow wideband applications at around 120 GHz. Additionally, the previous assumption regarding foam dielectric properties may be reassessed. According to Equation (A-1) recalled from Chapter 2, if the foam dielectric constant is only a fraction of the one of PTFE, let us assume 10 % or 20 %, the cut-off frequency is increased by 5.4 % or 11.8 % respectively. Combining those possible explanations could turn the waveguide into a practically single-mode one in the above-mentioned operating range.

$$f_c = \frac{2.405}{2\pi a}\frac{c_0}{\sqrt{\varepsilon_{r1} - \varepsilon_{r2}}} \tag{A-1}$$

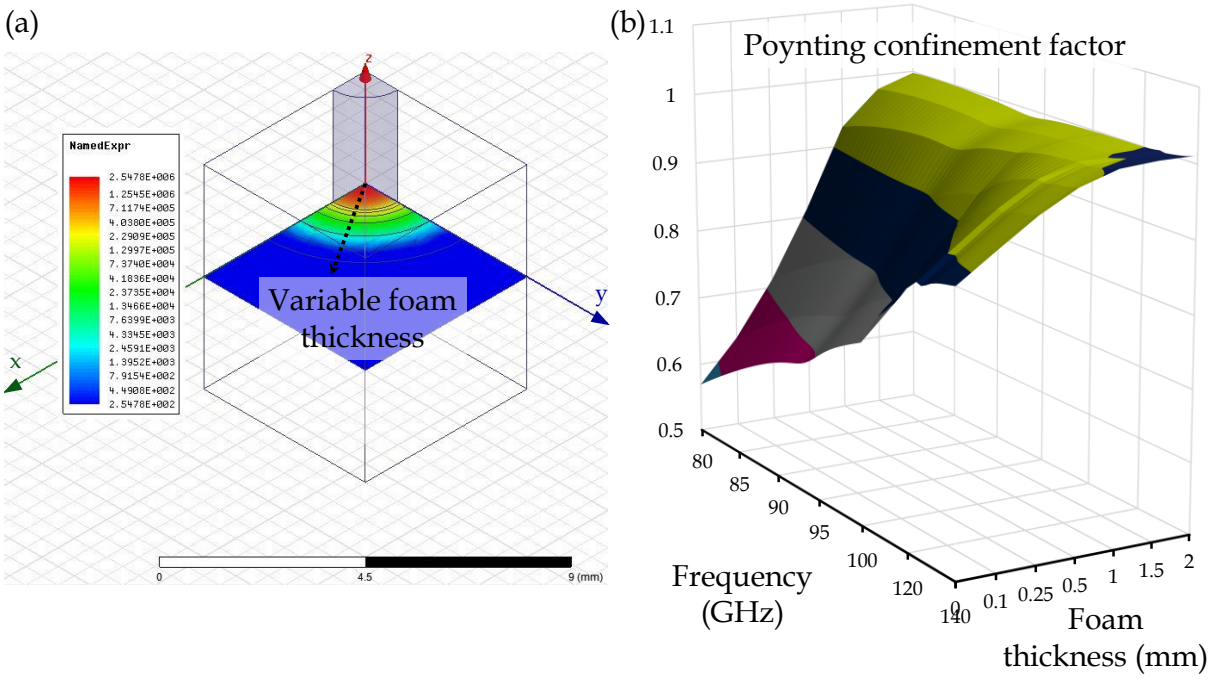

Figure A-1: Computation of the Poynting confinement factor for the fundamental HE_{11} mode. (a) Representation of the z-component of the real part of the Poynting vector and (b) 3D-surface plot of the computed Poynting confinement factor as a function of the frequency and the foam thickness.

With this first conclusion in mind, such a waveguide clearly operates in a high confinement regime, as confirmed in Figure A-1 (b) for a foam having a null thickness. From 80 GHz to 140 GHz, the Poynting confinement factor enhances from 57 % to 89 %. Besides, if the integrated power is integrated through a wider section corresponding to a variable foam thickness as illustrated in Figure A-1 (a), the confinement quickly reaches 100 % especially at high frequencies (Figure A-1 (b)). Note that numerical biases are visible in this simulation since the Poynting confinement should be strictly inferior to 1 as well as an increasing function with respect to frequency. Although the accuracy of these results could be enhanced, we can still observe that the foam captures the part of the energy traveling outside the waveguide by pushing away the boundary of the foam-coated waveguide. The benefit is particularly important at lower frequencies, where the confinement is smaller. From Figure A-1 (b), the Poynting confinement at 80 GHz increases from 57 % to almost 100 % when the foam thickness evolves from 0 (no foam) to 2 mm (as reported in [**Reynaert, 2017**]). Increasing the foam thickness further would certainly improve the Poynting confinement even more, but it is also clear from Figure A-1 (b) that the progress is asymptotical while the section of the foam-coated waveguide grows quadratically. This situation advocates for a trade-off. Although specifying a minimum confinement requirement is application dependent, one can still note that a 1 mm-

thick foam drastically improves the Poynting confinement at 80 GHz from 57 % to 93 % at less than a halve of the section of the reference design.

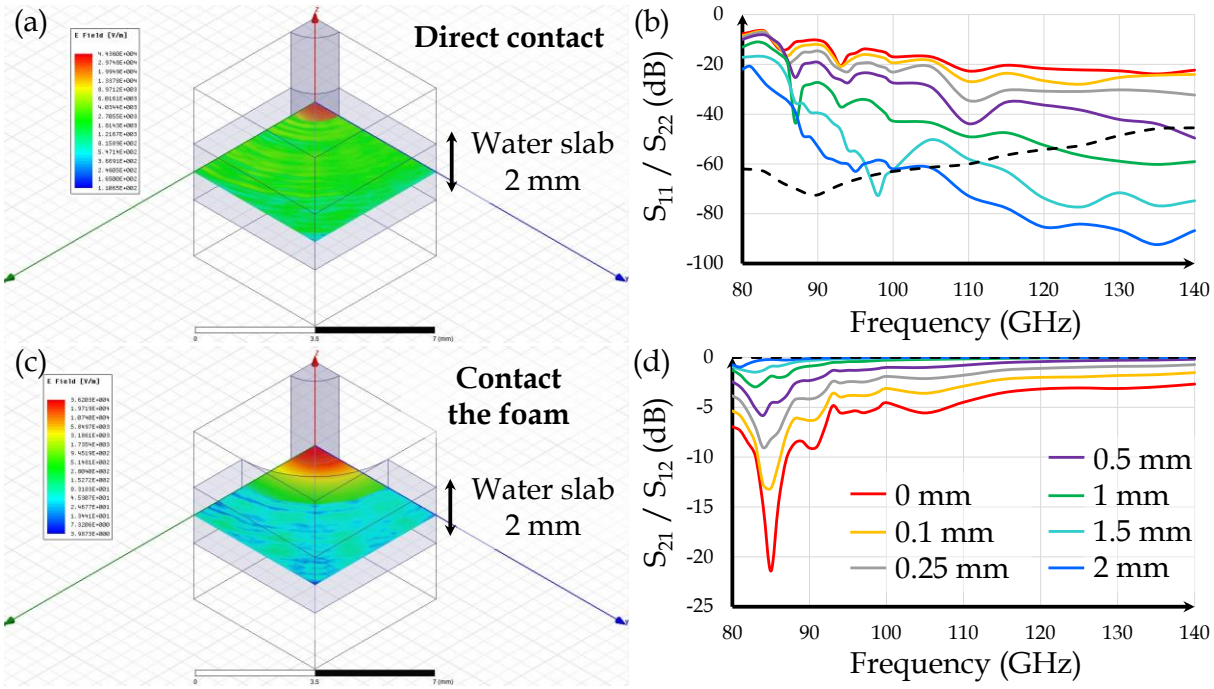

Figure A-2: Impact of a 2 mm-thick semi-infinite water slab on transmission. E-field envelope is computed at 120 GHz (log scale) when the slab is directly in contact with the waveguide (a) and when the slab is in contact of a 2 mm-thick air foam (c). Reflection and transmission parameters are provided in (b) and (d) respectively for different foam thicknesses. Undisturbed propagation represented in black dashed lines for reference. Besides, simulation resolution is estimated at – 40 dB.

Now that confinement outcomes of the foam has been described, the robustness regarding the presence of a high dielectric constant perturbation is discussed. Indeed, such a perturbation breaks the propagation condition once in contact with the waveguide and affects significantly the propagation. The simulation model is shown in Figure A-2 (a) where a water slab ($\varepsilon_r = 80$) is introduced around the waveguide. This situation could represent the impact of a user touching the waveguide, although the thickness of the slab is only 2 mm in this simulation due to computing limitations. By introducing a variable thickness foam around the waveguide (not shown in Figure A-2 (c) for simplicity), the water slab perturbation is pushed away of a distance corresponding to the considered foam thickness. From Figure A-2 (b) and Figure A-2 (d), the slab detrimental effects on reflection and transmission parameters are quantified. As expected, the larger the foam, the more robust the transmission. Furthermore, the strongest perturbations are introduced at lower frequencies, where the confinement is lower and the propagation more sensitive to the surrounding environment. Since the simulation resolution may be estimated at around – 40 dB, the slab introduces noticeable reflections (- 7.7 dB in the worst case). The latter are not sufficient to explain observed transmission losses. A portion of the energy is in fact absorbed directly by the slab, probably because of lateral radiation. As the foam thickness increases, less energy may be disturbed, thus reducing the quantitative impact of this mechanism on transmission. Figure A-3 summarizes this discussion at different frequencies. Interestingly, the cross-section area growth is also represented to highlight the penalty of large foams. Finally, a slab resonance characterized by low transmission and low reflection is notable at 85 GHz in Figure A-2. At this particular frequency, the double slab / air interface actually resonates in the z-direction.

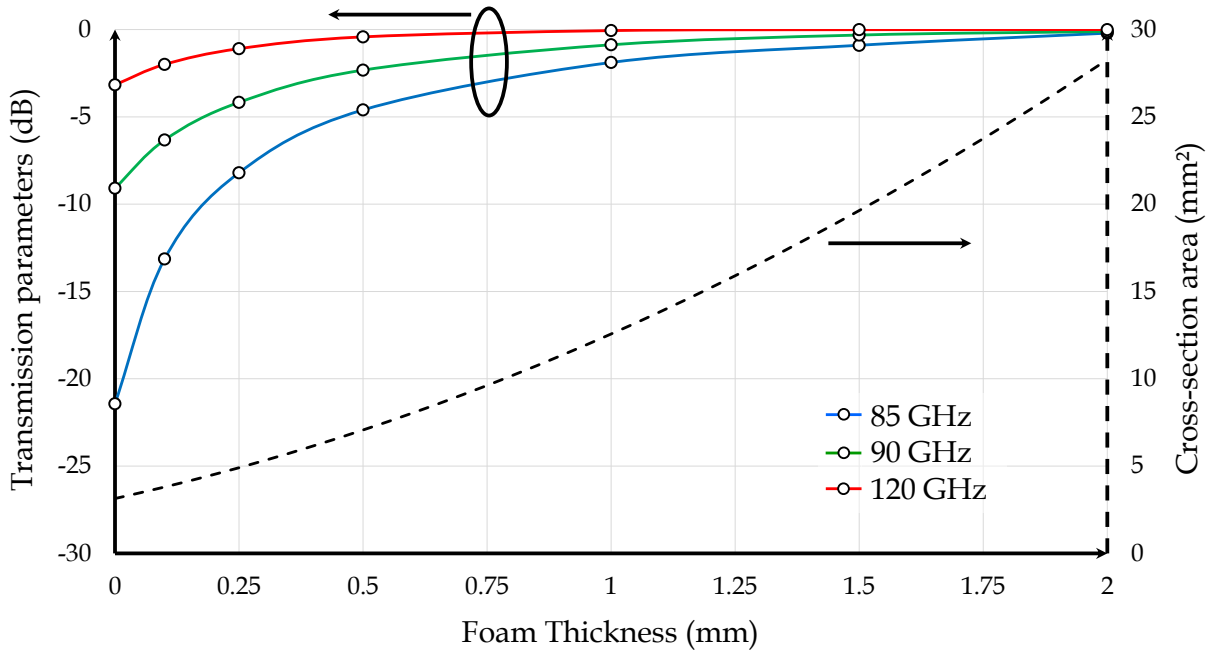

Figure A-3: Foam-thickness impact on transmission parameters for 3 different frequencies (left scale) and cross-section area (right scale).

To complete the analysis of the foam-coated waveguide, a 3D perturbative object is introduced instead of the slab, which was only 1D (infinite in x and y directions). A water drop ($\varepsilon_r = 80$) is positioned on the surface of the Ø 2 mm diameter PTFE waveguide, as shown in Figure A-4 (a). Similarly, a foam coating (approximated by pure air) is considered as well for the comparison. From Figure A-4 (b), the very strong impact of the drop on electric fields is prominent. A resonating behavior is also noticed, as the drop is actually responsible for 3D-cavity modes. This observation is confirmed with simulated S-parameters presented in Figure A-5.

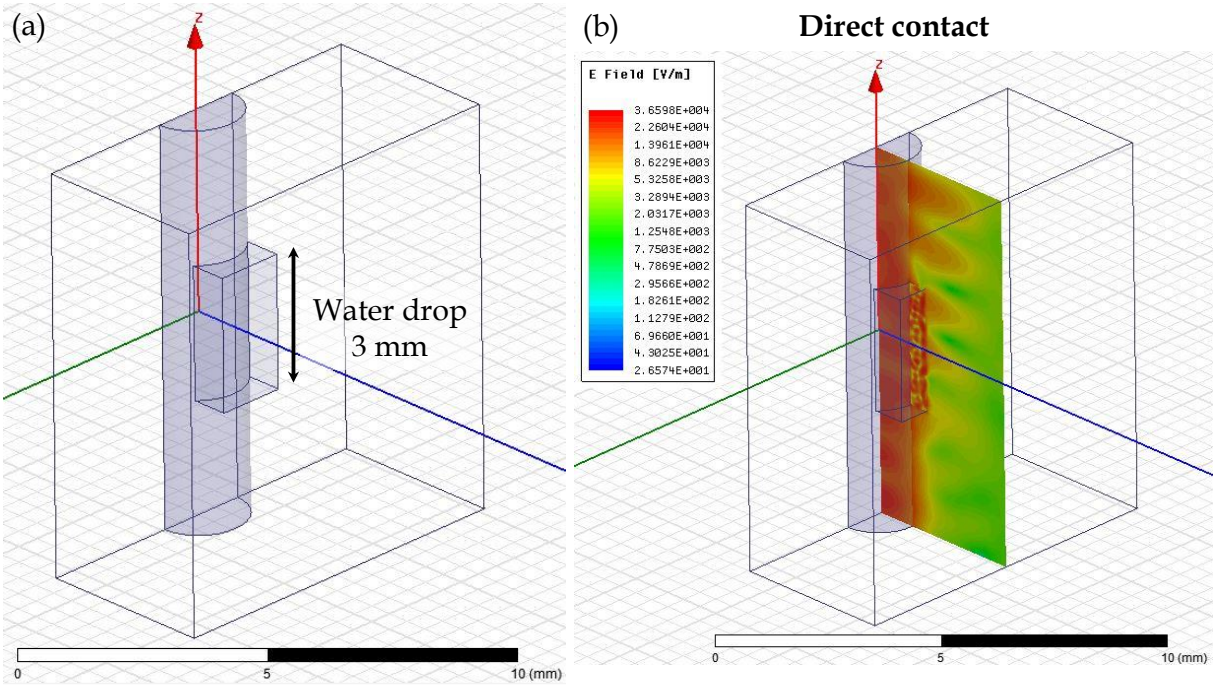

Figure A-4: Simulation of a simplified water drop positioned on the waveguide. (a) simulation model and (b) complex magnitude of the E-field computed at 120 GHz.

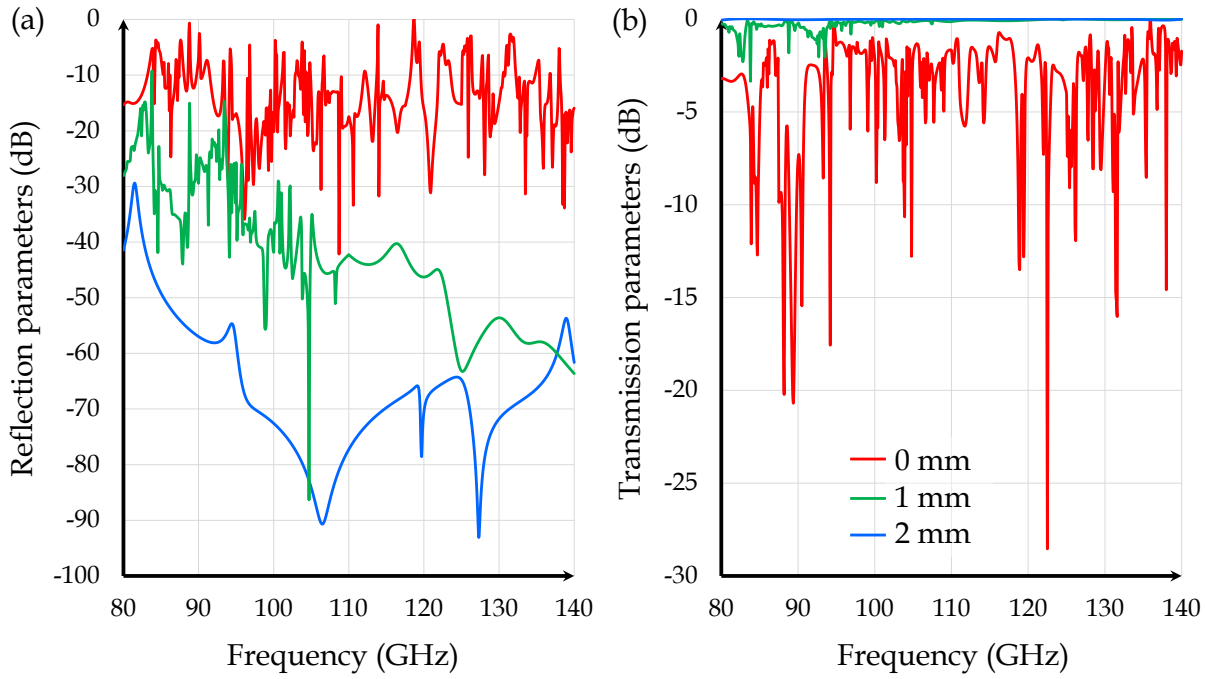

Figure A-5: Simulated S-parameters of the model presented in Figure A-4 (a). Reflection (a) and transmission (b) parameters are presented for a 0, 1 and 2 mm foam thickness in red, green and blue respectively.

From simulated reflection and transmission parameters reported in Figure A-5 (a) and Figure A-5 (b), the 2 mm thick foam-coated configuration can be considered as perfectly robust with negligible induced insertion loss (< 0.1 dB) and very high return loss (> 30 dB). On the contrary, it is clear that a direct contact (0 mm foam thickness) leads to a much more detrimental frequency-dependent behavior, which is characterized by strong resonances in the whole bandwidth. Note that such chaotic results are actually difficult to predict accurately, therefore causing frequency interpolation issues. Unfortunately, the possibility that proper results in this particular case could be even more chaotic as a function of frequency should not be eliminated at all. Finally, in an attempt to provide a suitable trade-off, an intermediate configuration having only 1 mm foam coating is investigated as well. Interestingly, this design provides excellent insensibility above 95 GHz. At lower frequencies, the confinement does not seem high enough to prevent small propagation perturbations. In simulation, return loss in the order of 10 to 30 dB are observed while maximal insertion loss is around 3 dB.

Appendix B

Return Losses in Low Loss Waveguides

The following discussion investigates the impact of imperfect matching at the ends of a low loss waveguide. Generally speaking:

- No assumption is made on the kind of waveguide considered here: it could be any metallic / plastic waveguides as well as coaxial or stripline transmission lines for example.
- The transmission loss budget, assuming perfectly matched input and output ports, should be *low*, possibly in the order of only a few dB. The impact of this quantity will of course be investigated in this study. Note that low transmission losses may result from low loss per unit length over moderate propagation distance or alternatively short distance in the case of moderate loss per unit length.
- No assumption is made on the nature of the loss (absorption, radiation, conductive loss, etc.). We will only assume a linear loss per unit length (in dB/m) without any frequency dependence.
- Imperfect mismatch excitations may have numerous root causes like impedance mismatch, EM fields map inconsistency, geometrical misalignment, etc. In this Appendix, we will mainly focus on impedance mismatch for simplicity.

Figure B-1 summarizes the discussed configuration. For the sack of simplicity the same input and output port impedance Z_0 is considered. The waveguide can be modeled thanks to the ABCD matrix given in Equation (B-1) where L, Z_L and γ are respectively the waveguide length, the waveguide characteristic impedance and the (complex) propagation constant.

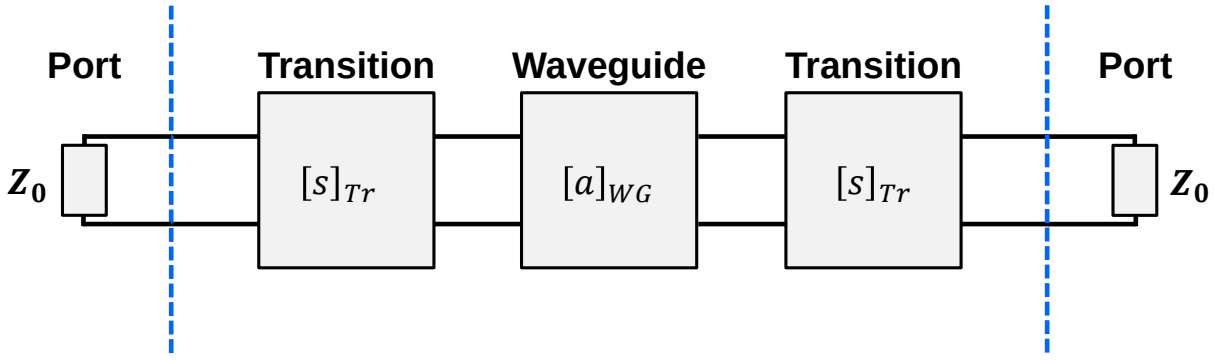

Figure B-1: Network resulting from the imperfect excitation of a waveguide.

$$[a]_{WG} = \begin{bmatrix} \cosh(\gamma L) & Z_L \sinh(\gamma L) \\ \frac{1}{Z_L}\sinh(\gamma L) & \cosh(\gamma L) \end{bmatrix} \tag{B-1}$$

$$\gamma = \alpha + j\beta \tag{B-2}$$

As regards the excitation of this waveguide, the general form of $[s]_{Tr}$ is given by Equation (B-3). In order to focus on the most relevant phenomenon, we can assume this transition to be reciprocal ($S_{22} = S_{11}$) and perfectly matched to the reference plane impedance Z_0. This assumption leads to a simplified expression $[s]_{Tr\_ideal}$ presented in Equation (B-4). Consequently, only impedance mismatch between the waveguide and the input / output ports is likely to produce reflections, as assumed earlier.

$$[s]_{Tr} = \begin{bmatrix} \Gamma_1 & \rho \\ \rho & \Gamma_2 \end{bmatrix} \tag{B-3}$$

$$[s]_{Tr\_ideal} = \begin{bmatrix} 0 & e^{j\theta_{Tr}} \\ e^{j\theta_{Tr}} & 0 \end{bmatrix} \tag{B-4}$$

To derive the expression of the cascaded network, $[a]_{WG}$ and $[s]_{Tr\_ideal}$ are first converted to T-parameters matrices, combined and finally translated back to a meaningful S-parameters matrix.

$$[T]_{Tr\_ideal} = \begin{bmatrix} e^{j\theta_{Tr}} & 0 \\ 0 & e^{-j\theta_{Tr}} \end{bmatrix} \tag{B-5}$$

$$[s]_{WG} = \frac{1}{N}\begin{bmatrix} \left(\frac{Z_L}{Z_0} - \frac{Z_0}{Z_L}\right)\sinh(\gamma L) & 2 \\ 2 & \left(\frac{Z_L}{Z_0} - \frac{Z_0}{Z_L}\right)\sinh(\gamma L) \end{bmatrix} \tag{B-6}$$

$$N = 2\cosh(\gamma L) + \left(\frac{Z_L}{Z_0} + \frac{Z_0}{Z_L}\right)\sinh(\gamma L) \tag{B-7}$$

The waveguide T-parameters matrix is then expressed in Equation (B-8). Consequently, cascaded T-parameters and S-parameters of the network are obtained in Equations (B-9) & (B-10).

$$[T]_{WG} = \begin{bmatrix} -\frac{\left(\frac{Z_L}{Z_0} - \frac{Z_0}{Z_L}\right)^2 \sinh(\gamma L)^2 - 4}{2N} & \frac{1}{2}\left(\frac{Z_L}{Z_0} - \frac{Z_0}{Z_L}\right)\sinh(\gamma L) \\ -\frac{1}{2}\left(\frac{Z_L}{Z_0} - \frac{Z_0}{Z_L}\right)\sinh(\gamma L) & \frac{N}{2} \end{bmatrix} \tag{B-8}$$

$$[T] = [T]_{Tr\_ideal}[T]_{WG}[T]_{Tr\_ideal}$$

$$= \begin{bmatrix} -\frac{\left(\frac{Z_L}{Z_0} - \frac{Z_0}{Z_L}\right)^2 \sinh(\gamma L)^2 - 4}{2N} e^{2j\theta_{Tr}} & \frac{1}{2}\left(\frac{Z_L}{Z_0} - \frac{Z_0}{Z_L}\right)\sinh(\gamma L) \\ -\frac{1}{2}\left(\frac{Z_L}{Z_0} - \frac{Z_0}{Z_L}\right)\sinh(\gamma L) & \frac{N}{2} e^{-2j\theta_{Tr}} \end{bmatrix} \tag{B-9}$$

$$[s] = \frac{e^{2j\theta_{Tr}}}{N}\begin{bmatrix}\left(\frac{Z_L}{Z_0}-\frac{Z_0}{Z_L}\right)\sinh(\gamma L) & 2\\ 2 & \left(\frac{Z_L}{Z_0}-\frac{Z_0}{Z_L}\right)\sinh(\gamma L)\end{bmatrix} \tag{B-10}$$

Additionally, to include potential insertion losses at transitions levels, it is possible to consider θ_{Tr} as a complex quantity without any loss of generality (Equations (B-11) - (B-12)).

$$\theta_{Tr} = \theta_{Tr}{}' + j\varphi \tag{B-11}$$

$$\rho = e^{-2\varphi} \tag{B-12}$$

Substituting Equations (B-11) & (B-12) in (B-10), we obtain the general Equation (B-13) of the network S-parameters.

$$[s] = \rho\frac{e^{2j\theta_{Tr}{}'}}{N}\begin{bmatrix}\left(\frac{Z_L}{Z_0}-\frac{Z_0}{Z_L}\right)\sinh(\gamma L) & 2\\ 2 & \left(\frac{Z_L}{Z_0}-\frac{Z_0}{Z_L}\right)\sinh(\gamma L)\end{bmatrix} \tag{B-13}$$

Among others, the magnitude of the transmission parameters S_{12} and S_{21} is of primary interest. Combining Equations (B-2), (B-7) and (B-13), Equation (B-14) is derived.

$$\begin{aligned}|S_{21}|^2 = |S_{12}|^2 &= \frac{4\rho^2}{|N|^2}\\ &= \frac{4\rho^2}{\left(2\cosh(\alpha L)+\left(\frac{Z_L}{Z_0}+\frac{Z_0}{Z_L}\right)\sinh(\alpha L)\right)^2+\sin(\beta L)^2\left(\frac{Z_L}{Z_0}-\frac{Z_0}{Z_L}\right)^2}\end{aligned} \tag{B-14}$$

This latter expression of the transmission is very instructive and will now be covered in detail.

- In the case of matched waveguide $Z_L = Z_0$, the resulting insertion loss is the following Equation (B-15).

$$10\log(|S_{21}|^2) = 2\cdot\underbrace{10\log(\rho)}_{\substack{Transition\\ insertion\ loss}} + \underbrace{10\log(e^{-2\alpha L})}_{\substack{Waveguide\\ insertion\ loss}} \tag{B-15}$$

In this specific case, it is worth noting that the insertion loss is simply the sum of the waveguide loss and the transition losses…just as expected.

- The insertion loss given in Equation (B-14) is also found to be independent of $\theta_{Tr}{}'$.

In other words, only the insertion loss of the transition influences the global insertion loss. This conclusion is a direct consequence of the ideal (matched) transition assumption made earlier.

- Another interesting characteristic of Equation (B-14) is the βL dependency as illustrated in the Figure B-2 below under the assumption of negligible propagation losses.

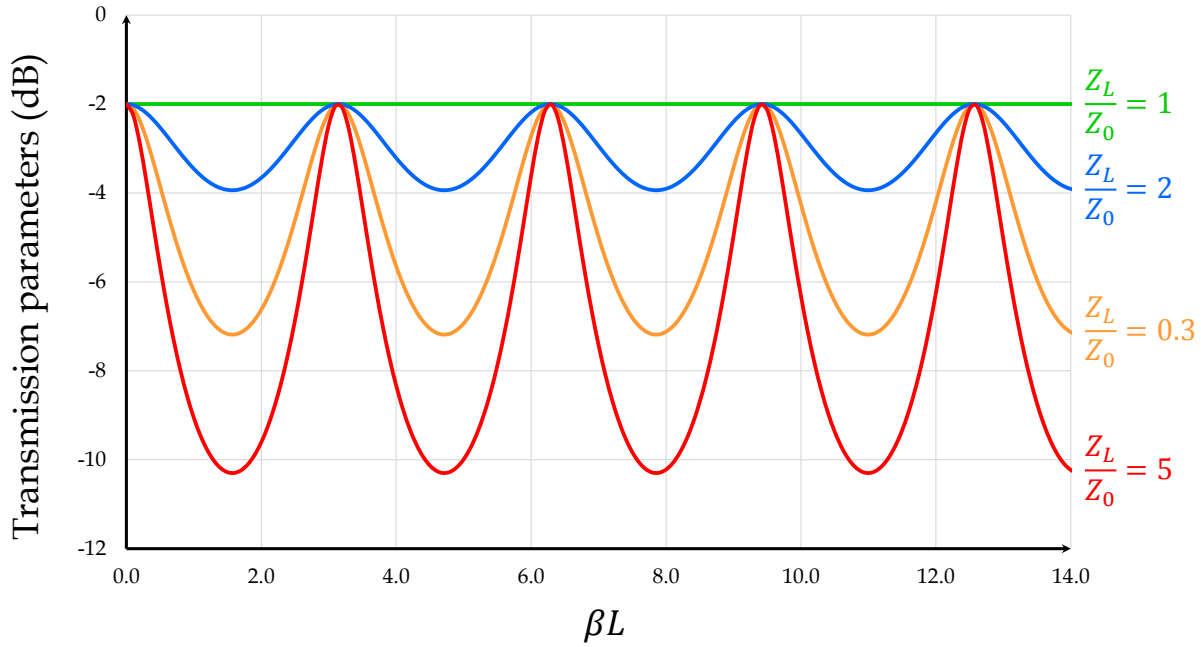

Figure B-2: Illustration of Equation (B-14) for different values of $\frac{Z_L}{Z_0}$ with a transition insertion loss of 1 dB per end. Propagation losses are neglected.

A detrimental phenomenon is observed and may be responsible for frequency dependent transmissions, which typically causes signal integrity degradation. The ripples amplitude *RipA* and ripples frequency *RipF* are expressed analytically in Equations (B-18) & (B-20). Note that *RipA* depends on both attenuation and mismatch conditions. In low loss waveguides, the situation depicted here may then arise. Furthermore, for long waveguides (≈ 3 m), *RipF* is in the order of 100 MHz, which is roughly two decades smaller than the typical bandwidth, so that around 100 ripples may be present in the desired bandwidth.

$$|S_{21}|^2{}_{MIN} = \frac{4\rho^2}{\left(2\cosh(\alpha L) + \left(\frac{Z_L}{Z_0} + \frac{Z_0}{Z_L}\right)\sinh(\alpha L)\right)^2 + \left(\frac{Z_L}{Z_0} - \frac{Z_0}{Z_L}\right)^2} \tag{B-16}$$

$$|S_{21}|^2{}_{MAX} = \frac{4\rho^2}{\left(2\cosh(\alpha L) + \left(\frac{Z_L}{Z_0} + \frac{Z_0}{Z_L}\right)\sinh(\alpha L)\right)^2} \tag{B-17}$$

$$RipA = 10\log\left(\frac{|S_{21}|^2_{MAX}}{|S_{21}|^2_{MIN}}\right) = 10\log\left(1 + \frac{\left(\frac{Z_L}{Z_0} - \frac{Z_0}{Z_L}\right)^2}{\left(2\cosh(\alpha L) + \left(\frac{Z_L}{Z_0} + \frac{Z_0}{Z_L}\right)\sinh(\alpha L)\right)^2}\right) \tag{B-18}$$

Free-space propagation approximation

$$\beta \cong {}^{\omega}/_{c} \tag{B-19}$$

$$RipF = \frac{c}{L} \tag{B-20}$$

This phenomenon can be interpreted as well by the presence of standing waves in the waveguide as a result of impedance mismatch at both ends. The situation is then similar to other well-known design contexts, like PCB or RFIC design involving standing waves…except that waveguides lengths corresponds to a huge number of wavelengths, thus involving strong frequency-dependent behaviors, compared to ≈ 1 wavelength in traditional contexts.

- To limit *RipA*, the impedance mismatch should be minimized, so that the ratio $\frac{Z_L}{Z_0}$ should be close as close as possible to 1.

Equation (B-18) is represented in Figure B-3 for different values of αL. With higher loss waveguides, the impedance matching constraint is clearly relaxed. On the other hand, low loss waveguides require more stringent impedance matching. With this conclusion in mind, it seems important to balance this design parameter in accordance with the maximum acceptable *RipA* for a given system. In the following derivations, we will now arbitrarily consider *RipA* ≤ 1 dB as a fair system level constraint. Starting from Equations (B-18) & (B-21), a set of 2 equations are finally obtained, defining a maximum and a minimum impedance ratio (Equations (B-22) & (B-23)).

$$RipA \leq 1\ dB \tag{B-21}$$

$$\frac{Z_L}{Z_0} \leq \frac{\sqrt{10^{0.1}-1}\cosh(\alpha L)+\sqrt{10^{0.1}}}{1-\sqrt{10^{0.1}-1}\sinh(\alpha L)} \tag{B-22}$$

$$\frac{Z_L}{Z_0} \geq \frac{\sqrt{10^{0.1}}-\sqrt{10^{0.1}-1}\cosh(\alpha L)}{1+\sqrt{10^{0.1}-1}\sinh(\alpha L)} \tag{B-23}$$

These bounds can be related to the Waveguide Loss Budget by Equation (B-25). However, one can note that both Equations (B-22) & (B-23) exhibit unphysical behaviors for large αL quantities. A common singularity actually appears for $\alpha L \geq \alpha L_{MAX}$ (Equation (B-26)).

$$\alpha_{dB/m} \cong 8.686\ \alpha \tag{B-24}$$

Waveguide Loss Budget (dB)

$$\alpha_{dB/m}\ L \cong 8.686\ \alpha L \tag{B-25}$$

$$\alpha L_{MAX} = \operatorname{asinh}\left(\frac{1}{\sqrt{10^{0.1}-1}}\right) = \operatorname{acosh}\left(\frac{\sqrt{10^{0.1}}}{\sqrt{10^{0.1}-1}}\right) \approx 12.4034\ \text{dB} \tag{B-26}$$

Minimum Return Loss (dB)

$$-20\log\left(\left|\frac{\frac{Z_L}{Z_0}-1}{\frac{Z_L}{Z_0}+1}\right|\right) \tag{B-27}$$

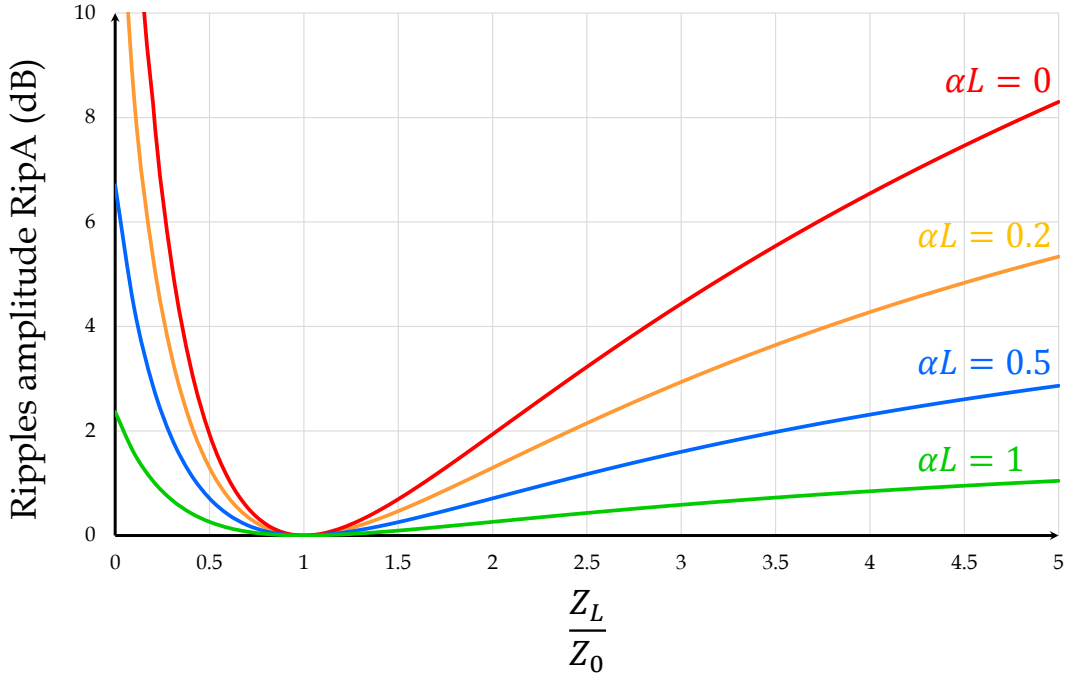

Figure B-3: Transmission ripples amplitude RipA as a function of the impedance mismatch for different attenuation conditions.

This effect is illustrated in Figure B-4, which relates Equations (B-22), (B-23) and (B-25). Using Equation (B-27), the two curves on the left graph correspond exactly to the same Minimum Return Loss on the right graph. Thanks to this representation, interpretation becomes straightforward.

For waveguides having loss budgets in excess of roughly 12.4 dB, any impedance ratio results in transmission ripples inferior or equal to 1 dB. While this conclusion sounds surprising, the standing waves explanation should be reminded. Because high propagation losses clearly induce strong damping of reflected waves, one can easily understand that interferences of waves with very different amplitudes cause limited transmission ripples. On the contrary, for lower loss waveguides, impedance matching should be considered carefully and the lower loss in the waveguide, the higher Minimum Return Loss required. Furthermore, this relation is perfectly linear, as shown in Figure B-4.

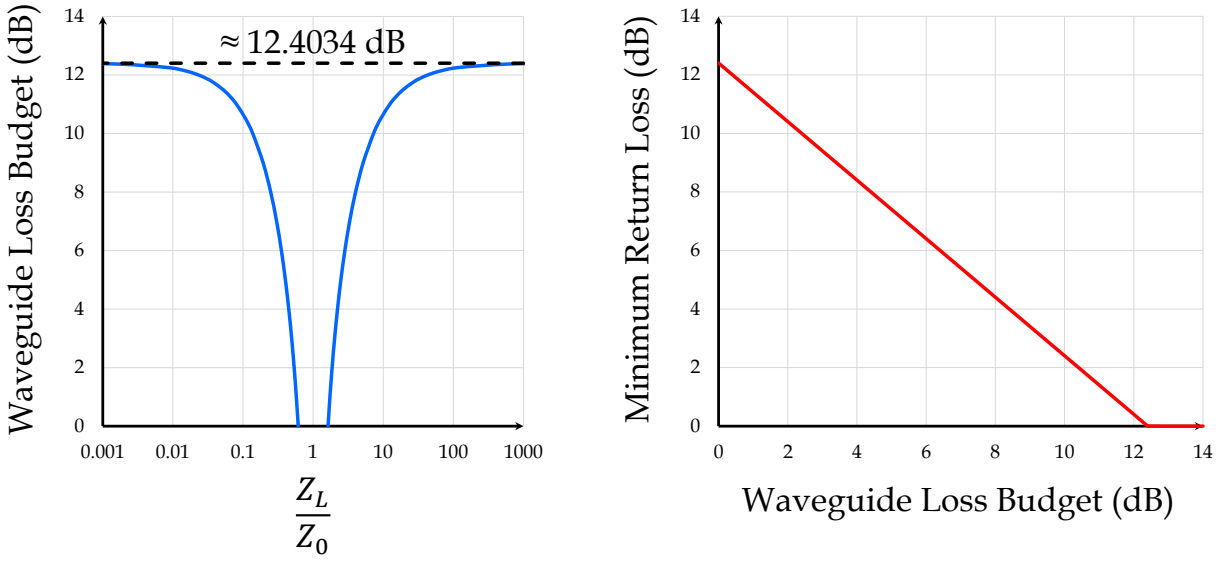

Figure B-4: Relation between Waveguide Loss Budget and impedance ratio (left) and corresponding Return Loss (right). All data are computed assuming RipA = 1 dB.

Appendix C

Influence of Bends in Plastic Waveguides

Capability to manage bends is an important figure of merit for a given wireline communication system. The influence of bending a plastic waveguide is therefore investigated in this Appendix. The simulation setup is presented in Figure C-1. Note that the z-scale has been shrank by a factor of 0.95 to remove modal degeneracy. This results in a slight asymmetry between horizontal (1st mode) and vertical (2nd mode) HE_{11} polarizations. Although these two modes are of primary interest in the context of high-speed communication, an additional 3rd mode (TM_{01}) is still defined in the simulation in order to quantify the possible excitation of higher order modes because of aggressive bends. It is still worth noting that such a mode is likely to be radiated over long distances. Consequently, the energy coupled on this mode may be considered as a loss.

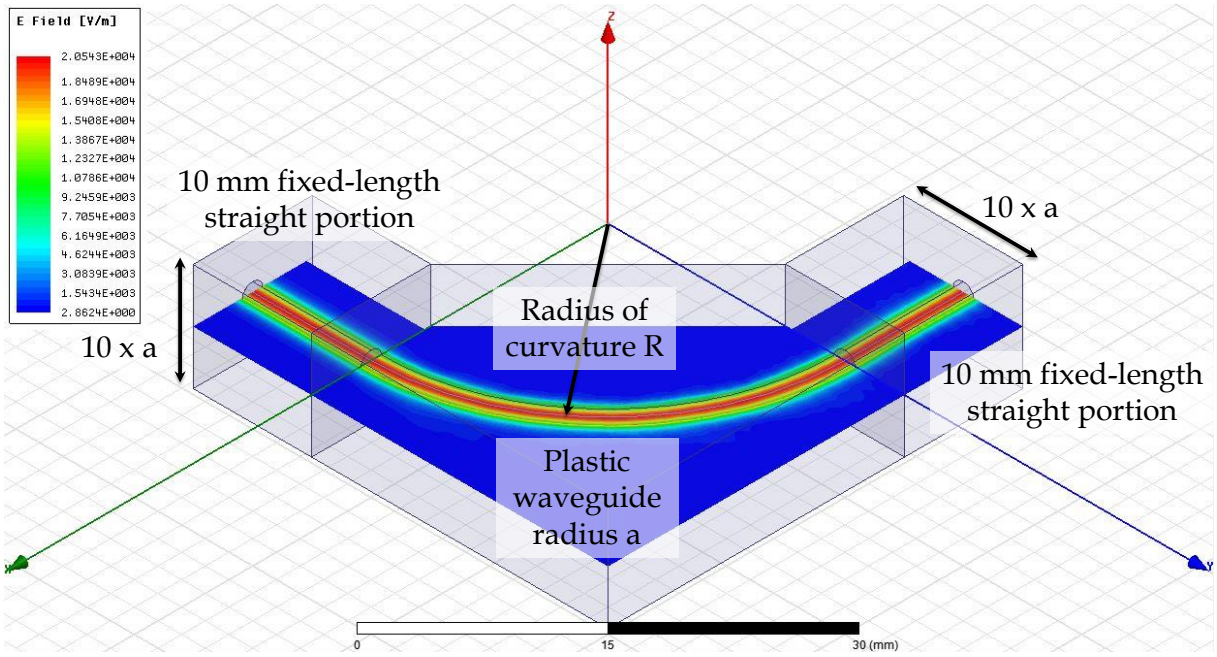

Figure C-1: Illustration of the simulation setup at 120 GHz for a 20 mm radius of curvature. Simulated bends are embedded with 10 mm straight waveguides at both ends. Waveports are used as excitation sources and radiation conditions are applied on all faces.

The study is realized using two plastic waveguide rods made of idealized Polyethylene (PE - $\varepsilon_r = 2.3, \tan(\delta) = 10^{-6}$) and surrounded by air. Their radii are chosen to obtain 60 GHz and 120 GHz maximum single-mode frequencies respectively. Using Equation (C-1), these radii are compiled in Table C-1.

Maximum single-mode frequency

$$f_{max} = \frac{2.405}{2\pi a} \frac{c_0}{\sqrt{\varepsilon_r - 1}} \quad \text{(C-1)}$$

Max. single-mode frequency	60 GHz	120 GHz
Radius a	1.677 mm	0.839

Table C-1: Considered radii of the PE plastic waveguide rods under scrutiny.

C.1 Impact on Transmission Parameters

To focus on bending losses without taking into account intrinsic propagation losses, an ultra-low loss PE material ($\tan(\delta) = 10^{-6}$) is considered. With a resulting attenuation much lower than 1 dB/m and simulated lengths inferior to 60 mm, it is a fair approximation to relate transmission parameters directly to bending losses under scrutiny. The impact of aggressive radius of curvature on the transmission is presented in Figure C-2. To simplify comparisons, all bending radii are normalized to the wavelength. Note that equivalent results are obtained whatever the considered polarization of the HE_{11} mode.

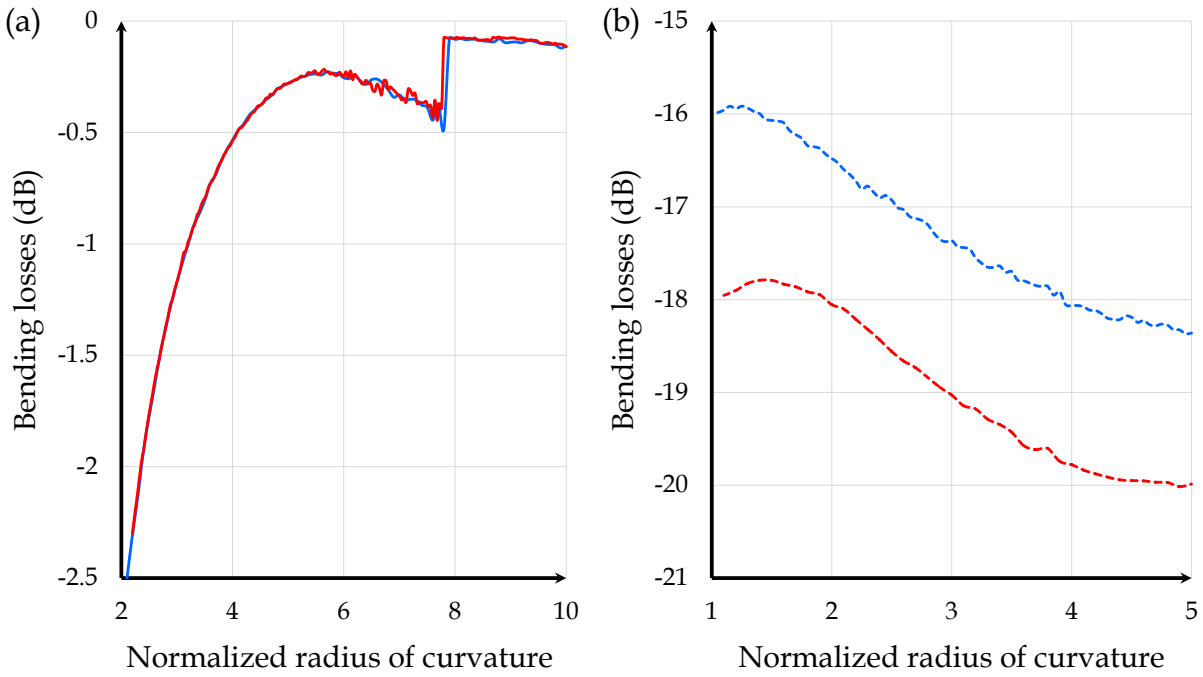

Figure C-2: Simulated transmission parameters of the HE_{11} modes as a function of the normalized radius of curvature. (a) Transmission at 60 GHz and 120 GHz maximum single-mode frequencies represented in blue and red respectively. (b) Transmission at half maximum single-mode frequencies (30 GHz and 60 GHz in blue and red respectively).

We can first conclude from Figure C-2 (a) that bending losses at 60 and 120 GHz are identical. This results from the appropriate design scaling and the use of normalized radii of curvature. In both cases, an unphysical discontinuity is obtained for abscissa values of around 7.8. Increasing losses from around 5.5 to 7.8 are also doubtful. After careful investigations, it appeared that this major inconsistency is actually caused by polygonal shape approximation during meshing resolutions. Above 7.8, an additional side is added to the polygonal approximation of the curvature, enhancing the approximation drastically. This simulation artefact suggests that bending losses in a perfect waveguide could be lower. However, attention should be paid on manufacturing tolerances that could end up with analogous geometrical deviations and thus additional losses. The impact is still limited here (only 0.5 dB inconsistency). We can estimate that bending loss is kept below 1 dB as long as the radius of curvature does not decreases below $3\lambda_0$.

While results in Figure C-2 (a) benefit from maximum confinement (77.5 %) because of their operation at maximum single-mode frequencies, Figure C-2 (b) investigates operation at lower frequencies. Waveguides are in fact studied at half the maximum single-mode frequency, namely 30 GHz and 60 GHz for the waveguides with radius of 1.677 mm and 0.839 mm respectively (Table C-1). When considering lower frequencies for a given bending radius, the normalized radius of curvature diminishes. Note that the abscissa in Figure C-2 (b) is thus different from the one in Figure C-2 (a) although the same practical configurations have been studied. In other words, a given bend appears more aggressive at lower frequency. While qualitatively valid, this conclusion is still not sufficient to explain larger bending losses although it is still not clear whether the simulated behavior in Figure C-2 (b) is correct.

Intuitively, one could actually expect higher losses for more aggressive bends. Remembering that the ability to simulate low-confinement waveguides accurately is a function of the size of the surrounding air box, the proposed setup in Figure C-1 may not be perfectly suitable. As simulations presented here are already very time-consuming, the verification with an enlarged simulation setup has not been carried out.

C.2 Impact on Reflection Parameters

In Figure C-3, the impact of the radius of curvature on reflection parameters is investigated, showing very small curvature-induced reflections. Note that equivalent results are obtained whatever the considered polarization of the HE_{11} mode. Because of the relaxed convergence criteria enforced in these very long simulations ($\Delta S < 0.02$), we can estimate simulation resolution limit at roughly -34 dB as shown in Figure C-3. Below this limit, it is not possible to distinguish quantities of interest from calculation noise. Consequently, we can state that reflections induced in bended plastic waveguides, if any, are completely negligible.

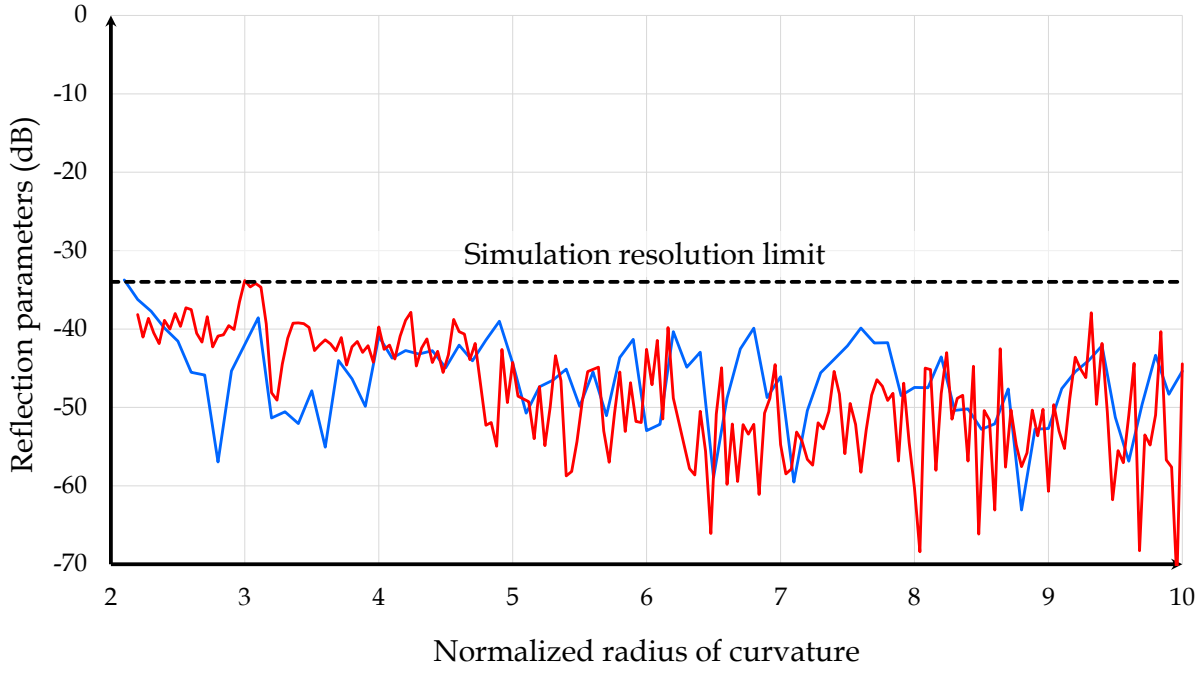

Figure C-3: Simulated reflection parameters for the 60 GHz (blue) and 120 GHz (red) configurations already introduced in Figure C-2. Results are below simulation resolution limit.

C.3 Impact on Polarization Isolation

In the context of polarization-duplexed systems, isolation between propagation modes is of paramount importance. While this specification is typically satisfied for orthogonal modes as long as the waveguide is straight, we can wonder whether bends could deteriorate it. Curvature-induced mode couplings are therefore analyzed in Figure C-4.

Horizontal / vertical HE_{11} polarization isolation is the most important quantity to be considered. Satisfyingly, Figure C-4 (a) clearly shows that polarization rotation remains negligible even for the most aggressive bends. In fact, this quantity is always below simulation resolution, except for a few singular points, for which the analysis should be pushed further. Anyway, slightly anticipating on these results, we can conclude that polarization rotation is negligible in practice.

Detrimental couplings to higher order modes is questioned in Figure C-4 (b). In spite of their incapacity to propagate over long distances due to low confinement features, such modes can still be excited due to discontinuities like bends. Unfortunately, the resulting coupled power can then be regarded as a pure loss. In the case considered here, while vertically polarized HE_{11}^{V} mode coupling to TM_{01} is well below simulation resolution, a horizontal HE_{11}^{H} mode coupling to TM_{01} is visible especially for short radii of curvature. Even if the simulated coupling is weak, it is definitely not the result of computation noise. Additionally, similar behaviors are obtained at 60 and 120 GHz. However, such a brutal behavior discrepancy between horizontal and vertical HE_{11} modes is arguable. In order to validate quantitatively this conclusion, additional simulations would be necessary because the TM_{01} mode suffers from low-confinement so that the simulation setup may not be appropriate. Some more modes may also be added in future simulations.

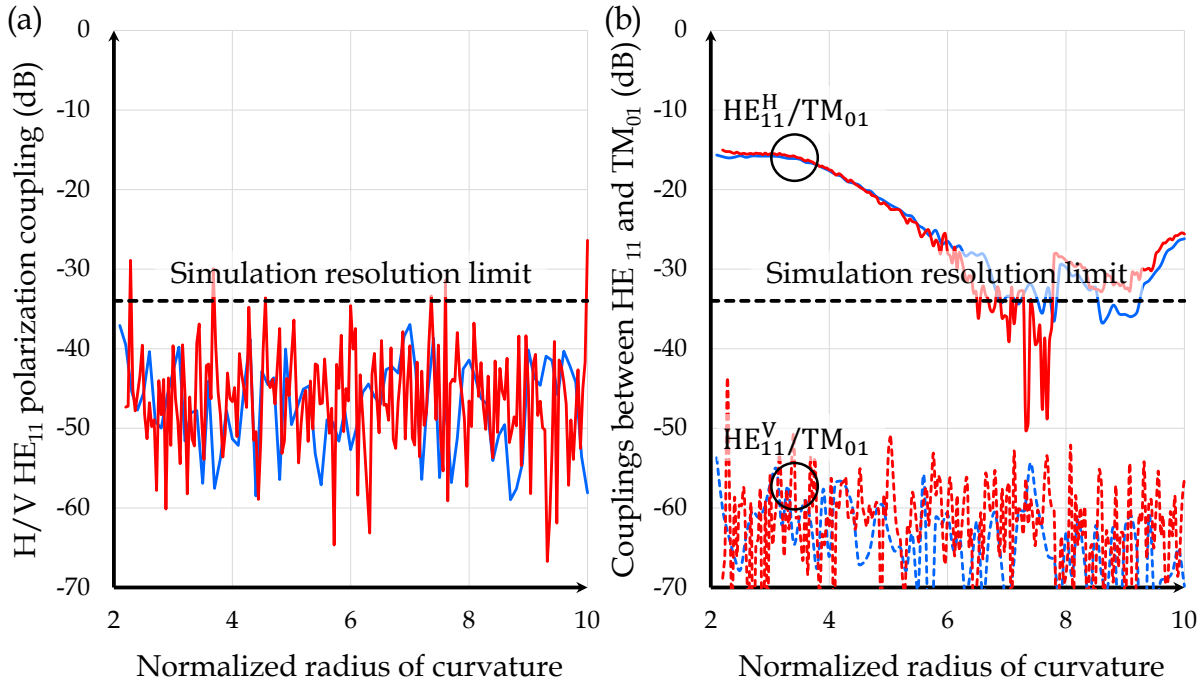

Figure C-4: Curvature-induced mode couplings. (a) HE_{11} polarization rotation and (b) HE_{11} horizontal (solid lines) and vertical (dotted lines) modes couplings to TM_{01} mode. Red and blue lines refer to 60 and 120 GHz plastic waveguides already introduced in Figure C-2.

C.4 Impact of the Dielectric Constant of the Cladding

Finally, the dielectric permittivity step between the core and the cladding is investigated as a design parameter. For a given maximum single-mode frequency, it is actually possible to scale the waveguide appropriately as long as the core material has a higher dielectric constant than the cladding. However, it is the purpose of this latter section to discuss briefly the influence of this design parameter on the bending capability.

For the particular needs of the investigation, the two previous waveguides have been surrounded by a hypothetical material having a dielectric permittivity of 2 instead of 1 (air) so that the dielectric constants step is only 0.3 instead of 1.3. To maintain maximum single-mode frequency at 60 and 120 GHz, both waveguides have been scaled by a factor of $\sqrt{\frac{2.3-1}{2.3-2}} \approx 2.08$.

Simulated E-fields magnitude are visible in Figure C-5. Compiled results in this figure clearly show that incoming signals tend to go straight… The comparison with Figure C-1 is especially insightful. Instead of following the curved direction imposed by the waveguide, signals are simply radiated, resulting in poor bending capability. These qualitative results are confirmed quantitatively because simulated transmission from one port to the other experiences around 30 dB attenuation, which is several orders of magnitude larger than the one in Figure C-2. Note that very similar results between the 60 GHz and the 120 GHz configurations are obtained, confirming that such an effect cannot be effectively mitigated by higher frequency carriers.

Interestingly, this study also sheds another light on the role of confinement as regards bend capability. While conventional designs presented in previous sections exhibit a Poynting confinement around 77.5 % at the maximum single-mode frequency, the new designs in

Figure C-5 actually feature a confinement close to 78.5 %. Note that this slightly higher confinement is the direct result of a lower dielectric permittivity difference. Nevertheless, the simulations in Figure C-5 clearly demonstrate that strong confinement is not a sufficient condition to provided bend insensitive propagation.

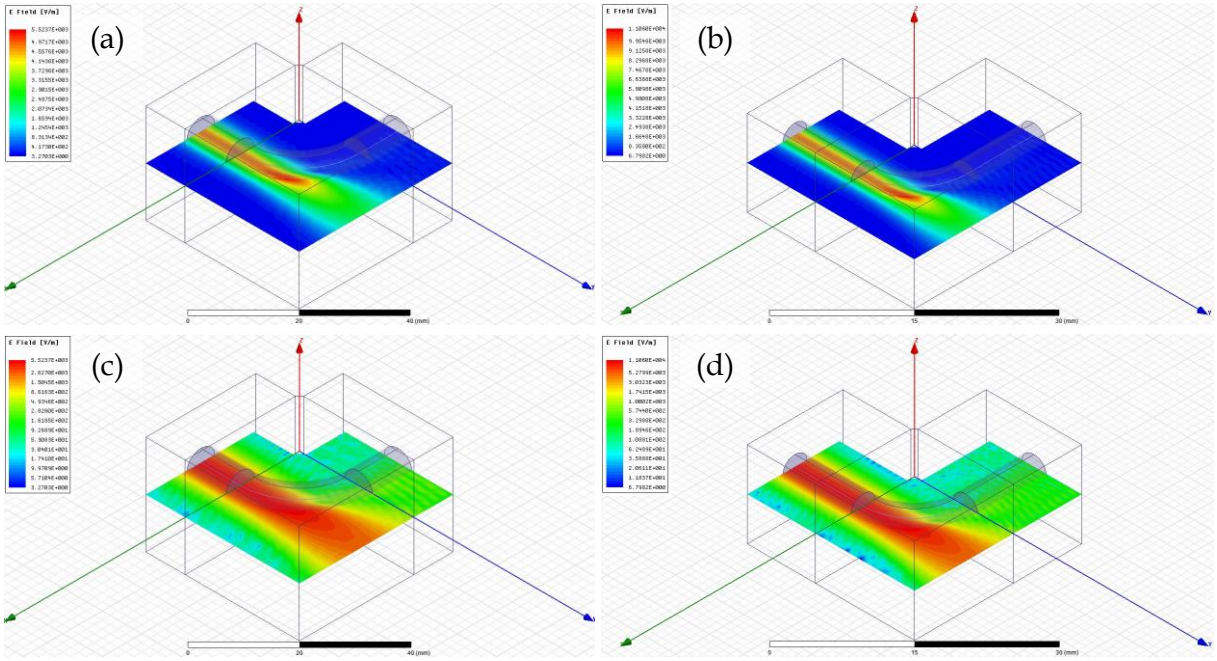

Figure C-5: Transmission through a bended plastic waveguide featuring a low dielectric permittivity step between the core and the cladding. Simulations at 60 GHz are presented in (a) and (c) with a 15 mm radius of curvature using linear and logarithmic scales respectively. (b) and (d) show similar simulations at 120 GHz with a 7.5 mm radius of curvature. All designs are scaled appropriately to operate at the maximum single-mode frequency.

C.5 Conclusion

To conclude, it has been demonstrated in this Appendix that the ability to manage bends in plastic waveguides improves as a function of frequency for a given design. A further study indicates that appropriate dimensioning for the considered frequency provide the very same bending capability once normalized with respect to the wavelength. Therefore, the two investigated waveguides here at 60 and 120 GHz exhibit equivalent bending losses for a given normalized bending radius. Consequently, the 120 GHz counterpart can be bent twice as much as the 60 GHz one in practice.

One could conclude hastily from these results that a large Poynting confinement is necessary to manage practical bends. We then demonstrate that this condition is actually not sufficient. In fact, when considering a cladding with a higher dielectric constant, yet leading to a slightly improved confinement, the bending capability decreases significantly. In other words, the Poynting confinement is definitely not the only parameter to be considered to characterize waveguides sensitivity to bends. This latter result is especially instructive if cladded or foam-coated plastic waveguides are envisioned to enhance external contact robustness. It clearly advocates for the use of materials with ultra-low dielectric permittivity in the cladding region, as close to air as possible, or ultimately air cavities as suggested in the Magic Wheel design.

Besides, negligible reflection losses and polarization rotations are obtained when sweeping the radius of curvature. Noticeable, but weak, couplings to higher order modes like the TM_{01} mode are reported. Although these modes may not be able to propagate over long distances due to lower confinement and stronger environment sensitivity, the limits of the simulation setup have been highlighted, requiring further investigations to improve the quantitative estimation of these effects.

Appendix D

The Energy - Bandwidth Trade-off in Digital RF Modulations

D.1 Introduction

In this Appendix, the fundamental trade-off between spectral and energy efficiencies is exposed and illustrated through the most popular examples of digital modulations. First, the Shannon-Hartley theorem is recalled in Equation (D-1) showing that a given channel capacity C expressed in bits per second actually depends on both the available bandwidth B and the signal to noise ratio S/N (SNR expressed linearly). In other words, this equation states that an error-free data transmission (excluding error-correction algorithms) is possible if the couple made of the bandwidth and the signal power is dimensioned appropriately. In a context of scarce available bandwidth, this relation is very important because it shows that higher data rates are made possible by increasing the SNR. However, for a given bandwidth, increasing the emitter output power, or reducing receiver noise factor, are not sufficient. In addition, the system modulation should be modified accordingly to enable more bits to be transmitted and received per second. Higher spectral efficiency modulations should therefore be chosen, as more bits are transmitted in the same bandwidth and during the same time unit. It is thus clear that higher SNR is necessary to operate, resulting in higher power consumption. For bandwidth-limited systems (SNR >> 1) as encountered in most high-speed applications, SNR requirements may in fact increase exponentially, as stated in Equation (D-2). This result means that the system energy efficiency, which is defined as the ratio of the power consumption and the achieved data rate, will drop rapidly as a function of the channel capacity, making such an approach prohibitive in certain applications. Note that in Equations (D-1) and (D-2) integrated noise power N accounts for Gaussian noise as well as interference sources.

Shannon-Hartley theorem

$$C = B \log_2\left(1 + \frac{S}{N}\right) \tag{D-1}$$

Bandwidth-limited regime

$$\frac{S}{N} \geq 2^{\frac{C}{B}} \tag{D-2}$$

Nevertheless, it is worth noting that the Shannon-Hartley theorem does not indicate how to implement the communication in practice. It only represents a theoretical limit that may be far from practical channel capacity realizations. Anyway, the fundamental trade-off opposing energy and spectral efficiencies definitely remains.

In the following, widespread digital RF modulation techniques are presented and concepts like bit error rate (BER) and symbol error rate (SER) are introduced. Furthermore, it is the purpose of this Appendix to provide insightful comparisons between these schemes.

D.2 On-Off Keying (OOK)

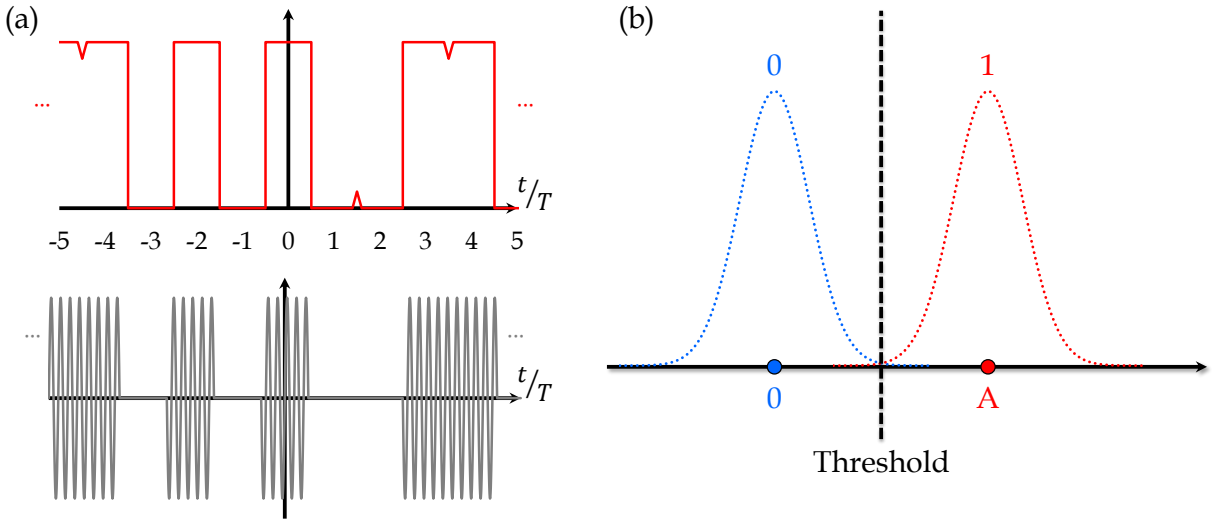

Figure D-1: Illustration of OOK operation. (a) Time-domain representation of transmitted bits (red) and symbols (grey), and (b) constellation diagram (blue and red points). In the latter, Gaussian distributions are superimposed showing possible demodulation errors.

In Figure D-1, the principle of On-Off Keying (OOK) is described. It actually represents the most basic form of RF modulation since the envelope of the RF signal is directly modulated in an On-Off fashion, irrespectively of its phase. Typically, bits 0 induce no signal transmission while bits 1 are characterized by a given amplitude RF signal. The RF waveforms associated to bits are called "symbols". They lead to the constellation diagram in Figure D-1 (b), which is thus extremely simple. This conventional representation makes it clear that a threshold should be placed in the middle of the two points to ensure correct recognition of the symbols.

However, in practical systems, some random noise is likely to *broaden* these points, turning them into density probabilities with Gaussian profiles (dotted lines). As illustrated in Figure D-1 (b), this phenomenon may occasionally leads to wrong symbols detections. The mean occurrence of these demodulation errors is known as the symbol error rate (SER), which directly translates into bit error rate (BER) in the particular case of OOK. From Figure D-1 (b), it is worth noting that minimizing SER or BER is achieved by increasing the distance between the points of the constellations (meaning more signal power) and / or reducing the characteristic width of the Gaussian profiles (meaning less noise power). The relation between SER and SNR is detailed later in section D.9.

D.3 Amplitude Shift Keying (ASK)

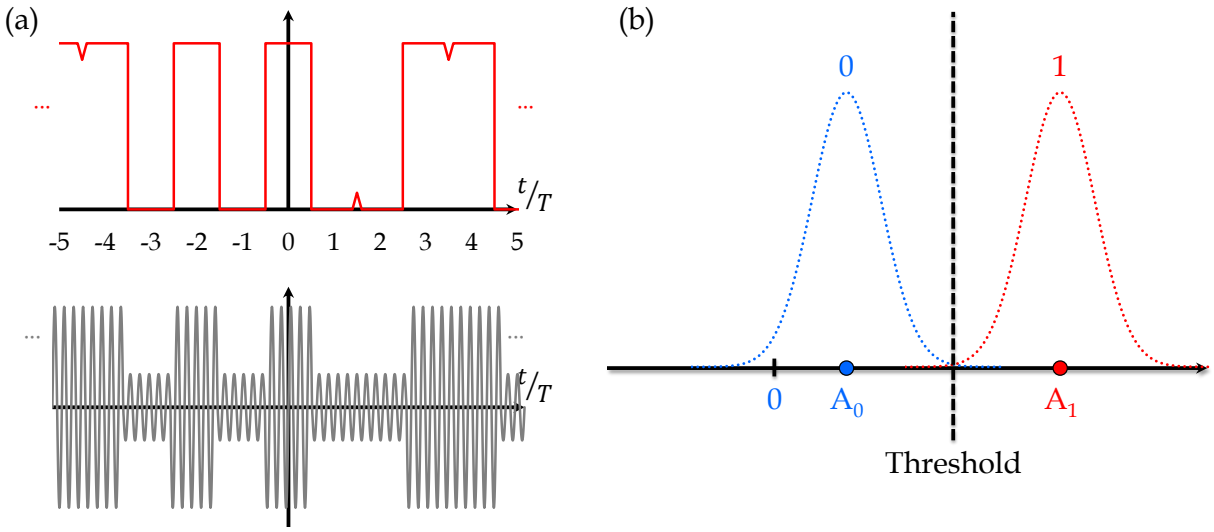

Figure D-2: Illustration of ASK operation. (a) Time-domain representation of transmitted bits (red) and symbols (grey), and (b) constellation diagram (blue and red points). In the latter, Gaussian distributions are superimposed showing possible demodulation errors.

A generalized version of OOK is obtained by allowing a non-zero amplitude transmission during bits 0 as shown in Figure D-2. As the information is still contained in the signal envelope, this modulation is known as Amplitude Shift Keying (ASK). From Figure D-2 (b), one can notice similarities and differences with OOK. If the threshold is still to be placed in the middle of the two points, the threshold value is actually higher because of a higher transmitted power on average. Moreover, the distance between the points of the constellation (which represents the good metric to quantify the useful signal power) is lower and results in degraded SER. Comparatively to OOK, this modulation scheme thus suffers from lower error robustness while still requiring higher average signal powers.

D.4 Pulse Amplitude Modulation (PAM)

Pulse Amplitude Modulation (PAM) generalizes the principle of ASK to M amplitude levels (Figure D-3 (a)). Typically, this number is expressed as a power of 2 so that $M = 2^N$. Consequently, N bits are effectively transferred per symbol, thus increasing achievable data rate in a given bandwidth by a factor N (with respect to OOK or ASK). We can thus define the following spectral efficiency in Equation (D-3). In the case of minimum channel bandwidth for ISI-free signaling ($T_s B = 1$), this definition naturally leads to N bit/s/Hz for PAM (Equation (D-4)) and 1 bit/s/Hz for OOK or ASK (Equation (D-5)).

Spectral Efficiency $$\eta_s = \frac{\log_2 M}{T_s B} \quad \text{(bit/s/Hz)} \qquad \text{(D-3)}$$

PAM $$\eta_s = \frac{N}{T_s B} = N \text{ bit/s/Hz} \qquad \text{(D-4)}$$

OOK / ASK $$\eta_s = \frac{1}{T_s B} = 1 \text{ bit/s/Hz} \qquad \text{(D-5)}$$

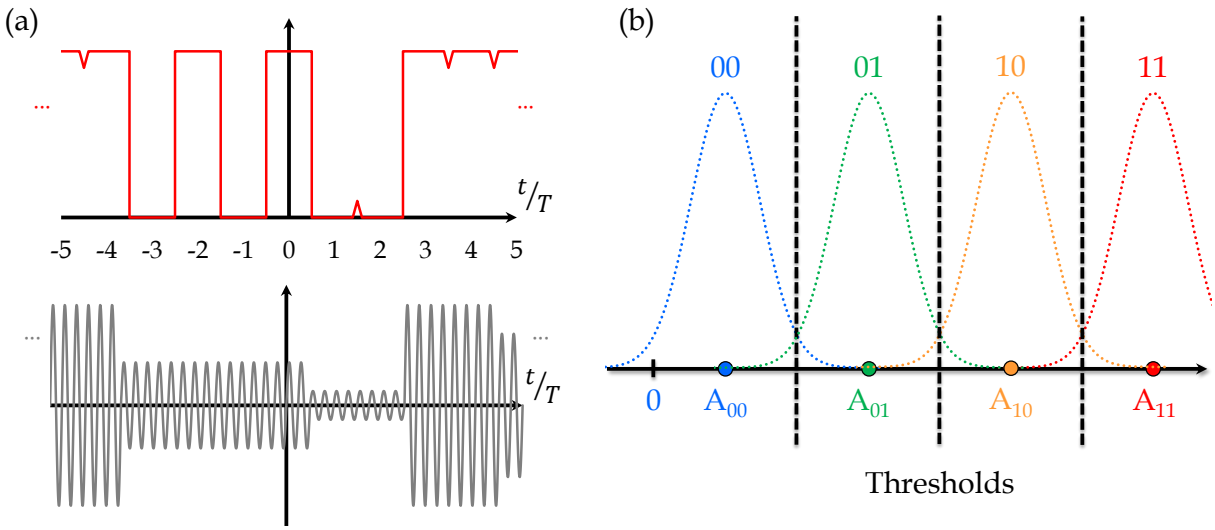

Figure D-3: Illustration of PAM4 operation. (a) Time-domain representation of transmitted bits (red) and symbols (grey), and (b) constellation diagram (colored points). In the latter, Gaussian distributions are superimposed showing possible demodulation errors.

The clear spectral efficiency progress is yet to be paid on the energy efficiency side. It is indeed obvious from Figure D-3 (b) that tolerance to noise diminishes with M as constellation states are more and more densely packed on the same axe. Assuming that M is increased from M to $M + 1$, the number of states is doubled and the distance between them in the constellation is divided by 2. To maintain SER performance, SNR requirements should be increased accordingly.

D.5 Binary Phase Shift Keying (BPSK)

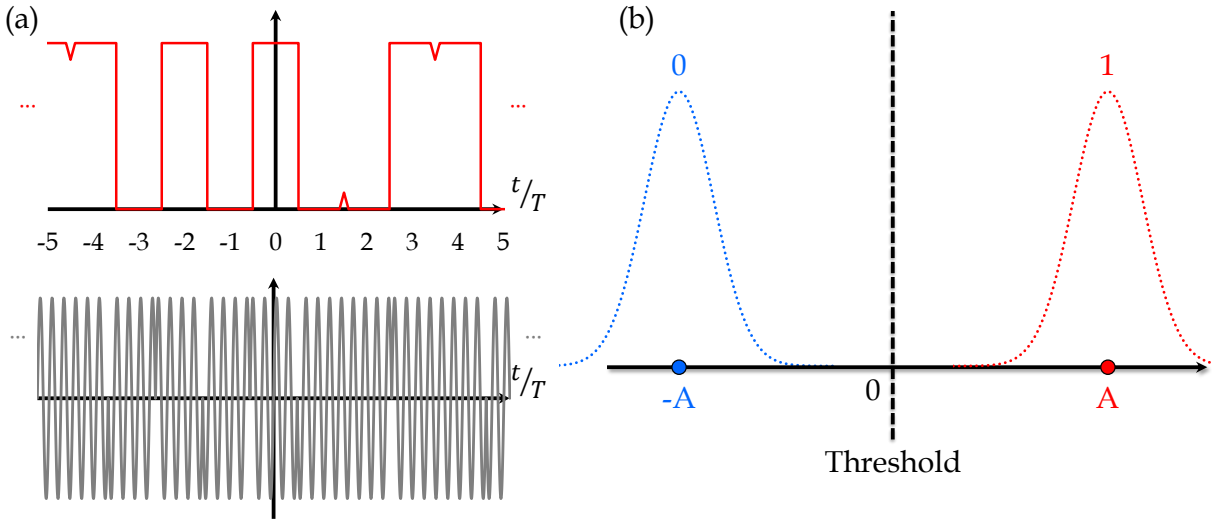

Figure D-4: Illustration of BPSK operation. (a) Time-domain representation of transmitted bits (red) and symbols (grey), and (b) constellation diagram (blue and red points). In the latter, Gaussian distributions are superimposed showing possible demodulation errors.

In opposition to previously described modulations that only contain useful data within their envelope irrespectively of the phase, Binary Phase Shift Keying (BPSK) makes use of the phase to carry the information in a phase-reversal manner as illustrated in Figure D-4. It is

worth noting that the envelope remains constant during the operation, which is therefore compliant with non-linear (and power efficient) amplification. Once again, the comparison with Figure D-1 (b) is particularly instructive. Between these two modulations, it is clear that BPSK exhibits a noticeably lower errors probability, meaning improved robustness, at the expense of a higher average transmitted power. The latter in a BPSK scheme is actually constant and is twice the one of OOK assuming equiprobable bits. To obtain a fair comparison at equal emitted / received powers, BPSK power should be lowered by a factor of 2. While the 0 threshold is maintained, the distance between the points of the constellation is reduced accordingly by a factor of $\sqrt{2}$. From 2A, this distance now becomes ≈ 1.414 A, which is still 40 % larger than the OOK constellation distance. Consequently, in the very same signal and noise conditions, BPSK provides a strong robustness advantage. Moreover, the balanced operation of BPSK simplifies threshold positioning compared to OOK since it is no longer dependent on the average received power.

D.6 *M*-ary Phase Shift Keying (MPSK)

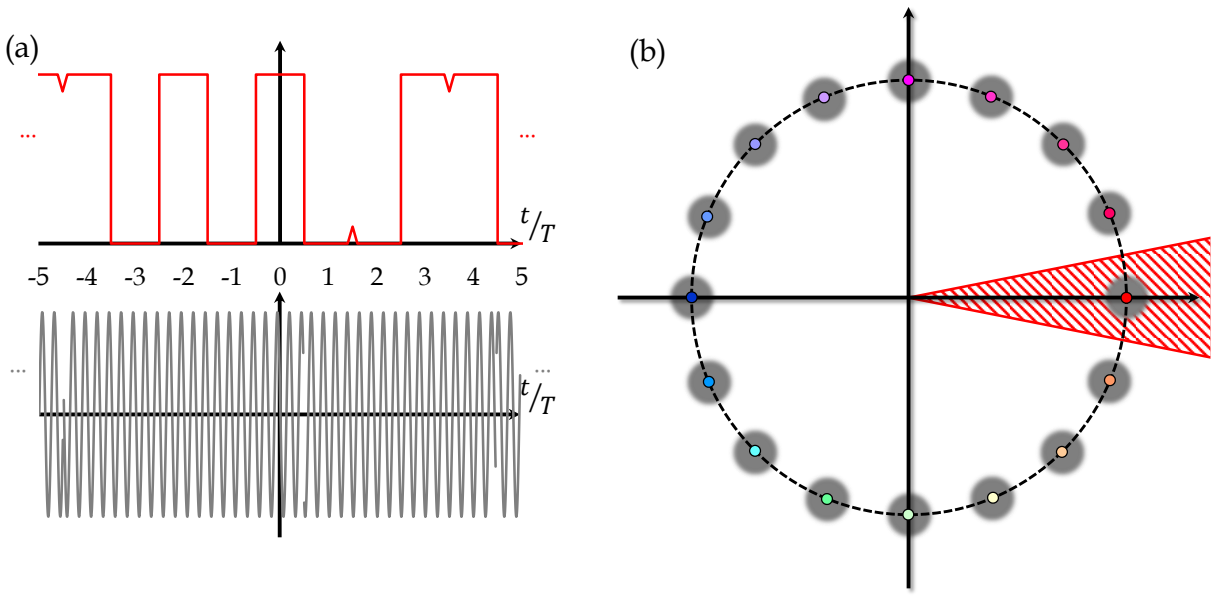

Figure D-5: Illustration of 16-PSK operation. (a) Time-domain representation of transmitted bits (red) and symbols (grey), and (b) constellation diagram (colored points). In the latter, points are broaden to illustrate the impact of noise.

Similarly as PAM offering better spectral efficiency than ASK, *M*-ary Phase Shift Keying (MPSK) increases accessible phase states per symbol. Considering $M = 2^N$ states as well results in the same spectral efficiency $\eta_s = N$ bit/s/Hz. Because the information is encoded in the signal phase, the constellation is better represented in a polar diagram, with each symbol associated to a given angular sector. It is worth noting that such a representation may be also decomposed in the sum of In-phase (I) and Quadrature (Q) components. Supposing that noise impact is similar on these two components, a Gaussian distribution should be superimposed in both vertical and horizontal directions. In practice, constellation states are therefore broaden in halos instead of points, as illustrated graphically in Figure D-5 (b). Note that it becomes very difficult to identify different symbols in the time domain (Figure D-5 (a)) for large *M* values although signals theoretically exhibit abrupt phase transitions. Furthermore, angular sectors

of the constellation diminish linearly with *M*. An analogous energy / bandwidth efficiency trade-offs is still pregnant, just as evocated before for PAM.

D.7 Quadrature Phase Shift Keying (QPSK)

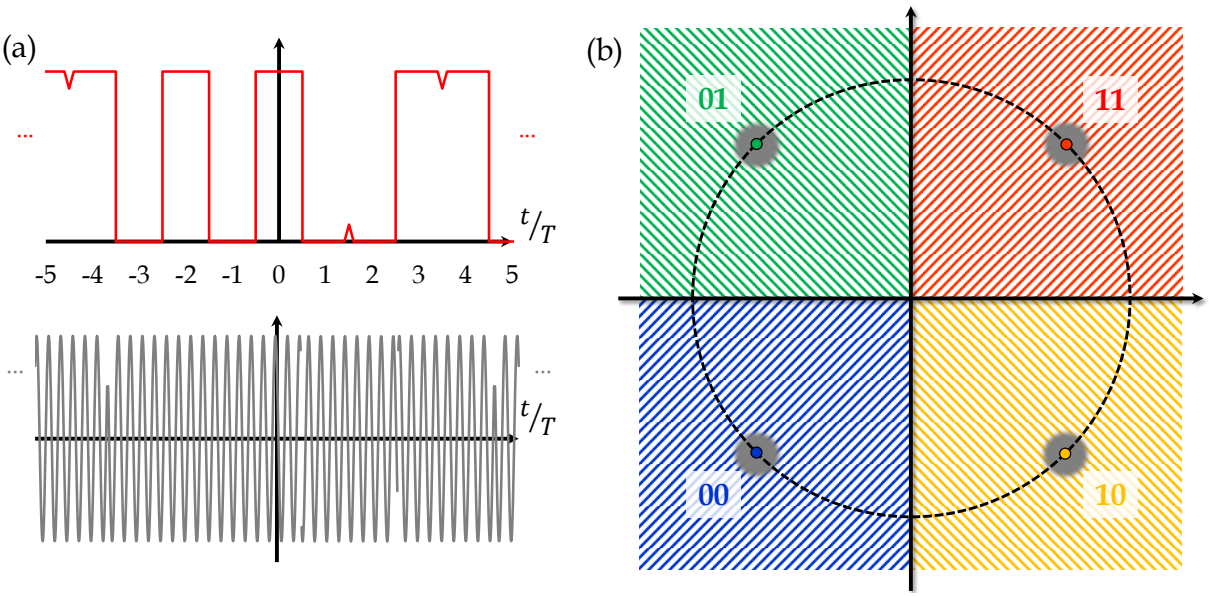

Figure D-6: Illustration of QPSK operation. (a) Time-domain representation of transmitted bits (red) and symbols (grey), and (b) constellation diagram (colored points). In the latter, points are broaden to illustrate the impact of noise.

The following Quadrature Phase Shift Keying (QPSK) can be either represented as a 4-PSK or equivalently as a superposition of two BPSK signals in quadrature. Leveraging on In-phase (I) and Quadrature (Q) components, the spectral efficiency is doubled compared to a conventional BPSK. Nevertheless, it is worth noting that this progress is achieved without compromising error robustness. Assuming that I and Q channels have equal and independent BER referred as to P_b, the SER is expressed in Equation (D-6). With appropriate symbol mapping like Grey encoding, it is possible to neglect double errors in the same symbol so that Equation (D-6) may be simplified.

Error probability $$\mathrm{SER} = P_b(1-P_b) + (1-P_b)P_b + {P_b}^2 \approx 2P_b = 2\ \mathrm{BER} \qquad \text{(D-6)}$$

This result is not surprising when recalling the orthogonal nature of I / Q signals. In principle, each component can be demodulated in parallel by two BPSK demodulators in quadrature. For the same data-rate, a conventional BPSK demodulator would require twice the bandwidth of a QPSK one, increasing integrated noise power by two. To maintain BER performance, received energy per symbol should then be doubled, resulting in an equal consumption with respect to the QPSK scheme.

To summarize, QPSK and BPSK require as much power for equal BER but QPSK benefits from a doubled spectral efficiency (2 bit/s/Hz). Theoretically, such an interesting feature clearly advocates for the use of QPSK in any digital RF system. Practical implementation constraints may still ruin a part of this great advantage. Now if we consider that QPSK is capable of delivering twice the data rate of BPSK in the same bandwidth, this higher data rate

obviously comes at a price of a higher energy requirement. For constant BER performance, doubling the data-rate also doubles the needed signal power at receiver level.

D.8 Quadrature Amplitude Modulation (QAM)

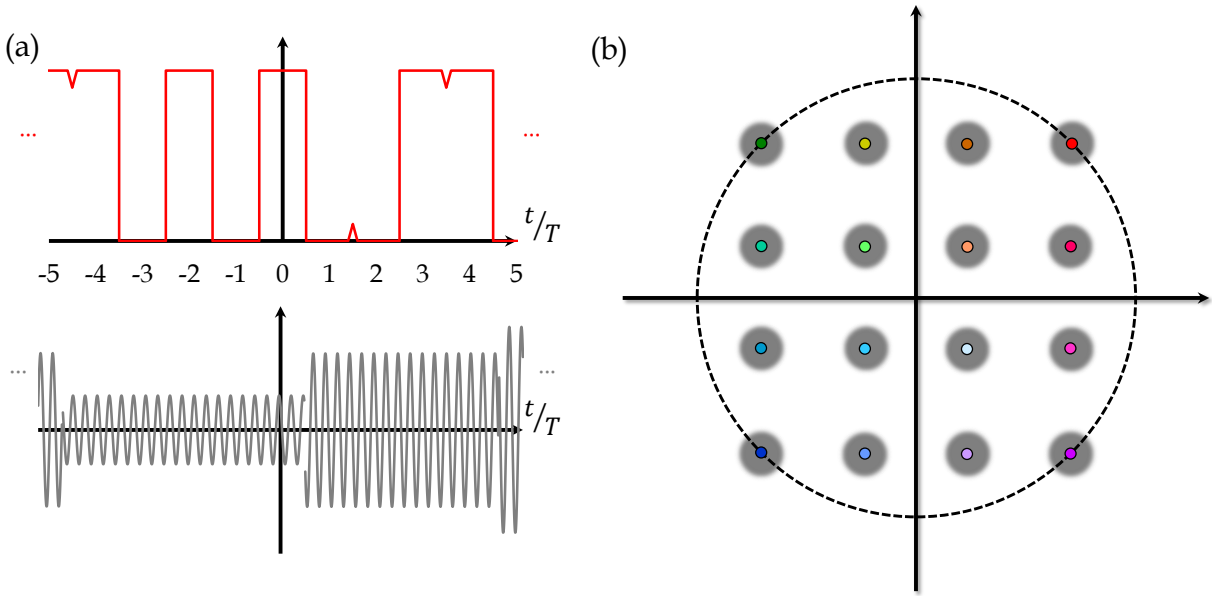

Figure D-7: Illustration of 16-QAM operation. (a) Time-domain representation of transmitted bits (red) and symbols (grey), and (b) constellation diagram (colored points). In the latter, points are broaden to illustrate the impact of noise.

Once again, a generalization of the simple QPSK is possible to increase further its spectral efficiency. It is actually the purpose of Quadrature Amplitude Modulation (QAM) to do so. Contrary to all other modulation schemes reported before, QAM makes use of both amplitude and phase to carry information (Figure D-7 (a)). Just as before, allowing $M = 2^N$ states results in the spectral efficiency $\eta_s = N$ bit/s/Hz. For example, the constellation of 16-QAM is represented in Figure D-7 (b). Note that each state corresponds to a unique combination of I and Q components.

Moreover, it is also clear from Figure D-7 (b) that the trick that allowed *free* spectral efficiency progress when moving from BPSK to QPSK will no longer apply here, since the distance between constellation points reduces drastically with M. This observation is confirmed in the derivations presented in section D.9.

D.9 BER Summary

In the following, SER and BER performances of the precedent modulations are derived from [**Glover, 2000**] and summarized in Table D-1 involving the Q function, which is recalled in Equation (D-7). Note that it is a monotonically decreasing function.

Tail probability function $$Q(x) = \frac{1}{2}\left[1 - \mathrm{erf}\left(\frac{x}{\sqrt{2}}\right)\right] \quad \text{(D-7)}$$

	SER	BER
OOK ASK (*)	$Q\left(\sqrt{\frac{S}{N}}\right) = Q\left(\sqrt{\frac{E_b}{N_0}}\right)$	
BPSK	$Q\left(\sqrt{2\frac{S}{N}}\right) = Q\left(\sqrt{2\frac{E_b}{N_0}}\right)$	
MPSK (M ≥ 4)	$2Q\left(\sin\frac{\pi}{M}\sqrt{2\frac{S}{N}}\right) = 2Q\left(\sin\frac{\pi}{M}\sqrt{2\log_2 M\frac{E_b}{N_0}}\right)$	$\frac{2}{\log_2 M}Q\left(\sin\frac{\pi}{M}\sqrt{2\frac{S}{N}}\right) = \frac{2}{\log_2 M}Q\left(\sin\frac{\pi}{M}\sqrt{2\log_2 M\frac{E_b}{N_0}}\right)$
QPSK	$2Q\left(\sqrt{\frac{S}{N}}\right) = 2Q\left(\sqrt{2\frac{E_b}{N_0}}\right)$	$Q\left(\sqrt{\frac{S}{N}}\right) = Q\left(\sqrt{2\frac{E_b}{N_0}}\right)$
QAM	$4\frac{\sqrt{M}-1}{\sqrt{M}}Q\left(\sqrt{\frac{3}{M-1}\frac{S}{N}}\right) = 4\frac{\sqrt{M}-1}{\sqrt{M}}Q\left(\sqrt{\frac{3\log_2 M}{M-1}\frac{E_b}{N_0}}\right)$	$\frac{4}{\log_2 M}\frac{\sqrt{M}-1}{\sqrt{M}}Q\left(\sqrt{\frac{3}{M-1}\frac{S}{N}}\right) = \frac{4}{\log_2 M}\frac{\sqrt{M}-1}{\sqrt{M}}Q\left(\sqrt{\frac{3\log_2 M}{M-1}\frac{E_b}{N_0}}\right)$

(*) For ASK signaling, signal power S should be interpreted as the *useful* signal power, that it is to say corrected from the power transmitted during low levels.

Table D-1: Summary of SER and BER closed-form formulas for different modulations.

Additionally, SER and BER closed-form expressions of PAM are reported from [**Cho, 2002**] in Equations (D-8) and (D-9) respectively. It is worth noting that all these formulas are based on an additive white Gaussian noise hypothesis under minimum ISI-free filtering. Furthermore, some approximations have been made that should only be valid in the case of high SNR. Appropriate bit mapping, like Grey encoding, is also supposed to make sure that misinterpreted symbols are likely to contain only a single bit error.

SER (PAM)
$$2\frac{M-1}{M}Q\left(\sqrt{\frac{6}{M^2-1}\frac{S}{N}}\right) = 2\frac{M-1}{M}Q\left(\sqrt{\frac{6\log_2 M}{M^2-1}\frac{E_b}{N_0}}\right) \quad \text{(D-8)}$$

BER (PAM)
$$2\frac{M-1}{M\log_2 M}Q\left(\sqrt{\frac{6}{M^2-1}\frac{S}{N}}\right) = 2\frac{M-1}{M\log_2 M}Q\left(\sqrt{\frac{6\log_2 M}{M^2-1}\frac{E_b}{N_0}}\right) \quad \text{(D-9)}$$

As expected, these closed-form formulas mainly depend on the SNR. Nevertheless, a more convenient ratio should be introduced when comparing modulations with each other. This ratio, referred to as $\frac{E_b}{N_0}$, represents the energy contained in one bit normalized by the noise power spectral density. It is therefore independent of the required bandwidth. These relations are plotted in Figure D-8.

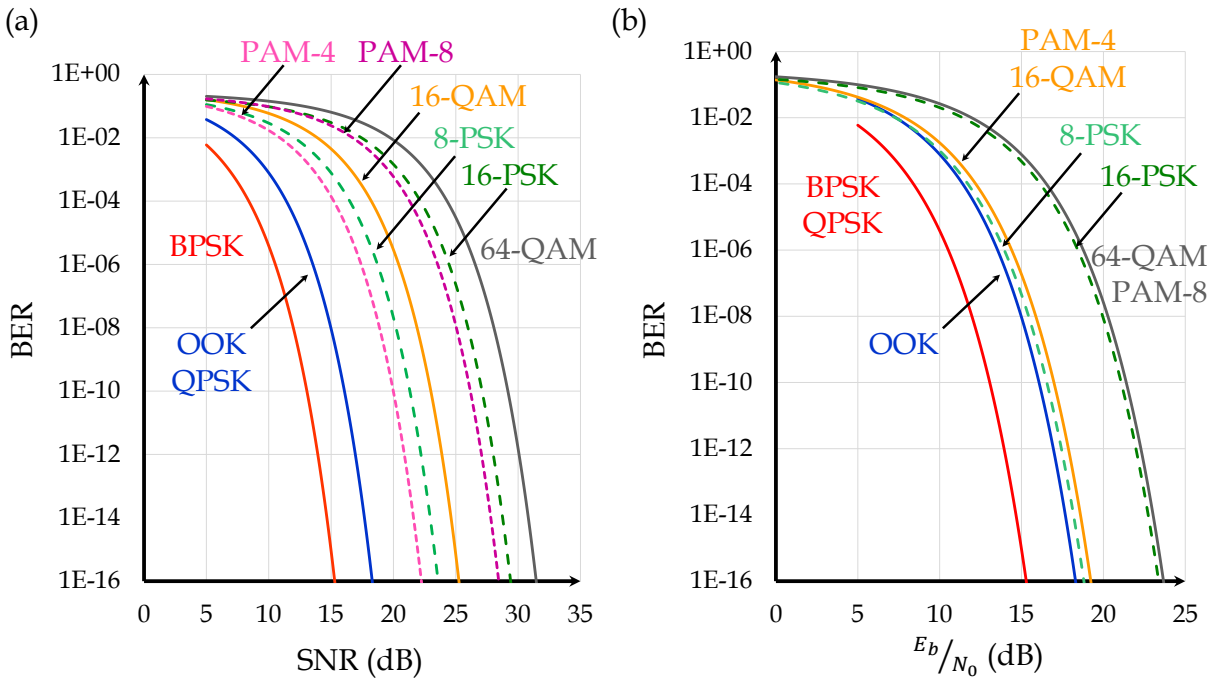

Figure D-8: BER performance for different modulation schemes as a function of SNR (a) or $\frac{E_b}{N_0}$ (b).

Indeed, it is particularly clear from Figure D-8 (b) that the energy efficiency degrades along with the spectral efficiency. Within this trend, QAM modulations typically offer improved performances, e.g. QPSK has the same energy efficiency as BPSK and 16QAM competes with PAM-4, 8-PSK and OOK while still benefiting from better spectral efficiency. Finally, SNR and $\frac{E_b}{N_0}$ requirements for a BER of 10^{-12} are summarized in Table D-2.

	SNR (dB)	$\boldsymbol{E_b/N_0}$ **(dB)**
OOK	17.0	17.0
PAM-4	20.9	17.9
PAM-8	27.1	22.3
BPSK	14.0	14.0
8-PSK	22.2	17.4
16-PSK	28.1	22.1
QPSK	17.0	14.0
16-QAM	23.9	17.9
64-QAM	30.1	16.1

Table D-2: Required SNR or $\frac{E_b}{N_0}$ to satisfy a BER of 10^{-12}.

References

[**Cho, 2002**] K. Cho and D. Yoon. "On the general BER expression of one- and two-dimensional amplitude modulations," *IEEE Transactions on Communications*, Vol. 50, No. 7, pp. 1074-1080, July 2002.

[**Glover, 2000**] I. Glover, P. M. Grant. "Bandpass modulation of a carrier signal" in *Digital Communications*, Prentice Hall, 2000.

Appendix E

Closed-Form Derivation of Adler's Equation

In this Appendix, Adler's equation describing the injection-locking phenomenon is first recalled and analyzed in order to derive a closed-form expression of its transient solution. In this context, a set of constants are introduced in Equations (E-2) and (E-3) corresponding to the (half) locking-range and the steady state phase offset respectively. Note that underlying Adler's physical hypotheses used to obtain Equation (E-1) are not recalled here because of exclusive mathematical concerns.

$$\begin{cases} \varphi(0) = \varphi_0 \\ \dfrac{d\varphi}{dt} = \left(\omega_0 - \omega_{inj}\right) - \omega_L \sin\varphi(t) \end{cases} \tag{E-1}$$

$$\omega_L = \frac{\omega_0}{2Q}\frac{I_{inj}}{I_0} \tag{E-2}$$

$$\phi_{ss} = \operatorname{asin}\left(\frac{\omega_0 - \omega_{inj}}{\omega_L}\right) \tag{E-3}$$

Using the definition in Equation (E-3), Equation (E-1) is formulated alternatively in Equation (E-4). Although a particular solution is easily found in Equation (E-5), the non-linearity of the differential equation prevents the solution of being the sum of a particular solution and a solution of the homogeneous differential equation. In other words, the superposition principle does not apply here. Consequently, the physical interpretation of this primary result is important. In fact, it indicates that the general solution is not an offset version of the solution of the homogenous equation so that the dynamics of the general solution actually depends on ϕ_{ss}.

$$\begin{cases} \varphi(0) = \varphi_0 \\ \dfrac{d\varphi}{dt} + \omega_L \sin\varphi(t) = \omega_L \sin\phi_{ss} \end{cases} \tag{E-4}$$

Particular solution of (E-4) $$\varphi(t) = \phi_{ss} \tag{E-5}$$

To deal with the non-canonical form of Equation (E-4), a first variable change is proposed in Equation (E-6) leading to Equations (E-7) and (E-8). Using a conventional trigonometric relation, Equation (E-9) is derived and therefore expresses the relation between $\varphi(t)$ and $y(t)$ differently. Equation (E-9) is then injected in (E-4) to obtain (E-10). Combining Equations (E-8) and (E-10), another differential equation system satisfied by $y(t)$ is finally formulated in Equation (E-11).

$$\varphi(t) = 2\,\mathrm{atan}\,y(t) \leftrightarrow y(t) = \tan\frac{\varphi(t)}{2} \tag{E-6}$$

$$\frac{d\varphi}{dt} = 2\frac{\frac{dy}{dt}}{1+y(t)^2} \tag{E-7}$$

$$\frac{dy}{dt} = \frac{1+y(t)^2}{2}\frac{d\varphi}{dt} \tag{E-8}$$

$$\sin\varphi(t) = \frac{2\tan\left(\frac{\varphi(t)}{2}\right)}{1+\tan\left(\frac{\varphi(t)}{2}\right)^2} = \frac{2\,y(t)}{1+y(t)^2} \tag{E-9}$$

$$\frac{d\varphi}{dt} = \omega_L \sin\phi_{ss} - \omega_L\frac{2\,y(t)}{1+y(t)^2} \tag{E-10}$$

$$\begin{cases} y(0) = \tan\dfrac{\varphi_0}{2} \\ \dfrac{dy}{dt} = \dfrac{\omega_L}{2}[1+y(t)^2]\sin\phi_{ss} - \omega_L\,y(t) \end{cases} \tag{E-11}$$

Equation (E-11) may be simply recognized as a Riccati's equation, which will guide the following derivation. In spite of its obvious non-linearity, the general Riccati's equation actually requires a particular solution. A constant solution y_0 is searched in Equation (E-12) leading to two possible solutions in Equation (E-13). Because $\cos\phi_{ss} > 0$, these latter simplify in Equation (E-14). Considering that any constant solution leads to a null solution for $\phi_{ss} = 0$, a solution can be eliminated and Equation (E-15) provides the desired constant solution. However, this solution needs to be defined by continuity for $\phi_{ss} = 0$. Without any loss of generality, a simplified formulation is proposed in Equation (E-16) removing any ambiguity. Note that equation is properly defined whatever $\phi_{ss} \in \left[-\frac{\pi}{2}, \frac{\pi}{2}\right]$.

$$\frac{\omega_L}{2}[1+{y_0}^2]\sin\phi_{ss} - \omega_L\,y_0 = 0 \tag{E-12}$$

$$y_0 = \frac{\omega_L \pm \sqrt{{\omega_L}^2 - {\omega_L}^2\sin{\phi_{ss}}^2}}{\omega_L\sin\phi_{ss}} = \frac{1 \pm \sqrt{1-\sin{\phi_{ss}}^2}}{\sin\phi_{ss}} \tag{E-13}$$

$$y_0 = \frac{1 \pm \cos\phi_{ss}}{\sin\phi_{ss}} \tag{E-14}$$

$$y_0 = \frac{1-\cos\phi_{ss}}{\sin\phi_{ss}} \tag{E-15}$$

$$y_0 = \tan\left(\frac{\phi_{ss}}{2}\right) \tag{E-16}$$

In Equation (E-17), a general solution $y(t)$ is then searched as the sum of y_0 and an unknown function $u(t)$. Injecting Equation (E-17) in (E-11), the condition in Equation (E-18) is obtained. Therefore, another variable change should be introduced as proposed in Equation (E-19). From Equations (E-18) and (E-19), Equation (E-20) comes easily and leads directly to Equation (E-21) after simplification (assuming $z(t) \neq 0$).

$$y(t) = y_0 + u(t) \tag{E-17}$$

$$\frac{dy}{dt} = \frac{du}{dt} = -\omega_L u(t)\left[\cos\phi_{ss} - u(t)\frac{\sin\phi_{ss}}{2}\right] \tag{E-18}$$

$$u(t) = \frac{1}{z(t)} \leftrightarrow z(t) = \frac{1}{u(t)} \tag{E-19}$$

$$\frac{-\frac{dz}{dt}}{z(t)^2} = -\omega_L \frac{1}{z(t)}\left[\cos\phi_{ss} - \frac{1}{z(t)}\frac{\sin\phi_{ss}}{2}\right] \tag{E-20}$$

$$\frac{dz}{dt} = \omega_L z(t)\cos\phi_{ss} - \omega_L\frac{\sin\phi_{ss}}{2} \tag{E-21}$$

Equation (E-21) is a canonical first-order differential equation whose solution is straightforwardly expressed in Equation (E-22). Using Equations (E-17) and (E-19), Equation (E-23) is derived. Finally, the constant λ is evaluated at $t = 0$ (initial condition). Equation (E-24) results from this operation, which is then arranged in Equation (E-25) showing the explicit dependence with respect to φ_0 and ϕ_{ss}. Thanks to (E-6), the closed-form solution of Adler's equation is expressed analytically in Equation (E-26). Note that Equation (E-25) is always defined except for the condition $\varphi_0 = \phi_{ss}$. Although this case is not of practical interest (steady-state condition, i.e. no perturbation), $\lambda \to \infty$ hence eliminating any time-dependence in the solution as expected.

$$\exists\, \lambda \in \mathbb{R} \mid z(t) = \lambda\exp(\omega_L t\cos\phi_{ss}) + \frac{\tan\phi_{ss}}{2} \tag{E-22}$$

$$y(t) = \frac{1}{z(t)} + y_0 = \tan\left(\frac{\phi_{ss}}{2}\right) + \frac{2}{\tan\phi_{ss} + \lambda\exp(\omega_L t\cos\phi_{ss})} \tag{E-23}$$

$$y(0) = \tan\frac{\varphi(0)}{2} = \tan\frac{\varphi_0}{2} = \tan\left(\frac{\phi_{ss}}{2}\right) + \frac{2}{\tan\phi_{ss} + \lambda} \tag{E-24}$$

$$\lambda(\varphi_0, \phi_{ss}) = \frac{2}{\tan\frac{\varphi_0}{2} - \tan\left(\frac{\phi_{ss}}{2}\right)} - \tan\phi_{ss} \tag{E-25}$$

$$\varphi(t) = 2\,\mathrm{atan}\left(\tan\left(\frac{\phi_{ss}}{2}\right) + \frac{2}{\tan\phi_{ss} + \lambda(\varphi_0, \phi_{ss})\exp(\omega_L t\cos\phi_{ss})}\right) \tag{E-26}$$

To prove the superiority of the closed-form expression derived in Equation (E-26) compared to the conventional expression, the limit $\phi_{ss} \to 0$ should be considered. Doing so directly leads to Equation (E-27) – as expected – without any mathematical difficulties.

$$\varphi(t) = 2\,\mathrm{atan}\left(\tan\frac{\varphi_0}{2}\exp(-\omega_L t)\right) \tag{E-27}$$

Appendix F

Demonstrator Comparison with the State of the Art

In this Appendix, the demonstrator presented in Chapter 3 is compared to the state of the art (Table F-1). Related references are provided hereafter.

References

[**Fukuda, 2011**] S. Fukuda, Y. Hino, S. Ohashi, T. Takeda, H. Yamagishi, S. Shinke, K. Komori, M. Uno, Y. Akiyama, K. Kawasaki and A. Hajimiri. "A 12.5+12.5 Gb/s full-duplex plastic waveguide interconnect," *IEEE Journal of Solid-State Circuits*, Vol. 46, No. 12, pp. 3113-3125, 2011.

[**Kim, 2013**] Y. Kim, L. Nan, J. Cong and M-C. F. Chang. "High-speed mm-wave data-link based on hollow plastic cable and CMOS transceiver," *IEEE Microwave and Wireless Components Letters*, Vol. 23, No. 12, pp. 674-676, Dec. 2013.

[**Tytgat, 2013**] M. Tytgat and P. Reynaert. "A plastic waveguide receiver in 40nm CMOS with on-chip bondwire antenna," *Proceedings of the IEEE European Solid-State Circuits Conference*, pp. 335-338, 2013.

[**Van Thienen, 2016**] N. Van Thienen, Y. Zhang, M. De Wit and P. Reynaert. "An 18Gbps polymer microwave fiber (PMF) communication link in 40nm CMOS," *Proceedings of the IEEE European Solid-State Circuits Conference*, pp. 483-486, 2016.

[**Voineau, 2018**] F. Voineau, C. Dehos, B. Martineau, M. Sié, M. Perchicot, N. H. Nguyen, A. Ghiotto and E. Kerhervé. "A 12 Gb/s 64QAM and OFDM compatible millimeter-wave communication link using a novel plastic waveguide design," *Proceedings of the IEEE Radio and Wireless Symposium*, pp. 250-252, 2018.

[**Volkaerts, 2015**] W. Volkaerts, N. Van Thienen and P. Reynaert. "An FSK Plastic Waveguide Communication Link in 40nm CMOS," *Proceedings of the International Solid-State Circuits Conference*, pp. 178-180, 2015.

References	[Fukuda, 2011]	[Kim, 2013]		[Tytgat, 2013]		[Volkaerts, 2015]			[Van Thienen, 2016]			**This work [Voineau, 2018]**
Technology	40 nm CMOS	65 nm CMOS		40 nm CMOS		40 nm CMOS			40 nm CMOS			**65 nm CMOS**
Carrier Frequency [GHz]	57 + 80	60		87		120			120			**60**
Medium material	PS	PTFE		PP		PTFE			PTFE			**PTFE**
Link distance [m]	0.12	2	7.6	0.6	9	1.0	4.0	7.0	1.0	8.0	15	**4**
Data Rate [Gb/s]	12.5 + 12.5	6	3.3	9	2.5	12.7	7.4	2.5	17.7	7.6	1.5	**12**
FoM* [m x b]	0.026 + 0.019	0.2	0.42	0.062	0.26	0.11	0.25	0.15	0.15	0.51	0.19	**0.8**
Modulation	Full duplex ASK	ASK		BPSK & multi ASK		CP-FSK			CP-FSK			**64QAM**

$$*\text{FoM} = \frac{\text{Data Rate x Link Distance}}{\text{Carrier Frequency}} \text{ [m x b]}$$

Table F-1: Demonstrator comparison with the state of the art.

Appendix G

Frequency Plan

In this Appendix, the frequency plan evocated in Chapter 4 is proven the only one satisfying the following conditions:

- Reference frequency between 15 and 20 GHz,
- Operating frequencies centered around 75 GHz in the E-band (60 – 90 GHz).

First, these conditions are translated into Equations (G-1) - (G-4).

$$15\ \text{GHz} \leq f_{ref} \leq 20\ \text{GHz} \tag{G-1}$$

$$60\ \text{GHz} < f_1 = n_1 f_{ref} < 90\ \text{GHz}, n_1 \in \mathbb{N} \tag{G-2}$$

$$60\ \text{GHz} < f_2 = n_2 f_{ref} < 90\ \text{GHz}, n_2 \in \mathbb{N} \tag{G-3}$$

$$\frac{f_1 + f_2}{2} = 75\ \text{GHz} \tag{G-4}$$

Combining all Equations (G-1) - (G-4), Equation (G-5) is obtained. Then, considering the integer nature of n_1 and n_2, Equation (G-5) leads directly to Equation (G-6). Moreover, assuming $f_2 > f_1$ so that $n_2 > n_1$, Equation (G-7) is derived from Equations (G-1) - (G-3). One more time, the integer nature of n_1 and n_2 brings a useful simplification leading to Equation (G-8).

$$\frac{75}{20} \leq \frac{n_1 + n_2}{2} \leq \frac{75}{15} \tag{G-5}$$

$$8 \leq n_1 + n_2 \leq 10 \tag{G-6}$$

$$0 < n_2 - n_1 < \frac{30}{15} = 2 \tag{G-7}$$

$$n_2 = n_1 + 1 = n + 1, n \in \mathbb{N} \tag{G-8}$$

Finally, injecting Equation (G-8) in Equation (G-6), the only possible solution is $n = 4$ (Equation (G-9)) resulting in a 16.7 GHz reference frequency (Equation (G-10)) and {66.7 GHz, 83.3 GHz} operating frequencies (Equation (G-11)).

$$8 \leq 2n + 1 \leq 10 \rightarrow n = 4 \tag{G-9}$$

$$f_{ref} = 2\frac{75}{9} \approx 16.667\ \text{GHz} \tag{G-10}$$

$$f_1 = 4f_{ref} \approx 66.667\ \text{GHz}\,,\ f_2 = 5f_{ref} \approx 83.33\ \text{GHz} \tag{G-11}$$

Résumé des travaux de recherche

Comme une lame de fond, l'émergence des communications numériques est en train de modifier sensiblement et indubitablement tous les aspects de notre société. A la fois cause et conséquence, l'essor de nouveaux services tels que la géolocalisation, la musique et la vidéo à la demande, l'informatique dans le nuage, les applications de réalité mixtes, et bien d'autres exemples (dont beaucoup n'existent peut-être pas encore !) entraîne un formidable cercle vertueux technologique. Ainsi, de nombreux objets deviennent « connectés » entraînant la prolifération de circuits électroniques embarqués (capteurs, microcontrôleurs, actuateurs, etc.) souvent associés à une connexion filaire pour l'alimentation et/ou la communication des données. Objet d'intenses recherches en raison de sa présence stratégique, la voiture « autonome » en est actuellement l'illustration parfaite.

Pour rendre possible cette évolution vers un monde de plus en plus numérique et connecté, des liens de communication filaires à la fois haut-débit et bas coûts seront nécessaires. A cette fin, les guides d'ondes en plastique proposés ces dernières années visant les bandes de fréquences millimétriques (mm) offrent un compromis performance / coût très attractif. Profitant en effet de larges bande-passantes de l'ordre de plusieurs gigahertz (GHz), des performances des technologies CMOS avancées aux fréquences mm mais également de tolérances d'assemblage relâchées, des systèmes de communication avec de tels guides d'ondes en plastique pourraient offrir des débits de plusieurs gigabits par seconde (Gb/s) sur des distances de plusieurs mètres à un prix abordable. Leurs caractéristiques les rapprochent ainsi naturellement des applications automobiles.

Dans ce travail, la conception d'un guide d'ondes en plastique est tout d'abord présentée en se basant à la fois sur des résultats théoriques et de simulations électromagnétiques. Bien que les promesses de faible atténuation aient effectivement été confirmées, certaines limitations du confinement et de la robustesse aux contacts extérieurs sont également apparues. De ce fait, compte tenu du fort intérêt des industriels pour leurs applications, ces résultats apportent une contribution importante à l'état de l'art. L'ajout d'une mousse protectrice est brièvement investiguée, confortant les résultats présentés dans l'état de l'art. Cependant une géométrie innovante de guide d'ondes (Magic Wheel) est principalement détaillée. Cette dernière a été brevetée [8] et a été présentée à la communauté en 2018 lors de la conférence *IEEE Radio and Wireless Symposium* [6]. Elle présente par construction des caractéristiques de propagation améliorées, notamment de confinement, grâce à la présence d'une gaine et de cavités d'air internes. De plus, l'absence de symétrie de révolution favorise l'isolation entre les polarisations verticales et horizontales.

Des thématiques « systèmes » sont ensuite explorées afin de construire un système de communication utilisant ce nouveau canal de propagation. Une architecture large-bande combinant la modulation de phase en quadrature (QPSK) et le multiplexage en fréquence est ainsi introduite. Celle-ci se démarque de l'état de l'art par la présence de quatre flux de données en parallèles de 10 Gb/s chacun et par l'utilisation de fréquences porteuses plus faibles pour augmenter l'efficacité énergétique totale de la solution. L'interface entre le circuit et le guide d'ondes a par ailleurs été identifiée comme une limitation potentielle à la bande-passante globale du système. Par conséquent, une transition très large-bande a été conçue à l'aide de moyens de simulations électromagnétiques. Une fois validés par la mesure entre 55 et 95 GHz, ces résultats ont fait l'objet d'un article à la conférence *IEEE International Microwave Symposium* [2, 4] en raison du caractère novateur de la structure imaginée et de la bande-passante obtenue (multipliée par 2 par rapport à l'état de l'art précédent). L'étude système aborde enfin une dernière limitation au niveau de la démodulation des signaux mm QPSK. En effet, comme les techniques usuelles nécessitent des compromis forts entre débit et consommation, une topologie originale a été développée dans ce travail. Basée sur l'utilisation des non-linéarités du mécanisme de verrouillage par injection au sein des oscillateurs, celle-ci s'avère intéressante pour réduire à la fois le nombre de blocs et la puissance électrique nécessaires. Grâce aux bases théoriques introduites dans ce travail, les limitations éventuelles de cette nouvelle technique sont présentées et les implications en termes d'implémentation circuit sont discutées [3].

Enfin, la conception d'un émetteur mm, qui reprend l'architecture précédemment décrite, est déclinée dans une technologie silicium avancée (CMOS 28 nm FD-SOI de STMicroelectronics). De par l'application visée, les spécifications du circuit ont été guidées par le besoin de fonctionner à haut-débit, avec une faible consommation et pour un faible coût. Les contributions majeures issues de ce travail incluent notamment l'introduction de coupleurs hybrides intégrés à haute-performance, répondant aux fortes contraintes de bande-passante imposées par l'architecture, tout en permettant une combinaison des signaux sur la puce de manière innovante. Ce composant a été revisité avec succès en technologie intégrée via l'utilisation de lignes de transmission différentielles couplées magnétiquement et verticalement, ce qui a donné naissance au concept de DVHC [5]. Celui-ci s'est par ailleurs montré facilement accordable en fréquence de 17 GHz à 83 GHz sans limitation, y compris pour la synthèse de signaux en quadrature avec une bonne précision [7]. De plus, des plots ont été optimisés pour réduire la capacité parasite en technologie 28 nm FD-SOI, tout en maintenant la compatibilité avec les règles d'assemblage de type *flip-chip* pour l'intégration future. Ce travail s'est révélé indispensable pour maximiser la bande-passante disponible en entrée / sortie du circuit aux fréquences mm. L'émetteur réalisé est également susceptible de fonctionner selon deux modes : soit en oscillation libre (faible consommation) soit en oscillation forcée (faible bruit de phase) via l'injection d'un signal de référence externe à une fréquence cinq

fois plus faible. Pour ce faire, un circuit de référence utilisant les non-linéarités des inverseurs CMOS a été dimensionné. Ce dernier présente une large plage de capture et des mesures ont confirmé le verrouillage à la cinquième harmonique, et ce avec un excellent bruit de phase. Des mesures sur signaux modulés ont également permis de mettre en évidence la capacité de l'émetteur à transmettre des débits très élevés jusqu'à 9 Gb/s malgré les limitations du banc de démodulation. Ces résultats valident le choix de la technologie et la capacité de fonctionnement à faible puissance [5, 7], ouvrant la voie à des systèmes performants de communication sur guide d'ondes en plastique [6].

Pour conclure, ces travaux de recherche menés au sein d'une collaboration entre le laboratoire IMS Bordeaux, le CEA Leti et l'entreprise STMicroelectronics, couvrent un large spectre de compétences allant de la modélisation / simulation électromagnétique à l'implémentation en technologie silicium, en passant par l'architecture système. Dans chaque thématique, des innovations sont apportées et contribuent par conséquent au développement d'une technologie promise à un bel avenir au cœur des voitures de demain. Ce travail a ainsi permis d'améliorer le niveau de maturité des technologies nécessaires à la transmission par guide d'ondes plastique, tant au niveau du guide d'ondes lui-même que des circuits mm CMOS, dans l'espoir d'accélérer son industrialisation. Depuis mi-2014, date à laquelle les travaux ont commencé à STMicroelectronics, l'enthousiasme excessif qui entourait la thématique en raison de publications prometteuses a peu à peu cédé sa place à une vision plus pragmatique puisque des limitations fondamentales sont apparues, comme le manque de confinement, la sensibilité à la courbure et à la dispersion par exemple. Ces points ont néanmoins été prédits, démontrés et quantifiés. Dans ce sens, il est clair que ces avancées intéresseront autant le monde académique que le monde industriel. Il en résulte malheureusement que les objectifs initiaux de délivrer des débits de plusieurs dizaines de Gb/s sur plusieurs dizaines de mètres semblent hors de portée pour quelques années au moins, restreignant alors les premières applications à des débits plus raisonnables de l'ordre de quelques Gb/s, en ligne avec les performances obtenues dans les démonstrateurs de ce travail.

Références

Publications dans des conférences nationales :

- **[1]** F. Voineau, R. Pilard, B. Martineau, M. Sié, A. Ghiotto, E. Kerhervé. "Conception d'un guide d'ondes en plastique pour le transfert de données à haut-débit et bas coût aux fréquences millimétriques," Proceedings of the XIXth Journées Nationales Microondes (JNM), Bordeaux, June 2015.
- **[2]** F. Voineau, A. Ghiotto, B. Martineau, M. Sié, E. Kerhervé. "Transition ligne micro-ruban / guide d'ondes de 55 à 95 GHz par l'ajout d'une pointe diélectrique et d'une section à double moulure," Proceedings of the XXth Journées Nationales Microondes (JNM), Saint-Malo, May 2017.
- **[3]** F. Voineau, B. Martineau, M. Sié, A. Ghiotto, E. Kerhervé. "Etude d'un concept de démodulation de signaux modulés en phase à haut débit basé sur les propriétés de verrouillage par injection," submitted to the XXIst Journées Nationales Microondes (JNM), Caen, May 2019.

Publications dans des conférences internationales :

- **[4]** F. Voineau, A. Ghiotto, E. Kerhervé, M. Sié, B. Martineau. "Broadband 55 – 95 GHz Microstrip to Waveguide Transition Based on a Dielectric Tip and a Tapered Double-Ridged Waveguide Section," *IEEE International Microwave Symposium (IMS)*, pp. 723-726, June 2017.
- **[5]** F. Voineau, B. Martineau, M. Sié, A. Ghiotto, E. Kerhervé. "A Differential Vertical Hybrid Coupler and Low Capacitance RF Pads for Millimeter-Wave Applications in 28 nm CMOS FDSOI," *18th IEEE Topical Meeting on Silicon Monolithic Integrated Circuits in RF Systems (SiRF)*, pp. 57-59, Jan. 2018.
- **[6]** F. Voineau, C. Dehos, B. Martineau, M. Sié, M. Perchicot, N. H. Nguyen, A. Ghiotto, E. Kerhervé. "A 12 Gb/s 64QAM and OFDM Compatible Millimeter-Wave Communication Link Using a Novel Plastic Waveguide Design," *IEEE Radio and Wireless Symposium (RWS)*, pp. 250-252, Jan. 2018.
- **[7]** F. Voineau, B. Martineau, M. Sié, A. Ghiotto, E. Kerhervé. "A High-Speed Millimeter-Wave QPSK Transmitter in 28 nm CMOS FD-SOI for Polymer Microwave Fibers Applications," submitted to the *IEEE International Microwave Symposium (IMS)*, June 2019.

Brevets :

- **[8]** F. Voineau, A. Ghiotto, E. Kerhervé. Patent reference WO2017191409A1. "Ensemble pour la propagation d'ondes dans la gamme de fréquences comprises entre 1 GHz et 10 THz,"Deposited on May, 3rd 2016.